

Journal of
Mechanics of
Materials and Structures

Volume 4, N° 9

November 2009

 *mathematical sciences publishers*

JOURNAL OF MECHANICS OF MATERIALS AND STRUCTURES

<http://www.jomms.org>

Founded by Charles R. Steele and Marie-Louise Steele

EDITORS

CHARLES R. STEELE Stanford University, U.S.A.
DAVIDE BIGONI University of Trento, Italy
IWONA JASIUK University of Illinois at Urbana-Champaign, U.S.A.
YASUhide SHINDO Tohoku University, Japan

EDITORIAL BOARD

H. D. BUI École Polytechnique, France
J. P. CARTER University of Sydney, Australia
R. M. CHRISTENSEN Stanford University, U.S.A.
G. M. L. GLADWELL University of Waterloo, Canada
D. H. HODGES Georgia Institute of Technology, U.S.A.
J. HUTCHINSON Harvard University, U.S.A.
C. HWU National Cheng Kung University, R.O. China
B. L. KARIHALOO University of Wales, U.K.
Y. Y. KIM Seoul National University, Republic of Korea
Z. MROZ Academy of Science, Poland
D. PAMPLONA Universidade Católica do Rio de Janeiro, Brazil
M. B. RUBIN Technion, Haifa, Israel
A. N. SHUPIKOV Ukrainian Academy of Sciences, Ukraine
T. TARNAI University Budapest, Hungary
F. Y. M. WAN University of California, Irvine, U.S.A.
P. WIGGERS Universität Hannover, Germany
W. YANG Tsinghua University, P.R. China
F. ZIEGLER Technische Universität Wien, Austria

PRODUCTION


PAULO NEY DE SOUZA Production Manager
SHEILA NEWBERY Senior Production Editor
SILVIO LEVY Scientific Editor

See inside back cover or <http://www.jomms.org> for submission guidelines.

Regular subscription rate: \$600 a year (print and electronic); \$460 a year (electronic only).

Subscriptions, requests for back issues, and changes of address should be sent to contact@mathscipub.org or to Mathematical Sciences Publishers, 798 Evans Hall, Department of Mathematics, University of California, Berkeley, CA 94720-3840.

©Copyright 2010. Journal of Mechanics of Materials and Structures. All rights reserved.

 mathematical sciences publishers

BUCKLING OF STIFFENED COMPOSITE PANELS WITH STRINGER TERMINATIONS

ENZO COSENTINO AND PAUL WEAVER

A meshless approach is developed and used to predict buckling of discretely assembled multibay composite panels made from skin and stiffeners. The effect of eccentricity is included in the formulation. Particular emphasis is given to stringer run-outs within a stiffened panel, where abrupt eccentricity can trigger very large transverse displacements of the skin in front of the run-out tip. The model is obtained by combining von Karman's formulation for moderately large deflections in plates with an extended Timoshenko approach for small initial perturbations. Solutions are calculated by means of a Rayleigh–Ritz approach in conjunction with a Galerkin technique. Hilbert's orthogonal eigenfunctions are employed to obtain a generalized Fourier series expansion of the variables of interest. Limits of applicability, convergence of results and further potential exploitations are discussed. Numerical results obtained are compared with finite element analysis.

A list of symbols can be found on page 1532.

1. Introduction

It is becoming increasingly important to make further weight savings with composite cocured/cobonded assemblies. With the new generation of integral composite assemblies, critical and sometimes unexpected failure modes are challenging the weight saving philosophy that is associated with the use of carbon fibre reinforced composites. A major advantage of composites is their inherent ability to tailor elastic properties for maximizing performance. A further advantage is that different components can be assembled together without making use of fasteners, since the load transfer can be achieved through the interlaminar shear stresses arising within the bond line of an adhesive. Unfortunately, laminated composites exhibit relatively poor response when the loads act perpendicular to the fibers' plane. The weakest areas are typically the bond lines. This weakness is sometimes exacerbated by the anisotropic response of laminated composites, which could trigger out-of-plane displacements when panels undergo loads that align with the fibers' plane. Hence, premature failure is likely to happen in the bond line due to disbond or delamination. This behavior is particularly critical in thick-sectioned composite laminates, where the induced through-the-thickness stresses are comparable in magnitude to the main in-plane stresses. The current level of confidence for the prediction of external loads that may cause delamination and/or disbond often precludes those phenomena, such as buckling, which might trigger significant out-of-plane displacements, leading to complex and potentially catastrophic failure modes. As a result, composite panels for aerospace applications are often designed to minimize or eliminate such failure modes, and to allow for redundant load paths, which are able to guarantee the fail safe requirements. "Chicken" fasteners are extensively used in the majority of primary aerospace composite structure, thwarting potential weight

Keywords: stringer terminations, buckling, composite panels.

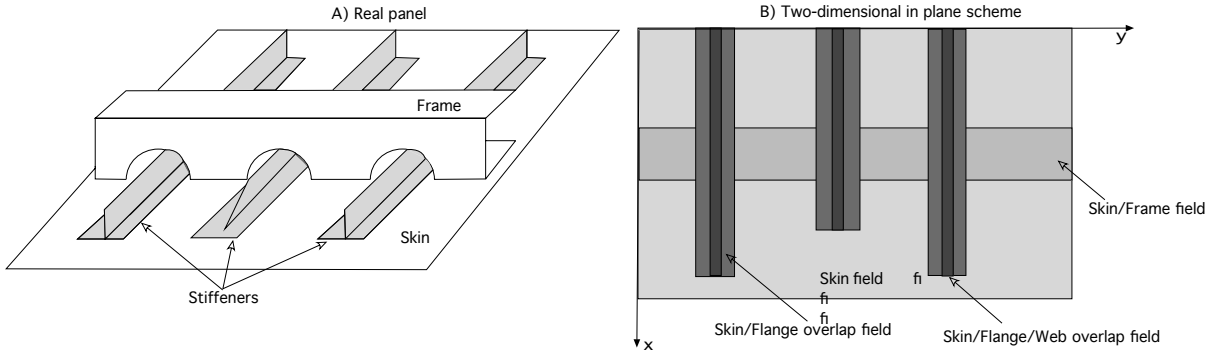


Figure 1. Example of the skin/stringers/frame multibay assembly. Left: realized structure; right: in-plane projections.

saving associated with an “integral” design. Also, as a general design principle (commonly accepted by many of the aerospace industries), the majority of thick-sectioned primary structures are designed not to buckle, thus penalizing the final weight. It is evident that a precise calculation of the buckling loads is vital in order to minimize the structural weight and reserve factors.

The present study is motivated by the need to develop a robust and reliable technique able to combine acceptable accuracy with low computational expense. It is intended to provide aerospace designers with a rapid method that can be used in the preliminary sizing phase, when the need for analyzing hundreds of load cases within restricted time scales, requires very low computational expenses.

2. Field equations

The purpose of the present study is to establish a fast, robust, and sufficiently accurate methodology to predict displacement and stress fields throughout the entire domain of composite skin/stiffeners assemblies in the prebuckling regime and then calculate buckling loads and mode shapes.

The buckling load calculation is done using the formulation developed in [Cosentino and Weaver 2008] with modified eigenfunctions [Cosentino and Weaver 2009] to improve the accuracy of the solution. Two different sets of eigenfunctions are employed to model the transverse displacement and the neutral plane, so providing a more accurate description of the internal loads distribution, particularly near boundaries. As a first approximation, a linear buckling analysis [Kollar and Springer 2003, Chapter 4], which neglects the effect of in-plane loads eccentricities, is proposed.

The use of von Karman nonlinear field equations allows a single variable, that is, the transverse deflection w , to be used. Following [Cosentino and Weaver 2008], the beam properties of the stiffeners are locally homogenized over the plate as represented in Figure 1, right (calculations are shown in Appendix A). The global domain is therefore partitioned into subdomains (fields).

The equivalent field properties are then smeared over the regions defined by the boundaries of the stiffeners' feet (areas in light gray in Figure 1). Abrupt discontinuities of the functions expressing the neutral plane (loads eccentricity) and the structural properties (that is, A , B , and D matrices) occur at the same boundaries.

Membrane strains and the curvatures are expressed as functions of the transverse displacement as follows:

$$\varepsilon_x^0 = \frac{\partial u_0}{\partial x} + \frac{1}{2} \left(\frac{\partial w}{\partial x} \right)^2, \quad \varepsilon_{xy}^0 = \frac{\partial u_0}{\partial y} + \frac{\partial v_0}{\partial x} + \frac{\partial w}{\partial x} \frac{\partial w}{\partial y}, \quad \varepsilon_y^0 = \frac{\partial v_0}{\partial y} + \frac{1}{2} \left(\frac{\partial w}{\partial y} \right)^2 \quad (1)$$

$$k_x = -\frac{\partial^2 w}{\partial x^2}, \quad k_y = -\frac{\partial^2 w}{\partial y^2}, \quad k_{xy} = -2 \frac{\partial^2 w}{\partial x \partial y}. \quad (2)$$

The constitutive equations of the laminate expressed in the partially inverted form are [Jones 1975; Reddy 2004]

$$\begin{bmatrix} \boldsymbol{\varepsilon}^0 \\ \mathbf{M} \end{bmatrix} = \begin{bmatrix} \mathbf{A}^* & \mathbf{B}^* \\ -\mathbf{B}^{*T} & \mathbf{D}^* \end{bmatrix} \begin{bmatrix} \mathbf{N} \\ \mathbf{k} \end{bmatrix}, \quad (3)$$

where

$$\boldsymbol{\varepsilon}^0 = \begin{bmatrix} \varepsilon_x^0 \\ \varepsilon_y^0 \\ \varepsilon_{xy}^0 \end{bmatrix}, \quad \mathbf{k} = \begin{bmatrix} k_x \\ k_y \\ k_{xy} \end{bmatrix}, \quad \mathbf{N} = \begin{bmatrix} N_x \\ N_y \\ N_{xy} \end{bmatrix}, \quad \mathbf{M} = \begin{bmatrix} M_x \\ M_y \\ M_{xy} \end{bmatrix}. \quad (4)$$

The rectangular panel sketched in Figure 1 is subjected to distributed external in-plane loads N_{x0} , N_{y0} , and N_{xy0} around the edges and to a transverse load $q(x, y)$ defined over the rectangular domain. Following, for example, [Mansfield 1989, pp. 85–90], the total strain energy U due to bending is

$$\begin{aligned} U &= \frac{1}{2} \int_0^{l_x} \int_0^{l_y} \mathbf{k}^T \mathbf{M} dx dy = \frac{1}{2} \int_0^{l_x} \int_0^{l_y} \mathbf{k}^T \mathbf{D}^* \mathbf{k} dx dy \\ &= \frac{1}{2} \int_0^{l_x} \int_0^{l_y} \left[D_{11}^* \left(\frac{\partial^2 w}{\partial x^2} \right)^2 + D_{22}^* \left(\frac{\partial^2 w}{\partial y^2} \right)^2 + 4D_{66}^* \left(\frac{\partial^2 w}{\partial x \partial y} \right)^2 + 2D_{12}^* \frac{\partial^2 w}{\partial x^2} \frac{\partial^2 w}{\partial y^2} \right. \\ &\quad \left. + 4D_{16}^* \frac{\partial^2 w}{\partial x^2} \frac{\partial^2 w}{\partial x \partial y} + 4D_{26}^* \frac{\partial^2 w}{\partial y^2} \frac{\partial^2 w}{\partial x \partial y} \right] dx dy. \quad (5) \end{aligned}$$

The potential Ω_N of external in-plane forces is [Cosentino and Weaver 2008]

$$\Omega_{N,L} = \frac{1}{2} \int_0^{l_x} \int_0^{l_y} \left[N_x \left(\frac{\partial w}{\partial x} + \frac{\partial e}{\partial x} \right)^2 + N_y \left(\frac{\partial w}{\partial y} + \frac{\partial e}{\partial y} \right)^2 + 2N_{xy} \frac{\partial(w+e)}{\partial x} \frac{\partial(w+e)}{\partial y} \right] dx dy, \quad (6)$$

where $e(x, y)$ is the neutral plane function which is treated as a moderately large initial perturbation and expanded in generalized Fourier series by means of a Galerkin technique [Cosentino and Weaver 2008; 2009].

Similarly, the potential Ω_Q of the transverse load is [Cosentino and Weaver 2008]

$$\Omega_Q = - \int_0^{l_x} \int_0^{l_y} q w dx dy. \quad (7)$$

The total linear potential energy Π_L of the system is therefore

$$\Pi_L = U + \Omega_{N,L} + \Omega_Q. \quad (8)$$

In order to properly utilize the Rayleigh–Ritz method, approximate expressions for the unknown variables w and for the eccentricity e in generalized coordinates are required, which satisfy the geometric

boundary conditions. The following series expansions satisfy the above conditions:

$$w = \sum_{m=1}^{M_w} \sum_{n=1}^{N_w} w_{mn} X_m(x) Y_n(y), \quad e = \sum_{m=1}^{M_w} \sum_{n=1}^{N_w} e_{mn} \bar{X}_m(x) \bar{Y}_n(y), \quad (9)$$

where $X_m(x)$, $Y_n(y)$, $\bar{X}_m(x)$, and $\bar{Y}_n(y)$ are continuous and indefinitely differentiable functions. Whenever possible, it is recommended to use beam eigenfunctions that satisfy the orthogonality relations [Cosentino and Weaver 2008; 2009] for both the transverse displacement and the neutral plane function.

To simplify software implementation the following vectors use only one index:

$$\begin{aligned} \varphi &= [X_1 Y_1 \quad X_1 Y_2 \quad \cdots \quad X_1 Y_{N_w} \quad X_2 Y_1 \quad X_2 Y_2 \quad \cdots \quad X_2 Y_{N_w} \quad \cdots \quad X_{M_w} Y_1 X_{M_w} Y_2 X_M Y_N]^T, \quad (10) \\ \bar{\varphi} &= [\bar{X}_1 \bar{Y}_1 \quad \bar{X}_1 \bar{Y}_2 \quad \cdots \quad \bar{X}_1 \bar{Y}_{N_w} \quad \bar{X}_2 \bar{Y}_1 \quad \bar{X}_2 \bar{Y}_2 \quad \cdots \quad \bar{X}_2 \bar{Y}_{N_w} \quad \cdots \quad \bar{X}_{M_w} \bar{Y}_1 \bar{X}_{M_w} \bar{Y}_2 \bar{X}_{M_w} \bar{Y}_{N_w}]^T, \\ \mathbf{W} &= [w_1 \quad w_2 \quad \cdots \quad w_{M \times N}]^T, \quad \mathbf{E} = [e_1 \quad e_2 \quad \cdots \quad e_{M_w \times N_w}]^T. \quad (11) \end{aligned}$$

Equations (9) can, therefore, be rewritten, more simply, as

$$w = \sum_{i=1}^{M \times N} w_i \varphi_i(x, y), \quad e = \sum_{j=1}^{M \times N} e_j \bar{\varphi}_j(x, y), \quad (12)$$

where it is straightforward to show that the functions φ_i and $\bar{\varphi}_j$ satisfy the two-dimensional orthogonality relations

$$\int_0^{l_x} \int_0^{l_y} \varphi_p(x, y) \varphi_q(x, y) dx dy \begin{cases} = 0 & p \neq q \\ \neq 0 & p = p \end{cases}, \quad \int_0^{l_x} \int_0^{l_y} \bar{\varphi}_l(x, y) \bar{\varphi}_m(x, y) dx dy \begin{cases} = 0 & l \neq m \\ \neq 0 & l = m \end{cases}. \quad (13)$$

Equations (12), combined with the definition of beam eigenfunctions, guarantee that every function defined inside the considered domain and fulfilling the same essential boundary conditions as the panel and the neutral plane, can be expressed as a linear combination of such eigenfunctions.

If M and N are reasonably large integers, then the error induced when truncating the summation is negligible. Yet, generic functions defined with different boundary conditions inside the domain can be expressed as truncated linear combinations by means of a Galerkin technique. This technique is used in [Cosentino and Weaver 2008; 2009] to calculate the e_j in (12).

Expressing the neutral plane as a linear combination of basis functions allows differentiation of the total potential energy in a closed form, obtaining a final compact formulation, which is derived and expressed in (19) and that is also readily implemented in software.

Substituting (12) into (5), (6), and (7) the total potential is expressed as a second order polynomial of the $M \times N$ unknown coefficients w_i . The expressions for U , Ω_N , and Ω_Q are

$$\begin{aligned} U &= \frac{1}{2} \int_0^{l_x} \int_0^{l_y} \sum_{i=1}^{M \times N} \sum_{j=1}^{M \times N} \left(D_{11}^* \varphi_{,xx,i} \varphi_{,xx,j} + D_{22}^* \varphi_{,yy,i} \varphi_{,yy,j} + 4D_{66}^* \varphi_{,xy,i} \varphi_{,xy,j} \right. \\ &\quad \left. + 2D_{12}^* \varphi_{,xx,i} \varphi_{,yy,j} + 4D_{16}^* \varphi_{,xx,i} \varphi_{,xy,j} + 4D_{26}^* \varphi_{,yy,i} \varphi_{,xy,j} \right) w_i w_j dx dy, \quad (14) \end{aligned}$$

$$\Omega_Q = - \int_0^{l_x} \int_0^{l_y} q(x, y) \sum_{i=1}^{M \times N} \phi_i w_i dx dy, \quad (15)$$

$$\begin{aligned} \Omega_{N,L} = & \frac{1}{2} \int_0^{l_x} \int_0^{l_y} \sum_{i=1}^{M \times N} \sum_{j=1}^{M \times N} (N_x \phi_{,x,i} \phi_{,x,j} + N_y \phi_{,y,i} \phi_{,y,j} + 2N_{xy} \phi_{,x,i} \phi_{,y,j}) w_i w_j dx dy \\ & + \frac{1}{2} \int_0^{l_x} \int_0^{l_y} \sum_{i=1}^{M \times N} \sum_{j=1}^{M \times N} (2N_x \phi_{,x,i} \bar{\phi}_{,x,j} + 2N_y \phi_{,y,i} \bar{\phi}_{,y,j} + 2N_{xy} (\phi_{,x,i} \bar{\phi}_{,y,j} + \phi_{,y,i} \bar{\phi}_{,x,j})) w_i e_j dx dy \\ & + \frac{1}{2} \int_0^{l_x} \int_0^{l_y} \sum_{i=1}^{M \times N} \sum_{j=1}^{M \times N} (N_x \bar{\phi}_{,x,i} \bar{\phi}_{,x,j} + N_y \bar{\phi}_{,y,i} \bar{\phi}_{,y,j} + 2N_{xy} \bar{\phi}_{,x,i} \bar{\phi}_{,y,j}) e_i e_j dx dy. \quad (16) \end{aligned}$$

Using the principle of stationary potential energy [Cosentino and Weaver 2008; 2009], we have

$$\frac{\partial \Pi_L}{\partial w_i} = 0, \quad \forall i = 1, \dots, M_w \times N_w. \quad (17)$$

Equations (14), (15), and (16) are now substituted into (17) with the result differentiated with respect to w_i . Algebraic manipulations result in the following linear system of $M \times N$ equations in the $M \times N$ unknowns w_i , $i = 1, \dots, N$:

$$(\mathbf{G} + \mathbf{H})\mathbf{W} = -\bar{\mathbf{H}}\mathbf{E} + \mathbf{Q}, \quad (18)$$

where the vectors \mathbf{Q} , \mathbf{E} and the matrices \mathbf{G} , \mathbf{H} , $\bar{\mathbf{H}}$ are defined as

$$\mathbf{Q}_i = \int_0^{l_x} \int_0^{l_y} q \phi_i dx dy, \quad (19)$$

$$\mathbf{E} = [e_1 \quad e_2 \quad \dots \quad e_{M \times N}]^T, \quad (20)$$

$$\begin{aligned} \mathbf{G}_{ij} = & \frac{1}{2} \int_0^{l_x} \int_0^{l_y} [2D_{11}^* \phi_{,xx,i} \phi_{,xx,j} + 2D_{22}^* \phi_{,yy,i} \phi_{,yy,j} + 8D_{66}^* \phi_{,xy,i} \phi_{,xy,j} + 2D_{12}^* (\phi_{,xx,i} \phi_{,yy,j} \\ & + \phi_{,xx,j} \phi_{,yy,i}) + 4D_{16}^* (\phi_{,xx,i} \phi_{,xy,j} + \phi_{,xx,j} \phi_{,xy,i}) + 4D_{26}^* (\phi_{,yy,i} \phi_{,xy,j} + \phi_{,yy,j} \phi_{,xy,i})] dx dy, \quad (21) \end{aligned}$$

$$\mathbf{H}_{ij} = \frac{1}{2} \int_0^{l_x} \int_0^{l_y} [2N_x \phi_{,x,i} \phi_{,x,j} + 2N_y \phi_{,y,i} \phi_{,y,j} + 2N_{xy} (\phi_{,x,i} \phi_{,y,j} + \phi_{,x,j} \phi_{,y,i})] dx dy, \quad (22)$$

$$\bar{\mathbf{H}}_{ij} = \frac{1}{2} \int_0^{l_x} \int_0^{l_y} [2N_x \phi_{,x,i} \bar{\phi}_{,x,j} + 2N_y \phi_{,y,i} \bar{\phi}_{,y,j} + 2N_{xy} (\phi_{,x,i} \bar{\phi}_{,y,j} + \bar{\phi}_{,x,j} \phi_{,y,i})] dx dy. \quad (23)$$

For a linear buckling analysis, the external transverse load $q(x, y)$ and the effect of the neutral plane eccentricity are neglected. Only the magnitude of the in-plane loads is noteworthy for the onset of buckling. It is assumed that the presence of transverse loads and/or eccentricity only influences the deformed shape of the panel when the external load has reached the critical buckling level. The effect of eccentricity is formally equivalent to a localized transverse bending moment, which does not affect the membrane stretching in a linear calculation. The right-hand side of (18), the associated eigenvalues problem is expressed by

$$(\mathbf{H}^{-1} \mathbf{G} + \lambda \mathbf{I})\mathbf{W} = \mathbf{0}, \quad (24)$$

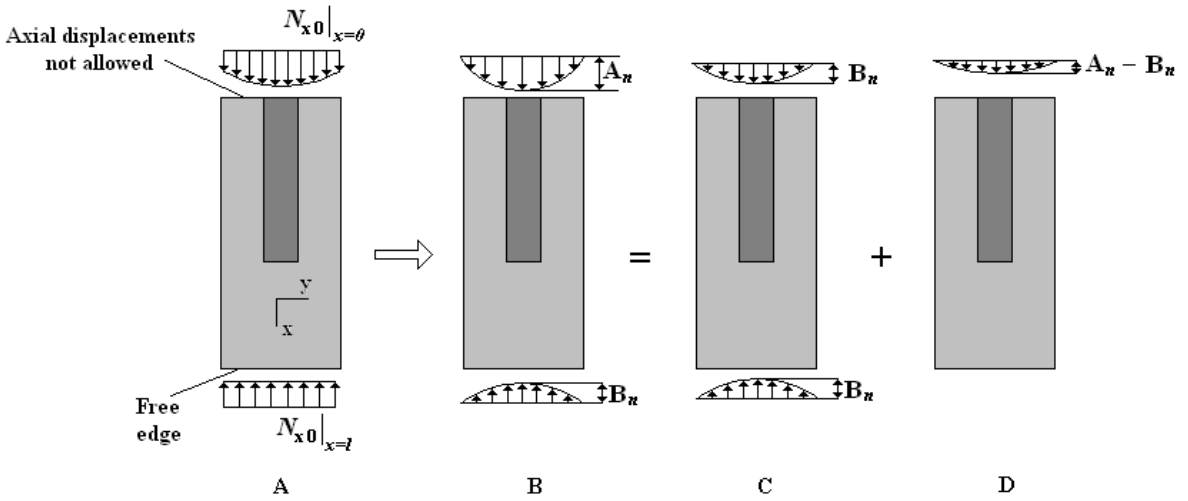


Figure 2. Loads on reinforced panel. (A) Constant axial load at the free edge. (B) Generalized Fourier series components of loads. (C) Uniform loading. (D) Reinforcement perturbation. The first component is shown for illustrative purposes only.

where I is the identity matrix. There are $N \times M$ eigenvalues λ_i and associated eigenvectors $\mathbf{W}_{cr,i}$. The lowest eigenvalue $\lambda_{cr,min}$ and its associated eigenvector $\mathbf{W}_{cr,min}$ are related to the buckling loads N_{cr} and to the buckling mode shape w_{cr} by

$$N_{cr} = \lambda_{min} \begin{bmatrix} N_{x0} \\ N_{y0} \\ N_{xy0} \end{bmatrix}, \quad w_{cr} = \sum_{j=1}^{M_w \times N_w} \varphi_j (\mathbf{W}_{cr,min})_j. \tag{25}$$

To solve the eigenvalues problem of (24), one must be able to integrate the expressions in (16), (22), and (23). This can only be done if the internal in-plane loads distribution is known throughout the domain. This load distribution is evaluated in the following section.

3. In-plane stress function

Consider the simple case, illustrated in Figure 2, of a composite assembly made of a skin (light gray area) and a reinforcement patch (dark gray area).

The panel is loaded by a constant axial load $N_{x0,l}$ acting upon the free edge ($x = l_x$). If an axial constraint acts on the opposite edge ($x = 0$), the axial load distribution (reaction) is not known a priori on that edge. The curve depicted in Figure 2A shows a potential $N_{x0,0}$ distribution on the edge $x = 0$. A peak in the region of the reinforced area is expected.

The magnitude of the peak load mostly depends on the axial stiffness ratio between the skin and the patch, and on the dimensions of the patch. Typically, if the patch free tip is sufficiently far from the constraint, we can assume that the local axial load transfer from the skin to the skin-patch region is complete; therefore the load is introduced in the skin-patch section proportionally to the local-to-global axial stiffness ratio. Assuming that the axial flow distribution N_{x0} at the constrained edge is known, let

us decompose the external edge loads by means of Fourier series:

$$N_{xo}|_{x=0} \cong \sum_{n=1}^{\bar{N}} A_n \sin(\alpha_n y), \quad N_{xo}|_{x=l_x} \cong \sum_{n=1}^{\bar{N}} B_n \sin(\alpha_n y). \quad (26)$$

The two series expansions are generally different if compared term by term (Figure 2B), but since the global equilibrium is satisfied

$$\sum_{n=1}^{\bar{N}} \int_0^{l_y} A_n \sin(\alpha_n y) = \sum_{n=1}^{\bar{N}} \int_0^{l_y} B_n \sin(\alpha_n y). \quad (27)$$

Using the principle of superposition, two stress fields are combined. These are:

- (1) a constant axial stress field equal to the constant axial load $N_{x0,0}$ acting upon the free edge $x = l_x$ (Figure 2C).
- (2) a perturbation $\Delta N_x = N_{x0,l} - N_{x0,0}$ caused by the presence of the reinforcement (Figure 2C) and acting as an external load on the constrained edge.

The first stress field is constant and represents a panel made of a skin only; therefore it is equilibrated and compatible. The elastic problem is completely determined by introducing the stress function Ψ

$$\Psi = \Gamma_x N_{x0,l} + \Gamma_{xy} N_{xy0} + \Gamma_y N_{y0}, \quad (28)$$

where Γ_x , Γ_{xy} , and Γ_y are the circulation functions [Jaunky et al. 1995] defined as

$$\Gamma_x = (y - l_y)^2, \quad \Gamma_{xy} = -(x - l_x)(y - l_y), \quad \Gamma_y = (x - l_x)^2. \quad (29)$$

The second stress field represents a perturbation introduced by the presence of the reinforcement. It is equilibrated, according to (27), but, in general, is not compatible.

Introducing a perturbation stress function $\Delta\Psi$

$$\Delta N_x = \Delta\Psi_{,yy}, \quad \Delta N_y = \Delta\Psi_{,xx}, \quad \Delta N_{xy} = -\Delta\Psi_{,xy} \quad (30)$$

then if no body forces are acting, then overall equilibrium is represented by the biharmonic equation

$$\frac{\partial^4 \Delta\Psi}{\partial y^4} + 2 \frac{\partial^4 \Delta\Psi}{\partial x^2 \partial y^2} + \frac{\partial^4 \Delta\Psi}{\partial x^4} = 0 \quad (31)$$

which is satisfied by

$$\Delta\Psi_n = \sin\left(n\pi \frac{y}{l_y}\right) f_n(x). \quad (32)$$

Substituting (31) into (30) and defining $\alpha_n = n\pi y/l_y$ creates the following ordinary differential equation:

$$\alpha_n^4 f_n(x) - 2\alpha_n^2 f_n''(x) + f_n^{IV}(x) = 0 \quad (33)$$

with the solution

$$f_n(x) = c_{1n} \cosh(\alpha_n x) + c_{2n} \sinh(\alpha_n x) + c_{3n} x \cosh(\alpha_n x) + c_{4n} x \sinh(\alpha_n x). \quad (34)$$

Hence, the stress function is

$$\Delta\Psi_n = (c_{1n} \cosh(\alpha_n x) + c_{2n} \sinh(\alpha_n x) + c_{3n} x \cosh(\alpha_n x) + c_{4n} x \sinh(\alpha_n x)) \sin(\alpha_n x). \quad (35)$$

Constants c_{in} are calculated by enforcing the boundary conditions. First, the distribution of ΔN_{x0} along the edge $x = 0$ must be determined. Rationales for calculation of piece-wise distribution of N_{x0} are given in Appendix B. Knowing the axial flow piecewise distribution at the constrained edge (Figure 2A), and making use of a Galerkin technique [Cosentino and Weaver 2008], the external axial load distributions can be expressed as a generalized Fourier series

$$\Delta N_{x0} \Big|_{x=0_x} \cong \sum_{n=1}^{\bar{N}} (A_n - B_n) \sin(\alpha_n y), \quad \Delta N_{x0} \Big|_{x=l_x} \cong 0. \quad (36)$$

Using the principle of superposition, we assume that the solution, in terms of stress functions, is given by the superposition of \bar{N} basic stress functions $\Delta\Psi_n$ that are solutions of the elastic problem illustrated in Figure 2D.

$$\Delta\Psi = \sum_{n=1}^{\bar{N}} \Delta\Psi_n, \quad (37)$$

where the $\Delta\Psi_n$ are given by (32) and the load amplitudes are given by (36). Following [Timoshenko and Goodier 1982], the constants of integration in (35) are determined by enforcing the following boundary conditions:

For $x = 0$:

$$\Delta N_{xy,n} = -\frac{\partial^2 \Delta\Psi_n}{\partial x \partial y} = 0, \quad \Delta N_{x,n} = \frac{\partial^2 \Delta\Psi_n}{\partial y^2} = A_n - B_n. \quad (38)$$

For $x = l_x$:

$$\Delta N_{xy,n} = -\frac{\partial^2 \Delta\Psi_n}{\partial x \partial y} = 0, \quad \Delta N_{x,n} = \frac{\partial^2 \Delta\Psi_n}{\partial y^2} = 0. \quad (39)$$

After algebraic manipulations, coefficients of integration are obtained and expressed as

$$c_{1n} = \lambda_{1n}(A_n - B_n), \quad c_{2n} = \lambda_{2n}(A_n - B_n), \quad c_{3n} = \lambda_{3n}(A_n - B_n), \quad c_{4n} = \lambda_{4n}(A_n - B_n),$$

where

$$\lambda_{1n} = \frac{1}{\alpha_n^2}, \quad \lambda_{2n} = \frac{1 - \omega_{1n} \sinh(\alpha_n l_x)}{l_x \alpha_n^3}, \quad \lambda_{3n} = \frac{1 - (\omega_{1n}/\omega_{21n}) \sinh(\alpha_n l_x)}{l_x \alpha_n^2}, \quad \lambda_{4n} = -\frac{\sinh(\alpha_n l_x)}{l_x \alpha_n \omega_{2n}} \quad (40)$$

and

$$\omega_{1n} = \frac{\cot \alpha_n}{\alpha_n} + \frac{1}{l_x \alpha_n^2}, \quad \omega_{2n} = (\sin \alpha_n - l_x \alpha_n \cos \alpha_n) \omega_{1n} + l_x \sin \alpha_n. \quad (41)$$

It must be emphasized that solutions $\Delta\Psi_n$ do not identically satisfy term-by-term x -wise equilibrium of the panels as, in general, $A_n \neq B_n$, but their summation does satisfy overall equilibrium. In fact,

$$\sum_{n=1}^{\bar{N}} (A_n - B_n) \sin(\alpha_n y) \cong 0. \quad (42)$$

Also, these stress functions satisfy the natural boundary conditions, given in Figure 2A, that is, only axial loads are acting. At the edges $y = 0$ and $y = l_y$, N_{y0} are zero and only shear forces N_{xy} are present, arising from each term in (37), necessary to satisfy x -wise equilibrium. Note that (42) implies that summation of shears due to its n components is zero [Timoshenko and Goodier 1982, pp. 53–56].

To account for the presence of external shears N_{xy0} and y -wise loads N_{y0} , which were neglected so far, the stress function Ψ defined in (28) must be added. To this end, the resultant stress function Ψ_e is

$$\Psi_e = \Psi + \sum_{n=1}^{\bar{N}} \Delta \Psi_n. \quad (43)$$

This function satisfies the biharmonic equilibrium equation

$$\frac{\partial^4 \Psi_e}{\partial y^4} + 2 \frac{\partial^4 \Psi_e}{\partial x^2 \partial y^2} + \frac{\partial^4 \Psi_e}{\partial x^4} = 0. \quad (44)$$

The resultant stress function Ψ_e is determined once coefficients A_n and B_n are derived. It satisfies the equilibrium equation (44) and the boundary conditions (38)–(39), but it does not satisfy the compatibility condition. To enforce compatibility, a supplementary stress function Ψ_c is superposed. This additional stress function must satisfy the boundary conditions (38)–(39) and guarantee that the resultant stress function Ω

$$\Omega = \Psi_e + \Psi_c \quad (45)$$

satisfies the compatibility equation.

The equilibrium and boundary conditions are fulfilled by choosing the supplementary stress function as

$$\Psi_c = \sum_{k=1}^{M_c \times N_c} \eta_k(x, y) \zeta_k, \quad (46)$$

where ζ_k are unknown coefficients and $\eta_k(x, y)$ are defined as

$$\eta = \begin{bmatrix} X_{c,1} Y_{c,1} & X_{c,1} Y_{c,2} & \cdots & X_{c,1} Y_{c,N_{c_{ew}}} \\ X_{c,2} Y_{c,1} & X_{c,2} Y_{c,2} & \cdots & X_{c,2} Y_{c,N_{c_{ew}}} & \cdots & X_{c,M_{c_{ew}}} Y_{c,1} & \cdots & X_{c,M_c} Y_{c,N_c} \end{bmatrix}^T. \quad (47)$$

If abrupt variations of cross section occur within the domain, the linearized compatibility condition is expressed by [Ashton et al. 1969]

$$\begin{aligned} \frac{\partial^2}{\partial y^2} (A_{11}^* \Omega_{,yy} + A_{12}^* \Omega_{,xx} - A_{16}^* \Omega_{,xy}) + \frac{\partial^2}{\partial x^2} (A_{12}^* \Omega_{,yy} + A_{22}^* \Omega_{,xx} - A_{26}^* \Omega_{,xy}) \\ + \frac{\partial^2}{\partial x \partial y} (-A_{16}^* \Omega_{,yy} - A_{26}^* \Omega_{,xx} + A_{66}^* \Omega_{,xy}) = 0. \end{aligned} \quad (48)$$

Differentiation and reordering gives

$$\begin{aligned} A_{11}^* \Omega_{,yyyy} - 2A_{26}^* \Omega_{,xyyy} + (2A_{12}^* + A_{66}^*) \Omega_{,xxyy} - 2A_{26}^* \Omega_{,xxxy} + A_{22}^* \Omega_{,xxxx} + (2A_{11,y}^* - A_{16,x}^*) \Omega_{,yyy} \\ + (2A_{12,x}^* - 3A_{16,y}^* + A_{66,x}^*) \Omega_{,xyy} + (2A_{12,y}^* - 3A_{26,x}^* + A_{66,y}^*) \Omega_{,xxy} + (2A_{22,x}^* - A_{26,y}^*) \Omega_{,xxx} \\ + (A_{11,yy}^* + A_{12,xx}^* - A_{16,xy}^*) \Omega_{,yy} - (A_{16,yy}^* + A_{26,xx}^* - A_{66,xy}^*) \Omega_{,xy} + (A_{12,yy}^* + A_{22,xx}^* - A_{26,xy}^*) \Omega_{,xx} \\ = 0. \end{aligned} \quad (49)$$

The coefficients ξ_k are determined by solving (46) by means of a Galerkin technique [Cosentino and Weaver 2008]. The weight functions employed are

$$\phi_n(x, y) = \Psi_e(x, y) + \eta_n(x, y). \quad (50)$$

Substituting (45) into (49) and carrying out the differentiations, then after algebraic manipulations we obtain the compact form

$$\Xi \xi = L, \quad (51)$$

where

$$\xi = [\xi_1, \xi_2, \dots, \xi_{N_c \times M_c}]^T, \quad (52)$$

$$\begin{aligned} (\Xi)_{ij} = & \int_0^{l_x} \int_0^{l_y} \left(A_{11}^* \frac{\partial^4 \Psi_{c,j}}{\partial y^4} - 2A_{26}^* \frac{\partial^4 \Psi_{c,j}}{\partial x \partial y^3} + (2A_{12}^* + A_{66}^*) \frac{\partial^4 \Psi_{c,j}}{\partial x^2 \partial y^2} - 2A_{26}^* \frac{\partial^4 \Psi_{c,j}}{\partial x^3 \partial y} \right. \\ & + A_{22}^* \frac{\partial^4 \Psi_{c,j}}{\partial x^4} + (2A_{11,y}^* - A_{16,x}^*) \frac{\partial^3 \Psi_{c,j}}{\partial y^3} + (2A_{12,x}^* - 3A_{16,y}^* + A_{66,x}^*) \frac{\partial^3 \Psi_{c,j}}{\partial x \partial y^2} \\ & + (2A_{12,y}^* - 3A_{26,x}^* + A_{66,y}^*) \frac{\partial^3 \Psi_{c,j}}{\partial x^2 \partial y} + (2A_{22,x}^* - A_{26,y}^*) \frac{\partial^3 \Psi_{c,j}}{\partial x^3} \\ & + (A_{11,yy}^* + A_{12,xx}^* - A_{16,xy}^*) \frac{\partial^2 \Psi_{c,j}}{\partial y^2} - (A_{16,yy}^* + A_{26,xx}^* - A_{66,xy}^*) \frac{\partial^2 \Psi_{c,j}}{\partial x \partial y} \\ & \left. + (A_{12,yy}^* + A_{22,xx}^* - A_{26,xy}^*) \frac{\partial^2 \Psi_{c,j}}{\partial x^2} \right) \phi_i dy dx, \quad (53) \end{aligned}$$

and

$$\begin{aligned} L_i = & - \int_0^{l_x} \int_0^{l_y} \left(A_{11}^* \frac{\partial^4 \Psi_e}{\partial y^4} - 2A_{16}^* \frac{\partial^4 \Psi_e}{\partial x \partial y^3} + (2A_{12}^* + A_{66}^*) \frac{\partial^4 \Psi_e}{\partial x^2 \partial y^2} - 2A_{26}^* \frac{\partial^4 \Psi_e}{\partial x^3 \partial y} \right. \\ & + A_{22}^* \frac{\partial^4 \Psi_e}{\partial x^4} + (2A_{11,y}^* - A_{16,x}^*) \frac{\partial^3 \Psi_e}{\partial y^3} + (2A_{12,x}^* - 3A_{16,y}^* + A_{66,x}^*) \frac{\partial^3 \Psi_e}{\partial x \partial y^2} \\ & + (2A_{12,y}^* - 3A_{26,x}^* + A_{66,y}^*) \frac{\partial^3 \Psi_e}{\partial x^2 \partial y} + (2A_{22,x}^* - A_{26,y}^*) \frac{\partial^3 \Psi_e}{\partial x^3} \\ & + (A_{11,yy}^* + A_{12,xx}^* - A_{16,xy}^*) \frac{\partial^2 \Psi_e}{\partial y^2} - (A_{16,yy}^* + A_{26,xx}^* - A_{66,xy}^*) \frac{\partial^2 \Psi_e}{\partial x \partial y} \\ & + (A_{12,yy}^* + A_{22,xx}^* - A_{26,xy}^*) \frac{\partial^2 \Psi_e}{\partial x^2} - (A_{16,yy}^* + A_{26,xx}^* - A_{66,xy}^*) \frac{\partial^2 \Psi_e}{\partial x \partial y} \\ & \left. + (A_{12,yy}^* + A_{22,xx}^* - A_{26,xy}^*) \frac{\partial^2 \Psi_e}{\partial y^2} \right) \phi_i dx dy. \quad (54) \end{aligned}$$

The components of vector L are computed once the equilibrium stress function (43) is derived. They are functions of the external loads $N_{x,0}$, $N_{y,0}$, and $N_{xy,0}$, and act as load terms in (49).

To calculate partial derivatives of the components A_{ij}^* of the in-plane compliance matrix, a Galerkin technique [Cosentino and Weaver 2008] is employed to express such components as generalized Fourier

series

$$A_{ij}^* = \sum_{k=1}^{M \times N} \omega_{ij,k} \bar{\varphi}_k, \tag{55}$$

where the same basis functions $\bar{\varphi}_k$ already used for the eccentricity are employed.

4. Model validation: in-plane stress field

A composite assembled panel (Figure 3) consisting of a square skin and a rectangular reinforcement (patch) was analyzed to compare and validate our analysis against finite element models (FEM). The in-plane stress field calculated by means of the proposed analytical solution was first compared with the finite element response. In-plane normal forces arising along the sections indicated in Figure 3, right, were compared for two different load cases. The finite element simulation was done using ABAQUS. The domain was discretized using quadratic quadrilateral elements (S8R) in a regular array. Each square has a 2.5 mm edge length. An offset was assigned to all the elements that represent the skin-reinforcement overlap region. The offset equals the difference of the two x -wise neutral planes, overlap and skin regions, respectively. The material properties of the lamina (patch and skin) are given by

$$E_L = 150000 \text{ MPa}, \quad E_T = 8800 \text{ MPa}, \quad G_{LT} = 4800 \text{ MPa}, \quad \nu_{LT} = 0.35, \quad \text{thickness} = 0.2 \text{ mm}.$$

The geometrical parameters are

$$l_x = 100 \text{ mm}, \quad l_y = 100 \text{ mm}, \quad l_p = 40 \text{ mm}, \quad b = 20 \text{ mm}.$$

The stacking sequences are

$$\text{patch: } [0/90/45/-45]_S, \quad \text{skin: } [0/90]_S$$

The enforced boundary conditions are summarized in Table 1. The following sets of functions were employed to model the compatibility stress function Ψ_c and the eccentricity e^2 :

$$X_{c,i} = \sin \frac{i\pi x}{l_x}, \quad Y_{c,j} = \sin \frac{j\pi y}{l_y}, \quad \bar{X}_i = 1 - \cos \frac{i\pi(l_x - x)}{2l_x}, \quad \bar{Y}_j = \sin \frac{j\pi y}{l_y}. \tag{56}$$

The same set of eigenfunctions is used to model both the eccentricity and the components of the in-plane flexibility A_{ij}^* . A total of 10 eigenfunctions for each coordinate were employed to expand the supplementary stress function and A_{ij}^* . Similarly, 10 functions were used to calculate and express the equilibrium stress function Ψ_e .

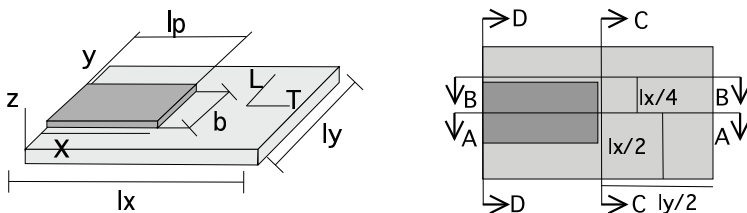


Figure 3. Reinforced panel: geometry (left) and plant view (right).

		Degrees of freedom				
		u_x	u_y	φ_x	φ_y	w
Load case A	<i>a</i>	restrained	restrained	free	—	restrained
	<i>b</i>	free	free	—	free	restrained
	<i>c</i>	free	restrained	free	—	restrained
	<i>d</i>	free	free	—	free	restrained
Load case B	<i>a</i>	restrained	restrained	free	—	restrained
	<i>b</i>	free	restrained	—	free	restrained
	<i>c</i>	free	restrained	free	—	restrained
	<i>d</i>	free	restrained	—	free	restrained

Table 1. Boundary conditions for in-plane stress field experiments.

The first comparison was carried out by imposing a negative unitary axial displacement to the edge *c* (Figure 4, left). Edges *b* and *d* are free to displace in the *y*-direction. Analytical and FEM results are reported in Figure 5, top. Boundary conditions are indicated in Table 1. For the second load case, a negative unit axial displacement was again enforced to edge *b*, but this time the *y*-wise displacements were restrained along the edges *b* and *d*. Results are reported in Figure 5, bottom.

Correlation between FEM and the proposed analytical model is generally very good for both cases. The overlap region is characterized by a considerable amount of in-plane axial load N_x , significantly larger than the far field applied load. Conversely, a noteworthy decrease of the axial load is observed in the portions of the skin that are adjacent to the reinforcement. This result is approximately predicted by assuming that the axial strains and displacements do not vary *y*-wise Appendix A, and it is confirmed by finite element results.

We stress that the predicted axial load transfer at the reinforcement tip is slightly smoother than the transfer calculated by finite element analysis. This is mostly caused by the generalized Fourier series expansion used to model both the compatibility stress function Ψ_c and the components of the in-plane flexibility A_{ij}^* and their partial derivatives.

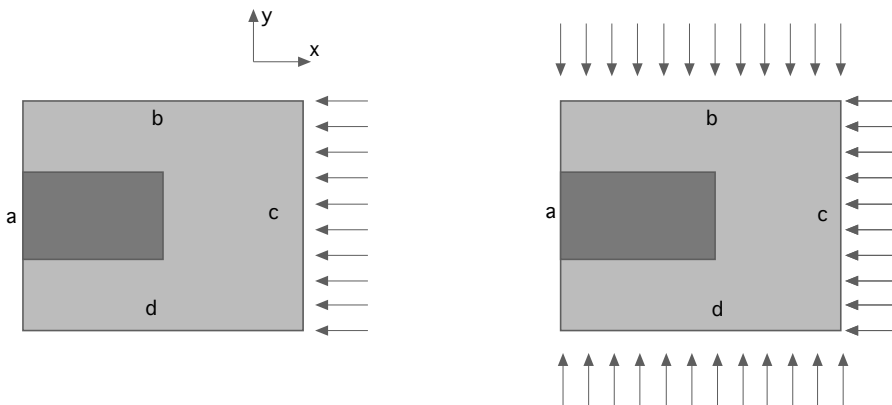


Figure 4. Load cases for in-plane stress field experiments: pure compression (left) and biaxial compression (right).

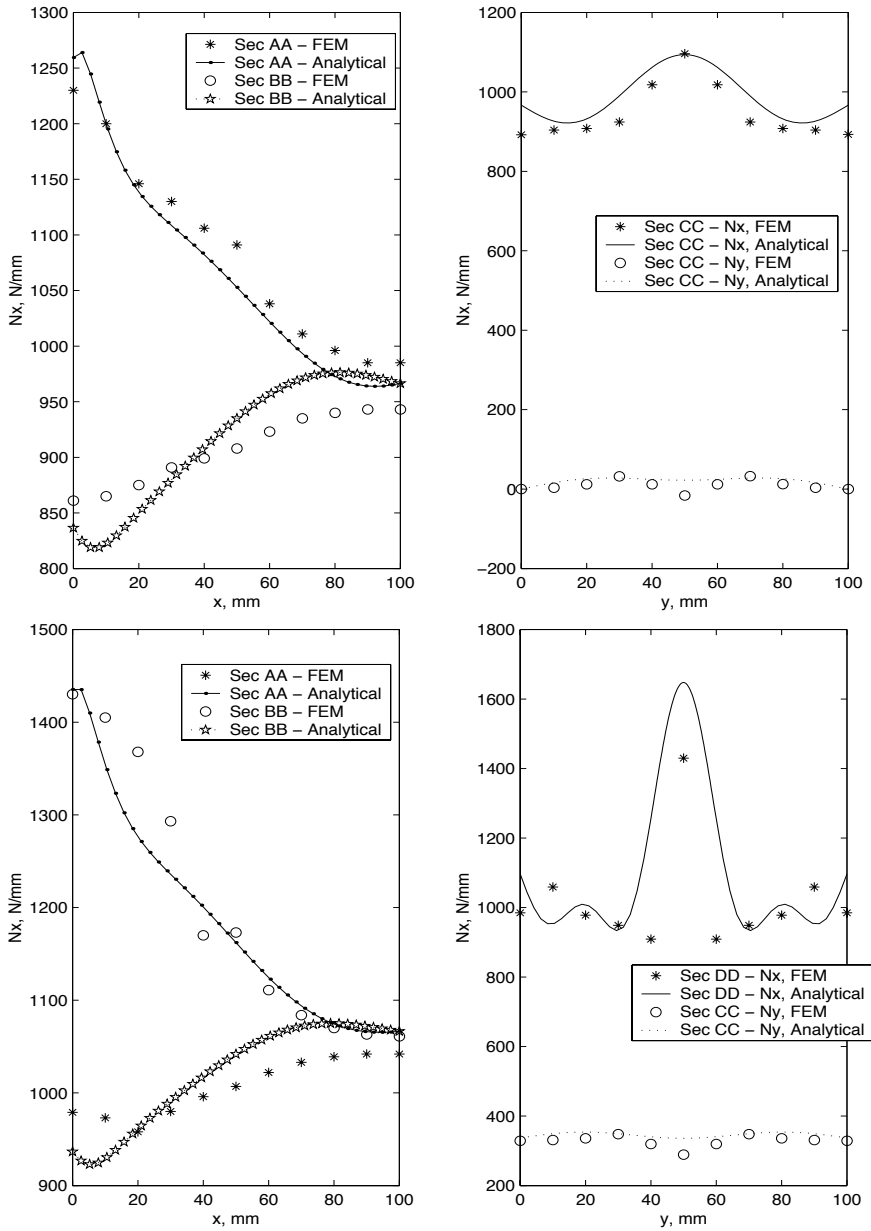


Figure 5. In-plane stress resultant correlation. Top, load case A; bottom, load case B. Left: sections AA and BB; right, section CC.

5. Model validation: convergence study and buckling loads

In order to validate the analytical calculation of critical buckling loads, a series of comparisons with finite element analysis were carried out for five different load cases. The reference structure is the same composite assembly previously analyzed in Section 4. The load cases studied are shown in Figure 6, and

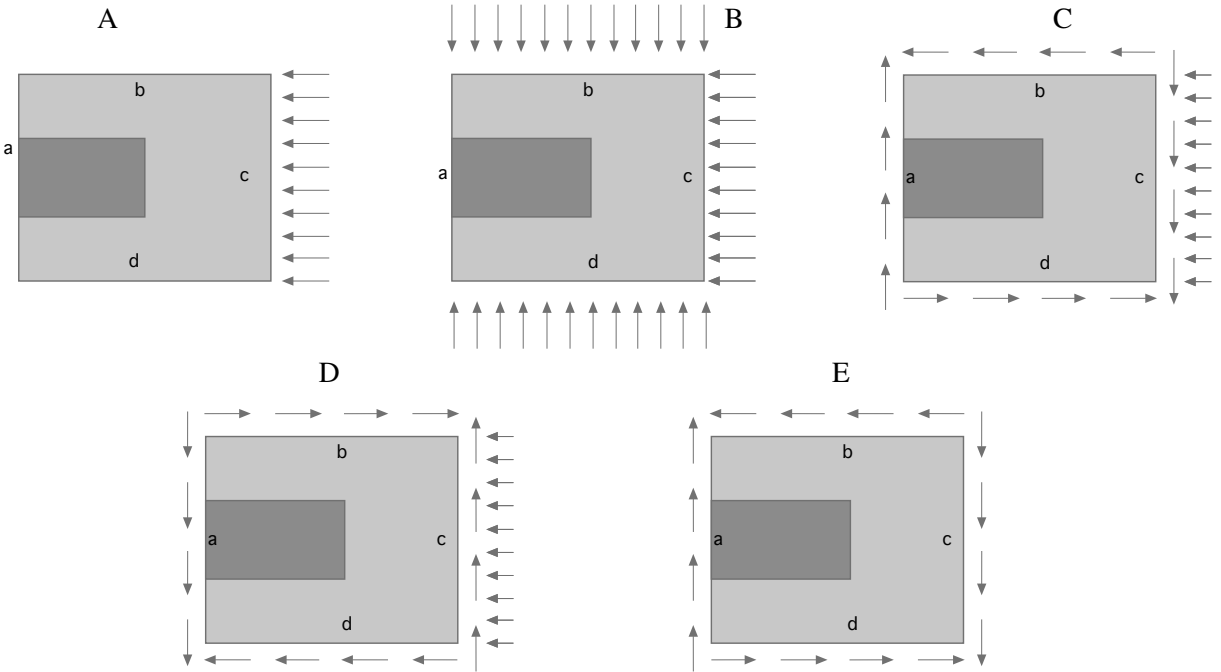


Figure 6. Load cases for buckling load study. Top: pure compression (left); biaxial compression (middle); combined shear-compression (right). Bottom: combined shear-compression with reverted shear (left); pure shear (right).

can be described as follows:

- A. axial compression;
- B. biaxial compression;
- C. combined shear and axial compression, shear/compression ratio equal to 1 ;
- D. combined shear and axial compression, shear/compression ratio equal to -1;
- E. pure shear.

For each load case analyzed, corresponding boundary conditions are reported in Table 2. The eigenfunctions used to model the compatibility stress function Ψ_c are

$$X_{c,i} = \sin \frac{i\pi x}{l_x}, \quad Y_{c,j} = \sin \frac{j\pi y}{l_y}. \tag{57}$$

Since the in-plane stress field cannot be assumed to be uniaxial, the same number of eigenfunctions was used for both the x - and y -directions ($M = N$).

Furthermore, to quantify the degree of accuracy provided by making use of the supplementary stress function, two different buckling analyses were carried out and compared with finite element results. The relative efficiencies of both solution techniques: the equilibrium solution (43) or the equilibrated and compatible solution (45) were assessed. Two different analytical solutions were calculated and compared

	Edge	Degrees of freedom				
		u_x	u_y	φ_x	φ_y	w
Load case A	a	restrained	restrained	free	—	restrained
	b	free	free	—	free	restrained
	c	free	restrained	free	—	restrained
	d	free	free	—	free	restrained
Load case B	a	restrained	restrained	free	—	restrained
	b	free	restrained	—	free	restrained
	c	free	restrained	free	—	restrained
	d	free	restrained	—	free	restrained
Load case C	a	restrained	restrained	free	—	restrained
	b	free	free	—	free	restrained
	c	free	free	free	—	restrained
	d	free	free	—	free	restrained
Load case D	a	restrained	restrained	free	—	restrained
	b	free	free	—	free	restrained
	c	free	free	free	—	restrained
	d	free	free	—	free	restrained
Load case E	a	restrained	restrained	free	—	restrained
	b	free	free	—	free	restrained
	c	free	free	free	—	restrained
	d	free	free	—	free	restrained

Table 2. Boundary conditions for buckling load experiments.

with finite element response. It is noted that the use of solution (43) does not require the compatibility equation (49) to be solved. Hence, it is significantly more efficient in terms of calculation time. Yet, the resultant stress function (45) is expected to be appreciably more accurate.

The first buckling analysis is done by solving (24) and calculating the critical minimum eigenvalues. Expressions for in-plane stress resultants are given by

$$N_x = \Omega_{,yy}, \quad N_y = \Omega_{,xx}, \quad N_{xy} = -\Omega_{,xy}. \quad (58)$$

The second analytical calculation was carried out by neglecting the compatibility equation and arresting the in-plane stress field calculation to the determination of the equilibrium stress function only. In this latter case, the in-plane stress resultants are

$$N_x = \Psi_{e,yy}, \quad N_y = \Psi_{e,xx}, \quad N_{xy} = -\Psi_{e,xy}. \quad (59)$$

Both the equilibrated and the equilibrated and compatible solutions were compared with finite element responses. The finite element model is the same as that employed in the previous section. The critical minimum eigenvalues found analytically were divided by the critical eigenvalues calculated by means of

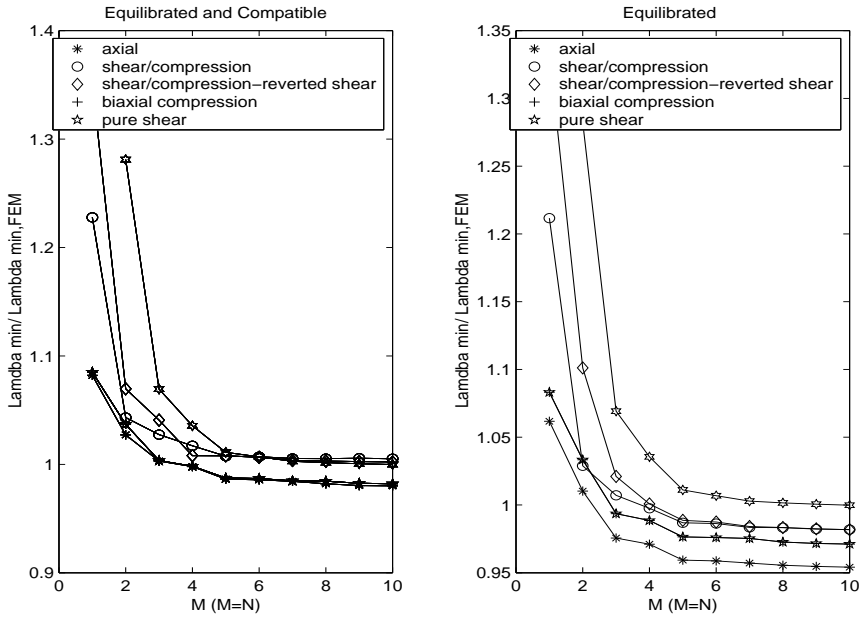


Figure 7. Convergence study: equilibrated and compatible solution (left); equilibrated solution (right).

FEM and results are reported in Figure 7. The sensitivity of both solutions to the total number of functions used to expand the transverse displacement and the compatibility stress function was studied to verify the convergence rate. Both solutions converge with five or more eigenfunctions, but the convergence rate and the accuracy obtained by employing the combined equilibrated and compatible solution are improved. However, the degree of accuracy is more than acceptable for both cases.

A further comparison between the two solutions is presented. The error discrepancy is plotted against the total time required to complete the analysis and results are reported in Figure 8. The error is defined as

$$\text{error} = \frac{\lambda_{\min} - \lambda_{\min,\text{FEM}}}{\lambda_{\min,\text{FEM}}} \times 100\%. \tag{60}$$

Despite guaranteeing better degree of accuracy and faster convergence rates, the use of the compatibility stress function implies calculation times that are between 80% and 90% greater than the calculation times required by solving the buckling problem making use of the equilibrium equation (27) only to determine the in-plane stress field. In the equilibrated and compatible case (Figure 8, left), the error induced is between -2.5% and 1.5% after 10 seconds of computation. In contrast, for the equilibrated case (Figure 8, right), the error is stably confined within a broader range (-4% to 2.5%), but after 4 seconds only. However, the computational effort required by either solution is negligible compared to those required by FEM, which were of more than 80 seconds per load case. (Naturally, the computation times reported do not include model set-up, which is also much larger in the case of FEM analysis.) The use of either solution techniques is shown to perform better than FEM. Of course, the degree of accuracy achievable is excellent if employed in a preliminary sizing phase of an aircraft design, when hundreds of load cases need to be analyzed. In such cases, a relatively simple parametric model may be

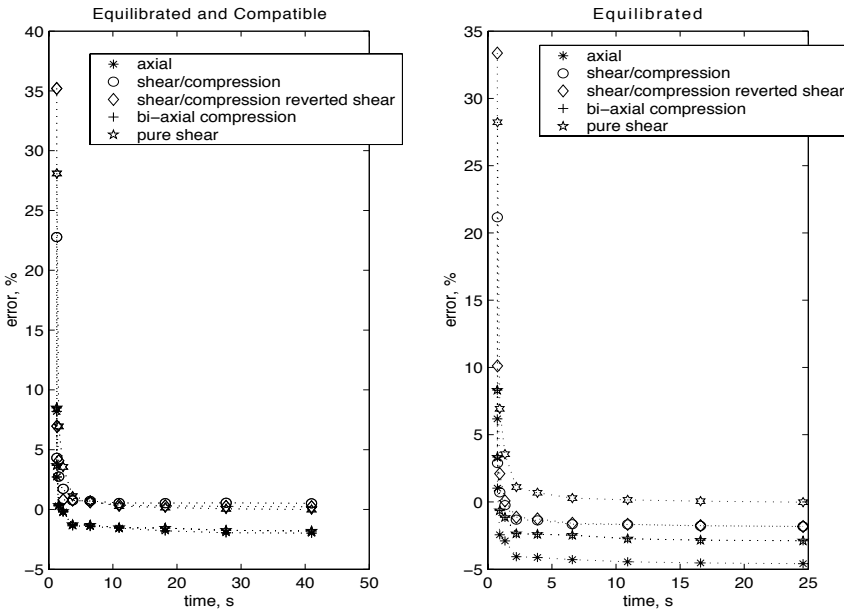


Figure 8. Calculation times: equilibrated and compatible solution (left); equilibrated solution (right).

more suitable than highly detailed analyses. It must be noted that, for each solution, at least half of the calculation time is utilized in computing the G matrix, as defined in (21). This matrix does not depend on the in-plane stress function, but only on the boundary condition assumed for the transverse displacement w . Therefore this calculation is only required once, and need not be repeated for different external loads.

6. Interaction curves and sensitivity analysis

To assess the sensitivity of buckling loads and mode shapes to the geometrical parameters and to the boundary conditions, additional analyses were carried out and compared with FEM. A typical aeronautical panel was taken as a baseline. A skin and a T-shaped stringer characterize the composite assembly. The stringer is run out as illustrated in Figure 9.

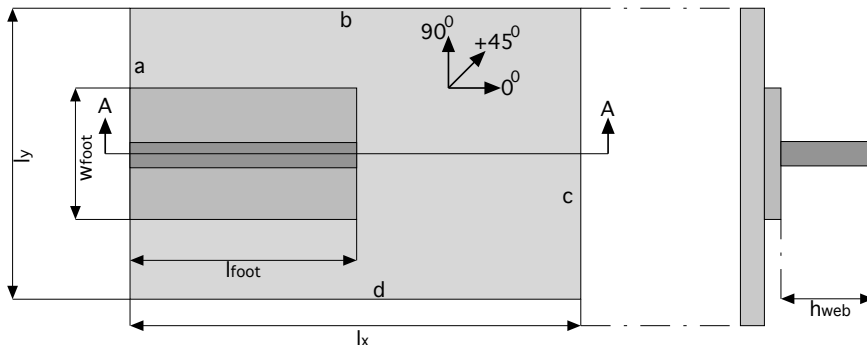


Figure 9. Panel geometry.

Geometry	Configuration	<i>a</i>	<i>b</i>	<i>c</i>	<i>d</i>
Baseline	B1	SS	SS	SS	SS
	B2	C	C	C	C
	B3	SS	C	SS	C
	B4	C	SS	C	SS

Table 3. Boundary conditions: SS = simply supported, C = clamped. (See [Figure 9](#) for the edge labels *a–d*.)

The geometrical parameters of the baseline are

$$l_x = 300 \text{ mm}, \quad l_y = 200 \text{ mm}, \quad l_{\text{foot}} = 200 \text{ mm}, \quad w_{\text{foot}} = 40 \text{ mm}, \quad h_{\text{web}} = 20 \text{ mm}.$$

The stacking sequences are as follows (ply thickness = 0.2 mm in all cases):

$$\text{skin: } [0/45/90/0/-45/0/90]_{2S}; \quad \text{foot: } [0/45/0/90/0/-45/0]_S; \quad \text{web: } [0/45/0/90/0/-45/0]_{2S}.$$

For convenience, the same material properties as the ones were assumed as in [Section 4](#); we list them again for convenience:

$$E_L = 150000 \text{ MPa}, \quad E_T = 8800 \text{ MPa}, \quad G_{LT} = 4800 \text{ MPa}, \quad \nu_{LT} = 0.35, \quad \text{thickness} = 0.2 \text{ mm}.$$

The first series of comparisons were carried out in order to assess the effect of several different boundary conditions. Several edge support configurations were studied, are listed in [Table 3](#).

To assess the effect of flexural/twist anisotropy on buckling loads, the nondimensional parameters

$$\delta = \frac{D_{26}}{\sqrt[4]{D_{11}D_{22}^3}}, \quad \gamma = \frac{D_{16}}{\sqrt[4]{D_{11}^3D_{22}}}, \quad \beta = \frac{D_{12} + 2D_{66}}{\sqrt{D_{11}D_{22}}} \quad (61)$$

(see [\[Weaver and Nemeth 2007\]](#)) were calculated for each subdomain, with results shown in [Table 4](#). The values of δ and γ are much less than 0.1, indicating that flexural/twist anisotropy effects are small [\[Weaver and Nemeth 2007\]](#). Furthermore, a value of $\beta < 1$ indicates relatively poor buckling performance compared with the quasiisotropic lay-up. As such, the lay-ups used are not highly efficient with respect to buckling resistance but do have relatively good axial strength characteristics (due to the relatively large percentage of 0° plies).

Subdomain	δ	γ	β
skin	0.03	0.0247	0.616
skin/foot	0.0153	0.0112	0.623
skin/foot/web	0.00063	0.00034	0.28
mean value	0.0283	0.0232	0.612

Table 4. Nondimensional parameters.

For each configuration, the smallest buckling loads were analytically calculated for a variety of shear/compression ratios and interaction curves were calculated and compared with finite element responses. Results are reported in Figure 10. Superposed are the values obtained from the interaction formula $R_x + R_s^{1.9+0.1\beta} \leq 1$, derived in [Weaver and Nemeth 2008] for long orthotropic plates under combined loading. Here x and s refer to the axial and shear load, respectively, and R represents the ratio of critical load for the combined-loading state to critical value of the corresponding load acting alone. Although this formula was not derived for buckling of panels with stringer run-outs under combined loading, the close match with the present analysis is notable.

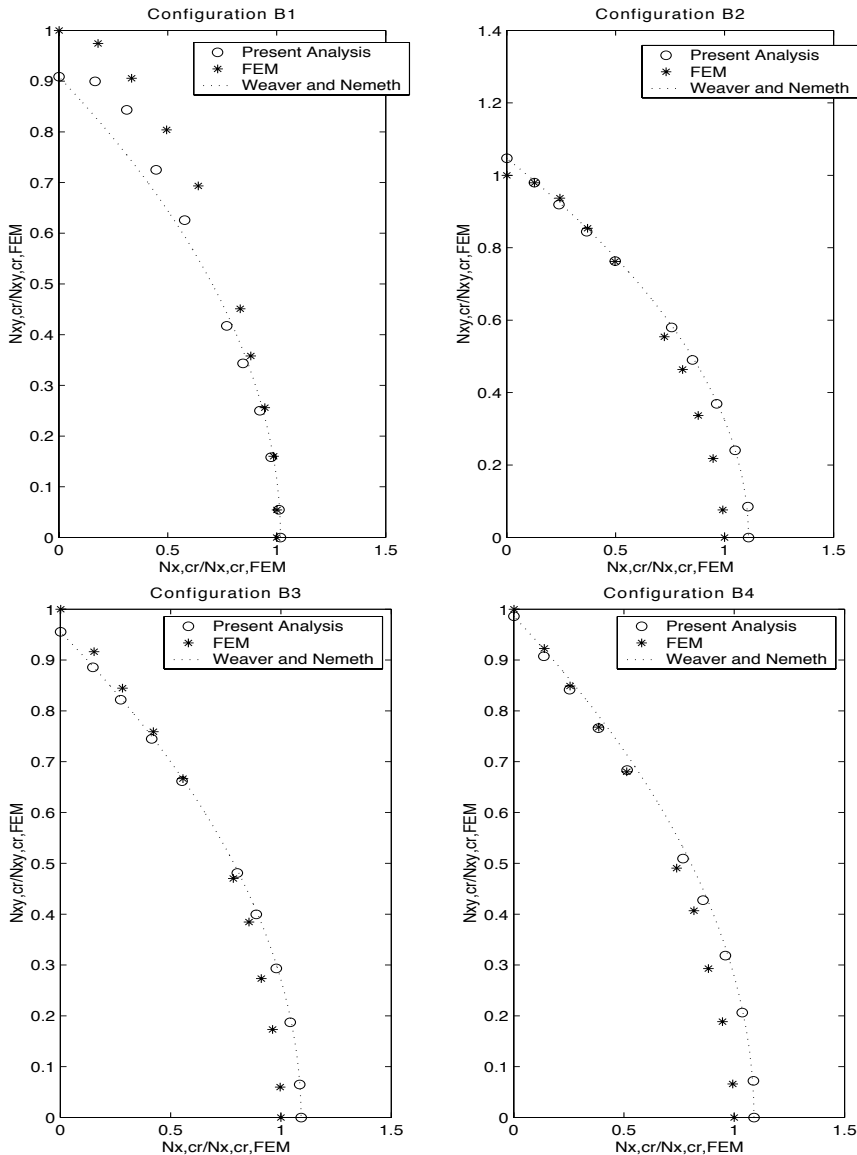


Figure 10. Interaction curves for configurations B1–B4 (top left to bottom right).

Comparisons show excellent correlation with FEM. However, a decrease of accuracy is noted with respect to the first simple configuration analyzed in Section 5. The analytical calculation shows an overall conservatism if compared with FEM, in the buckling loads prediction for configuration B1 (Figure 10, top left), where the induced error in the calculation of the buckling load under pure compression is negligible, while the shear buckling load is underestimated. In contrast, configurations B2 and B4 (right column in 10) show excellent correlation for the buckling loads under pure compression, but increasingly overpredict as the shear/compression ratio tends to zero. Finally, configuration B3 (Figure 10, bottom left) shows overestimated compression-buckling loads and slightly underestimated shear-buckling loads. However, it must be emphasized that the induced error is constant within the range -8% to $+10\%$ for all of the examined configurations and for all of the shear/compression ratios. Calculation times were negligible and also possess the advantage provided by a fully parametric model. Finally, it is noted that the use of different sets of functions to model the out-of-plane displacement may reduce the induced error, but this analysis is beyond the scope of the present research.

Examples of analytically calculated mode shapes are provided in Figures 11 and 12 for there different loading and boundary conditions. Comparisons with FEM show that the shapes are adequately captured by the analytical model.

To assess the sensitivity of the panel's buckling loads to the geometrical parameters, additional sensitivity analyses were performed. In the first set of analyses, the effect of the panel length l_x was studied. Configurations B1 and B2 were analyzed and buckling loads were calculated under pure compression loading condition. Results are reported in Figure 13.

Comparisons show that the average trend is reasonably captured by the analytical approach. However, the effect of the panel x -wise length appears to be smoother in the analytical predictions than in FEM. For configuration B1, in the range of l_x between 300 mm and 250 mm, the buckling loads decrease as the total length decreases. The trend is then reversed in the lower range (l_x between 250 mm and 200 mm). With reference to Figure 9, mode shapes are plotted x -wise along the central Section AA. Results are reported in Figure 14. A noticeable change in the mode shapes occurs when the length varies from 300 mm to 260 mm (first three parts of Figure 14). While for long panels a buckling mode could occur which is localized in the skin in front of the run-out tip (Figure 14, top left), as the length decreases the buckling of the panel alters from a more localized mode involving part of the panel only (the skin

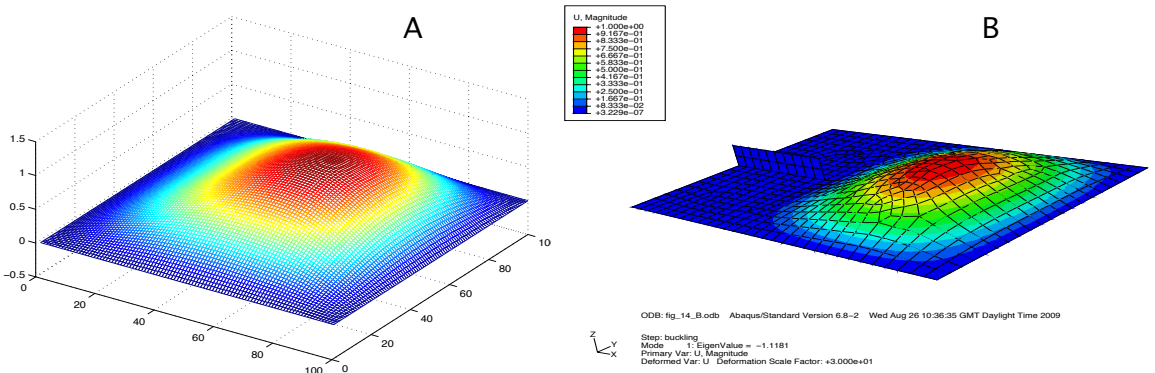


Figure 11. First buckling mode for configuration B1 under pure compression. Left: model; right: FEM.

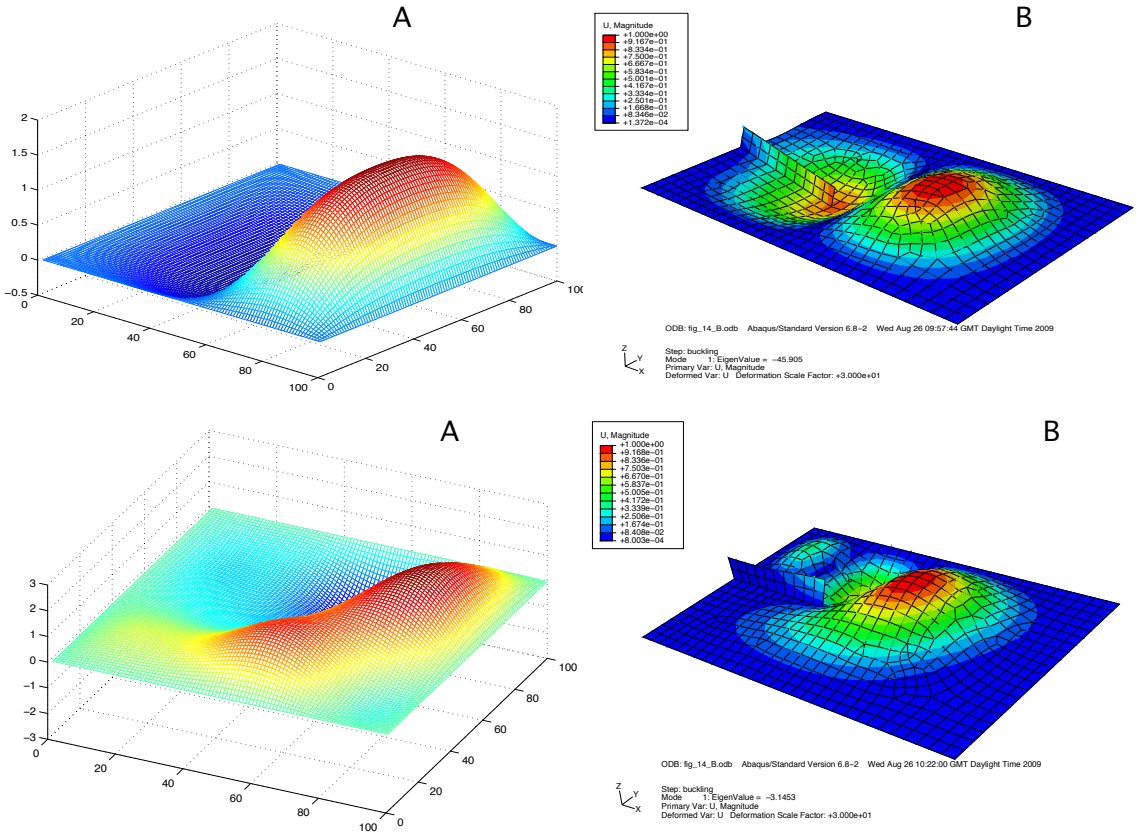


Figure 12. First buckling mode for configuration B2 under pure compression (top) and under combined shear and compression, ratio = 1 (bottom). Left: model; right: FEM.

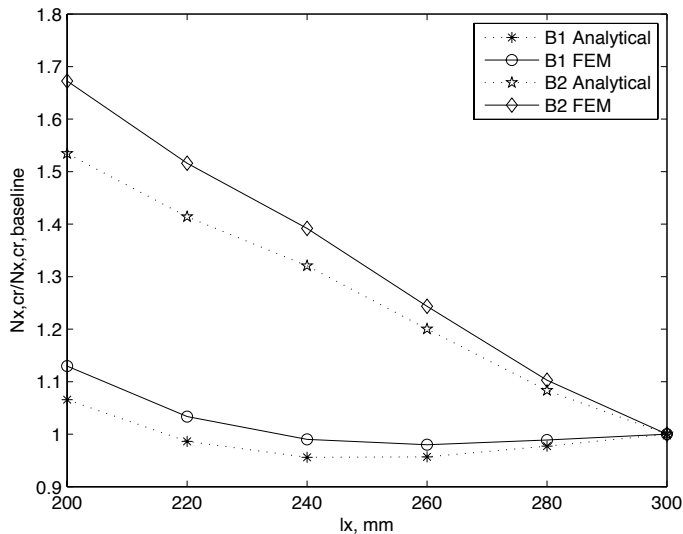


Figure 13. Buckling load sensitivity to panel length.

beyond the stiffener tip), to a more global phenomenon involving the stiffener. In this phase, the effective free x -wise length panel increases, hence a reduction of the buckling loads is observed. As the length continues to decrease, the buckling modes remain self-similar (that is, a global buckling mode with a single x -wise half wave) and the buckling loads increase (last three parts of Figure 14.) The buckling localisation for larger length is also believed to cause the interaction curve to significantly deviate from the formula proposed in [Weaver and Nemeth 2008], as seen in Figure 10, top left.

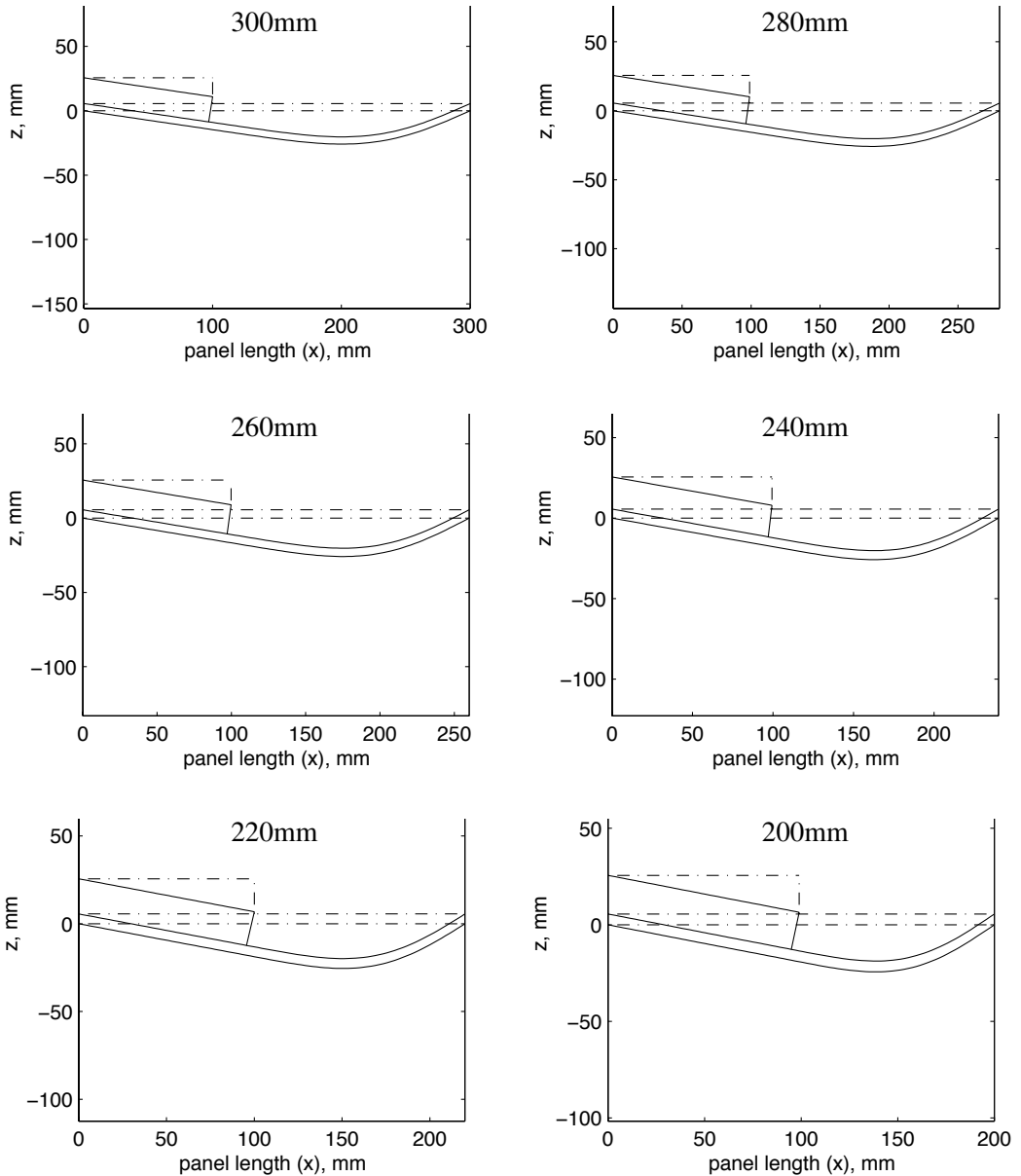


Figure 14. Mode I shapes (section AA) for panel B1 of x -wise lengths equal to 300, 280, 260, 240, 220 and 200 mm.

For configuration B2, the buckling loads increase almost linearly as the panel length decrease; the deformations are shown in [Figure 15](#). When the length varies from an initial value of 300 mm to 260 mm, the buckling modes appear to be self-similar; therefore the buckling loads increase as the length decreases. As the length continues to decrease, a change in the mode shape occurs. Again, the buckling of the panel

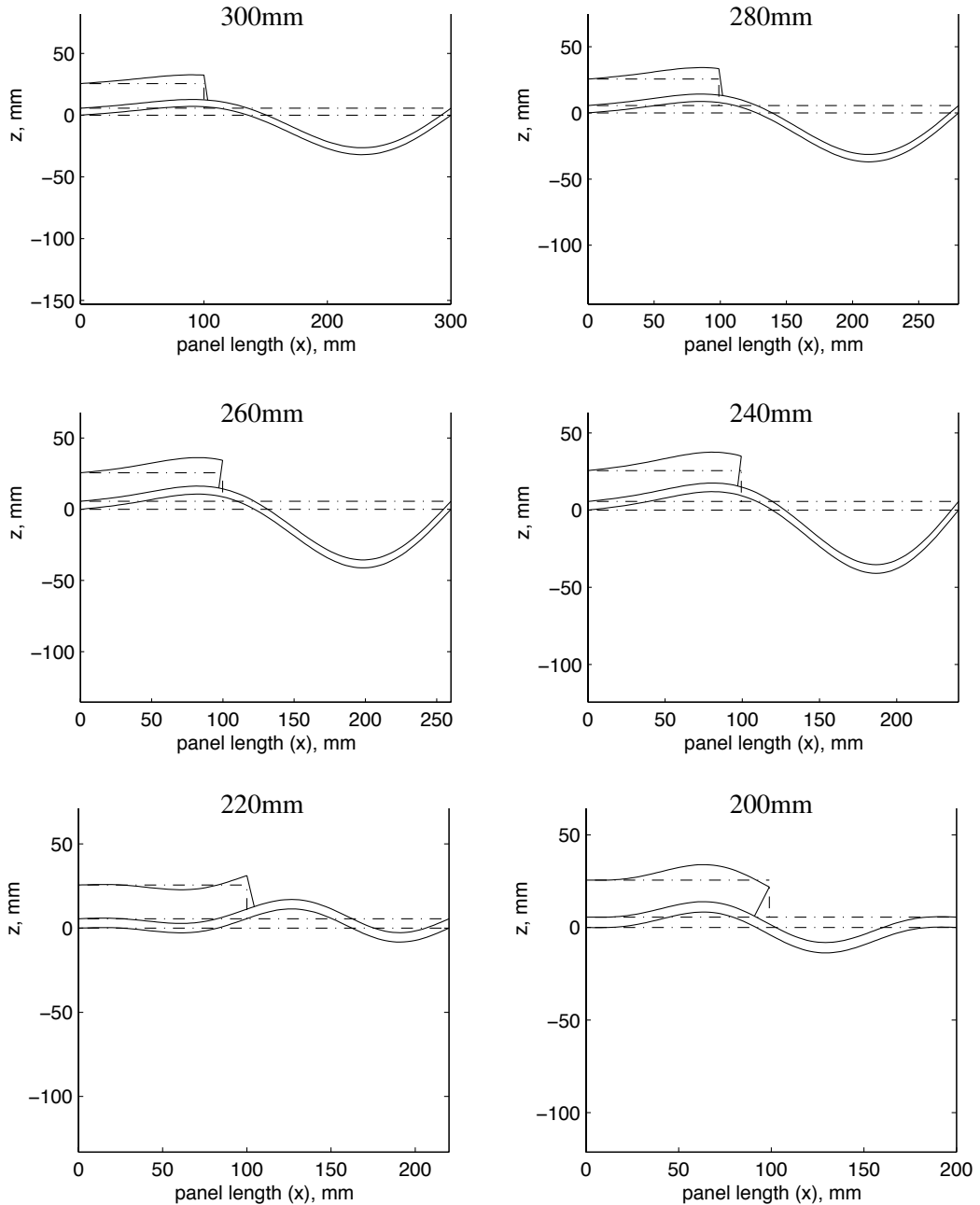


Figure 15. Mode I shapes (section AA) for panel B2 of x -wise lengths equal to 300, 280, 260, 240, 220 and 200 mm.

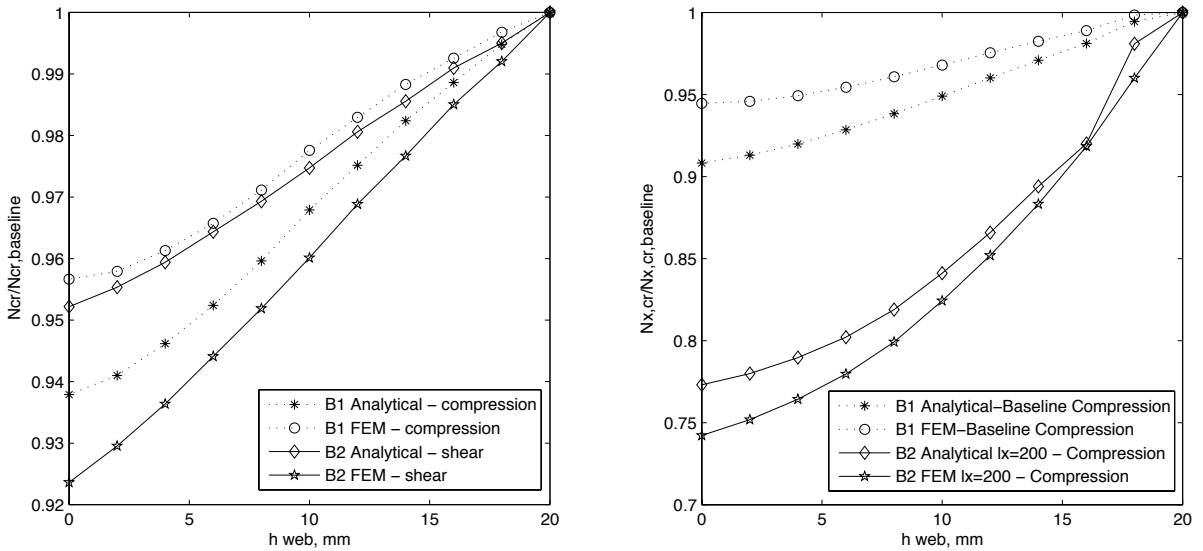


Figure 16. Buckling load sensitivity to web height.

alters from a two x -wise half waves phenomenon (more accentuated in the skin beyond the stiffener tip), to a more global phenomenon also involving the stiffener. The buckling loads then increase as the length decreases. The increase takes place at a smaller rate (Figure 13) as the amount of energy required to include the effects of the stiffener in the global deformation increases.

In the second set of analyses, the effect of the web height h_{web} was studied. Configurations B1 was analyzed in a first step and buckling loads were calculated under pure compression and pure shear loadings. Results are reported in Figure 16, left. A second set of analyses was carried out. The effect of h_{web} was assessed in configuration B2 under pure compression and with two different panel lengths: $l_x = 300$ mm (baseline geometry) and $l_x = 200$ mm. Results are reported in Figure 16, right. Comparison with FE analyses show that the trend is well captured by the analytical approach. It must be emphasized that, for configuration B2, short panels are significantly more sensitive to the web height than long panels (Figure 16, right). In fact, as already seen in Figure 15, the buckling modes of panels with lengths between 300 mm and 250 mm are characterized by two half waves with an accentuated transverse displacement that is localized in the free skin region in front of the stringer termination. For lengths that are below 250 mm, the panel buckles in to mode shapes, which are more global, that is, the web is characterized by increased transverse displacements. Therefore short panels are more sensitive to the web height than corresponding long configurations.

7. Discussion

The results presented in Section 6 generally show more than acceptable agreement between analysis and FEM. As shown in Figures 10–12, the present analysis guarantees good level of accuracy both in terms of buckling interaction curves and mode shape calculation. Although the method is in some cases slightly nonconservative (if compared to FEM) with regards to the calculation of buckling loads in pure compression, there is significant merit for the method in comparison with FEM.

- (1) In preliminary phases of aircraft design, there is an objective need for simple analytical solutions that guarantee considerable reduction of computational effort. There are often many (often extending to hundreds) of load cases to consider as well as optimisation studies to be done. Currently, FEM is too computationally expensive to be employed for all load cases and optimisation studies, except for particular exemplar cases. The slight nonconservative nature of some of the results does not pose a significant problem for practical use by industry because predictions that are slightly non-conservative are factored by subsequent introduction of statistical and environmental knockdown factors.
- (2) Despite the fact that FEM is able to provide realistic predictions, the large computational times associated in conjunction with the rather significant sensitivity of the results to the mesh size discourage its use as main tool for at least preliminary phases of aircraft design. In the present study no sensitivity analyses were undertaken to show that FEM predictions had converged and the mesh size was chosen based on the authors' engineering judgment (ref. to Figures 11 and 12). The employed mesh appears to be sufficiently refined to offer reasonably acceptable results within computational times, which are suitable for the purpose of this study. It is realistic to expect the use of more refined meshes for industrial purposes, which lead to much larger computational effort and time. The present analysis shows that computational times are already more than 10 times smaller than the ones associated with the use of coarse, two-dimensional FEM. This difference in analysis speed would be exacerbated if a more refined mesh were used, especially in conjunction with a fully three-dimensional model.

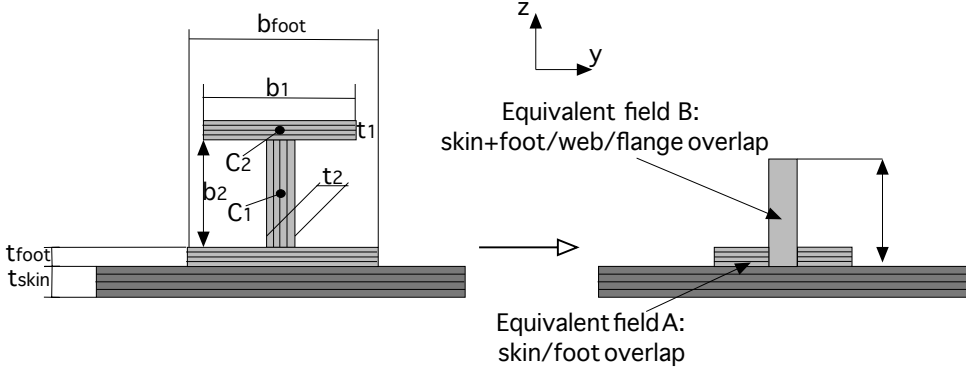
For the reasons described above, the present analysis is suitable for preliminary design calculations. To the best of our knowledge there are no analytical methods available in the literature, which predict the in-plane loads redistribution due to the presence of an incomplete stiffener terminated mid-bay along the bay length—a problem of significant interest to aircraft designers. It is recognized that further potential exploitations of the present analysis are also possible. For example, in cobonded and cocured composite assemblies, interlaminar shear stresses arising within the bond-line enable in-plane load transfer from the skin to the skin/stringer section. An extended model that also includes transverse shear stresses could be implemented and employed in conjunction with the present approach in order to provide fast and accurate calculation of interlaminar stresses.

8. Conclusions

A meshless approach was developed and used to predict local and global buckling of discretely assembled multibay composite panels made from skin and stiffeners. Numerical results obtained are compared with finite element analysis and show very good correlation in terms of in-plane loads distribution and buckling loads calculation. The use of either solution (equilibrated, and equilibrated and compatible) found for in-plane linear equilibrium appears to offer noteworthy level of accuracy and remarkable efficiency and flexibility compared with complementary finite element calculations. A robust and efficient method for quick evaluation of buckling loads of composite panels with stringer run-outs is presented. If used for industrial purposes, the accuracy could be further improved by defining knockdown factors in order to render conservative predictions.

Appendix A. Condensation of stringer properties

Consider a composite I-beam is used as stiffener on a composite skin, as shown in the figure:



As before, the width of the panel field equals the foot width. We need to assign an equivalent thickness and an equivalent local lamina stiffness matrix \mathbf{Q}^{eq} to the equivalent layer that represents the stiffener. Therefore, we need to properly assess five quantities: the equivalent thickness t_{eq} , the equivalent stiffnesses E_x^{eq} and E_y^{eq} in the x - and y -directions, the equivalent shear modulus G_{xy}^{eq} in the y -direction, and the equivalent Poisson's ratio ν_{xy}^{eq} .

If x is the direction of the main stiffener dimension, E_x^{eq} and t_{eq} are calculated by deriving the global axial (EA_{tot}) and bending (EI_{tot}) of the T-beam formed by the web and upper flange, and then imposing the conditions

$$EA_{\text{tot}} = E_x^{\text{eq}} b_{\text{foot}} t_{\text{eq}}, \quad EI_{\text{tot}} = E_x^{\text{eq}} \frac{1}{12} b_{\text{foot}} t_{\text{eq}}^3. \quad (\text{A.1})$$

The equivalent elastic modulus in the y -direction, orthogonally to the direction of the main stiffener dimension, can be set equal to zero. In fact, it is straightforward to demonstrate that, apart from the lower flange, the remaining part of the stringer does not contribute significantly if in-plane y -loads or transverse y bending moments are applied

$$E_y^{\text{eq}} \cong 0. \quad (\text{A.2})$$

The equivalent shear modulus is calculated as

$$G_{xy}^{\text{eq}} = \frac{1}{b_{\text{foot}} t_{\text{eq}}} \sum_{k=1}^{n_{\text{flanges}}} G_{xy,k} A_k, \quad (\text{A.3})$$

where n_{flanges} is the total number of flanges, $G_{xy,k}$ is the shear modulus of the k -th flange, and A_k is the area of k -th flange.

Note that formula (A.3) neglects the contribution of the vertical webs. Therefore the formula is appropriate if thin walled beams are used as stiffeners. The Poisson's ratios are derived from the assumption that the portion of the stiffener that lies on top of the skin but not directly in contact with it (namely the web and upper flange, see figure) does not affect the effective structural Poisson's ratio when axial loads in x -direction are applied. Hence, the Poisson's ratio ν_{xy}^{eq} equals the Poisson's ratio of the lower flange.

Appendix B. Derivation of the edge loads

To determine the expansion coefficients A_n and B_n , the in-plane unit width loads N_{xi} are assumed to be constant within each subdomain, which may be represented as a spring with a concentrated stiffness. The whole domain is schematized as a system of springs in series and in parallel (Figure A.1, right), which can be reduced to a single equivalent spring constant:

$$k_{eq} = \frac{k_1(k_2 + k_3 + k_4)}{k_1 + k_2 + k_3 + k_4}. \tag{B.1}$$

The axial flows N_{xi} are calculated throughout the domain under the assumption that every straight line parallel to the y -axis remains straight after the deformation. This assumption does not represent the real strain field throughout the panel's domain. Nonetheless, since only the stress field at the boundary is of interest at this stage, the assumption of discrete variation of N_x is not restrictive if stringer length is sufficiently large. In such a case, the skin-to-stiffener load transfer is already completed far from the boundary, and we can assume that the uniform axial (x -wise) strain condition is reestablished. An example calculation is provided here.

For convenience, we consider a geometry formally identical to the skin-patch composite assembly of Sections 4 and 5. We apply a constant axial flow $N_{x,1}$ on the free edge of the panel (Figure A.1, left). The total force acting is therefore $F_{tot} = N_{x,1}l_y$. The total axial displacement is calculated as

$$\delta_{tot} = \frac{F_{tot}}{k_{eq}}, \tag{B.2}$$

where k_{eq} is as in (B.1), with spring constants given by

$$k_1 = \frac{l_y}{A'_{11,1}} \frac{1}{l_x - l_P}, \quad k_2 = \frac{l_2}{A'_{11,2}} \frac{1}{l_P}, \quad k_3 = \frac{l_3}{A'_{11,3}} \frac{1}{l_P}, \quad k_4 = \frac{l_4}{A'_{11,4}} \frac{1}{l_P}. \tag{B.3}$$

To calculate how the total force distributes into the springs 1, 2, and 3, the axial displacement δ_{234} calculated at $x = l_P$ is first derived; it equals $\delta_{234} = \delta_{tot} F_1 / k_1$, where $F_1 = F_{tot}$. The force distribution is now given by $F_i = k_i \delta_P$, for $i = 2, 3, 4$. The x -wise axial flows are given by

$$N_{xi} = F_i / l_i.$$

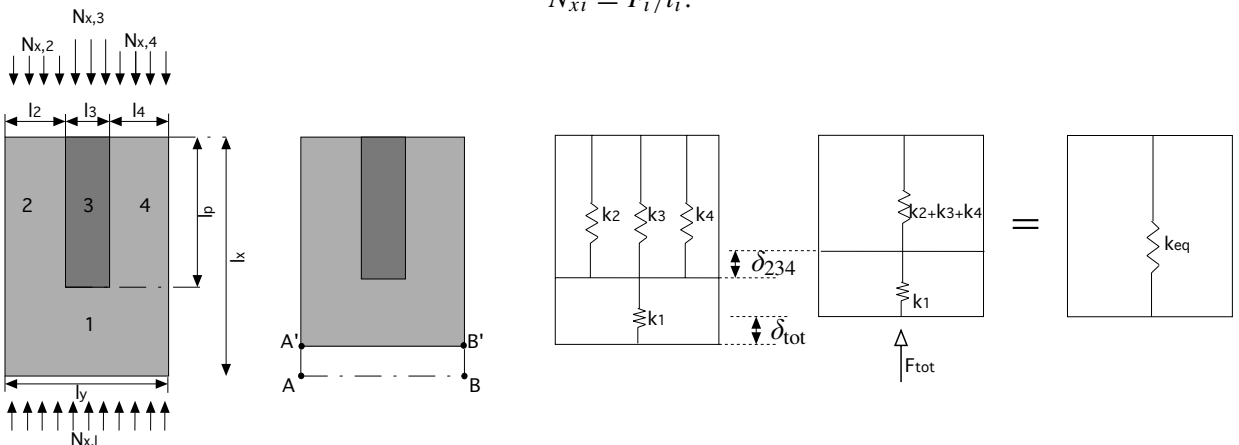


Figure A.1. Domain schematisation and system reduction scheme.

List of symbols

$\mathbf{u}_0, \mathbf{v}_0$	in-plane displacement of neutral plane in x and y directions
w	out-of-plane displacement
$\varepsilon_x, \varepsilon_y, \varepsilon_{xy}$	in-plane strains
$\varepsilon_x^0, \varepsilon_y^0, \varepsilon_{xy}^0$	in-plane strains at neutral plane level
e	neutral plane function
l_x, l_y	length and width of panel
\mathbf{N}, \mathbf{M}	unit width stresses and bending moments vectors
\mathbf{A}, \mathbf{D}	laminate in-plane and transverse stiffness matrices
\mathbf{B}	laminate coupling stiffness matrix
Ψ	equilibrium stress function for uniform loading
$\Delta\Psi$	equilibrium stress function for perturbation loading
Ψ_e	equilibrium stress function
Ψ_c	compatibility stress function for perturbation loading
Ω	stress function
X, Y, \bar{X}, \bar{Y}	beam eigenfunctions
φ_j	transverse displacement eigenfunctions
$\bar{\varphi}_j$	transverse displacement eigenfunctions
Ψ_j	stress function eigenfunctions
$N_{x,o}, N_{y,o}, N_{xy,o}$	external in-plane loads per unit width
N_x, N_y, N_{xy}	internal in-plane loads per unit width
w_i	generalized coordinates of the displacement function
e_i	generalized coordinates of the neutral plane function
ζ_j	generalized coordinates of the Airy stress function
\mathbf{u}	generalized coordinates vector
U	internal elastic potential energy
$\Omega_{N,L}$	linear component of the total potential of internal in-plane loads
$\Omega_{N,NL}$	nonlinear component of the total potential of internal in-plane loads
Ω_N	total potential of internal in-plane loads
Π_L	linear component of total potential
Π_{NL}	nonlinear component of total potential
Π	total potential
Ω_Q	potential of external transverse loads
$\mathbf{A}^*, \mathbf{D}^*$	matrices of in-plane and flexural flexibility in partially inverted laminate constitutive equations
\mathbf{B}^*	coupling matrix in partially inverted laminate constitutive equations
\mathbf{Q}	vector defined in (19)
$\mathbf{G}, \mathbf{H}, \bar{\mathbf{H}}$	matrices defined in (21), (22), and (23)
$\Gamma_x, \Gamma_y, \Gamma_{xy}$	circulation functions
ϕ_n	weight functions

Acknowledgments

The authors thank Airbus UK Ltd. for the financial support provided, and Pippi Goia for his valuable contribution to the graphics.

References

- [Ashton et al. 1969] J. E. Ashton, J. C. Halpin, and P. H. Petit, *Primer on composite materials: analysis*, Technomic, Stamford, CT, 1969.
- [Cosentino and Weaver 2008] E. Cosentino and P. M. Weaver, “Approximate non linear analysis method for debonding of skin/stringer composite assemblies”, *AIAA J.* **46**:5 (2008), 1144–1159.
- [Cosentino and Weaver 2009] E. Cosentino and P. M. Weaver, “Nonlinear analytical approach for sizing of discrete composite stringer terminations”, *AIAA J.* **47**:3 (2009), 606–617.
- [Jaunky et al. 1995] N. Jaunky, N. F. J. Knight, and D. R. Ambur, “Buckling of arbitrary quadrilateral anisotropic plates”, *AIAA J.* **33**:5 (May 1995), 938–944.
- [Jones 1975] R. M. Jones, *Mechanics of composite materials*, Scripta, Washington, 1975.
- [Kollar and Springer 2003] L. P. Kollar and G. S. Springer, *Mechanics of composite structures*, Cambridge University Press, Cambridge, 2003.
- [Mansfield 1989] E. H. Mansfield, *The bending and stretching of plates*, 2nd ed., Cambridge University Press, New York, 1989.
- [Reddy 2004] J. N. Reddy, *Mechanics of laminated composite plates and shells*, CRC Press, Boca Raton, FL, 2004.
- [Timoshenko and Goodier 1982] S. P. Timoshenko and J. N. Goodier, *Theory of elasticity*, 3rd ed., McGraw-Hill, New York, 1982.
- [Weaver and Nemeth 2007] P. M. Weaver and P. M. Nemeth, “Bounds on flexural properties and buckling response for symmetrically laminated composite plates”, *J. Eng. Mech.* **133**:11 (Nov 2007), 1178–1191.
- [Weaver and Nemeth 2008] P. M. Weaver and M. P. Nemeth, “Improved design formulas for buckling of orthotropic plates under combined loading”, *AIAA J.* **46**:9 (September 2008).

Received 18 Nov 2008. Revised 4 Mar 2009. Accepted 26 Aug 2009.

ENZO COSENTINO: enzo.cosentino@airbus.com

Composite Stress Analysis, Composite Structures Development Centre, Airbus UK Ltd., Bristol BS34 7AR, United Kingdom

PAUL WEAVER: paul.weaver@bristol.ac.uk

Advanced Composite Centre for Innovation and Science, Department of Aerospace Engineering, University of Bristol, Queen's Building 2.39, University Walk, Bristol BS8 1TR, United Kingdom

AN ASYMPTOTIC ANALYSIS OF ANISOTROPIC HETEROGENEOUS PLATES WITH CONSIDERATION OF END EFFECTS

JUN-SIK KIM

A finite element-based asymptotic analysis tool is developed for general anisotropic plates. The formulation begins with three-dimensional equilibrium equations in which the thickness coordinate is scaled by the characteristic length of the plate. This allows us to split the equations into two parts, such as the one-dimensional microscopic equations and the two-dimensional macroscopic equations, via the virtual work concept. The one-dimensional microscopic analysis yields the through-the-thickness warping function at each level, which does not require two-dimensional macroscopic analysis. The two-dimensional macroscopic equations provide the governing equations of the plate at each level in a recursive form. These can be solved in an orderly manner, in which proper macroscopic boundary conditions should be incorporated. The displacement prescribed boundary condition is obtained by introducing the orthogonality condition of asymptotic displacements to the plate fundamental solutions. In this way, the end effects of the plate are kinematically corrected without applying the sophisticated decay analysis method. The developed asymptotic analysis method is applied to semiinfinite plates with simply supported and clamped-free boundary conditions. The results obtained are compared to those of three-dimensional FEM, three-dimensional elasticity, and Reissner–Mindlin plate theory. The usefulness of the present method is also discussed.

1. Introduction

Analysis of anisotropic plates has been extensively carried out since the Kirchhoff–Love and Reissner–Mindlin plate theories were developed. It has been a challenging class of problems, involving the prediction of the behavior of anisotropic elastic bodies, including plates made of emerging composite materials, with sufficient accuracy while maintaining a low number of degrees of freedom. Accordingly many higher-order plate theories have been developed beyond the classical Kirchhoff–Love and Reissner–Mindlin plate theories. One can categorize them into three classes: smeared theories, zig-zag theories, and layerwise theories. Comprehensive reviews and assessments can be found in the surveys [Kapania and Raciti 1989; Noor and Burton 1989; Reddy and Jr. 1994; Carrera 2003].

Most theories reported in the literature are based on an a priori kinematic assumption which describes the higher-order behavior of plates especially for transverse shear deformation. This kinematic assumption leads to the improved prediction of transverse shear stresses that is crucial for stress analysis of laminated composite plates. Some of the higher-order theories are quite successful at describing such composite plates by increasing the number of degrees of freedom. For example, the higher-order theory developed by Lo et al. [1977] provides the accurate through-the-thickness distribution of transverse shear stresses for the plates made of isotropic materials. However the accuracy of this theory is degraded when

Keywords: composite plate, sandwich plate, formal asymptotic method, end effect, boundary condition, FAMPA.

a plate made of highly anisotropic materials is considered, especially one weak in shear. This triggered the development of various higher order plate theories in the last two decades.

One of the major drawbacks of these higher-order theories is that we do not know how accurate they are. These theories strongly depend on a priori assumed warping functions that are generally functions of the material properties and loading conditions. Thus it is crucial to find and/or assume the proper warping functions and desirable to obtain these from the three-dimensional (3D) elasticity if possible. One can derive them from the 3D elasticity by applying asymptotic methods which are mathematically rigorous. There are three types of asymptotic methods: the formal asymptotic method [Niordson 1979], the variational-asymptotic method (VAM) [Berdichevskii 1979; Berg 1991], and the asymptotic integration method [Novotny 1970; Wang and Tarn 1994; Tarn et al. 1996]. There is however a critical bottleneck associated with these asymptotic methods, and that is a proper set of boundary conditions. It is not trivial to exactly satisfy 3D boundary conditions especially for a displacement prescribed boundary condition [Duva and Simmonds 1992]. One can obtain asymptotically correct boundary conditions without solving the boundary layer problems by applying the decay analysis method [Gregory and Wan 1984]. Fan and Widera [1994] demonstrated that the displacement prescribed boundary conditions obtained via this method are different from those derived by variational principles. It is however too difficult to obtain these boundary conditions via the decay analysis method for engineering applications. For this very reason, an asymptotic analysis is often limited to the classical approximation for clamped plates and plates with simply supported boundary conditions. Another way to avoid the problem associated with boundary conditions is to derive a Reissner–Mindlin-like (RM-like) plate theory. Recently, Yu et al. [2002] and Yu [2005] have developed the RM-like plate models by applying the VAM and using the through-the-thickness finite element analysis. These models are not claimed to be asymptotically correct. And the asymptotically correct solutions up to $\mathcal{O}(\epsilon^2)$, which are comparable to those of the Reissner–Mindlin theory, have not been known for general anisotropic heterogeneous plates with clamped boundaries.

In this paper, a formal asymptotic expansion method is employed to derive a set of recursive equilibrium equations and boundary conditions from the 3D linear elasticity. We first split the 3D equilibrium equations into two sets of one-dimensional (1D) microscopic and two-dimensional (2D) macroscopic problems by introducing the virtual work concept. A conventional finite element discretization is then applied to solve the problems. The 1D microscopic analysis, which is the through-the-thickness analysis, yields the warping functions corresponding to the classical strain measure at each level. These functions are smeared into the stiffness models used for the 2D macroscopic formulation. Once the microscopic and macroscopic equations are derived, one has to determine a proper set of boundary conditions. We recast the strong forms of the equilibrium equations obtained in their corresponding weak forms. During this process, the displacement boundary conditions are treated as constraints in the weak form. In this way, the asymptotic displacement can be correlated to the boundary condition, and the asymptotically correct boundary condition up to $\mathcal{O}(\epsilon^2)$ can be derived. Thus one can obtain the asymptotically correct solution immediately next to the classical solution for general boundary conditions.

The results obtained are compared to those of the 3D FEM, 3D elasticity, and RM plate theory. Through numerical examples, this paper demonstrates how the edge zone affects the interior solution via a proper set of boundary conditions. This defines the term “end effects” used in this paper. The microscopic solutions, which can be obtained without solving the macroscopic problems, are also discussed to convey the usefulness of the proposed approach.

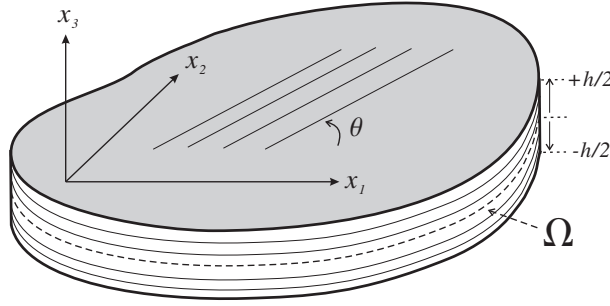


Figure 1. Geometry and coordinates of laminated plates.

2. Formal asymptotic formulation

A 3D composite plate with material anisotropy is considered in this study (see Figure 1). In order to apply the asymptotic expansion method, one needs to define a small parameter (ϵ) in terms of the thickness dimension which is much less than the in-plane dimension. To this end, the coordinates are scaled as

$$y_\alpha = x_\alpha, \quad y_3 = \frac{x_3}{\epsilon}, \tag{1}$$

in which ϵ is defined to be $\epsilon = h/l_c$, where h and l_c represent the thickness and characteristic length of the plate, respectively.

2.1. 3D equilibrium equations and boundary conditions. In the scaled coordinates from (1), the 3D static problem of linear elasticity, which consists of equilibrium equations, strain-displacement relationships, and constitutive equations, can be expressed as

$$\begin{aligned} \sigma_{ij,j} + \tilde{\mathbf{b}}_i &= 0 & \rightarrow & \quad \frac{1}{\epsilon} \mathcal{L}_3^t \sigma_{,3} + \mathcal{L}_\alpha^t \sigma_{,\alpha} + \tilde{\mathbf{b}} = 0, \\ \epsilon_{ij} &= \frac{1}{2} (u_{i,j} + u_{j,i}) & \rightarrow & \quad \boldsymbol{\epsilon} = \frac{1}{\epsilon} \mathcal{L}_3 \mathbf{u}_{,3} + \mathcal{L}_\alpha \mathbf{u}_{,\alpha}, \\ \sigma_{ij} &= c_{ijkl} \epsilon_{kl} & \rightarrow & \quad \boldsymbol{\sigma} = \frac{1}{\epsilon} \mathbf{C} \mathcal{L}_3 \mathbf{u}_{,3} + \mathbf{C} \mathcal{L}_\alpha \mathbf{u}_{,\alpha}, \end{aligned} \tag{2}$$

where a subscript $(\cdot)_{,i}$ indicates the partial derivative with respect to the coordinate y_i , a superscript t denotes the transpose of a matrix or vector, c_{ijkl} represent components of the 3D elasticity tensor, a body force vector $\tilde{\mathbf{b}}$, and a displacement vector \mathbf{u} . Stress and strain tensors are expressed in the vector form

$$\boldsymbol{\epsilon} = [\epsilon_{11} \ \epsilon_{22} \ \epsilon_{33} \ 2\epsilon_{23} \ 2\epsilon_{13} \ 2\epsilon_{12}]^t, \quad \boldsymbol{\sigma} = [\sigma_{11} \ \sigma_{22} \ \sigma_{33} \ \sigma_{23} \ \sigma_{13} \ \sigma_{12}]^t. \tag{3}$$

The linear operators \mathcal{L}_i are defined by

$$\mathcal{L}_1 = \begin{bmatrix} 1 & 0 & 0 \\ 0 & 0 & 0 \\ 0 & 0 & 0 \\ 0 & 0 & 0 \\ 0 & 0 & 1 \\ 0 & 1 & 0 \end{bmatrix}, \quad \mathcal{L}_2 = \begin{bmatrix} 0 & 0 & 0 \\ 0 & 1 & 0 \\ 0 & 0 & 0 \\ 0 & 0 & 1 \\ 0 & 0 & 0 \\ 1 & 0 & 0 \end{bmatrix}, \quad \mathcal{L}_3 = \begin{bmatrix} 0 & 0 & 0 \\ 0 & 0 & 0 \\ 0 & 0 & 1 \\ 0 & 1 & 0 \\ 1 & 0 & 0 \\ 0 & 0 & 0 \end{bmatrix}. \tag{4}$$

The boundary conditions considered herein are summarized as

$$\mathbf{u} = \bar{\mathbf{u}} \text{ on } S_u, \quad \boldsymbol{\sigma} \boldsymbol{\nu} = \tilde{\mathbf{p}} \text{ on } S_\sigma, \quad \boldsymbol{\sigma} \boldsymbol{\nu} = \tilde{\mathbf{g}} \text{ on } \Omega^\pm, \tag{5}$$

where S_u and S_σ represent the edge boundaries with prescribed displacements $\bar{\mathbf{u}}(x_i)$ and prescribed traction $\tilde{\mathbf{p}}(x_i)$, respectively. Ω^\pm denotes the top and bottom surfaces of the plate, and $\boldsymbol{\nu}$ is the direction cosine of the outward normal to the boundaries S_σ and Ω^\pm .

2.2. Asymptotic expansion and scaling. The displacement is expanded in terms of the small parameter

$$\mathbf{u} = \mathbf{u}^{(0)} + \epsilon \mathbf{u}^{(1)} + \epsilon^2 \mathbf{u}^{(2)} + \epsilon^3 \mathbf{u}^{(3)} + \dots, \tag{6}$$

where the 0th order displacement needs special attention, because it is related to the asymptotic convergence [Buannic and Cartraud 2001; Kim et al. 2008]. Each order displacement is given by

$$\mathbf{u}^{(0)}(y_\alpha) = [0 \ 0 \ u_3^{(0)}]^t, \quad \mathbf{u}^{(k)}(y_i) = [u_1^{(k)} \ u_2^{(k)} \ u_3^{(k)}]^t, \quad k \geq 1, \tag{7}$$

where $u_3^{(0)}(y_i) \equiv v_3^{(0)}(y_\alpha)$. The variables v_i represent functions of the in-plane coordinates y_α only.

The components of body force and surface traction, which are regarded as prescribed quantities, are also scaled as follows:

$$\tilde{b}_\alpha = \epsilon b_\alpha, \quad \tilde{b}_3 = \epsilon^2 b_3, \quad \tilde{p}_\alpha = \epsilon p_\alpha, \quad \tilde{p}_3 = \epsilon^2 p_3, \quad \tilde{g}_\alpha = \epsilon^2 g_\alpha, \quad \tilde{g}_3 = \epsilon^3 g_3, \tag{8}$$

and the prescribed displacement is presupposed by

$$\bar{u}_3 \sim \mathcal{O}(1), \quad \bar{u}_\alpha \sim \mathcal{O}(\epsilon). \tag{9}$$

Substituting (6) and (8) into (2) yields the recursive forms

$$\mathcal{L}_3^t \boldsymbol{\sigma}_{,3}^{(k+1)} = -\mathcal{L}_\alpha^t \boldsymbol{\sigma}_{,\alpha}^{(k)} - \mathbf{b}^{(k)}, \quad \boldsymbol{\epsilon}^{(k+1)} = \mathcal{L}_3 \mathbf{u}_{,3}^{(k+2)} + \mathcal{L}_\alpha \mathbf{u}_{,\alpha}^{(k+1)}, \quad \boldsymbol{\sigma}^{(k+1)} = \mathbf{C} \boldsymbol{\epsilon}^{(k+1)}, \quad k \geq -1, \tag{10}$$

where $\boldsymbol{\sigma}^{(k+1)}$ and $\boldsymbol{\epsilon}^{(k+1)}$ are expanded based on the displacement expansions, (6), and the coordinate scale, (1).

The associated boundary conditions at the edge boundaries are

$$\mathbf{u}^{(k+1)} = \bar{\mathbf{u}}^{(k+1)} \text{ on } S_u, \quad \boldsymbol{\sigma}^{(k+1)} \boldsymbol{\nu} = \mathbf{p}^{(k+1)} \text{ on } S_\sigma, \tag{11}$$

and at the top and bottom surfaces of the plate

$$\boldsymbol{\sigma}^{(k+1)} \boldsymbol{\nu} = \mathbf{g}^{(k+1)} \text{ on } \Omega^\pm, \tag{12}$$

where $\bar{\mathbf{u}}^{(k)} = \mathbf{0}$ if $k \neq 0$ or 1 , $\mathbf{b}^{(k)} = \mathbf{0}$ and $\mathbf{p}^{(k)} = \mathbf{0}$ if $k \neq 1$ or 2 , and $\mathbf{g}^{(k)} = \mathbf{0}$ if $k \neq 2$ or 3 . Notice here that the negative powers of the quantities vanish.

2.3. Fundamental solution. The very first equation ($k = -1$) from (10) can be obtained as

$$\mathcal{L}_3^t \boldsymbol{\sigma}_{,3}^{(0)} = \mathbf{0}. \tag{13}$$

Its solution can be easily found by $\boldsymbol{\sigma}^{(0)} = \boldsymbol{\epsilon}^{(0)} = \mathbf{0}$ since it is well posed [Buannic and Cartraud 2001; Kim et al. 2008]. From $\boldsymbol{\epsilon}^{(0)} = \mathbf{0}$ the particular solution is obtained by

$$\mathbf{u}_p^{(1)} = [-y_3 v_{3,1}^{(0)} \ -y_3 v_{3,2}^{(0)} \ 0]^t. \tag{14}$$

The solution is defined up to a rigid body displacement ($\mathbf{u}_R = \{v_1, v_2, v_3\}$). This forms the fundamental solutions such that

$$\mathbf{u}^{(1)} = \tilde{\mathbf{u}}^{(1)} \equiv \mathbf{u}_p^{(1)} + \mathbf{u}_R^{(1)} = \Theta(y_3)\tilde{\mathbf{v}}^{(1)}(y_\alpha), \quad (15)$$

where

$$\Theta(y_3) = \begin{bmatrix} 1 & 0 & 0 & -y_3 & 0 \\ 0 & 1 & 0 & 0 & -y_3 \\ 0 & 0 & 1 & 0 & 0 \end{bmatrix}, \quad \tilde{\mathbf{v}}^{(1)}(y_\alpha) = \begin{Bmatrix} v_i^{(1)} \\ v_{3,\alpha}^{(0)} \end{Bmatrix}. \quad (16)$$

This fundamental solution appears repeatedly in each order problem.

2.4. Virtual displacement concept to recursive equations. It is more convenient to rewrite the recursive equilibrium equation, (10), in terms of virtual displacements in order to find the solutions of microscopic and macroscopic problems as well as to handle the surface traction on Ω^\pm . To this end, one can multiply by the virtual displacement $\delta\mathbf{u}^{(k+2)t}$ in (10) and (12). By applying integration by parts for the y_3 coordinate, it takes the form

$$\int_{\Omega} \left[\int_{h_\epsilon} \delta\mathbf{u}_{,3}^{(k+2)t} \mathcal{L}_3^t \boldsymbol{\sigma}^{(k+1)} dy_3 - \int_{h_\epsilon} \delta\mathbf{u}^{(k+2)t} \mathcal{L}_\alpha^t \boldsymbol{\sigma}_{,\alpha}^{(k)} dy_3 - \int_{h_\epsilon} \delta\mathbf{u}^{(k+2)t} \mathbf{b}^{(k)} dy_3 - \delta\mathbf{u}^{(k+2)t} \mathbf{g}^{(k+1)} \Big|_{y_3=\Omega^\pm} \right] d\Omega = 0, \quad (17)$$

where h_ϵ denotes the scaled thickness of a plate. The edge boundary conditions on S_u and S_σ will be considered and discussed in Section 4.

Furthermore the asymptotic displacement $\mathbf{u}^{(k)}$ can be decomposed into two terms such that

$$\mathbf{u}^{(k)}(y_i) = \tilde{\mathbf{u}}^{(k)}(y_i) + \mathbf{u}_w^{(k)}(y_i), \quad k \geq 2, \quad (18)$$

where the first term is the fundamental solution and the second the warping solution. By substituting this into (17), one can obtain two equations corresponding to $\delta\tilde{\mathbf{u}}^{(k+2)}$ and $\delta\mathbf{u}_w^{(k+2)}$. They are referred to as the *macroscopic* problem (or the plate analysis) and the *microscopic* problem (or the through-the-thickness analysis), respectively.

3. Microscopic and macroscopic problems

In this section, we seek the solutions of the microscopic problems and the macroscopic 2D plate equations from (17). The through-the-thickness 1D finite analysis for the microscopic problems is described first. Then the macroscopic 2D plate equilibrium equations, which are built upon the results of microscopic analysis, are derived.

3.1. Microscopic problems. The microscopic problems can be obtained from (17) by collecting the terms associated with the virtual displacement form of the warping solution, $\delta\mathbf{u}_w^{(k)}$. These can be solved by applying the through-the-thickness 1D finite element discretization. Subsequently the warping solution is generalized for each level of the problems.

The second microscopic problem and finite element discretization. The first nontrivial microscopic problem ($k = 0$), which is associated with $\delta \mathbf{u}_w^{(2)}$ in (17), is given by

$$\int_{h_\epsilon} \delta (\mathcal{L}_3 \mathbf{u}_{w,3}^{(2)})^t \mathbf{C} (\Phi \mathbf{e}^{(1)} + \mathcal{L}_3 \mathbf{u}_{w,3}^{(2)}) dy_3 = 0, \tag{19}$$

where

$$\Phi(y_3) = \begin{bmatrix} 1 & 0 & 0 & -y_3 & 0 & 0 \\ 0 & 1 & 0 & 0 & -y_3 & 0 \\ 0 & 0 & 0 & 0 & 0 & 0 \\ 0 & 0 & 0 & 0 & 0 & 0 \\ 0 & 0 & 0 & 0 & 0 & 0 \\ 0 & 0 & 1 & 0 & 0 & -y_3 \end{bmatrix}, \quad \mathbf{e}^{(1)} = [v_{1,1}^{(1)} \quad v_{2,2}^{(1)} \quad v_{1,2}^{(1)} + v_{2,1}^{(1)} \quad v_{3,11}^{(0)} \quad v_{3,22}^{(0)} \quad 2v_{3,12}^{(0)}]^t. \tag{20}$$

In order to solve (19), the finite element discretization is employed by using the standard 1D Lagrangian interpolation function. The warping solution is then expressed by

$$\mathbf{u}_w(y_i) = \mathbf{N}_u(y_3) \bar{\mathbf{u}}_w(y_\alpha), \tag{21}$$

where \mathbf{N}_u is the shape function matrix and $\bar{\mathbf{u}}_w$ is the nodal vector. Plugging (21) into (19) yields

$$\mathbf{K} \bar{\mathbf{u}}_w^{(2)} + \mathbf{F}_{3E} \mathbf{e}^{(1)} = \mathbf{0}, \tag{22}$$

where

$$\mathbf{K} \equiv \langle B_3^t \quad \mathbf{C} \quad B_3 \rangle, \quad \mathbf{F}_{3E} \equiv \langle B_3^t \quad \mathbf{C} \quad \Phi \rangle, \quad B_3 \equiv \mathcal{L}_3 \mathbf{N}_{u,3}, \tag{23}$$

in which

$$\langle \bullet \rangle = \int_{h_\epsilon} \bullet dy_3. \tag{24}$$

One can solve (22) by applying the orthogonality condition to a rigid body displacement [Cesnik et al. 1996; Kim et al. 2008]. Consequently its solution is represented by

$$\bar{\mathbf{u}}_w^{(2)} = \Gamma^{(1)} \mathbf{e}^{(1)}, \quad \Gamma^{(1)} \equiv \mathbf{K}_I \mathbf{F}_{3E}, \tag{25}$$

where the matrix \mathbf{K}_I is related to the inverse matrix of \mathbf{K} and the orthogonality condition to a rigid body displacement [Kim et al. 2008]. Note that each column of $\Gamma^{(1)}$ represents the warping distribution through the thickness of a plate, which corresponds to six warping functions due to two in-plane extensions, one in-plane shear, two bending curvatures, and one twisting curvature. These functions explain the 3D Poisson effect.

The third and higher microscopic problems. The third microscopic problem ($k = 1$) from (17) can be summarized as follows:

$$\int_{h_\epsilon} \delta \mathbf{u}_{w,3}^{(3)t} \mathcal{L}_3^t \boldsymbol{\sigma}^{(2)} dy_3 = \int_{h_\epsilon} \delta \mathbf{u}_w^{(3)t} \mathcal{L}_\alpha^t \boldsymbol{\sigma}_{,\alpha}^{(1)} dy_3 + \int_{h_\epsilon} \delta \mathbf{u}_w^{(3)t} \mathbf{b}^{(1)} dy_3 + \delta \mathbf{u}_w^{(3)t} \mathbf{g}^{(2)} \Big|_{y_3=\Omega^\pm}, \tag{26}$$

where the last term represents the prescribed surface shear traction on Ω^\pm , which is explicitly expressed by

$$\sigma_{\alpha 3}^{(2)\pm} = g_\alpha^\pm \text{ at } y_3 = \pm \frac{h_\epsilon}{2}. \tag{27}$$

After applying the finite element discretization and carrying out tedious but straightforward manipulation, one can obtain

$$\mathbf{K}\bar{\mathbf{u}}_w^{(3)} = -\mathbf{F}_{3E}\mathbf{e}^{(2)} + [V_\alpha + (W_\alpha - W_\alpha^t) \Gamma^{(1)}] \mathbf{e}_{,\alpha}^{(1)} + \mathbf{F}_g^{(2)} + \mathbf{F}_b^{(1)}, \quad (28)$$

where

$$V_\alpha \equiv \langle B_\alpha^t \mathbf{C} \Phi \rangle, \quad W_\alpha \equiv \langle B_\alpha^t \mathbf{C} B_3 \rangle, \quad B_\alpha \equiv \mathcal{L}_\alpha \mathbf{N}_u, \quad (29)$$

and the last two terms on the right side are force vectors that represent the prescribed traction and the body force, respectively. Once we solve (28), the warping solution has the form

$$\bar{\mathbf{u}}_w^{(3)} = \Gamma^{(1)} \mathbf{e}^{(2)} + \Gamma_\alpha^{(2)} \mathbf{e}_{,\alpha}^{(1)} + \bar{\mathbf{u}}_f^{(3)}, \quad (30)$$

where

$$\Gamma_\alpha^{(2)} \equiv \mathbf{K}_I [V_\alpha + (W_\alpha - W_\alpha^t) \Gamma^{(1)}], \quad \bar{\mathbf{u}}_f^{(3)} \equiv \mathbf{K}_I (\mathbf{F}_g^{(2)} + \mathbf{F}_b^{(1)}). \quad (31)$$

By following the same procedure described in the previous microscopic problems, the solution of the fourth microscopic problem ($k = 2$) can be obtained by

$$\bar{\mathbf{u}}_w^{(4)} = \Gamma^{(1)} \mathbf{e}^{(3)} + \Gamma_\alpha^{(2)} \mathbf{e}_{,\alpha}^{(2)} + \Gamma_{\alpha\beta}^{(3)} \mathbf{e}_{,\beta\alpha}^{(1)} + \bar{\mathbf{u}}_f^{(4)}, \quad (32)$$

where

$$\begin{aligned} \Gamma_{\alpha\beta}^{(3)} &\equiv \mathbf{K}_I [W_{\alpha\beta} \Gamma^{(1)} + (W_\alpha - W_\alpha^t) \Gamma_\beta^{(2)}], & W_{\alpha\beta} &\equiv \langle B_\alpha^t \mathbf{C} B_\beta \rangle, \\ \bar{\mathbf{u}}_f^{(4)} &\equiv \mathbf{K}_I [(W_\alpha - W_\alpha^t) \bar{\mathbf{u}}_{f,\alpha}^{(3)} + \mathbf{F}_g^{(3)} + \mathbf{F}_b^{(2)}]. \end{aligned} \quad (33)$$

Similarly, the solutions of the higher than fourth microscopic problems can be now generalized as follows:

$$\bar{\mathbf{u}}_w^{(k)} = \Gamma^{(1)} \mathbf{e}^{(k-1)} + \Gamma_\alpha^{(2)} \mathbf{e}_{,\alpha}^{(k-2)} + \dots + \Gamma_{\alpha\beta\dots\psi}^{(k-2)} \mathbf{e}_{,\psi\dots\beta\alpha}^{(2)} + \Gamma_{\alpha\beta\dots\psi\omega}^{(k-1)} \mathbf{e}_{,\omega\psi\dots\beta\alpha}^{(1)} + \bar{\mathbf{u}}_f^{(k)}, \quad (34)$$

where $k \geq 5$, and

$$\bar{\mathbf{u}}_f^{(m+1)} \equiv \mathbf{K}_I [W_{\alpha\beta} \bar{\mathbf{u}}_{f,\beta\alpha}^{(m-1)} + (W_\alpha - W_\alpha^t) \bar{\mathbf{u}}_{f,\alpha}^{(m)}], \quad (35)$$

$$\Gamma_{\alpha\beta\gamma\dots\psi\omega}^{(m)} \equiv \mathbf{K}_I [W_{\alpha\beta} \Gamma_{\gamma\dots\psi\omega}^{(m-2)} + (W_\alpha - W_\alpha^t) \Gamma_{\omega\psi\dots\gamma\beta}^{(m-1)}], \quad (36)$$

in which $m \geq 4$.

3.2. Macroscopic problems. One can also derive the macroscopic 2D equilibrium equations from (17) by collecting the terms associated with $\delta\bar{\mathbf{u}}^{(k)}$. In this subsection, the equations at each level are derived and the macroscopic 2D constitutive equations are set up, in which the warping solutions obtained in Section 2 are smeared into the macroscopic 2D stiffness.

Equilibrium equations. From (17), the k -th macroscopic problem that is associated with $\delta\bar{\mathbf{u}}^{(k+2)}$ can be summarized as follows:

$$\begin{aligned} \delta v_\alpha^{(k+2)} : & \quad N_{\alpha\beta,\beta}^{(k)} + n_\alpha^{(k)} = 0, \\ \delta v_{3,\alpha}^{(k+1)} : & \quad M_{\alpha\beta,\beta}^{(k)} + Q_\alpha^{(k+1)} - m_\alpha^{(k)} = 0, \quad k \geq 0, \\ \delta v_3^{(k+2)} : & \quad Q_{\alpha,\alpha}^{(k)} + q^{(k)} = 0, \end{aligned} \quad (37)$$

where

$$N_{\alpha\beta}^{(k)} \equiv \langle \sigma_{\alpha\beta}^{(k)} \rangle, \quad M_{\alpha\beta}^{(k)} \equiv \langle -y_3 \sigma_{\alpha\beta}^{(k)} \rangle, \quad Q_\alpha^{(k)} \equiv \langle \sigma_{\alpha 3}^{(k)} \rangle, \quad (38)$$

and the other terms are the contributions of the body force and prescribed traction, which are

$$\begin{aligned} n_\alpha^{(k)} &\equiv \{ \langle b_\alpha \rangle + g_\alpha^+ + g_\alpha^- \} \delta(k-1), \\ m_\alpha^{(k)} &\equiv \left\{ \langle y_3 b_\alpha \rangle + \frac{h_\epsilon}{2} (g_\alpha^+ - g_\alpha^-) \right\} \delta(k-1), \\ q^{(k)} &\equiv \{ \langle b_3 \rangle + g_3^+ + g_3^- \} \delta(k-2), \end{aligned} \quad (39)$$

where $\delta(k-n)$ indicates the Kronecker delta function.

The very first macroscopic problem, which corresponds to $k=0$ in (37), yields the classical assumption of zero shear force such that $Q_\alpha^{(1)} = 0$. The second macroscopic problem ($k=1$) forms the classical plate theory, which contains the trivial terms related to the first-order shear forces $Q_\alpha^{(1)} = 0$ from the previous macroscopic problem. This problem also includes the second-order shear forces $Q_\alpha^{(2)}$ that are presented in the third macroscopic problem. From these one obtains the first set of equilibrium equations,

$$N_{\alpha\beta,\beta}^{(1)} + n_\alpha^{(1)} = 0, \quad M_{\alpha\beta,\beta\alpha}^{(1)} + m_{\alpha,\alpha}^{(1)} = q^{(2)}. \quad (40)$$

Similarly the second and higher sets of equilibrium equations are now generalized by

$$N_{\alpha\beta,\beta}^{(k)} = 0, \quad M_{\alpha\beta,\beta\alpha}^{(k)} = 0, \quad k \geq 2. \quad (41)$$

It is worth noting that there are no external loadings in the equations with $k \geq 2$ but the solutions of the equations of the preceding level form the fictive volume force acting like the external loading.

Constitutive equations. The k -th order stress resultants ($k \geq 1$) can be defined by

$$\tilde{\mathcal{N}}^{(k)} \equiv \langle \Phi^t \boldsymbol{\sigma}^{(k)} \rangle = \mathcal{A}^{(1)} \mathbf{e}^{(k-1)} + \mathcal{A}_\alpha^{(2)} \mathbf{e}_{,\alpha}^{(k-2)} + \dots + \mathcal{A}_{\alpha\beta\dots\psi\omega}^{(k-1)} \mathbf{e}_{,\omega\psi\dots\beta\alpha}^{(1)} + \tilde{\mathcal{N}}_f^{(k)}, \quad (42)$$

where

$$\tilde{\mathcal{N}}^{(k)} \equiv [N_{11}^{(k)} \quad N_{22}^{(k)} \quad N_{12}^{(k)} \quad M_{11}^{(k)} \quad M_{22}^{(k)} \quad M_{12}^{(k)}]^t, \quad \tilde{\mathcal{N}}_f^{(k)} \equiv V_\alpha^t \bar{\mathbf{u}}_{f,\alpha}^{(k)} + \mathbf{F}_{3E}^t \bar{\mathbf{u}}_f^{(k+1)}, \quad (43)$$

and

$$\begin{aligned} \mathcal{A}^{(1)} &\equiv \langle \Phi^t \mathbf{C} \Phi \rangle + \mathbf{F}_{3E}^t \Gamma^{(1)}, \\ \mathcal{A}_\alpha^{(2)} &\equiv V_\alpha^t \Gamma^{(1)} + \mathbf{F}_{3E}^t \Gamma_\alpha^{(2)}, \end{aligned} \quad (44)$$

...

$$\mathcal{A}_{\alpha\beta\dots\omega}^{(n)} \equiv V_\alpha^t \Gamma_{\beta\dots\omega}^{(n-1)} + \mathbf{F}_{3E}^t \Gamma_{\alpha\beta\dots\omega}^{(n)}, \quad n \geq 3.$$

The macroscopic constitutive equations include the terms related to the prescribed surface traction on Ω^\pm , $\tilde{\mathcal{N}}_f^{(k)}$, which are not considered in a conventional way to derive the constitutive equations.

4. Weak form of macroscopic 2D equations

A finite element formulation for the macroscopic 2D equilibrium equations presented in Section 3 is described. To this end, we first apply a Galerkin method to the 2D equilibrium equations with edge boundary conditions as constraints, and then transform them to a weak form through integrating by parts

with respect to the in-plane coordinates y_α . This process allows us to have boundary conditions for the problem.

4.1. 2D plate finite element formulation. To convert the sets of macroscopic equilibrium equations in (40) and (41) to the corresponding weak formulations, it is essential to consider the edge boundary conditions given in (11). These edge boundary conditions can be rewritten in the weak forms

$$\int_{S_\sigma} \delta \mathbf{u}^{(k+2)t} (\boldsymbol{\sigma}^{(k+1)} \mathbf{v} - \mathbf{p}^{(k+1)}) dS + \int_{S_u} \delta \mathbf{u}^{(k+2)t} (\boldsymbol{\sigma}^{(k+1)} \mathbf{v} + \boldsymbol{\lambda}^{(k+1)}) dS = 0, \quad (45)$$

which are subject to the constraint

$$\int_{S_u} \delta \boldsymbol{\lambda}^{(k+1)t} (\mathbf{u}^{(k+2)} - \bar{\mathbf{u}}^{(k+2)}) dS = 0, \quad (46)$$

where $k \geq 0$, and $\boldsymbol{\lambda}$ is a Lagrange multiplier which is introduced to enforce the displacement boundary condition on S_u .

The sets of macroscopic equilibrium equations in (40) and (41) can be recast by applying a Galerkin method, where the weighting function is chosen to be a displacement vector such that

$$\mathbf{v}^{(k)} = [v_1^{(k)} \ v_2^{(k)} \ v_3^{(k-1)}]^t, \quad k \geq 1, \quad (47)$$

combining (45). Subsequently integrating by parts yields the following weak formulation for the problem:

$$\int_{\Omega} \left\{ (\delta \mathbf{e}^{(k)})^t \tilde{\mathcal{N}}^{(k)} - (\delta \hat{\mathbf{v}}^{(k)})^t \tilde{\mathcal{B}}^{(k)} \right\} \delta \Omega = (\delta \hat{\mathbf{v}}^{(k)})^t \int_{S_\sigma} \tilde{\mathcal{F}}^{(k)} dS, \quad k \geq 1, \quad (48)$$

where

$$\hat{\mathbf{v}}^{(k)} = [v_\alpha^{(k)} \ v_3^{(k-1)} \ v_{3,\alpha}^{(k-1)}]^t, \quad \tilde{\mathcal{B}}^{(k)} = [n_\alpha^{(k)} \ q^{(k+1)} \ m_\alpha^{(k)}]^t, \quad \tilde{\mathcal{F}}^{(1)} = \Theta^t [p_1 \ p_2 \ p_3]^t, \quad (49)$$

where $\tilde{\mathcal{F}}^{(k)} = 0$ if $k \geq 2$. Notice here that there are remaining boundary conditions associated with $\delta \mathbf{u}_w^{(k+2)}$ which will be discussed in Section 4.2.

Applying a standard finite element discretization procedure to (48) yields the following recursive linear equations:

$$\mathbf{K}_{2D}^{(1)} \hat{\mathbf{V}}^{(k)} = \mathbf{P}_F^{(k)} - \mathbf{P}_N^{(k)} (\mathbf{K}_{2D}^{(n)}, \hat{\mathbf{V}}^{(n)})_{n=2,3,\dots,k}, \quad (50)$$

where $k \geq 1$, $\hat{\mathbf{V}}^{(k)}$ is the k -th order nodal degrees of freedom vector, and $\mathbf{P}_F^{(k)}$ indicates the forcing vector coming from $\tilde{\mathcal{F}}^{(k)}$ and $\tilde{\mathcal{B}}^{(k)}$. The calculation of the 2D stiffness matrices $\mathbf{K}_{2D}^{(k)}$ is associated with the k -th order stress resultant vector $\tilde{\mathcal{N}}^{(k)}$ that includes higher order derivatives with respect to the coordinates y_α . The fictive volume force vector $\mathbf{P}_N^{(k)}$ is computed from the preceding nodal vectors and 2D stiffness matrices. Their explicit forms are omitted for brevity, since they are lengthy but straightforward.

4.2. Boundary conditions. In the process of integrating by parts in Section 4.1, there are remaining boundary conditions associated with $\delta \mathbf{u}_w^{(k+2)}$ and the displacement boundary S_u . These are summarized as follows:

$$\int_{S_\sigma} \delta \mathbf{u}_w^{(k+2)t} (\boldsymbol{\sigma}^{(k+1)} \mathbf{v} - \mathbf{p}^{(k+1)}) dS + \int_{S_u} \delta \mathbf{u}_w^{(k+2)t} (\boldsymbol{\sigma}^{(k+1)} \mathbf{v} + \boldsymbol{\lambda}^{(k+1)}) dS + \int_{S_u} \delta \tilde{\mathbf{u}}^{(k+2)t} \boldsymbol{\lambda}^{(k+1)} dS = 0, \quad (51)$$

with the constraint given in (46). These boundary conditions carry physical significance, which implies that one cannot exactly satisfy the 3D edge boundary conditions even for stress edge data unless the boundary layer problem is solved. The first term, which is the edge traction, is dismissed in the weighted average sense. The second and third terms are also dismissed if one can properly prescribe the fundamental and warping displacements at the edge on S_u .

A clue to this displacement boundary condition can be sought by examining the displacement constraint. From (51), a Lagrange multiplier can be found. Substituting this into the constraint in (46) yields

$$\int_{S_u} \delta(\boldsymbol{\sigma}^{(k+1)} \mathbf{v})^t (\mathbf{u}^{(k+2)} - \bar{\mathbf{u}}^{(k+2)}) dS = 0, \tag{52}$$

which leads to the so-called averaged displacement boundary condition. For example, this can be simplified for the straight edge perpendicular to the y_1 coordinate by

$$\int_{S_u} \delta \sigma_{i1}^{(k+1)} (u_i^{(k+2)} - \bar{u}_i^{(k+2)}) dS = 0. \tag{53}$$

Furthermore if one assumes linear variations of in-plane stresses and a constant transverse shear stress, the stress edge data is expressed by $\sigma_{\alpha 1} = \tau_\alpha + y_3 \omega_\alpha$ and $\sigma_{31} = \tau_3$. Plugging this into (53) yields five equations such that

$$\begin{aligned} \delta \tau_\alpha &: \quad \langle u_\alpha^{(k+2)} - \bar{u}_\alpha^{(k+2)} \rangle = 0, \\ \delta \omega_\alpha &: \quad \langle y_3 (u_\alpha^{(k+2)} - \bar{u}_\alpha^{(k+2)}) \rangle = 0, \\ \delta \tau_3 &: \quad \langle u_3^{(k+2)} - \bar{u}_3^{(k+2)} \rangle = 0, \end{aligned} \tag{54}$$

which in matrix form is

$$\delta \boldsymbol{\tau}^t \langle \boldsymbol{\Theta}^t (\mathbf{u}^{(k+2)} - \bar{\mathbf{u}}^{(k+2)}) \rangle = 0. \tag{55}$$

This actually yields the same form as the orthogonality condition of asymptotic displacements to the fundamental displacement [Kim et al. 2008]. The displacement condition given in (55) was proven to be asymptotically correct up to $\mathcal{O}(\epsilon^2)$ for a transversely isotropic semiinfinite beam [Horgan and Simmonds 1991]. In this way, one can avoid the overwhelming complexity of using the decay analysis method [Gregory and Wan 1984] to find the asymptotically correct boundary conditions up to any desired order. It is however limited to asymptotic analysis up to $\mathcal{O}(\epsilon^2)$ when the displacement prescribed boundary is considered (for example, for clamped boundaries) [Horgan and Simmonds 1991; Duva and Simmonds 1992].

The orthogonality condition of asymptotic displacements [Kim et al. 2008], which generalizes the averaged displacement boundary condition, is given by

$$\int_{S_u} (\delta \tilde{\mathbf{u}}^{(k)})^t (\mathbf{u}^{(k)} - \bar{\mathbf{u}}^{(k)}) dS = 0, \tag{56}$$

in which $\bar{\mathbf{u}}^{(k)}$ is the scaled displacement edge data. Plugging (15) into this yields

$$(\delta \tilde{\mathbf{v}}^{(k)})^t \mathbf{U}^{(k)} = 0, \quad \mathbf{U}^{(k)} \equiv \int_{S_u} \boldsymbol{\Theta}^t (y_3) (\mathbf{u}^{(k)} - \bar{\mathbf{u}}^{(k)}) dS, \tag{57}$$

where $\mathbf{U}^{(k)}$ is a 6×1 residual displacement vector. This yields five kinematic boundary conditions. For instance, the clamped boundary condition (that is, $\bar{\mathbf{u}}^{(k)} = \mathbf{0}\forall k$) can be realized as follows:

$$\tilde{\mathbf{v}}^{(1)} = \mathbf{0}, \quad \tilde{\mathbf{v}}^{(2)} = -\mathbf{H}_\theta^{-1} \langle \Theta^t \mathbf{N}_u \rangle \Gamma^{(1)} \mathbf{e}^{(1)}, \quad \dots, \quad \tilde{\mathbf{v}}^{(k)} = -\mathbf{H}_\theta^{-1} \langle \Theta^t \mathbf{N}_u \rangle (\bar{\mathbf{u}}_w^{(k)} + \bar{\mathbf{u}}_f^{(k)}), \quad k \geq 3, \quad (58)$$

where $\mathbf{H}_\theta \equiv \langle \Theta^t \Theta \rangle$. This however should be rearranged for each macroscopic problem so that

$$\hat{\mathbf{v}}^{(k)} = [\tilde{\mathbf{v}}_1^{(k)} \quad \tilde{\mathbf{v}}_2^{(k)} \quad \tilde{\mathbf{v}}_3^{(k-1)} \quad \tilde{\mathbf{v}}_4^{(k)} \quad \tilde{\mathbf{v}}_5^{(k)}]^t. \quad (59)$$

5. Numerical examples and discussion

Laminated and sandwich plates are considered as illustrative examples for the present asymptotic formulation. In order to investigate the edge effects, semiinfinite plates (that is, the 3D plane strain problem) with simply supported or clamped-free boundary conditions are analyzed (see Figure 2). The present results are compared to those obtained by 3D elasticity and Reissner–Mindlin plate theory, also known as first-order shear deformation theory (FSDT). The shear correction factor is assumed to be 5/6 for FSDT. For convenience, the present approach is referred to as a formal asymptotic method-based plate analysis (FAMPA) throughout the numerical examples.

The ply material properties of all the laminated plates are taken from [Pagano 1970], and are

$$E_L = 172.4 \text{ GPa}, \quad E_T = 6.9 \text{ GPa}, \quad G_{LT} = 3.45 \text{ GPa}, \quad G_{TT} = 1.38 \text{ GPa}, \quad \nu_{LT} = \nu_{TT} = 0.25, \quad (60)$$

where L denotes the direction of the fiber and T denotes the direction perpendicular to the fiber. For sandwich plates, the material properties of the face sheets are the same as those in (60), and the core material properties are given by

$$\begin{aligned} E_1 &= 0.1 \text{ GPa}, & G_{12} &= 0.04 \text{ GPa}, & \nu_{12} &= 0.25, \\ E_2 = E_3 &= E_1, & G_{23} = G_{13} &= G_{12}, & \nu_{23} = \nu_{13} &= \nu_{12}. \end{aligned} \quad (61)$$

Four cases including a sandwich plate are considered for two sets of boundary conditions, which are listed in Table 1. The elastic constants c_{ijkl} can be then calculated by using the moduli given in (60) and (61) and the fiber angle given in Table 1. Their explicit form can be found in [Reddy 2004].

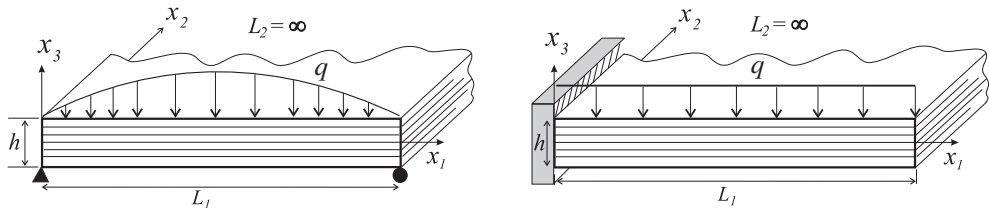


Figure 2. Loading and boundary conditions of semiinfinite plates: simply supported plate under sinusoidal pressure (left) and clamped-free plate under uniform pressure (right).

In all figures and tables, the k -th order solutions of the FAMPA are represented by

$$\mathbf{u}^{<k>} = \sum_{i=0}^k [\epsilon^{i+1} u_{\alpha}^{(i+1)} \quad \epsilon^i u_3^{(i)}]^t, \quad \boldsymbol{\sigma}^{<k>} = \sum_{i=1}^{k+1} \epsilon^i \boldsymbol{\sigma}^{(i)}, \quad k \geq 0, \quad (62)$$

so that the zeroth-order solution represents that of classical lamination theory (CLT) with $\sigma_{i3} = 0$ and the second-order solution represents that of the FSDT-like theory. Unlike in FSDT, the present second-order solution produces all the stress states including the transverse normal stress via the constitutive law. In the figures, the transverse stresses of the FSDT are calculated by using 3D equilibrium equations.

The displacement and stresses reported herein are normalized as follows [Pagano 1970]:

$$u_{\alpha}^* = 100E_T \frac{u_{\alpha}}{q_o} h S^3, \quad u_3^* = 100E_T \frac{u_3}{q_o} h S^4, \quad \sigma_{\alpha\beta}^* = \frac{\sigma_{\alpha\beta}}{q_o} S^2, \quad \sigma_{\alpha 3}^* = \frac{\sigma_{\alpha 3}}{q_o} S, \quad \sigma_{33}^* = \frac{\sigma_{33}}{q_o}, \quad (63)$$

where $S = L_1/h$ is the length-to-thickness ratio and q_o is the maximum of the applied pressure q .

5.1. Simply supported plates. For the problem of simply supported laminated and sandwich plates under sinusoidal pressure, the elasticity solution is available from [Pagano 1970], and has been used as the benchmark problem. In this case, problematic displacement prescribed boundary conditions are not involved. It is therefore possible to find the asymptotic solutions up to any desired order. For the purpose of comparison, the solutions of 3D elasticity and FSDT are also reproduced.

Case	Layup	x_3/h
1	[0.5 / 90.5 / 90.5 / 0.5]	{-1/2, -1/4, 0, 1/4, 1/2}
2	[90.5 / 0.5 / 90.5 / 0.5]	{-1/2, -1/4, 0, 1/4, 1/2}
3	[-30 / 30 / -30 / 30]	{-1/2, -1/4, 0, 1/4, 1/2}
4	[0.05 / Core / 0.05]	{-1/2, -2/5, 0, 2/5, 1/2}

Table 1. Lamination sequences for laminated and sandwich plates.

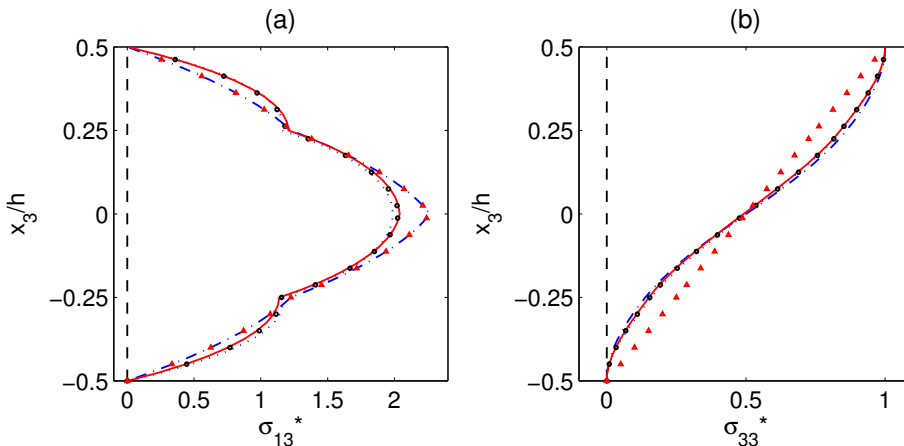


Figure 3. Transverse stresses of a simply supported plate, case 3, $S = 4$: σ_{13}^* (a) and σ_{33}^* (b). Exact (\bullet), FSDT (Δ), FAMPA 0th (—), FAMPA 2nd (— · —), FAMPA 4th (\cdots), and FAMPA 6th (—).

S	Models	Case 1	$\epsilon\%$	Case 2	$\epsilon\%$	Case 3	$\epsilon\%$	Case 4	$\epsilon\%$
4	Exact	3.3364	0	4.1812	0	3.2915	0	75.58	0
	FSDT	2.7299	-18	3.2964	-21	2.7868	-15	8.27	-89
	FAMPA 0th	0.5586	-83	1.1251	-73	0.9988	-70	1.01	-99
	FAMPA 2nd	3.5912	8	4.5380	9	3.4428	5	108.07	43
	FAMPA 4th	3.2689	-2	4.0805	-2	3.2655	-1	61.00	-19
	FAMPA 6th	3.3553	1	4.2121	1	3.2963	0	82.15	9
10	Exact	1.0359	0	1.6600	0	1.3854	0	17.01	0
	FSDT	0.9061	-13	1.4726	-11	1.2849	-7	2.17	-87
	FAMPA 0th	0.5586	-46	1.1251	-32	0.9988	-28	1.01	-94
	FAMPA 2nd	1.0438	1	1.6712	1	1.3899	0	18.14	7
	FAMPA 4th	1.0356	-0	1.6595	-0	1.3853	-0	16.93	-0
	20	Exact	0.6794	0	1.2609	0	1.0963	0	5.22
FSDT		0.6455	-5	1.2120	-4	1.0703	-2	1.30	-75
FAMPA 0th		0.5586	-18	1.1251	-11	0.9988	-9	1.01	-81
FAMPA 2nd		0.6799	0	1.2617	0	1.0966	0	5.29	1

Table 2. Comparison of center deflections of simply supported plates under sinusoidal loads.

Normalized center deflections of simply supported plates are listed and compared to the 3D elasticity solution in Table 2. FSDT shows significant improvement compared to the FAMPA-0th or CLT for laminated plates, cases 1–3. It however does not yield accurate predictions for the case of a sandwich plate. In fact, FSDT just produces comparable results to CLT even for $S \geq 20$. In contrast, the FAMPA-2nd results are practically identical to the 3D elasticity solution. Although the FAMPA-6th is necessary for accurate prediction in the case of very thick plates, $S = 4$, the FAMPA-2nd produces reasonable accuracy when $S \geq 10$ for both laminated and sandwich plates. Local through-the-thickness distributions of stresses are also important in analysis of composite plates. Transverse stresses for an antisymmetric laminated plate are presented in Figure 3 and those for a sandwich plate in Figure 4. It is seen that the FAMPA asymptotically converges to the 3D elasticity with increasing ϵ -order level. The transverse shear stress of the FAMPA-2nd is identical to that of FSDT, whereas the transverse normal stress of FSDT significantly deviates from the FAMPA-2nd and the 3D elasticity, which is clearly shown in Figure 4b.

5.2. Clamped-free plates. We now consider clamped-free plates, investigating displacement-prescribed and traction-free boundary conditions. Unlike the simply supported plate with sinusoidal loadings, our analysis is restricted to the FAMPA-2nd because the asymptotically correct displacement boundary condition is only available up to the second order, which is given in (59). In addition, there is difficulty in calculating higher-order derivatives with respect to y_α in the framework of a finite element method.

Normalized tip deflections of clamped-free laminated and sandwich plates with a function of the length-to-thickness ratio S are shown in Figure 5 for cases 3 and 4. The FAMPA-2nd performs similarly to FSDT for case 3. For a sandwich plate, FSDT significantly deviates from the 3D FEM, whereas the FAMPA-2nd is very close to it. This clearly indicates that it is of great importance to apply a proper

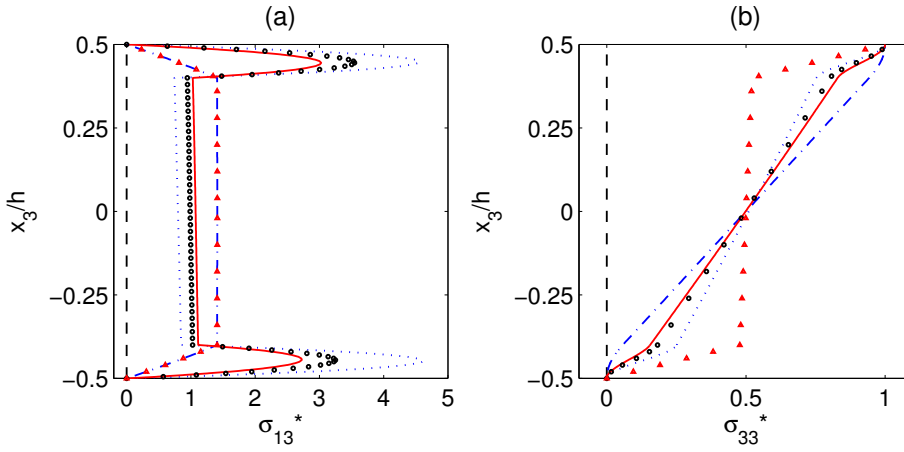


Figure 4. Transverse stresses of a simply supported plate, case 4, $S = 4$: σ_{13}^* (a) and σ_{33}^* (b). Exact (\bullet), FSDT (Δ), FAMPA 0th (—), FAMPA 2nd (— · —), FAMPA 4th (\cdots), and FAMPA 6th (—).

set of edge boundary conditions especially for a plate weak in shear. To more clearly demonstrate this, the bending deflection and slope along the normalized in-plane coordinate are illustrated in Figure 6 for a sandwich plate with $S = 10$. The error of the FSDT is more than 400% in terms of tip deflection, whereas the FAMPA-2nd shows reasonable accuracy. This is achieved by improving a clamped boundary condition in which the bending slope is not zero, as shown in Figure 6b, where the interior solution is approximately valid for 30% to 80% from the clamped end. Local stress distributions are also investigated, and stresses of a thick antisymmetric cross-ply plate at the midspan of the plate are illustrated in Figure 7. The transverse shear stress of the FAMPA-2nd coincides with that of FSDT, since σ_{13} is calculated by using the 3D equilibrium equation for FSDT. In-plane and transverse normal stresses calculated by the

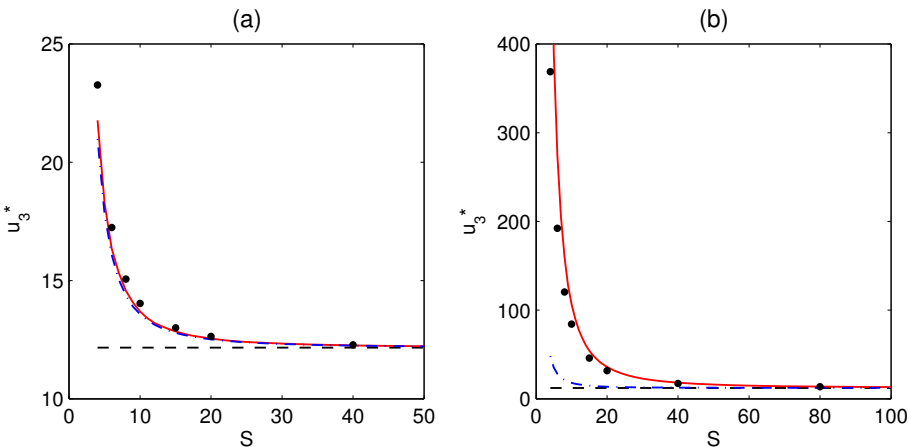


Figure 5. Tip deflections of clamped-free laminated and sandwich plates: antisymmetric angle-ply (a), case 3, and sandwich (b), case 4. 3D FEM (\bullet), FSDT (— · —), FAMPA 0th (—), and FAMPA 2nd (—).

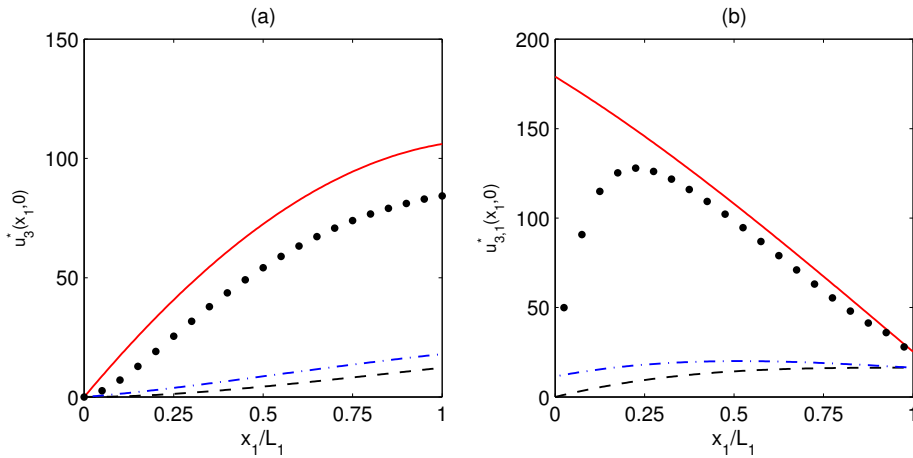


Figure 6. A clamped-free sandwich plate, **case 4**, $S = 10$: bending deflection (a), and bending slope (b). 3D FEM (\bullet), FSDT ($- \cdot -$), FAMPA 0th ($- -$), and FAMPA 2nd ($-$).

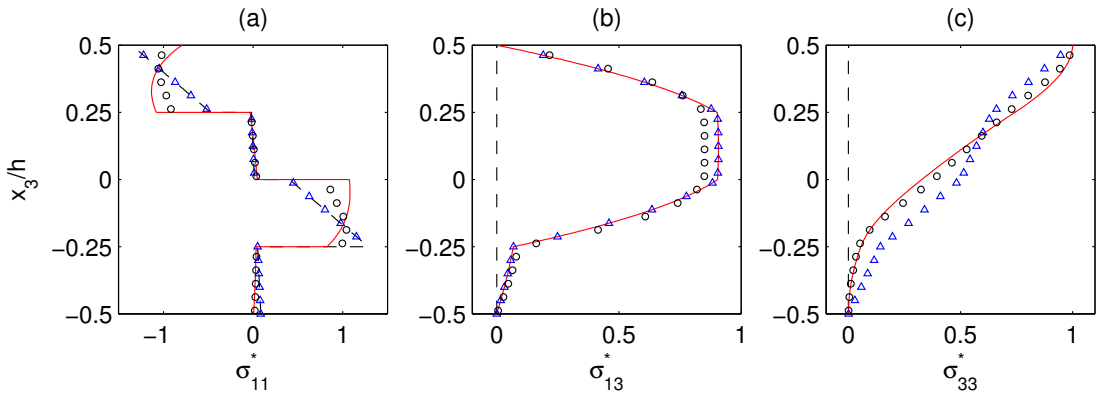


Figure 7. Stresses of a clamped-free antisymmetric cross-ply laminated plate, **case 2**, $S = 4$: σ_{11}^* (a), σ_{13}^* (b), and σ_{33}^* (c). 3D FEM (\circ), FSDT (Δ), FAMPA 0th ($- -$), and FAMPA 2nd ($-$).

FAMPA-2nd are well correlated with the 3D FEM, whereas FSDT yields erroneous results qualitatively as well as quantitatively.

To investigate the edge layer effects, the in-plane normal stresses calculated at near the clamped-end, midspan, and near the free-end, which are located at the 12%, 49%, and 87% axial positions from the clamped end, respectively, are plotted in **Figure 8** for a thick symmetric cross-ply plate. The best approximation of the FAMPA-2nd to the 3D FEM can be seen in the midspan where the interior solution is valid. Near the clamped end, the FAMPA-2nd tends to produce a through-the-thickness stress distribution similar to that in the interior region because we applied the asymptotically correct boundary condition up to the second order only. It can however accurately capture the stress-free edge layer effect, as shown in **Figure 8c** where the FAMPA-2nd drastically improves the prediction of the in-plane stress compared

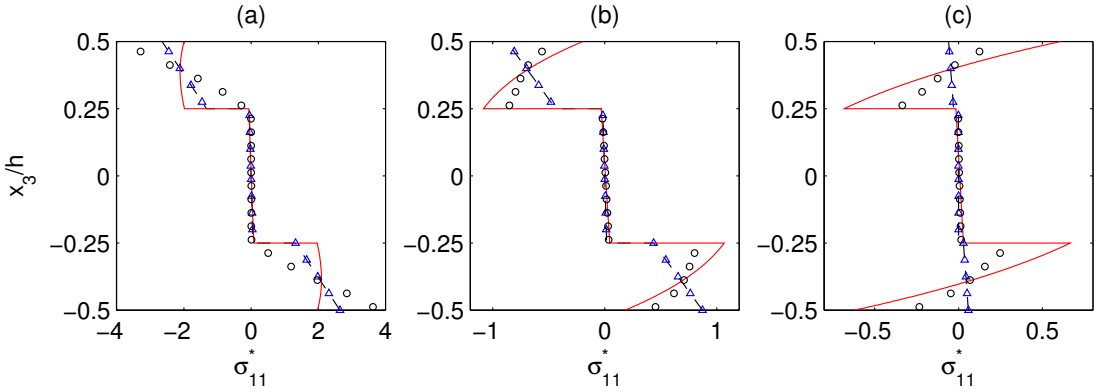


Figure 8. In-plane normal stress of a clamped-free symmetric cross-ply laminated plate, **case 1**, $S = 4$: near the clamped-end (a), midspan (b), and near the free-end (c). 3D FEM (\circ), FSDT (Δ), FAMPA 0th (---), and FAMPA 2nd (—).

to FSDT and the FAMPA-0th. It is of interest that the in-plane normal stress is not that small even if the in-plane stress is zero at the free-end.

5.3. Usefulness of the FAMPA. Through-the-thickness warping functions are discussed in this subsection. An antisymmetric angle-ply laminated plate, **case 3**, is considered as an example. The proposed asymptotic analysis method may be limited to second-order analysis because higher-order analysis requires both higher-order asymptotically correct displacement boundary conditions as well as higher-order derivatives. The requirement of higher-order derivatives of the macroscopic strain measure $\mathbf{e}^{(k)}$ makes it difficult to realize the FAMPA with a finite element method. Although the FAMPA-2nd yields reasonable accuracy for most engineering applications, one may want to look at higher-order effects. In this case, the warping functions $\Gamma_{\alpha\beta\dots\psi\omega}^{(k)}$ can provide useful information without solving the macroscopic problems.

The first-order through-the-thickness deformation mode of **case 3** is shown in **Figure 9**. This mode mainly illustrates the 3D Poisson effect that represents the deformation along the thickness direction. **Figure 9** implies that the out-of-plane displacements consist of linear and quadratic variations, in which the linear variation accounts for the in-plane tension induced deformation and the quadratic variation explains the bending induced deformation. In general these variations are smeared into the reduced stiffness models that are often derived by applying the plane stress assumption of $\sigma_{33} = 0$. The first nonclassical through-the-thickness mode, such as a transverse shear deformation effect, can be found in $\Gamma_{\alpha}^{(2)}$. For example, $\Gamma_1^{(2)}$ are plotted in **Figures 10** and **11**. Unlike the first deformation mode $\Gamma^{(1)}$, the in-plane displacements u_{α} play a major role in this mode. **Figure 10** depicts the displacement component u_1 , which clearly shows a transverse shear deformation effect due to the bending deformations corresponding to $\kappa_{11,1}$ and $\kappa_{22,1}$. The contribution of $\kappa_{22,1}$ to u_1 is obvious because of the antisymmetric configuration. For this reason, the higher-order bending curvature $\kappa_{11,1}$ also contributes to the displacement component u_2 as shown in **Figure 11**. The through-the-thickness warping functions presented in **Figure 11** have a unique pattern depending on the lamination configurations, which could be very difficult to presuppose.

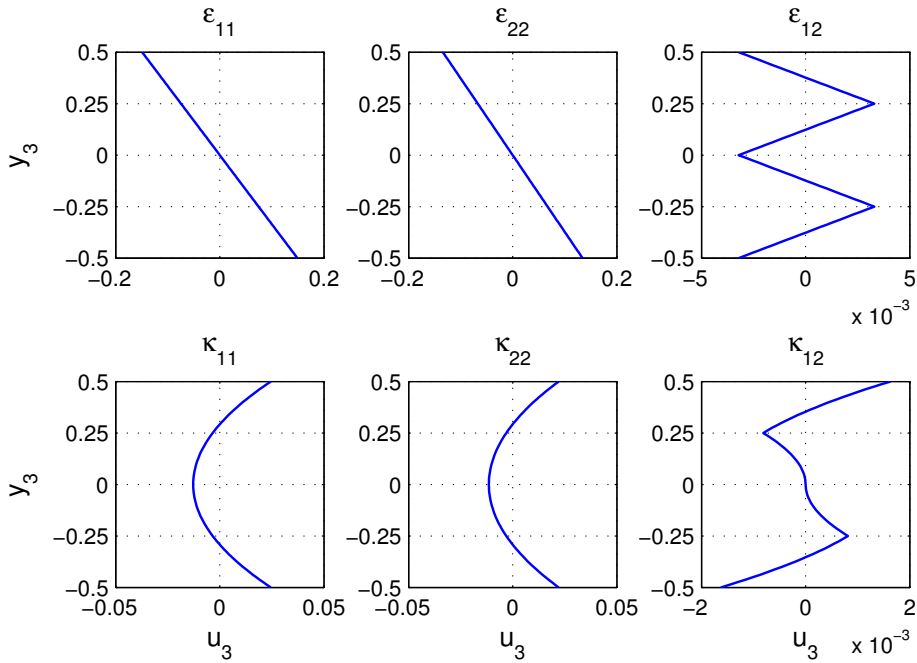


Figure 9. The first-order through-the-thickness deformation mode (u_3) of an antisymmetric angle-ply laminated plate, case 3, $\Gamma^{(1)}$.

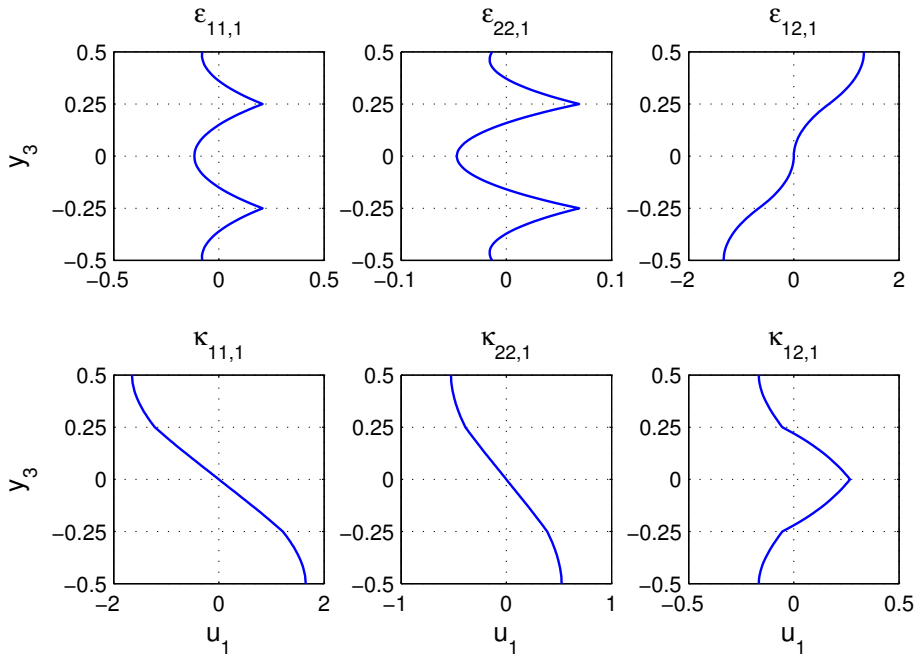


Figure 10. The second-order through-the-thickness deformation mode (u_1) of an antisymmetric angle-ply laminated plate, case 3, $\Gamma_1^{(2)}$.

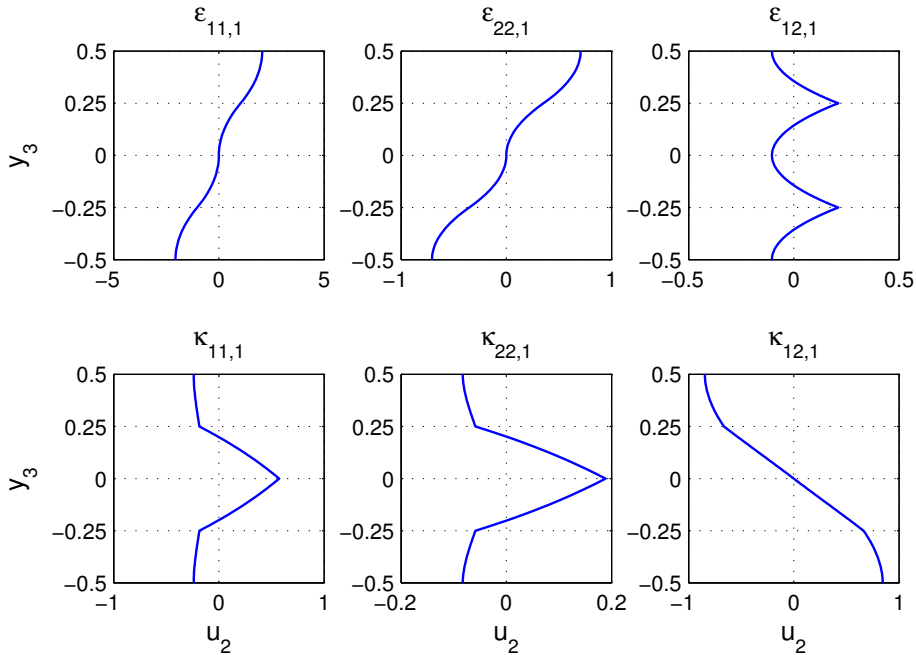


Figure 11. The second-order through-the-thickness deformation mode (u_2) of an anti-symmetric angle-ply laminated plate, *case 3*, $\Gamma_1^{(2)}$.

6. Conclusions

A formal asymptotic method-based plate analysis (FAMPA) is developed to analyze general anisotropic plates. To assess the FAMPA capability for various sets of boundary conditions, simply supported and clamped-free boundary conditions are considered. For a simply supported boundary condition, it is demonstrated that the FAMPA can provide the exact solutions by increasing the order up to the sixth order for very thick plates. The orthogonality condition of asymptotic displacements to the fundamental solution is adopted to avoid the complexity of using the decay analysis method for a displacement prescribed boundary. The boundary conditions obtained, which are asymptotically correct up to the second order, are applied to plates with clamped-free boundary conditions. The results are compared to those of the three-dimensional FEM and FSDT. It is demonstrated that the FAMPA-2nd is simple enough for engineering applications and accurate enough for high precision analysis. It can also simulate the free-edge boundary layer effect qualitatively, whereas FSDT cannot. Although a higher-order computation of the FAMPA is practically limited due to the displacement boundary conditions and the higher order derivatives of the macroscopic strain measure, one can have in-depth understanding of the higher-order behaviors of such composite plates via the microscopic analysis up to any desired order. The through-the-thickness warping functions obtained can be also used for development and validation of any higher-order plate theories.

References

- [Berdichevskii 1979] V. L. Berdichevskii, “Variational-asymptotic method of constructing a theory of shells”, *J. Appl. Math. Mech.* **43**:4 (1979), 711–736.

- [Berg 1991] L. J. Berg, “Asymptotic variational methods in large deflection small strain plate theory”, *Int. J. Solids Struct.* **27**:11 (1991), 1401–1417.
- [Buannic and Cartraud 2001] N. Buannic and P. Cartraud, “Higher-order effective modeling of periodic heterogeneous beams, I: Asymptotic expansion method”, *Int. J. Solids Struct.* **38**:40–41 (2001), 7139–7161.
- [Carrera 2003] E. Carrera, “Historical review of Zig-Zag theories for multilayered plates and shells”, *Appl. Mech. Rev. (ASME)* **56**:3 (2003), 287–308.
- [Cesnik et al. 1996] C. E. S. Cesnik, V. G. Sutyryn, and D. H. Hodges, “Refined theory of composite beams: the role of short-wavelength extrapolation”, *Int. J. Solids Struct.* **33**:10 (1996), 1387–1408.
- [Duva and Simmonds 1992] J. M. Duva and J. G. Simmonds, “The influence of two-dimensional end effects on the natural frequencies of cantilevered beams weak in shear”, *J. Appl. Mech. (ASME)* **59**:1 (1992), 230–232.
- [Fan and Widera 1994] H. Fan and G. E. O. Widera, “On the use of variational principles to derive beam boundary conditions”, *J. Appl. Mech. (ASME)* **61**:2 (1994), 470–471.
- [Gregory and Wan 1984] R. D. Gregory and F. Y. M. Wan, “Decaying states of plane strain in a semi-infinite strip and boundary conditions for plate theory”, *J. Elasticity* **14**:1 (1984), 27–64.
- [Horgan and Simmonds 1991] C. O. Horgan and J. G. Simmonds, “Asymptotic analysis of an end-loaded, transversely isotropic, elastic, semi-infinite strip weak in shear”, *Int. J. Solids Struct.* **27**:15 (1991), 1895–1914.
- [Kapania and Raciti 1989] R. K. Kapania and S. Raciti, “Recent advances in analysis of laminated beams and plates, I: shear-effects and buckling”, *AIAA J.* **27**:7 (1989), 923–935.
- [Kim et al. 2008] J.-S. Kim, M. Cho, and E. C. Smith, “An asymptotic analysis of composite beams with kinematically corrected end effects”, *Int. J. Solids Struct.* **45**:7–8 (2008), 1954–1977.
- [Lo et al. 1977] K. H. Lo, R. M. Christensen, and F. M. Wu, “A higher-order theory of plate deformation, II: Laminated plates”, *J. Appl. Mech. (ASME)* **44** (1977), 669–676.
- [Niordson 1979] F. I. Niordson, “An asymptotic theory for vibrating plates”, *Int. J. Solids Struct.* **15**:2 (1979), 167–181.
- [Noor and Burton 1989] A. K. Noor and W. S. Burton, “Assessment of shear deformation theories for multilayered composite plates”, *Appl. Mech. Rev. (ASME)* **42** (1989), 1–13.
- [Novotny 1970] B. Novotny, “On the asymptotic integration of the three-dimensional non-linear equations of thin elastic shells and plates”, *Int. J. Solids Struct.* **6**:4 (1970), 433–451.
- [Pagano 1970] N. J. Pagano, “Influence of shear coupling in cylindrical. Bending of anisotropic laminates”, *J. Compos. Mater.* **4**:3 (1970), 330–343.
- [Reddy 2004] J. N. Reddy, *Mechanics of laminated composite plates and shells: theory and analysis*, 2nd ed., CRC Press, Boca Raton, FL, 2004.
- [Reddy and Jr. 1994] J. N. Reddy and D. H. R. Jr., “Theories and computational models for composite laminates”, *Appl. Mech. Rev. (ASME)* **47** (1994), 147–169.
- [Tarn et al. 1996] J.-Q. Tarn, Y.-B. Wang, and Y.-M. Wang, “Three-dimensional asymptotic finite element method for anisotropic inhomogeneous and laminated plates”, *Int. J. Solids Struct.* **33**:13 (1996), 1939–1960.
- [Wang and Tarn 1994] Y.-M. Wang and J.-Q. Tarn, “A three-dimensional analysis of anisotropic inhomogeneous and laminated plates”, *Int. J. Solids Struct.* **31**:4 (1994), 497–515.
- [Yu 2005] W. Yu, “Mathematical construction of a Reissner-Mindlin plate theory for composite laminates”, *Int. J. Solids Struct.* **42**:26 (2005), 6680–6699.
- [Yu et al. 2002] W. Yu, D. H. Hodges, and V. V. Volovoi, “Asymptotic construction of Reissner-like composite plate theory with accurate strain recovery”, *Int. J. Solids Struct.* **39**:20 (2002), 5185–5203.

Received 23 Nov 2008. Revised 5 Mar 2009. Accepted 18 Mar 2009.

JUN-SIK KIM: junsik.kim@kumoh.ac.kr

School of Mechanical Engineering, Kumoh National Institute of Technology, Gumi, Gyeongbuk 730-701, Korea

REMARKS ON THE ACCURACY OF ALGORITHMS FOR MOTION BY MEAN CURVATURE IN BOUNDED DOMAINS

SIMON COX AND GENNADY MISHURIS

Simulations of motion by mean curvature in bounded domains, with applications to bubble motion and grain growth, rely upon boundary conditions that are not necessarily compatible with the equation of motion. Three closed form solutions for the problem exist, governing translation, rotation, and expansion of a single interface, providing the only benchmarks for algorithm verification. We derive new identities for the translation solution. Then we estimate the accuracy of a straightforward algorithm to recover the analytical solution for different values of the velocity V given along the boundary. As expected, for large V the error can reach unacceptable levels especially near the boundary. We discuss factors influencing the accuracy and propose a simple modification of the algorithm which improves the computational accuracy.

1. Introduction

Motion by mean curvature and the dynamics of two-dimensional foams are closely related subjects in the study of materials [Smith 1952]. In the ideal model of the evolution of crystalline grains in a polycrystalline metal, known as normal grain growth, the size of each grain evolves due to the normal motion of each of its boundaries [Weaire and McMurry 1996]. Each boundary has a certain mobility λ , and moves in such a way as to reduce the total perimeter of the pattern. The ideal soap froth is a model of a two-dimensional foam [Weaire and Hutzler 1999], such as the one studied by Bragg and Nye [1947] and which has recently enjoyed a renaissance, in which interface curvature and pressure differences are balanced, again due to minimization of the total perimeter. Both ideal models arise naturally as limits of the following viscous froth model (VFM) [Kern et al. 2004], derived as a force balance per unit length of the interface:

$$\Delta p = \gamma \kappa + \lambda v_n. \quad (1-1)$$

Here Δp is the pressure difference across the interface and γ its surface tension (assumed constant); κ is the local curvature and v_n the velocity normal to the interface.

The aim of this paper is to investigate the accuracy of algorithms for (1-1), and for this reason we restrict ourselves to the simplest case, when $\Delta p = 0$. In the case of grain growth, there are no area (volume in 3D) constraints, and pressure differences between cells are negligible. This limit is also appropriate to ordered (hexagonal) foams and single soap films.

We ask how a solution to the equations of motion by mean curvature can be commensurate with the boundary of the domain. That is, even though we can find an interface *shape* at a particular instant in time, by solving the governing equation, it is not always possible to match this with the imposed

Keywords: motion by mean curvature, grain growth, foam rheology, algorithms, measures of accuracy.
Cox was financially supported by EPSRC (EP/D048397/1, EP/D071127/1).

boundary condition on *velocity*. We then ask how well solutions that satisfy both the governing equation and boundary condition can be calculated numerically.

The most stringent test of a numerical algorithm here is an initial interface shape that is far from satisfying the boundary conditions. It is this that we use for our preliminary numerical tests. We develop a general class of less severe solutions, that can be used to test numerical algorithms, based upon this simple interface shape (rather than the more complicated shapes found in a real foam or metal). We propose three identities which provide measures of accuracy and, further, can be implemented within an existing algorithm to improve its performance.

2. Curvature-driven motion of a bounded interface

2A. Problem formulation. In vector form, the motion of an interface in the model of ideal grain growth can be described by

$$\mathbf{v} = \kappa \mathbf{n}, \tag{2-1}$$

where \mathbf{n} and \mathbf{s} are the normal and tangential unit vectors to the interface (see [Figure 1](#)):

$$\mathbf{n} = [n_1, n_2], \quad \mathbf{s} = [n_2, -n_1]. \tag{2-2}$$

If the representation of the interface is taken in the form

$$x = x(y, t), \quad y \in [\underline{y}(t), \bar{y}(t)], \tag{2-3}$$

then the vector components n_1, n_2 are calculated as follows:

$$n_1 = -\frac{dy}{ds} = -\sin \theta = -\frac{1}{\sqrt{1 + (x_y)^2}}, \quad n_2 = \frac{dx}{ds} = \cos \theta = \frac{x_y}{\sqrt{1 + (x_y)^2}}, \tag{2-4}$$

where $x_y = dx/dy$, $ds = \sqrt{(dx)^2 + (dy)^2}$, and θ is the tangential angle to the interface (see [Figure 1](#)). Finally, the vector $\mathbf{v} = [v_1, v_2]$ is the instantaneous velocity of the point (x, y) lying on the interface at time t and κ is the curvature of the interface at that point:

$$\kappa = \frac{d\theta}{ds} = \frac{-x_{yy}}{\sqrt{(1 + (x_y)^2)^3}}. \tag{2-5}$$

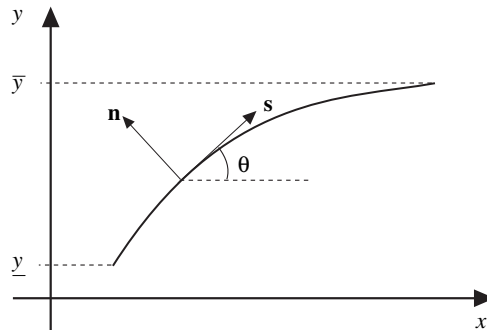


Figure 1. The bounded interface considered here.

Equation (2-1) can also be written in component form:

$$v_n = \mathbf{v} \cdot \mathbf{n} = v_1 n_1 + v_2 n_2 = \kappa, \tag{2-6}$$

$$v_s = \mathbf{v} \cdot \mathbf{s} = v_1 n_2 - v_2 n_1 = 0. \tag{2-7}$$

In this paper we will consider only Mullins’ translational solution [Mullins 1956] (see below), also known as the grim reaper because of the way in which it scythes through space without change of shape, which is symmetrical with respect to the x -axis. Invariant solutions for rotation have been considered elsewhere [Mullins 1956; Wood 1996]. Taking into account the direction of the interface motion, we can assume that

$$n_1 < 0, \quad n_2 > 0, \quad x_y > 0, \quad 0 < \theta < \pi/2, \quad x_{yy} > 0, \quad \kappa < 0, \tag{2-8}$$

$$v_n < 0 \quad (v_2 < 0, v_1 > 0). \tag{2-9}$$

Equation (2-6) is widely discussed in the literature [Mullins 1956; Peleg et al. 2001], while (2-7) is somehow usually forgotten in this context. If one is only interested in reconstructing the interface position at any time step an approach based only on (2-6) is sufficient. However, if it is required that the position of each material point along the interface is controlled, as in the case of numerical computation, then both equations are equally important. Note that there has previously been an attempt to control both the velocity components in a specific way [Green et al. 2006]. Equation (2-7) allows us to find a relation between the two unknown components of the velocity vector \mathbf{v} and the normal vector \mathbf{n} in the form

$$n_2 = \frac{v_2}{v_1} n_1. \tag{2-10}$$

This allows us to eliminate components of the normal vector \mathbf{n} from (2-6) to give

$$-\left(v_1 + \frac{v_2^2}{v_1}\right) = \frac{d\theta}{dy}. \tag{2-11}$$

2B. Mullins’ solution for translation revisited. Let us assume that the interface conserves its shape but moves in the x -direction with a constant speed V . We consider two points A and C having the same y -coordinate $y = y_0$ at two consecutive time steps t_0 and $t_0 + dt$ (see Figure 2). It is clear that these two points correspond to two different material points. Namely, there exists a point B on the interface at

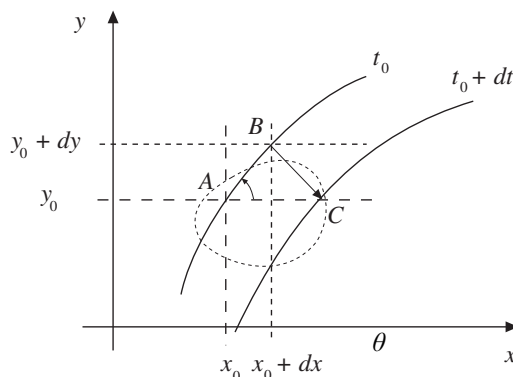


Figure 2. Interface under translational motion at two consecutive instants in time.

time t_0 which moves according to the curvature law (2-1) to the point C for an infinitesimally small time step dt . If the coordinates of the point A are (x_0, y_0) then the coordinates of B and C can be written $(x_0 + dx, y_0 + dy)$ and $(x_0 + Vdt, y_0)$.

Note that

$$\overline{BC} = \mathbf{v}(x_0 + dx, y_0 + dy)dt = \mathbf{v}(x_0, y_0)dt + O(dt ds).$$

On the other hand, $|BC| = V \sin \theta dt$, and $\tan \theta = v_1/|v_2|$. As a result one can conclude:

$$V = \frac{1}{v_1(y)}(v_1^2(y) + v_2^2(y)), \tag{2-12}$$

in some interval $y \in [0, h]$. This relation follows immediately from (2-11) in the case of translation of the interface in the x -direction.

Now, to reconstruct the solution obtained by Mullins [1956] it is sufficient to substitute (2-12) into (2-11) to give

$$\frac{\pi}{2} - Vy = \theta. \tag{2-13}$$

Here we have taken into account the second of the two symmetry conditions at the point $y = 0$:

$$v_2(0) = 0, \quad \theta(0) = \frac{\pi}{2}. \tag{2-14}$$

Equation (2-13) can be written in the form

$$\cot Vy = y_x, \tag{2-15}$$

which after direct integration leads to Mullins' solution:

$$x(y) = x(0) + Vt - \frac{1}{V} \log \cos(Vy), \quad y \in [0, h], \tag{2-16}$$

where $x(0)$ is the arbitrary initial position of the centre of the interface. This solution exists only under the condition $h < h_{\max}$, where

$$h_{\max} = \frac{\pi}{2V}. \tag{2-17}$$

Note also that the angle θ defined by such a solution monotonically decreases in the interval $y \in (0, h)$ ($h < h_{\max}$), taking values

$$\theta(y) \in \left(\theta_{\min}, \frac{\pi}{2}\right), \quad \theta_{\min} = \theta_{\min}(h) = \frac{\pi}{2} - Vh. \tag{2-18}$$

It is now possible to write analytical representations of all problem variables in the interval $y \in (0, h)$:

$$v_1 = V \cos^2 Vy, \quad v_2 = -\frac{1}{2} V \sin 2Vy, \quad n_1 = \sin Vy, \quad n_2 = \cos Vy, \quad \kappa = V \cos Vy. \tag{2-19}$$

Note that the first symmetry condition (2-14) has not been used but the reconstructed Mullins solution (2-16) satisfies it automatically, by (2-4) and (2-10). The solution exhibits the following asymptotics near the symmetry axis:

$$x(y) = x(0) + Vt + \frac{1}{2} Vy^2 + O(y^4), \quad y \rightarrow 0; \tag{2-20}$$

thus near $y = 0$ the interface is close to a parabola. Close to the other end of the reaper (in the case of the maximal thickness $h = h_{\max}$), the following asymptotic estimate can be obtained:

$$x(y) = -\frac{1}{V} \log(h_{\max} - y) + O(1), \quad y \rightarrow h_{\max}, \quad \text{or} \quad y - h_{\max} \sim -de^{-Vx}, \quad x \rightarrow +\infty, \quad (2-21)$$

where $d = (1/V) \exp\{V(x(0) + Vt)\}$ is a positive constant.

Note that relation (2-12) also represents the boundary condition for any moving interface whose upper point lies on the line $y = \bar{y} = h$ and which moves in the x -direction with velocity V . Moreover, the velocity can be in that case a function of time $V = V(t)$:

$$V(t)v_1(h, t) = v_1^2(h, t) + v_2^2(h, t). \quad (2-22)$$

Substituting (2-1) into (2-22) such a boundary condition can be equivalently rewritten in other forms:

$$\kappa(h, t) = V(t)n_1(h, t), \quad \text{or} \quad x_{yy}(h, t) = V(t)(1 + (x_y(h, t))^2). \quad (2-23)$$

Note that we have not used (2-16) to define (2-23).

2C. Arbitrary instantaneous solution of equations (2-6) and (2-7) in a bounded domain. Let us consider any instantaneous solution of the equations (2-6) and (2-7) with the prescribed boundary condition (2-22), by which we mean an instantaneous state of the film which may or may not be commensurate with the boundary conditions and could or could not be a steady state. Effectively this means that, for a particular time t , the end points of the interface $y = \underline{y}(t)$ and $y = h$ are defined and the velocity components $v_1(y, t)$ and $v_2(y, t)$ are known functions of the variable y , while the problem is now to determine, using this information, the position of the interface in space variables (y, x) .

We introduce a function which in what follows is considered known:

$$F(y) = v_1(y) + \frac{v_2^2(y)}{v_1(y)} > 0, \quad y \in (\underline{y}, h). \quad (2-24)$$

Note that the condition (2-12) may be not valid at all inside the interval $y \in (\underline{y}, h)$ as it was for Mullins' solution; as a result, $F(y)$ is not a constant, in general. Equation (2-11) can be integrated to give

$$-\int_{\underline{y}}^y F(\zeta) d\zeta = \theta(y) - \underline{\theta}. \quad (2-25)$$

Here, recall that F depends upon time t , so that $\underline{y} = \underline{y}(t)$ and the constant of integration is $\underline{\theta} = \underline{\theta}(t)$. Equation (2-25) should be considered together with (2-10) which, in this case, takes the form

$$\frac{dx}{dy} = -\frac{v_2}{v_1} = \cot \theta, \quad (2-26)$$

or

$$x(y) = \underline{x} - \int_{\underline{y}}^y \frac{v_2(\zeta)}{v_1(\zeta)} d\zeta. \quad (2-27)$$

Equations (2-25) and (2-26) together indicate that the functions v_1 and v_2 cannot be chosen arbitrarily to satisfy the vectorial (2-1) as one might expect. Instead, the following identity has to be satisfied:

$$\arctan \frac{v_1}{v_2} = \int_{\underline{y}}^y F(\zeta) d\zeta - \underline{\theta}, \quad (2-28)$$

or writing $w = v_1/v_2$ and using (2-24), the derivative of (2-28) becomes

$$\frac{w_y}{1+w^2} = \frac{(1+w^2)v_2}{w}, \tag{2-29}$$

where the subscript y denotes differentiation, which leads to the following identity valid within the entire interval $y \in (\underline{y}, h)$:

$$v_1^2(y) = -v_2^2(y) \left(\frac{1}{2 \int_{\underline{y}}^y v_2(\xi) d\xi + c} + 1 \right), \tag{2-30}$$

where the constant of integration clearly depends on time too: $c = c(t) = 1/(1+w^2)|_{y=\underline{y}}$. Note that any solution of equations (2-6) and (2-7) satisfies this additional relation, which makes sense only under the constraint

$$-1 \leq 2 \int_{\underline{y}}^y v_2(\xi) d\xi + c \leq 0. \tag{2-31}$$

As $0 < \theta < \underline{\theta}$, one can also deduce another condition which has to be true for any admissible velocities:

$$0 \leq \int_{\underline{y}}^y F(\xi) d\xi \leq \underline{\theta}. \tag{2-32}$$

Note that the constant \underline{x} in (2-27) is arbitrary (it changes only the position of the interface in the x -direction and does not influence any other variables). To determine the other constants $\underline{\theta}(t)$ and $c(t)$, we need to use the boundary conditions at the ends of the interface. Thus, condition (2-22) together with (2-30) leads to

$$v_1(h) = V(1+c+2I_2), \quad v_2(h) = -V\sqrt{-(1+c+2I_2)(c+2I_2)}. \tag{2-33}$$

where we have set

$$I_2 \equiv I_2(t) = \int_{\underline{y}(t)}^h v_2(\xi) d\xi.$$

If the boundary condition on the other end is given in the form

$$\theta(\underline{y}(t)) = \underline{\theta}(t), \tag{2-34}$$

then all the constants have been defined. Such an instantaneous solution, assuming that the functions $v_1(y)$ and $v_2(y)$ satisfy (2-28), conditions (2-33), and restrictions (2-31) and (2-32), can be realized during the interface evolution at some step.

In the case of the symmetrical solution, where both symmetry conditions (2-14) and the additional condition $v_1(0) = W > 0$ have to be satisfied, one can show that

$$c(t) \equiv 0, \quad v_2(y) \sim -W^2y, \quad y \rightarrow 0. \tag{2-35}$$

Note here that the value $W = W(V, h)$ should be found from the constructed solution and is not an additional (arbitrary or given) constant.

Finally, both restrictions (2-31) and (2-32) should be valid for the symmetrical interface:

$$\int_0^h v_2(\xi) d\xi \geq -\frac{1}{2}, \quad \int_0^h F(\xi) d\xi \leq \frac{\pi}{2}. \tag{2-36}$$

Note that the tangential angle θ for this solution is a monotonically decreasing function in the interval $y \in (0, h)$ so that

$$\theta(y) \in \left(\theta_{\min}, \frac{\pi}{2}\right), \quad \theta_{\min} = \frac{\pi}{2} - \int_0^h F(\xi) d\xi. \tag{2-37}$$

It is straightforward to see that Mullins’ solution (2-19) satisfies all these relationships with $c(t) = 0$, $\underline{\theta}(t) = \pi/2$, and $W = V$, as expected. In the next section, we construct analytical examples of symmetrical instantaneous solutions which are different from Mullins’.

3. A family of symmetrical instantaneous solutions

In this section we present analytical representations of some instantaneous symmetrical solutions for the interface satisfying the same boundary (2-22) and symmetry (2-14) conditions as Mullins’ solution. Those solutions are not, generally speaking, steady-state ones. This means that they can be reached at some time step t , given the interface boundary velocity $V(t)$ and the position of the ends $h(t)$, but all these parameters may later change with time. What is extremely interesting about these solutions is that some of them are well-defined for any velocity $V > 0$ and an arbitrary position of the boundary $y = h$. This shows a rich behaviour of possible instantaneous solutions. It is also clear that there is an infinite number of admissible instantaneous solutions. Some of them can be realized during some specific non-steady-state interface motion. For example, *any* instantaneous solution obtained during a numerical computation, for any particular time step, boundary velocity, and topology, has to satisfy all the relations (2-24)–(2-34). This will allow us to use the relations as indicators of the accuracy of computations. Moreover, they could provide a means to improve the accuracy of the algorithms.

(One could also consider the family of arbitrary, not necessarily symmetric, instantaneous solutions, which is even larger than the symmetric case. In fact, the family of symmetrical solutions has one degree of freedom — since $c(t)$ vanishes in this case — and correspondingly one less boundary condition; compare (2-34) and (2-14). In the context of further applications of this result to a given algorithm, where the angle-type boundary condition has to be preserved at the interface intersection point, it is worth mentioning that the boundary condition (2-34) is therefore more important for application than the symmetry condition. On the other hand, symmetrical instantaneous solutions can also be considered a subset of the asymmetric solutions if one considers the interval (h_0, h) instead of $(0, h)$ ($0 < h_0 < h$). This idea has been exploited previously in [Green et al. 2009].)

3A. First example. We consider the following simple combination of compatible velocities

$$v_2(y) = -W^2y, \quad v_1(y) = W\sqrt{1 - W^2y^2}, \quad W = \frac{V}{\sqrt{1 + V^2h^2}}, \tag{3-1}$$

which satisfy (2-30) with $c = 0$ and $\underline{y} = 0$ and, as a result, can be used to construct a symmetrical instantaneous solution. Here W is the same constant as in (2-35). Natural restrictions (2-36) for the existence of such a solution give the same estimate:

$$W < \frac{1}{h}, \quad \text{or} \quad \frac{V}{\sqrt{1 + V^2h^2}} < \frac{1}{h}, \tag{3-2}$$

which holds true for any values of V and h . The shape of the interface is an ellipse described by (2-27):

$$x(y, t) = x(0, t) - \sqrt{1 - W^2 y^2}. \tag{3-3}$$

The tangential angle θ for this solution is a monotonically decreasing function in the interval $y \in (0, h)$ and

$$\theta(y) \in \left(\theta_{\min}, \frac{\pi}{2}\right), \quad \theta_{\min} = \frac{\pi}{2} - \arcsin(Wh) > 0. \tag{3-4}$$

3B. Second example. We now consider another specific instantaneous solution assuming that $v_1(y) = W < V$. Then the second component of the velocity satisfies the equation

$$\frac{W^2}{v_2^2(y)} = -\frac{1}{2 \int_0^y v_2(\zeta) d\zeta} - 1. \tag{3-5}$$

To find $v_2(y)$ it is more convenient to return to the differential equation (2-29) rather than working with the nonlinear integral equation (3-5). After integration it takes the form

$$\Phi\left(\frac{v_2}{W}\right) = -Wy, \tag{3-6}$$

where the odd function Φ is defined as

$$\Phi(\zeta) = \frac{1}{2} \left(\arctan \zeta + \frac{\zeta}{1 + \zeta^2} \right), \quad \Phi'(\zeta) = \frac{1}{(1 + \zeta^2)^2}. \tag{3-7}$$

Note that $\Phi : \mathbb{R}_+ \rightarrow [0, \pi/4)$ is a monotonic function. Moreover, one can easily obtain the constraint $Wh < \pi/4$, which is similar to (2-36) and (3-2). Then the required velocity component v_2 can be found from

$$v_2 = -W\Phi^{-1}(Wy), \tag{3-8}$$

and we can finally find the complete solution using (2-26):

$$x(y, t) = x(0, t) + \frac{1}{W} \int_0^{Wy} \Phi^{-1}(\xi) d\xi. \tag{3-9}$$

Finally, note that the tangential angle θ for this solution is a monotonically decreasing function in the interval $y \in (0, h)$:

$$\theta(y) \in \left(\theta_{\min}, \frac{\pi}{2}\right), \quad \theta_{\min} = \frac{\pi}{2} - \int_0^{Wh} (1 + (\Phi^{-1}(\xi))^2) d\xi. \tag{3-10}$$

It remains only to find possible values of the unknown constant W in order to satisfy the boundary condition (2-22). The relevant equation takes the form

$$\Phi^{-1}(Wh) = \sqrt{\frac{Vh}{Wh} - 1}. \tag{3-11}$$

This equation has the unique solution $W = W_*(V, h) < V$. In fact, the left-hand side is an increasing function from zero to infinity as $Wh \rightarrow \pi/4$, whereas the right-hand side is a decreasing function taking values between ∞ when $Wh \rightarrow 0$ and 0 when $Wh \rightarrow Vh$. Additionally one can conclude from this that $Wh < \min\{Vh, \pi/4\}$, so the restriction defined after (3-7) always holds. In other words, this solution,

as well as that of the first example, is well-defined for arbitrary velocity V and position of the boundary $y = h$. We can also show that θ_{\min} is always positive:

$$\theta_{\min} > \frac{\pi}{2} - \int_0^{\pi/4} (1 + (\Phi^{-1}(\xi))^2) d\xi = \frac{\pi}{2} - \int_0^\infty (1 + \eta^2)\Phi'(\eta) d\eta = \frac{\pi}{2} - \int_0^\infty \frac{d\eta}{1 + \eta^2} = 0. \tag{3-12}$$

It is interesting to note that in the case $V \ll 1$ both of the instantaneous solutions constructed above coincide with Mullins' solution to within an accuracy of $O(V^2)$ for any fixed value of h . On the other hand, in this case the solution is practically (with the same accuracy) a straight line (or at the next order of accuracy, a parabola).

3C. General case. The previous example indicates how to build a wider class of symmetrical instantaneous solutions. Let us introduce the set $\mathfrak{A} \subset C^2([-a, a])$ ($a > 0$) of even functions ψ satisfying the following four conditions:

$$\psi(\xi) = \frac{1}{2}\xi^2 + O(\xi^4), \quad \xi \rightarrow 0; \quad \psi(a) \leq \frac{1}{2}; \quad \psi' > 0; \quad \left(\frac{\psi'}{\sqrt{\psi(1-2\psi)}} \right)' \geq 0, \quad \xi \in (0, a). \tag{3-13}$$

Note that a may differ from function to function, but it is necessary that for every function there exists some $a > 0$ for which all four conditions hold.

For example, the following three functions belong to the set \mathfrak{A} :

$$\psi_1(\xi) = \frac{1}{2} \sin^2 \xi, \quad \psi_2(\xi) = \frac{1}{2} \xi^2, \quad \psi_3(\xi) = \int_0^\xi \Phi^{-1}(\zeta) d\zeta = \frac{1}{2} \left(1 - \frac{1}{1 + (\Phi^{-1}(\xi))^2} \right), \tag{3-14}$$

with $a = \pi/2, 1,$ and $\pi/4,$ respectively. These three functions have been collected from Mullins' solution and the two previous examples. Thus, the set \mathfrak{A} is not empty.

Using any function from this set we can construct a symmetrical instantaneous solution with velocity components in the form

$$v_2(y) = -W\psi'(Wy), \quad v_1(y) = W\psi'(Wy)\sqrt{\frac{1 - 2\psi(Wy)}{2\psi(Wy)}}, \tag{3-15}$$

that identically satisfies (2-30) with $c = 0$. Then the unknown constant W should be taken to be of the form $W = W_*(Vh)/h$ where $W_*(Vh) > 0$ is a solution of the implicit equation

$$\frac{\psi'(W_*)}{\sqrt{2\psi(W_*)(1 - 2\psi(W_*))}} = \frac{Vh}{W_*}, \tag{3-16}$$

which follows from (2-22).

Because of the last condition in (3-13), there may exist only one solution of this equation. If, in addition, the left-hand side of (3-16) tends to infinity as $W_* \rightarrow a$, then the solution always exists and $W_* < a$. However, if the left-hand side of (3-16) tends to a finite value $L_* > 0$ as $W_* \rightarrow a$, then the solution exists only under the additional condition

$$Vh < L_*a. \tag{3-17}$$

One can check that for Mullins' solution $L_* = 1$ and (3-17) coincides with (2-17). For the other two cases previously discussed above, we have $L_* = \infty$ so the solution of the implicit equation (3-16) always exists and no solvability condition (3-17) is needed in these cases.

To reconstruct the complete symmetrical instantaneous solution based on (3-15) it is enough to substitute it in (2-24), (2-25), and (2-27).

Note that in the case $V \ll 1$, the solution to (3-16) gives $W_* \sim V$, as one can conclude from the first part of (3-13). This means that any constructed instantaneous solution differs negligibly from the Mullins' solution for small values of the velocity V .

It remains to investigate two important constraints (2-36). Taking into account that

$$\int_0^h v_2(\xi) d\xi = -\psi(Wh), \quad \int_0^h F(\xi) d\xi = \frac{1}{2} \left(\arcsin(4\psi(Wh) - 1) + \frac{\pi}{2} \right),$$

then the two constraints (2-36) are equivalent in this case and correspond to $\psi(Wh) \leq 1/2$, which coincides with the second part of (3-13).

In fact, the third condition, $\psi' > 0$, from (3-13) is not required: it guarantees that the instantaneous solution is convex but without it we can construct nonconvex interfaces.

4. Numerical simulations

To indicate the computational inaccuracy of the algorithms, we discuss Mullins' solution for a symmetrical reaper, for which all quantities are known in closed form (see (2-13) and remarks thereafter), and compare it with the result of a numerical computation using a simple algorithm, implemented in the Surface Evolver [Brakke 1992]. This takes the form of a single interface separating two cells of equal pressure being pulled at a velocity V at each boundary (see Figure 3).

The numerical procedure can be briefly described as follows. We start from a straight (vertical) line joining the two walls a distance $2h = 2$ apart. This is subdivided into 2^5 short elements (edges which

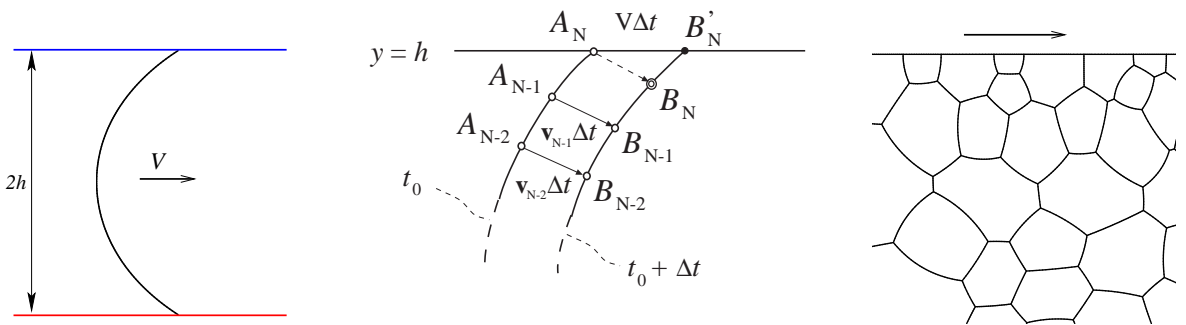


Figure 3. Left: The test problem considered here consists of a single interface that is sheared symmetrically by translating the boundaries. The shape should correspond to Mullins' solution. Middle: Standard algorithm for implementation of the boundary condition at each time step Δt . A_j and B_j are the respective material points on the interface at times t_0 and $t_0 + \Delta t$. Right: Example of a multi-bubble foam simulation, for which the numerical procedure developed here will be of use.

meet at points). A time step $\Delta t = 1 \times 10^{-5}$ is chosen for the computations and bounds on the possible length L of each edge ($0.01 \leq L \leq 0.05$). The algorithm proceeds as follows:

- (i) Each boundary point is moved in the x -direction a distance $V \Delta t$.
- (ii) The curvature at each point that is not on the boundary is calculated from $\kappa = \mathbf{F} \cdot \mathbf{n} / \bar{L}$, where \bar{L} is the average length of the neighbouring edges, \mathbf{F} is the negative energy (perimeter) gradient [Brakke 1992], and \mathbf{n} is the normal to the line joining the other ends of the neighbouring edges.
- (iii) Each point that is not on the boundary is then moved according to $\Delta \mathbf{x} = \Delta t \kappa \mathbf{n}$ (see Figure 3, middle).

This procedure (one step) is repeated until the difference in the x component of velocity between the centre-point of the interface and the boundary is less than a critical value (1×10^{-8}). Every 20 steps we check the edge-length bounds and add or remove edges as necessary. Thus, each tessellation point corresponds to the same material point within the step; nonetheless from step to step the algorithm may use different material points because of the refinement of the tessellation. Note that this standard algorithm preserves a reasonable restriction on the length of the edges, mainly following the initial distribution of material points; however, it works in a way that does not guarantee equal-length edges.

Note that this choice of the parameters for numerical simulation is standard and allows us to obtain acceptable accuracy in reasonable computational time [Cox 2005]. On the other hand, when one computes the dynamics of foams with many bubbles, the total computational error accumulates. Therefore information about the error is crucial, since it gives us a lower bound for the total computational error.

Two important observations illustrating the weakness of the algorithm should be noted here:

- The density of the tessellation points near the symmetry axis ($y = 0$) increases with each time step (see Figure 3, middle). Since the time step is constant, this may lead to failure of the stability condition for the linearized finite difference (FD) scheme applied to the nonlinear parabolic equation (2-1) due to this algorithm.
- The opposite effect occurs near the external boundary $y = h$. However, the situation here is even worse. In fact, there is not enough information to reconstruct the curvature and the unit vector at a point A_N lying on the boundary, and the algorithm, in fact, simply eliminates it. It creates instead the point B'_N along the boundary which should be the next point B_{N+1} (see again Figure 3, middle). See [Green et al. 2006] for more details.

We stress that the computations were stable (the stable steady-state regime has been reached) for every value of the external velocity V under consideration. Note that in our computations at high V , the number of tessellation points has increased from 2^5 to about 220 at the steady state. As expected, the worst situation in the sense of computational time, as shown in Figure 4, occurs for the largest value of the velocity, $V = 1.560796$, which is slightly less than the critical value $V_{cr} = \pi / (2h)$ predicted by the analytical solution [Mullins 1956]. The algorithm could not reach the steady-state regime at all for $V > 1.560796$; physically this is because films are being stretched indefinitely until they burst, which is manifested in the computations by the interface developing a branch lying outside the external boundary $y = h$. All this illustrates that the existing algorithm is well organized and works according to expectations but it is naturally sensitive to the value of the boundary velocity V . Thus it makes sense to ask about algorithm accuracy for a specific velocity versus space and time steps.

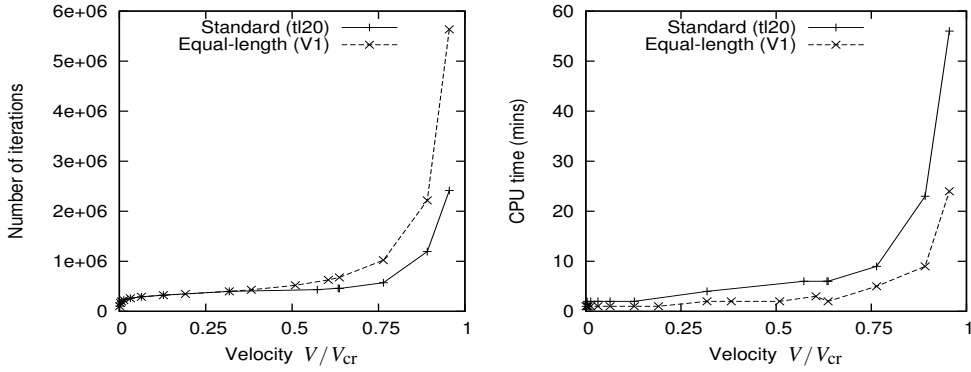


Figure 4. The number of iterations and the computational time both increase as the driving velocity approaches the critical value. The equal-length algorithm requires more iterations to converge, but does so in a faster time. The calculations were performed on a 2.66 GHz desktop PC; error bars are ± 1 minute.

As the exact analytical solution to the Mullins’ problem is known, we can estimate errors in the computations for all the physical and geometrical quantities: position of the interface $x(y)$, curvature $\kappa(y)$, and the velocity components $v_1(y)$ and $v_2(y)$. Corresponding relative errors for all solution parameters are presented in Figure 5 for different applied velocities.

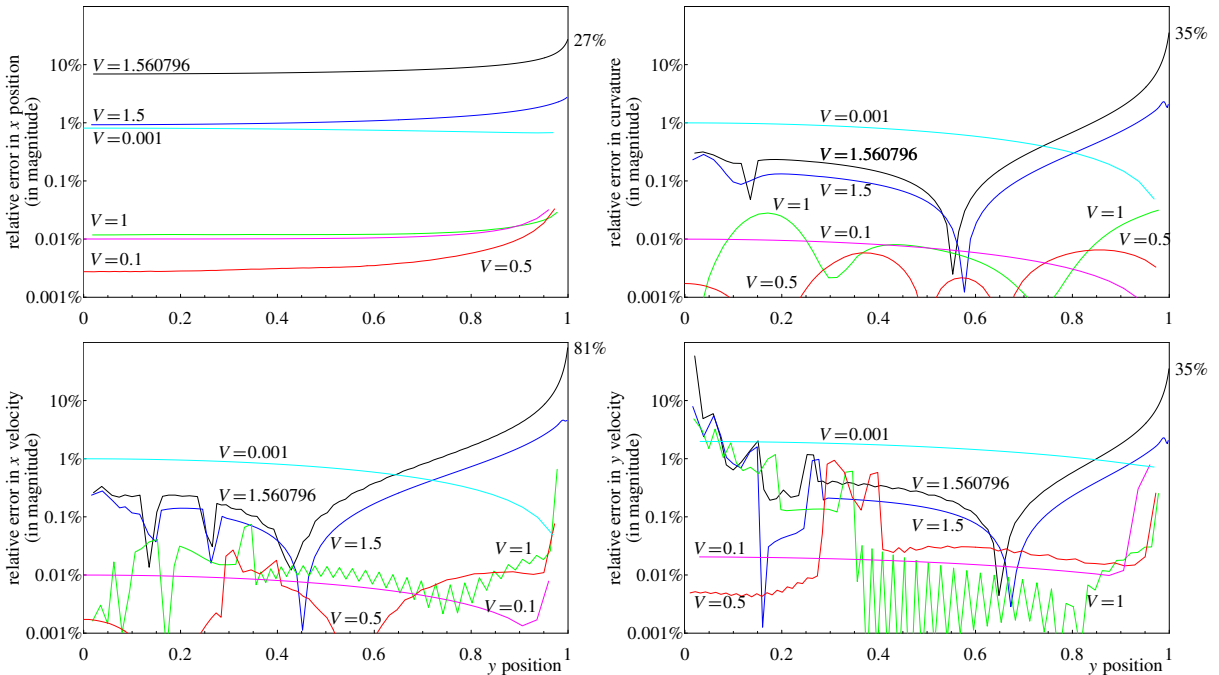


Figure 5. Relative error, compared to Mullins’ solution (2-16) and (2-19), in the position $x(y)$ of the interface (top left), its curvature κ (top right), and the x - and y -velocity components v_1 and v_2 (bottom row), for different velocities V of the external boundary.

As expected, the least accurate solutions are those for the largest velocity $V = 1.560796$. The error can be as large as 90% near the boundary ($y = h = 1$) in the x component of velocity v_1 and 60% near the symmetry axis for the y component. The former error is due to the fact that the interface is almost parallel to the boundary, while the latter is naturally related to the fact that the value of the velocity is equal to zero at the symmetry point. However, the drastic difference in value for this *numerical noise*, and its distance from the axis, indicates that at the larger values of V it exceeds reasonable expectations and is really related to the computational accuracy.

One can also consider that the error near the external boundary is due to parametrization of the numerical solution in y rather than x , but the standard numerical algorithm tries to preserve edge lengths. Moreover, the algorithm introduces new points in a regular fashion.

Thus both the errors (near the interface ends) are a consequence of the phenomena discussed in the two observations above. As V decreases, the accuracy increases for given bounds on the edge lengths L .

At first glance, it would appear that the position of the interface, $x(y)$, should be computed with better accuracy than all other solution parameters, which are, in fact, the results of some derivative procedure. However, our computations show that this is not the case and the relative error for $x(y)$ varies from 6% to 28% for the velocity $V = 1.560796$ while the curvature error is lower. Note also that the error for smaller velocities reaches a few percent near the boundary or symmetry axis.

The maximal absolute errors for all solution parameters mostly appear near the external boundary $y = h (= 1)$. This highlights that the implementation of the boundary condition in the existing algorithm cannot be considered as sufficient and should be improved.

Moreover, in the case of Mullins' solution an additional simple local indicator defined by identity (2-12) (independent of the integration of the solution variables) could equally be considered. It is clear from the results presented in Figure 6, left, that the error in this condition is not localized near the ends of the interface, as one might expect from the above. This so-called *internal* error is present for all values of V and is comparable with that near the interface ends.

To investigate accurately this internal error we repeated the computations for a specific velocity $V = 1$ and decreased both the time step, Δt , and the minimum edge length, L_{\min} (see Figure 6, right). This

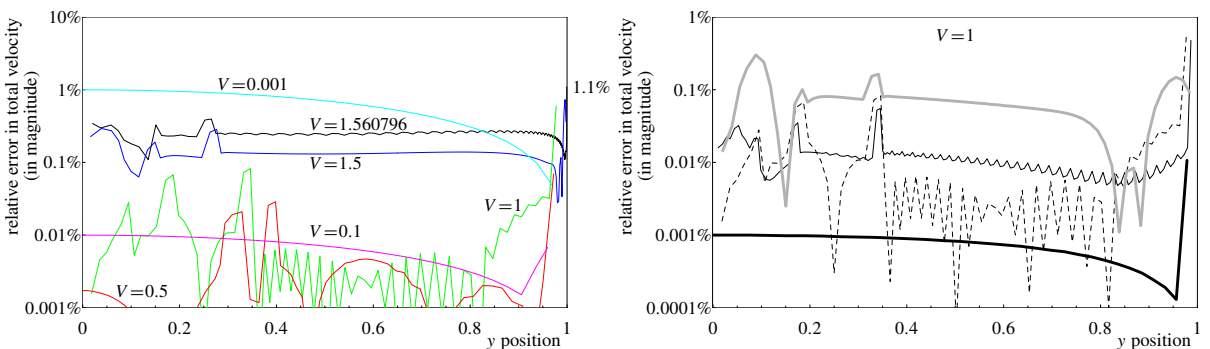


Figure 6. Relative error for the characteristic relation (2-12) for varying velocity V (left diagram) and varying numerical parameters Δt , L (right diagram: thick black line = equal length; dashed line = standard algorithm; thin black line = halve timestep and minimum length; grey line = decrease timestep by factor of 10). The best accuracy is obtained by keeping the line segments of equal length.

has improved the quality of the computations, but there is still an error at some internal points of the interval that is comparable with the error near the ends. Unfortunately the computational time increases considerably. The obvious route of decreasing Δt but fixing L_{\min} , to ameliorate this effect, leads to greater error in the solution (see again Figure 6, right). The accuracy of the solution can be improved internally by making the line segments of equal length [Green et al. 2006]; although this doesn't affect the error at the boundary, it does make the calculations faster (see Figure 4).

Possible sources of internal error include: (a) nonoptimal distribution of the tessellation points along the interface after some time; (b) imperfections in the correction procedure (which adds and eliminates points from the interface at some prescribed time); and (c) point-to-point error variation related to the fact that the diffusion-type coefficient changes from point to point along the interface (recall that (2-1) is a nonlinear parabolic equation which is solved by a direct FD scheme with a fixed time step).

In the last computation in Figure 6, right, for the line segments of equal length, we have redistributed points to make the segments equal at every time step (note that this length may change in time). Apart from the fact that the number of tessellation points is smaller than for the standard algorithm, such a comparison is not absolutely fair as the redistribution in the standard algorithm (removing or subdividing edges with lengths outside the range $0.01 \leq L \leq 0.05$) was done every 20 time steps. To discover if there

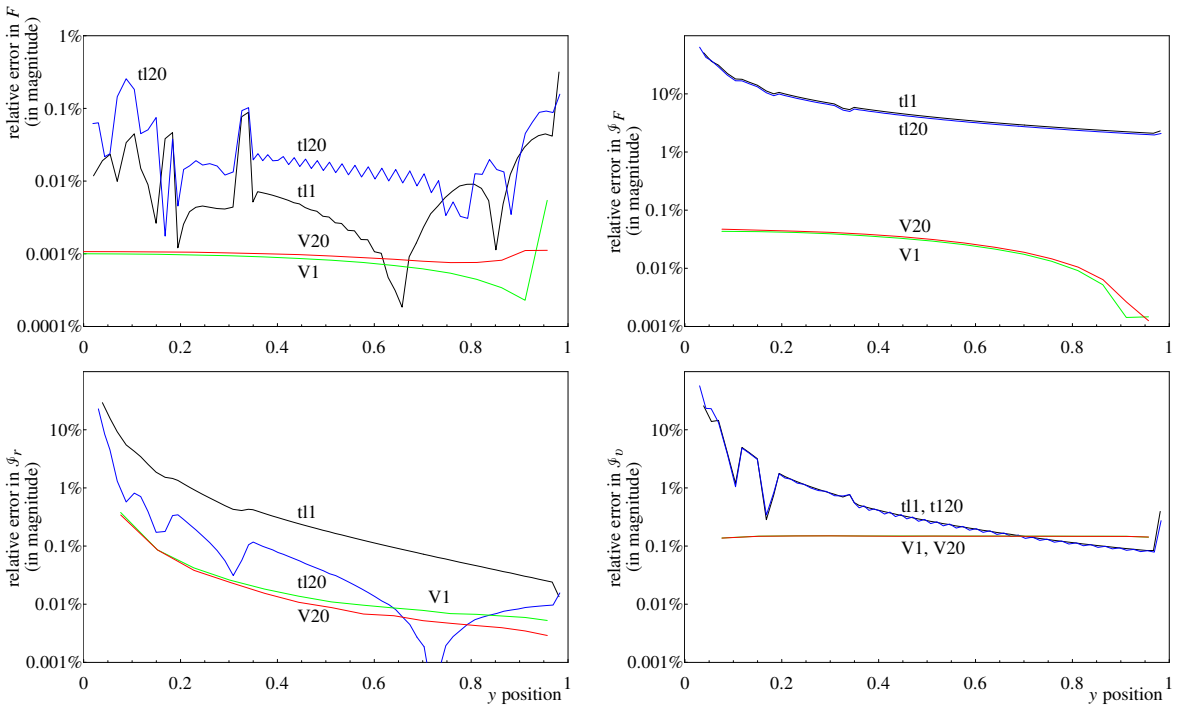


Figure 7. Relative error in the computations shown by the integral measures for unit velocity of the external boundary, $V=1.0$, obtained with four different computational strategies: the standard redistribution of the tessellation points, t1 and t20; and uniform length segment redistribution, V1 and V20, at every time step and every twentieth step, respectively. The top left graph shows the function F of (2-24) (as in Figure 6); the other three graphs correspond to the three error indicators defined in (4-1)–(4-3). All integrals were computed with the trapezium rule.

is an effect of redistribution frequency on the accuracy, we have tested these two algorithms under the same strategy by redistributing the points (in a different way) every time step and every twentieth time step. The error in the function F defined in (2-24), which is a constant in the case of the Mullins solution, are presented in Figure 7, top left. It is evident that the standard algorithm is quite sensitive to the chosen strategy. For a given position of the points on the interface, the relative error may differ by as much as two orders of magnitude, whereas this is not the case for the equal segment strategy. In this case, only near the external boundary is there some small fluctuation in the accuracy. Comparing the two redistribution algorithms for the same frequency of redistribution, the largest error always appears in the case of the standard algorithm — by up to two orders of magnitude — despite the fact that the number of tessellation points was greater. Moreover, in the standard algorithm this error is irregularly distributed along the interface. Recall that the number of tessellation points in the standard algorithm changes during the computations from 2^5 initially to around 150 (for $V = 1$) in the steady-state regime, while the number of the points in the second (equal length) algorithm remains constant. Therefore the computational time for the second algorithm was less by a factor of approximately two. On the other hand, the difference in the computational time between the different frequencies for redistribution for the equal length algorithm was only a few percent. This indicates the further possibility of optimizing this algorithm by redistributing points every M_T time steps. It is clear that $M_T = M_T(V)$ and this needs further investigation [Green et al. 2006].

Note that the function F from (2-24) can be used as an indicator of the accuracy of the computation only for the Mullins’ solution. However, there are three universal indicators which can be helpful to estimate the accuracy for any computations, namely, the relative errors of the numerical representations of the identities (2-25), (2-27), and (2-30), embodied in the following explicit definitions:

$$\text{After (2-25): } \mathcal{F}_F = - \int_0^y F(\xi) d\xi; \quad \text{relative error} = \frac{\mathcal{F}_F}{\theta(y) - \pi/2} - 1. \tag{4-1}$$

$$\text{After (2-27): } \mathcal{F}_r = \int_0^y \frac{v_2(\xi)}{v_1(\xi)} d\xi; \quad \text{relative error} = \frac{\mathcal{F}_r}{x(0) - x(y)} - 1. \tag{4-2}$$

$$\text{After (2-30): } \mathcal{F}_v = \int_0^y v_2(\xi) d\xi; \quad \text{relative error} = \mathcal{F}_r / \left(\frac{v_2^2(y)}{2(v_2^2(y) + v_1^2(y))} \right) - 1. \tag{4-3}$$

The respective results are shown in the remaining three parts of Figure 7. All four indicators suggest that the equidistant distribution of the tessellation points is much better than the standard algorithm, regardless of the chosen strategy, as recommended in [Green et al. 2006]. Moreover, even near the symmetry point, $y = 0$, where the value of the indicators all tend to zero and have a large influence on the relative errors, the accuracy of the computations for the second algorithm is extremely high. However, this is not the case for the standard algorithm.

In Figure 8, the relative errors of the solution variables are presented for both algorithms: the standard one and the equidistant distribution. The result for $x(y)$, shown in the top left part of the figure, looks surprising at first glance; although the accuracy of the computations performed with these two algorithms is of the same order and the error related to the new algorithm is distributed more uniformly, it appears that the accuracy of the standard algorithm is better than the equal-segment-length algorithm, at least with respect to the accuracy of the position of the interface. However, this is not the case. In fact, as

was shown above, the computational error for the standard algorithm is redistributed along the interface irregularly whereas that for the equal-segment algorithm is practically uniform. As a result, the criterion to stop the iteration process to find the steady-state solution works differently for the two algorithms. The prescribed maximal growth 10^{-8} in each time-step, measured on the axis of symmetry, is reached more quickly for the new algorithm. This is the second reason (together with number of tessellation points) why this algorithm is faster. If one were to run both algorithms for the same time, or for the same number of iterations, and compare the corresponding results, the discussed paradox should not appear and the new algorithm always provides better accuracy by as much as two orders of magnitude.

For the accuracy of other problem variables — the interface curvature, κ , and the interface velocities, v_1 and v_2 — the new algorithm is more accurate, notwithstanding the above argument, as can be seen in the last three parts of [Figure 8](#).

Finally, we stress again that the proposed three indicators are more versatile measures than a comparison of the numerical steady-state solution with the analytical one, since the latter comparison includes an additional error related to the determination of the steady-state regime, while the indicators show us accuracy of the solution even if the steady state has not been reached.

5. Discussion and conclusions

All these results clearly indicate that the existing algorithm should be used with caution, especially when investigating the behaviour of a many-bubble foam near the critical velocity. Moreover, when there

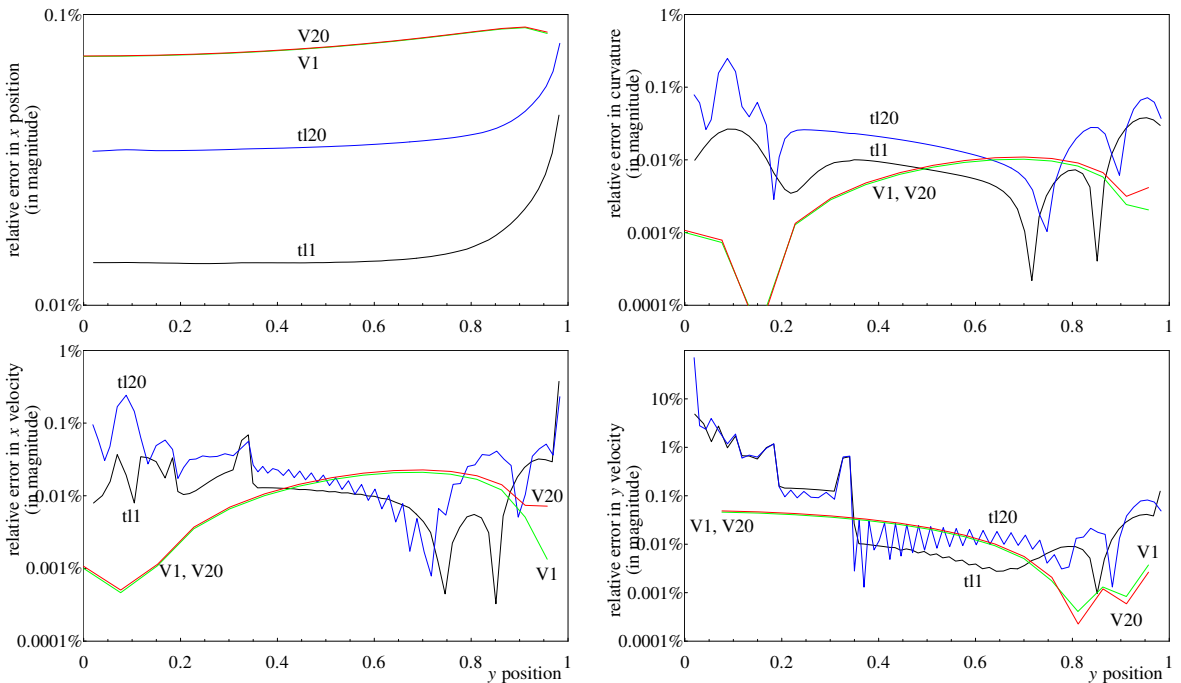


Figure 8. Relative error in the position $x(y)$ of the interface (top left), its curvature κ (top right), and the x - and y - velocity components v_1 and v_2 (bottom row), for different numerical algorithms with velocity of the external boundary $V = 1$.

are many cells in a simulation (see [Figure 3](#), right), the user is restricted to some critical number of tessellation points M_P , which gives a limitation on accuracy even for low velocity. In fact, the material structure is highly nonuniform, in the sense that the cells may have different sizes. Effectively this means that every interface has its own critical velocity and the bigger cells thus introduce larger errors. In addition, it takes longer for curvature to diffuse along a longer interface and set it in motion. This creates the following duality: to accurately describe the process of cell motion it is necessary to have the computational error as small as possible, while the error generated near the critical velocity takes its greatest value. This is true for boundary or internal cells equally. Problems requiring high accuracy of the solution near the external boundary are related to the investigation of the boundary effects describing the total phenomenological behaviour of the foam structures.

Another important remark is that the choice of the initial condition for testing the numerical procedure here (a straight-line interface) is much more severe than any of the instantaneous solutions reported in [Section 3](#). One could even think of worse situations to test the algorithm, for example if the initial interface is not convex or even not smooth. This may lead to supercritical velocities and so on.

To revise and improve the existing numerical algorithm, we propose to use another strategy for the redistribution of the tessellation points: an equal-segment-length distribution of the tessellation points is much more favourable [[Green et al. 2006](#)]. However, this strategy is not sufficient to eliminate inaccuracy in the computation near the maximum velocity in the steady-state regime. The reason for this is the behaviour of the steady-state solution near the wall (2-21). In fact, there exist two possible realizations of this algorithm. One, which we have used in our computations, is to keep the same number of tessellation points, M_P , then with time the length between consecutive points, L , will increase significantly when V is near V_{cr} . This leads to an effective loss of accuracy. Another strategy would be to keep the same distance between points during the computations. However, M_P will then increase to infinity as V approaches V_{cr} . Formally this should preserve computational accuracy but will lead to an unacceptable increase in computational time and memory use. Thus, further adaptations to the algorithm are required if high accuracy is required, for example in the steady-state regime with velocities near the critical value [[Cox 2005](#)].

Taking advantage of the auxiliary identities (2-25), (2-27), and (2-30), we may correct the instantaneous solution obtained within any algorithm at any or even every time step without time-consuming computations, as the identities are valid for any instantaneous solution. They also make possible further investigation of the asymptotic behaviour of the bounded interface solution near the ends. For example, any possible solution behaves at the symmetry axis according to (2-35), which allows us to tackle the error in the solution near the symmetry axis. On the other hand, the results obtained in [Section 2C](#) may allow us to construct and implement a new numerical procedure/elements tackling the boundary condition in a more accurate way (without losing any near-boundary points, using, for example, a boundary layer result [[Grassia et al. 2008](#)]).

Finally, as we have shown, the identities (2-25), (2-27), and (2-30) may be used to probe the accuracy of computations. These indicators are extremely helpful as they are not based on information about the exact solution and can therefore illuminate inaccuracy of the numerical solution without any preliminary knowledge about the exact solution itself.

Summarizing, we have shown that an improvement of the numerical algorithm is highly desirable and possible. Apart from the fact that some of the improvements have been indicated and proven in this

paper, there is still an open question how to deal with the accuracy of the computations near the critical velocities and near the external boundaries. We have also suggested possible directions for future investigation: improved implementation of the boundary condition and creation of additional near-boundary points. Further, to check new results related to the numerical algorithm we need a larger set of analytical benchmarks.

Acknowledgements

The authors thank P. Grassia for his many helpful remarks on an earlier version, and the unknown referees for their insightful comments.

References

- [Bragg and Nye 1947] L. Bragg and J. F. Nye, “A dynamical model of a crystal structure”, *Proc. R. Soc. Lond. A* **190**:1023 (1947), 474–481.
- [Brakke 1992] K. Brakke, “The Surface Evolver”, *Exp. Math.* **1**:2 (1992), 141–165.
- [Cox 2005] S. J. Cox, “A viscous froth model for dry foams in the Surface Evolver”, *Colloid. Surface. A* **263**:1–3 (2005), 81–89.
- [Grassia et al. 2008] P. Grassia, G. Montes-Atenas, L. Lue, and T. E. Green, “A foam film propagating in a confined geometry: analysis via the viscous froth model”, *Eur. Phys. J. E* **25**:1 (2008), 39–49.
- [Green et al. 2006] T. E. Green, A. Bramley, L. Lue, and P. Grassia, “Viscous froth lens”, *Phys. Rev. E* **74**:5 (2006), 051403.
- [Green et al. 2009] T. E. Green, P. Grassia, L. Lue, and B. Embley, “Viscous froth model for a bubble staircase structure under rapid applied shear: an analysis of fast flowing foam”, *Colloid. Surface. A* **348** (2009), 49–58.
- [Kern et al. 2004] N. Kern, D. Weaire, A. Martin, S. Hutzler, and S. J. Cox, “Two-dimensional viscous froth model for foam dynamics”, *Phys. Rev. E* **70**:4 (2004), 041411.
- [Mullins 1956] W. W. Mullins, “Two-dimensional motion of idealized grain boundaries”, *J. Appl. Phys.* **27**:8 (1956), 900–904.
- [Peleg et al. 2001] A. Peleg, B. Meerson, and A. Vilenkin, “Area-preserving dynamics of a long slender finger by curvature: a test case for globally conserved phase ordering”, *Phys. Rev. E* **63**:6 (2001), 066101.
- [Smith 1952] C. S. Smith, “Grain shapes and other metallurgical applications of topology”, pp. 65–108 in *Metal interfaces* (Detroit, MI, 1951), American Society for Metals, Cleveland, OH, 1952.
- [Weaire and Hutzler 1999] D. Weaire and S. Hutzler, *The physics of foams*, Clarendon, Oxford, 1999.
- [Weaire and McMurry 1996] D. Weaire and S. McMurry, “Some fundamentals of grain growth”, *Solid State Phys.* **50** (1996), 1–36.
- [Wood 1996] G. P. Wood, *Some problems in nonlinear diffusion*, Ph.D. Thesis, University of Nottingham, 1996.

Received 14 Jan 2009. Revised 11 Mar 2009. Accepted 8 May 2009.

SIMON COX: foams@aber.ac.uk

Institute of Mathematics and Physics, Aberystwyth University, Aberystwyth SY23 3BZ, United Kingdom

GENNADY MISHURIS: ggm@aber.ac.uk

Institute of Mathematics and Physics and Wales Institute of Mathematical and Computational Sciences, Aberystwyth University, Aberystwyth SY23 3BZ, United Kingdom

LAMINATED AND SANDWICH PANELS SUBJECT TO BLAST PULSE LOADING

UGO ICARDI AND LAURA FERRERO

A recently developed optimisation technique is employed for relaxing the interlaminar stress concentration of laminated and sandwich flat panels undergoing impulsive pressure loading. We determine the through-the-thickness distribution of the core properties of sandwich panels and the in-plane distribution of the stiffness properties of their face sheets, as well as that of the constituent layers of laminates maximizing the energy absorbed through wanted modes (e.g., membrane and bending contributions) and minimizing the energy absorbed through unwanted modes (e.g., interlaminar shears). As a structural model, we employ a refined zigzag model with a piecewise high-order variation of in-plane and transverse displacements that fulfils *a priori* the interfacial stress and displacement contact conditions. The zigzag model, a characteristic feature of the method, is incorporated through a strain energy updating into a conventional shear deformable plate element, for the sake of reducing the computational effort required for accurately computing the stresses. The dynamic equations are solved using the Newmark implicit time integration scheme; various pulse pressure time histories are employed. Simple, suboptimal distributions of reinforcement fibres and core density compatible with current manufacturing processes are considered in the numerical applications. It appears that these distributions can effectively reduce the critical interlaminar stress concentration under impulsive loadings, with beneficial effects on the strength at the onset of damage, and improve the dynamic response properties as well.

1. Introduction

Pulse pressure loading due to an accidental cause, an explosive device, fuel and nuclear explosions, gust and sonic boom represents for aircraft a major hazard responsible for catastrophic failure of structures. Much research work has been carried out recently in assessing aircraft structures subjected to explosive pressure pulses and for finding configurations able to alleviate their detrimental effects; see [CAA 2001], for example. Although very expensive, full-scale tests of fuselage large sections have been undertaken, showing how the pressure loading hazard could be consistently reduced using hardened luggage containers and sandwich structures. However most of the research is carried out considering panels that are representative of real structural components, often using finite elements for the analysis.

As examples of papers dealing with metallic stiffened panels we mention [Simmons and Schleyer 2006; Rudrapatna et al. 2000; Zhu 1996; Langdon and Schleyer 2006]. Since the structure of modern combat and civil transportation aircraft is often made of or incorporates composite material parts with higher specific strength and stiffness than metals, a growing number of studies have been published about their response to pulse pressure loading. Moreover, new manufacturing techniques render their use economically feasible for large scale applications.

Keywords: optimised tailoring, impulsive loading, stress relaxation, damage resistance improvement.

The response of marine sandwich panels to explosion loading has been addressed in [Hayman 1996], [Makinen 1999], [Shin and Geers 1994], [Jiang and Olson 1994] (underwater explosion) and [Houlston et al. 1985] (in air explosion). Studies of the response of aircraft composite panels under impulsive loading include [Cheng and Benveniste 1968; Crocker and Hudson 1969; Rajamani and Prabhakaran 1980; Dobyns 1981; Birman and Bert 1987; Cederbaum et al. 1988; 1989; Librescu and Nosier 1990; Librescu and Na 1998; Song et al. 1998; Librescu et al. 2004; 2006; 2005; Hause and Librescu 2005; 2007; Xue and Hutchinson 2004]. In these studies the blast loads considered were of moderate intensities, so as to not induce damage. The only exception is the last paper, where an elastic-perfectly plastic behaviour was considered. Likewise in other fields, it appears that to realistically describe the dynamic response under impulsive loading, the structural models have to accurately account for the high transverse shear deformation of composites. The present paper, dealing with blast loading of composites, also takes into account the contact conditions at the interfaces of dissimilar constituent materials necessary to keep equilibrium and kinematic compatibility, since many studies have shown their importance for both the overall and the local behaviour.

To account for the interlayer contact conditions and accurately predict the stress fields with an affordable computational effort, we choose as the structural model a refined zigzag model with a piecewise high-order variation of the displacements. The displacement field is postulated in a way that fulfils *a priori* the interfacial stress and displacement contact conditions (namely, continuity of the transverse shear and normal stress components and of displacement), through an appropriate definition of the continuity. The transverse displacement is assumed variable across the thickness, because sandwich composites often fail by crushing, due to the low compressive strength of the core. The model also accounts for internal damage accumulation mechanisms; since composites suffer from microstructures failures while they absorb the incoming energy, they can fail in service at load levels much lower than the ultimate design load. The model has been successfully applied to impact studies of laminated [Icardi 2007] and sandwich [Icardi and Ferrero 2009] flat panels, where it efficiently predicted the impact induced damage, as shown by comparisons with the damage detected by ultrasonic cartography, and to the stress analysis of thick damaged sandwich panels, as shown by comparisons with the exact elasticity solution [Icardi and Ferrero 2009].

To lower the cost of the analysis, both this paper and in the works just mentioned, the zigzag model is incorporated into a standard eight-node plate element based on first-order shear deformation plate theory (FSDPT) through an energy updating procedure that is locally carried out in the post-processing phase.

A recently developed optimisation technique [Icardi and Ferrero 2008] is employed for finding the appropriate spatial distribution of the stiffness properties (fibers orientation and core density) that minimize the out-of-plane stresses due to impulsive loading. It is found solving the Euler–Lagrange equations of an optimisation problem in which the absorbed energy due to out-of-plane stresses is minimised, while that due to membrane stresses is maximised. As a preparatory step to the response analysis, the structural model and the optimisation technique will be briefly discussed.

2. Structural model

As mentioned, the present structural model uses a conventional plate element for a preliminary analysis and locally improves its predictive capability by updating its strain energy to that of a zigzag model with

a piecewise cubic variation of the membrane displacements across the thickness and a fourth-order variation of the transverse displacement. The merit of the zigzag model is to provide accurate results with low computational effort, since the interfacial stress and displacement contact conditions are fulfilled *a priori* and not as constraints that increase the number of the governing equations. Its drawback is the involvement of displacement derivatives as nodal degrees of freedom, which prevents a direct implementation into a finite element. To overcome this problem, we use the updating process of [Icardi 2007; Icardi and Ferrero 2009] with some improvements (outlined below) and the same failure and post-failure models.

2.1. Kinematics of the zigzag model. Assume the laminated or sandwich panel to consist of S layers of different thickness and material properties, the core being treated as a thick layer in a multilayer construction. The accuracy of this hypothesis have been extensively assessed in a number of previous papers, even in the case of a thick, damaged sandwich panel as previously mentioned .

As reference system use a Cartesian coordinate system (x, y, z) , with (x, y) on the reference midplane and z as the thickness coordinate. Indicate with U, V the in-plane and W the out-of-plane displacement components and with σ_{xz}, σ_{yz} and σ_{zz} the out-of-plane stresses. Use a subscript comma to indicate differentiation. The displacement field is represented as

$$\begin{aligned} U(x, y, z) &= u(x, y, z) + U(x, y, z), \\ V(x, y, z) &= v(x, y, z) + V(x, y, z), \\ W(x, y, z) &= f_w^1(x, y, z) + f_w^2(x, y, z). \end{aligned} \tag{1}$$

That is, the in-plane components are expressed as sums of contributions u, v that are continuous and have continuous first derivatives across the thickness, as in the equivalent single layer models

$$\begin{aligned} u(x, y, z) &= u^\circ + z(\gamma_x^\circ - w_{,x}^\circ) + z^2 C_x(x, y) + z^3 D_x(x, y), \\ v(x, y, z) &= v^\circ + z(\gamma_y^\circ - w_{,y}^\circ) + z^2 C_y(x, y) + z^3 D_y(x, y). \end{aligned} \tag{2}$$

and contributions U and V that are continuous but have discontinuous first derivatives at the interfaces:

$$U(x, y, z) = \sum_{k=1}^{S-1} {}^{(k)}\phi_x(x, y)(z - {}^{(k)}Z^+)H_k, \quad V(x, y, z) = \sum_{k=1}^{S-1} {}^{(k)}\phi_y(x, y)(z - {}^{(k)}Z^+)H_k. \tag{3}$$

The transverse displacement is the sum of a contribution

$$f_w^1(x, y, z) = a(x, y), \tag{4}$$

representing the displacement of the reference midplane w° , and a field with discontinuous derivatives at the interfaces,

$$\begin{aligned} f_w^2(x, y, z) &= zb(x, y) + z^2c(x, y) + z^3d(x, y) + z^4e(x, y) \\ &+ \sum_{k=1}^{S-1} {}^{(k)}\psi_x(x, y)(z - {}^{(k)}Z^+)H_k \sum_{k=1}^{S-1} {}^{(k)}\psi_y(x, y)(z - {}^{(k)}Z^+)^2H. \end{aligned} \tag{5}$$

The piecewise continuous contributions to the displacements, namely (3) and (5), are expressed in terms of functions ${}^{(k)}\Phi_x, {}^{(k)}\Phi_y, {}^{(k)}\Psi_1, {}^{(k)}\Psi_2$, which we call continuity functions, and which are determined by enforcing the continuity of the transverse shear and normal stresses $\sigma_{xz}, \sigma_{yz}, \sigma_{zz}$ and of the gradient $\sigma_{zz,z}$

at the interfaces, as prescribed by elasticity theory. Since the Heaviside unit step function H_k appearing in the previous equations is defined only in \mathbb{R}^+ , the continuity functions are computed starting from the bottom layer, the choice of the starting layer as the upper- or lowermost being immaterial.

The remaining functions $C_x, C_y, D_x, D_y, b, c, d, e$ are determined enforcing the fulfilment of the boundary conditions at the upper ^(u) and lower ^(l) bounding faces, namely the stress-free boundary conditions on the transverse shears and the conditions

$$\sigma_{zz}^u = p_o^u, \quad \sigma_{zz}^l = p_o^l, \quad \sigma_{zz,z}^u = \sigma_{zz,z}^l = 0$$

on the transverse normal stress. The symbols p_o^u, p_o^l represent the transverse distributed loading at the upper and lower bounding faces, respectively.

As mentioned, this model will be implemented operating an updating of the nodal degree of freedoms (DOFs) of a FSDPT parent element through an energy updating process in the post-processing phase. This updating process avoids a direct implementation of the zigzag model, which turns out to be inefficient by the computational viewpoint, because derivatives should appear in the vector of nodal DOFs that are consequent to the enforcement of the stress continuity conditions.

The updating is carried out through corrective terms that in the present paper are determined in closed form using a symbolic calculus tool. This technique will be outlined in the following Section. No details will be given about the eight node FSDPT parent element because it has standard features; the reader finds the omitted details in [Icardi 2007].

Note that since the functional degrees of freedom of this model $u^{(o)}, v^{(o)}, w^{(o)}, \gamma_x$ and γ_y coincide with those of the FSDPT model, it is possible to update the strain energy of such a lower order model to that of the current zigzag model, with the purpose and by the technique described hereafter. Also note that the FSDPT and the HSDPT models can be particularized from the zigzag model neglecting the contributions (3) and (5) and, in the case of the FSDPT model, considering only the linear case (2).

A finite element approach is chosen in order to easily treat the spatially variable material properties that result from the tailoring optimization process, and in order to enable the analysis of a spatially variable pressure pulse loading such as the NOL pressure model profile [Proctor 1972], that will be the object of a future application.

2.2. Energy updating and post-processing. As is well known, any model that cannot be refined across the thickness, like the present one, needs integration of the local equilibrium differential equations

$$\begin{aligned} (*\sigma_{xz} - \underline{\sigma}_{xz}) &= -(\langle \underline{\sigma}_{xx,x} + \underline{\sigma}_{xy,y} \rangle + \underline{\sigma}_{xz}), \\ (*\sigma_{yz} - \underline{\sigma}_{yz}) &= -(\langle \underline{\sigma}_{xy,x} + \underline{\sigma}_{yy,y} \rangle + \underline{\sigma}_{yz}), \\ (*\sigma_{zz} - \underline{\sigma}_{zz}) &= -(\langle * \underline{\sigma}_{xz,x} + * \underline{\sigma}_{yz,y} \rangle + \underline{\sigma}_{zz}) \end{aligned} \tag{6}$$

to provide a realistic description of the interlaminar stress fields (in the former equations the underlined stresses are those computed from the constitutive equations). To make integration computationally efficient and preserve accuracy, we adopt two procedures in this paper:

- (i) The strain energy of the FSDPT eight-node elements is updated to that of the zigzag model.
- (ii) The results by the FSDPT elements are interpolated and smoothed with spline functions in the region where the stress analysis is carried out.

The goal is to derive these interpolations instead of the shape functions, because the interpolated quantities have a higher-order representation and thus they do not lose accuracy. So, although standard, efficient parabolic shape functions are used in the finite element model, no accuracy is lost integrating the local differential equilibrium equations.

It is remarked that the post-processing operations are much more cost-effective than using discrete-layer models with a large number of DOFs, because they are carried out only locally and their convergence is fast. The present approach achieves the accuracy of closed-form approaches with a low computational effort, but it is more versatile, because it allows complex geometry, loading, boundary conditions and a point-to-point material property variation to be treated. Note that the updating procedure prevents the locking effects, since the transverse displacement and the shear rotations are described with their right interdependence; see Equations (7) immediately below.

2.2.1. Computation of the continuity constants. The first operation is the computation of the constants appearing in the continuity functions. The readers are referred to [Icardi 2001] for a detailed discussion of these functions, whose purpose is to ensure the fulfilment of the interfacial contact conditions. To make this operation more efficient than in the former versions of the software, here a symbolic calculus tool is employed to provide expressions in closed form. The DOFs of the FSDPT must be rearranged in order to be consistent with the representation of the zigzag model:

$$\theta_x = z(\gamma_x^\circ - w_{,x}^\circ), \quad \theta_y = z(\gamma_y^\circ - w_{,y}^\circ). \quad (7)$$

Assume $u^{(o)}$, $v^{(o)}$, $w^{(o)}$, γ_x and γ_y are the functional DOFs of the FSDPT model; the homologous terms with a tilde $\tilde{}$ be those of the zigzag model, are obtained from the earlier ones adding unknown corrective terms:

$$\begin{aligned} \tilde{u}^\circ &= \hat{u}^\circ + \Delta \hat{u}^\circ, & \tilde{v}^\circ &= \hat{v}^\circ + \Delta \hat{v}^\circ, & \tilde{w}^\circ &= \hat{w}^\circ + \Delta \hat{w}^\circ, \\ \tilde{\gamma}_x^\circ &= \hat{\gamma}_x^\circ + \Delta \hat{\gamma}_x^\circ, & \tilde{\gamma}_y^\circ &= \hat{\gamma}_y^\circ + \Delta \hat{\gamma}_y^\circ. \end{aligned} \quad (8)$$

In the current version of the software is no longer necessary to start with $f_w^2 = 0$ and then make them consistent in a subsequent step. The continuity functions computed in this way are those corresponding to the DOFs provided by the preliminary calculus using the FSDPT finite elements. The result of this calculus will be improved by the following operations.

2.2.2. Updating of the energy due to transverse shears. This operation is performed equating again the homologous quantities of the FSDPT and zigzag models, using the representation of Equations (8):

$$(\mathbf{q}_e + \Delta \mathbf{q}_{eK})^T \mathbf{K}_{\text{fsdpt}} (\mathbf{q}_e + \Delta \mathbf{q}_{eK}) = \mathbf{q}_e^T \mathbf{K}_{\text{zigzag}} \mathbf{q}_e. \quad (9)$$

The symbol \mathbf{q}_e represents the vector of nodal DOFs; $\Delta \mathbf{q}_{eK}$ are the corrective terms; \mathbf{K} is the stiffness matrix (only the rows and columns relative to the out-of-plane shears). The left hand size member is based on the FEM model, while the right hand side is an analytic expression. The solution is found in closed form via symbolic calculus assuming as unknown only the transverse shear rotations. Subsequently, the other DOFs are updated one at a time, reiterating the entire process till convergence.

2.2.3. Transverse normal stress and strain. Since this contribution that plays a primary role for sandwich panels is disregarded in the FSDPT parent element, it is approximated at a local point in the post-processing phase. This operation is carried out integrating the third local differential equilibrium

equation, where a spline interpolation of the previously computed transverse shear stresses is used. Then an approximate expression of the transverse normal strain ${}^0\varepsilon_{zz}$ is obtained by the stress–strain relation of elasticity

$${}^0\varepsilon_{zz} = \sigma_{xx}S_{13} + \sigma_{yy}S_{23} + {}^0\sigma_{zz}S_{33} + \sigma_{yz}S_{34} + \sigma_{xz}S_{35} + \sigma_{xy}S_{36}. \quad (10)$$

Using these approximated transverse normal stress and strain, their contribution to the strain energy is computed. In the current version, the energy balance is used to compute improved transverse shear stress rotations and the variation of the out-of-plane displacement across the thickness in closed form, in combination with the local differential equilibrium equations. Once the improved stresses have been computed, they are interpolated with spline functions for the subsequent operations. This process is restarted with the improved transverse shear and transverse displacement DOFs and repeated till convergence.

2.2.4. Updating of the membrane energy. The displacements and stresses computed at this stage are used for improving the membrane energy and thus for computing refined in-plane DOFs. To this purpose, the in-plane displacements are represented as in (8)_{1,2} and the strain energy as in Equation (9), where only the rows and columns relative to the membrane energy contributions are retained. The solution is found substituting the corrected displacements one at a time and reiterating the entire process till convergence.

2.2.5. Updating of the work of inertial forces. The expression of the work of inertial forces is used to make the dynamics of the FSDPT model with that of the zigzag model:

$$(\mathbf{q}_e + \Delta\mathbf{q}_{eM})^T \mathbf{M}_{\text{fsdpt}}(\mathbf{q}_e + \Delta\mathbf{q}_{eM})^T F_f(t) = \mathbf{q}_e^T \mathbf{M}_{\text{zigzag}}\mathbf{q}_e^T F_{zz}(t). \quad (11)$$

$\mathbf{M}_{\text{fsdpt}}$ and $\mathbf{M}_{\text{zigzag}}$ being their consistent mass matrices, \mathbf{q}_e the converged vector of nodal DOFs after the steps up to 2.2.4, and $\Delta\mathbf{q}_{eM}$ the corrective terms. Since the previous equation must hold irrespective of the time evolution of the solution, it can be rearranged as:

$$(\mathbf{q}_e + \Delta\mathbf{q}_{eM})^T \mathbf{M}_{\text{fsdpt}}(\mathbf{q}_e + \Delta\mathbf{q}_{eM})^T = \mathbf{q}_e^T \mathbf{M}_{\text{zigzag}}\mathbf{q}_e^T. \quad (12)$$

The corrective terms are computed in closed form at each iteration one at a time and reiterating till convergence. The sequence of steps 2.2.1–2.2.5 is repeated till convergence, using the current stresses and displacements at the end of each iteration as entry values for the subsequent one. The convergence of the energy updating procedure appeared fast whenever applied. The energy updating appeared always able to consistently improve the quality of the stress predictions and did not heavily affect the overall computational costs.

2.3. Failure and progressive damage accumulation. The present structural model incorporates criteria for matrix cracking, fibres failure, delamination and core crushing in order to account for all the possible failure modes and their reciprocal interactions. Only macromechanical, stress-based criteria using standard, easy to assess, engineering properties are here employed, since they are the only ones with an affordable computational effort for the transient analysis. The formulation is that successfully adopted in [Icardi 2007; Icardi and Ferrero 2009]. A 3D version of the Hashin’s criterion with in situ strengths is used to predict the failure of fibres and matrix. For the tensile failure of fibres we have

$$\left(\frac{\sigma_{11}}{X^t}\right)^2 + \frac{1}{S_{12=13}^2}(\tau_{12}^2 + \tau_{13}^2) = 1 \quad (\sigma_{11} > 0) \quad (13)$$

while for compressive failure we have

$$\sigma_{11} = -X^c \quad (\sigma_{11} < 0).$$

The expression for the matrix failure under traction is

$$\left(\frac{\sigma_{22} + \sigma_{33}}{Y^t}\right)^2 + \frac{1}{S_{23}^2}(\tau_{23}^2 - \sigma_{22}\sigma_{33}) + \left(\frac{\tau_{12}}{S_{12=13}}\right)^2 + \left(\frac{\tau_{13}}{S_{12=13}}\right)^2 = 1 \quad (\sigma_{22} + \sigma_{33} > 0),$$

while for compressive failure it is

$$\frac{1}{Y^c} \left(\left(\frac{Y^c}{2S_{23}} \right)^2 - 1 \right) (\sigma_{22} + \sigma_{33}) + \frac{1}{4S_{23}^2} (\sigma_{22} + \sigma_{33})^2 + \frac{1}{S_{23}^2} (\tau_{23}^2 - \sigma_{22}\sigma_{33}) + \frac{1}{S_{12=13}^2} (\tau_{12}^2 + \tau_{13}^2) = 1 \quad (\sigma_{22} + \sigma_{33} < 0).$$

To compare the same failures with a different formulation, the criterion of Hou et al. is incorporated into the structural model, which predicts the failure of fibres by the formula

$$\left(\frac{\sigma_{11}}{X^t}\right)^2 + \left(\frac{\tau_{12} + \tau_{13}}{S_f}\right)^2 = 1$$

and the tensile and compressive failures of the matrix, respectively, by

$$\left(\frac{\sigma_{22}}{Y^t}\right)^2 + \left(\frac{\tau_{12}}{S_{12}}\right)^2 + \left(\frac{\tau_{23}}{S_{m23}}\right)^2 = 1, \quad \frac{1}{4} \left(\frac{-\sigma_{22}}{S_{12}}\right)^2 + \frac{(Y^c)^2 \sigma_{22}}{4S_{12}^2 Y^c} - \frac{\sigma_{22}}{Y^c} + \left(\frac{\sigma_{12}}{S_{12}}\right)^2 = 1.$$

This criterion is also used to predict the onset of delamination, together with the Chang–Springer criterion. The criterion of Hou et al. predicts delamination by the expressions

$$\begin{aligned} \left(\frac{\sigma_{33}}{Z_T}\right)^2 + \frac{(\tau_{12}^2 + \tau_{13}^2)}{S_{13}^2(d_{ms}d_{fs} + \delta)} &= 1 \quad (\sigma_{33} \geq 0), \\ \frac{(\tau_{12}^2 + \tau_{13}^2 - 8\sigma_{33}^2)}{S_{13}^2(d_{ms}d_{fs} + \delta)} &= 1 \quad \left(-\sqrt{\frac{1}{8}(\sigma_{13}^2 + \sigma_{23}^2)} \leq \sigma_{33} < 0\right), \end{aligned}$$

while the Chang–Springer criterion uses the expression

$$\left(\frac{\sigma_{33}}{Y^t}\right)^2 + \left(\frac{\tau_{13}}{S_{13=23}}\right)^2 + \left(\frac{\tau_{23}}{S_{13=23}}\right)^2 = 1.$$

To predict the sandwich core failure in crushing mode, we use the criterion by Besant et al.,

$$\left(\frac{\sigma_{zz}}{\sigma_{cu}}\right)^n + \left(\frac{\tau_{xz}}{\tau_{lu}}\right)^n + \left(\frac{\tau_{yz}}{\tau_{lu}}\right)^n = e_{core},$$

where σ_{cu} and τ_{lu} being the core strengths in compression and transverse shear; it predicts failure of the core when $e_{core} > 1$.

The exponent $n = 1.5$ is assumed, since it best fits the experimental results. In the event of crushing, the work done by the inner crush force has to be accounted for; therefore the through-the-thickness variation of the transverse displacement by the updating subprocedure of Section 2.2.3 has to be considered.

The degradation of the properties after failure is simulated using the ply-discount theory. Namely, the elastic moduli in the subelement regions where the spline interpolation is performed are locally degraded according to the rule

$$Q_{\text{after}} = Q_{\text{before}} 10^{-m} \quad \text{with } 0 \leq m \leq 20,$$

Q_{after} and Q_{before} being Young's and shear elastic moduli selected according to the type of failure occurred. This implies that within the time steps, the stiffness coefficients have to be locally reduced in the region where the damage arose and the stiffness properties locally modified during the process, choosing an appropriate exponent m . In event of fibre failure, E_{11} , G_{12} , and ν_{12} are reduced, while for matrix failure E_{22} , G_{12} , and ν_{12} are reduced. In the event of delamination, G_{13} and G_{23} are reduced. More complex degradation models in a better harmony with the physics are not considered, their effort being too large.

Nevertheless a failure model is implemented with the features outlined above, in the numerical applications the pulse pressure loading will be of a moderate intensity that will not induce damage, so the analysis of the effects of an intense loading is left to a future study.

3. Blast pulse modelling

When a pressure pulse is generated, a shock wave is transmitted in all directions. Once this wave reaches a structure, it produces an instantaneous pressure peak, followed by a decrease. Various expressions have been proposed for describing the overpressure time history, either of theoretical or numerical nature. Also results of experiments have been published in the literature.

Since most of the studies are analytical or based on a finite element analysis, usually an analytical overpressure time history is adopted. Customarily the blast-type loading is described in terms of the modified Friedlander exponential decay equation¹

$$P_z(t) = P_m(1 - t/t_p)e^{-a't/t_p}, \quad (14)$$

P_m being the peak pressure in excess of the ambient one, t_p the positive phase duration measured from the time of arrival of the blast and a' decay parameter that can be adjusted in order to approximate the result of an experimental test. Customarily the pressure is assumed to be uniformly distributed over the entire panel and the impact is assumed to occur with a normal incidence having in view the large dimension of the blast front. This is not the case of gun blast pressure pulses, which require the spatial distribution of the pressure pulse to be considered; the readers find a recent study about gun blast in the paper by [Kim and Han 2006].

Assuming a'/t_p equal to zero, the limiting case of the triangular loading is featured. As other special cases, the rectangular, step and sine pressure pulses have been considered in literature.

The sonic boom-type loading is customary modelled as an N -shaped pressure pulse corresponding to an idealized far-field pulse impacting at a normal incidence:

$$P_z(t) = \begin{cases} P_m(1 - t/t_p) & \text{for } 0 < t < rt_p, \\ 0 & \text{for } t < 0 \text{ and } t > rt_p, \end{cases} \quad (15)$$

¹See the pioneering papers [Gupta 1985; Gupta et al. 1986] and applications in [Cederbaum et al. 1988; 1989; Librescu and Nosier 1990; Librescu and Na 1998; Song et al. 1998; Librescu et al. 2004; 2006; 2005; Hause and Librescu 2005].

where r denotes the shock pulse length factor and the other symbols are as in (14). For the case $r = 1$, the N -shaped pulse degenerates into a triangular distribution, while for $r = 2$ a symmetric pulse is obtained.

The former pulse pressure time histories of (14) and (15) have been incorporated in the impact computational model of [Icardi 2007] at the place of the contact force time history. However any other analytical or computational model could be used.

The dynamic response problem resulting from blast pulse pressure loading $M\ddot{q}_e + C\dot{q}_e + Kq_e = F$, where M , C and K denote the mass, damping and stiffness matrices, respectively, while q_e is the vector of nodal DOFs and F is the vector of the nodal forces, is solved using the Newmark implicit time integration scheme, because this technique, at the contrary of explicit schemes, is stable for reasonably large time steps.

In the present numerical applications only the undamped motions will be considered; work is in progress in order to account for damping, which has implications on the thermodynamic constraints involved in the tailoring optimization process.

4. Tuning of the energy absorption properties

In this paper, a technique for tuning the energy absorption properties of laminated and sandwich composites is presented, which is based on a new tailoring concept. The purpose is to minimize the energy absorbed through unwanted modes (those involving interlaminar strengths) and maximize the energy absorbed through desired modes (those involving membrane strengths). This is done by finding a suited variable distribution of stiffness properties, an extension of the one developed by the authors in [Icardi and Ferrero 2008]. While this former version only dealt with an in-plane variation of properties of laminates, in the current version either a variation of the stiffness properties of the face sheets over their plane, or of the core properties across the thickness of sandwich composites are considered.

The suitable distribution of stiffness properties is obtained solving the Euler–Lagrange equations of a problem where the strain energy contributions of interest are made extremal under spatial variation of such properties.

The effect of this technique is to act as an energy absorption tuning, since the amount of energy absorbed by specific modes can be minimized or maximized. Minimization of the energy due to out-of-plane strains and stresses can result in a reduction of these very critical parameters by the viewpoint of damage accumulation in service, as shown by the numerical applications. This result can be obtained without any stiffness loss, since the membrane and bending energy contributions can be maximized, while the energy of out-of-plane stresses is minimized.

The present technique can be seen as a non classical optimization technique in which the design variables to be modified are the stiffness properties (through spatial variation of the ply angles and/or of fibre volume fraction and constituent materials) and the constraints are represented by imposition of constant thickness of individual layers, constant overall properties (e.g. averaged stiffness of the “optimized” layers equal to the stiffness of classical layers made of the same constituent materials), the thermodynamic constraints for energy conservation and the Lempriere, Lekhnitski and Chentsov’s conditions. The objective function is the extremization of wanted energy contributions of interest, while the optimization algorithm can be seen as the variational calculus rule, i.e. imposition of the first variation vanishing.

Note that in the applications, pre-existing conventional layers will be substituted with layers that either (i) minimizes bending and maximizes membrane energy, (ii) minimizes bending and maximizes transverse shear, or (iii) maximizes bending and minimizes transverse shear, because for each of these three cases a solution was found in [Icardi and Ferrero 2008] that does not make contradictory these requirements.

The following simplified version of the structural model with a constant transverse displacement is employed in this context:

$$\begin{aligned}
 U(x, y, z) &= u^\circ + z(\gamma_x^\circ - w_{,x}^\circ) + z^2 C_x(x, y) + z^3 D_x(x, y) + \sum_{k=1}^{S-1} {}^{(k)}\phi_x(x, y)(z - {}^{(k)}Z^+)H, \\
 V(x, y, z) &= v^\circ + z(\gamma_y^\circ - w_{,y}^\circ) + z^2 C_y(x, y) + z^3 D_y(x, y) + \sum_{k=1}^{S-1} {}^{(k)}\phi_y(x, y)(z - {}^{(k)}Z^+)H_k, \\
 W(x, y, z) &= w^\circ,
 \end{aligned} \tag{16}$$

since the model of (1)–(5) requires too big a mathematical effort. Higher-order contributions neglected in the simplification will be accounted for by updating its strain energy to that of the model (1)–(5).

4.1. Tailoring of constituent plies. This optimisation is carried out finding spatially variable stiffness properties which makes the bending, in-plane and out-of-plane strain energy contributions stationary, with the purpose to minimise the energy absorbed by modes involving out-of-plane stresses and strains and maximise that related to membrane stresses and strains. The stiffness properties of the constituent layers (i.e., the face sheets in the case of sandwich panels) represent the master field, while the other variables not subjected to variation represent the slave and data fields. The optimisation starts writing the first variation of the strain energy under variation of the functional DOFs that represents the constraint of dynamic equilibrium.

A rather intricate system of coupled partial differential equations are obtained, the so-called Euler-Lagrange equations and related natural boundary conditions, enforcing the vanishing of the first variation of the strain energy under variation of the stiffness properties, that define the optimised distributions of these properties (i.e., that make the considered energy contributions extremal). We report as an example the stationary condition for the bending energy:

$$\begin{aligned}
 -WR_1 \delta u^\circ - WR_2 \delta v^\circ - WR_3 \delta w^\circ + (WR_4 - \frac{4}{3}WR_5 + WR_6 + WR_7) \delta \gamma_x^\circ \\
 + (WR_8 - \frac{4}{3}WR_9 + WR_{10} + WR_{11}) \delta \gamma_y^\circ = 0,
 \end{aligned} \tag{17}$$

where the WR 's are sums of partial derivatives of various orders of the stiffness quantities; for instance

$$WR_3 = D_{11,1111} + 2D_{12,1122} + 4D_{16,1112} + 4D_{26,1222} + 4D_{66,1122} + D_{22,2222}. \tag{18}$$

Similarly, the expression for the transverse shear energy in the plane (x, z) is a sum of multiples of δu° , δv° , δw° , $\delta \gamma_x^\circ$ and $\delta \gamma_y^\circ$; the coefficient of the first of these is one of the simplest and will serve to give the flavor:

$$\left\{ XR_{R1} + XR_{R1}^a + XR_{R1}^d + XR_{R44} + XR_{R44}^a + XR_{S44}^d - \frac{4}{3}(XR_{P1} - XR_{P6})/h^2 \right. \\
 \left. - \frac{1}{2}(XR_{26X2} + XR_{31X2} + XR_{36X2} + XR_{41X2})/h - \frac{2}{3}(XR_{26X3} + XR_{31X3} + XR_{36X3} + XR_{41X3})/h^2 \right\} \delta u^\circ.$$

(The XR are also defined in terms of partial derivatives of the stiffness quantities.)

At this point, we must add to the system of governing equations also the constraint conditions representing the energy updating from the simplified model of (16) to that of the model of (1) with variable transverse displacement. An approximate solution of technical interest to this governing system of equations is a second-order polynomial approximation of the transformed reduced stiffness coefficients distribution, since it can be easily obtained by current manufacturing techniques:

$$\begin{aligned}
 Q_{11} &= A_1 + A_2x + A_3x^2, & Q_{12} &= C_1 + C_2x + C_3y + C_4x^2 + C_5y^2 + C_6xy, \\
 Q_{16} &= E_1 + E_2x + E_3x^2 + E_4xy, & Q_{22} &= B_1 + B_2y + B_3y^2, \\
 Q_{26} &= F_1 + F_2y + F_3y^2 + F_4xy, & Q_{44} &= G, & Q_{55} &= L, \\
 Q_{45} &= M, & Q_{66} &= D_1 + D_2x + D_3y + D_4x^2 + D_5y^2 + D_6xy.
 \end{aligned} \tag{19}$$

This approximation holds at the laminate level (i.e., for a group of layers that together makes extremal the energy contributions of interest), or at the single ply level (i.e., of a layer able itself to minimise or maximise certain energy contributions).

The quantities $A_1, A_2, \dots, B_1, \dots, F_1, \dots, M$ appearing in (19) are determined by enforcing conditions that make the solution physically consistent. The thermodynamic constraints, the conservation of energy and the conditions formulated by Lempriere, Lekhnitski and Chentsov's are enforced in this paper. In addition, a mean value of the stiffness coefficients is imposed; it is assumed equal to that of the conventional layers that are replaced with the optimised ones. Also a convex or a concave shape can be chosen, together with the value of the stiffness at the bounds of the region. The coefficients of Q_{12} and Q_{66} are determined enforcing the mean value and the thermodynamic constraints. Q_{16}, Q_{26} are enforced to have a zero mean value, while the coefficients of Q_{44}, Q_{45} and Q_{55} are determined enforcing Chentsov's relations.

We remark that the variable distribution of stiffness properties, (19), can be obtained either varying the orientation of the reinforcement fibres, the fibre volume rate or the constituent materials (i.e. fibres and matrix) over the plane of the plies. It is also remarked that as shown in [Icardi and Ferrero 2008], even a rough approximation of the elastic coefficients of (19) using patches with a step variation of the orientation can be effective.

4.2. Core with variable properties. The stiffness discontinuity at the face sheet/core interface results in a large increase in interfacial shear stresses, so debonding at or near the core/face sheet interface is a major problem in sandwich construction. An alternative for overcoming this problem is a sandwich structure with a functionally graded core: grading the core properties in the thickness direction allows a reduction in the stiffness discontinuity. Although their technology is still in its infancy, functionally graded materials are of great interest for their potential in many applications. New fabrication methods are expected to be developed in the next years that will control the foaming process parameters as required [Apetre et al. 2006]. For such reason, the advantages of these new sandwich structures are here assessed. Assuming that the core properties can be controlled across the thickness, the strain energy due to transverse stresses and strains have to be made extremal for finding core property distributions that reduce the interlaminar stress concentration at the face sheet/core interfaces. As an example we report the extremal condition for the energy due to the shear in the plane (x, z) :

$$\int \left(Q_{11}(z^2 G_{,x}^y - z^2 W_{,xx}^y + z U_{,x}^y) + Q_{12}(zV - z^2 W_{,y} + z^2 H) \right. \\ \left. + Q_{16}(2zU + 2z^2 G - 3z^2 W_{,x} - zV_{,x}^y + z^2 H_{,x}^y) + Q_{26}(zV_{,y}^x - z^2 W_{,yy}^x + z^2 H_{,y}^x) \right. \\ \left. + Q_{66}(zV + zU_{,y}^x - 2z^2 W_{,y} + z^2 H + z^2 G_{,y}^x) + Q_{44}G^{xy} + Q_{45}H^{xy} \right) dz. \quad (20)$$

We give some of the expressions for the symbols appearing in this equation, as examples:

$$\int u_{,x}^0 dx = U, \quad \int v_{,x}^0 dx = V, \quad \int w_{,x}^0 dx = W, \quad \int \gamma_{x,x} dx = G, \quad \int \gamma_{y,x} dx = H, \\ \int U dy = U^y, \quad \int V dy = V^y, \quad \int W dy = W^y, \quad \int G dy = G^y, \quad \int H dy = H^y.$$

The terms not reported here also contain derivatives of the DOFs integrated over the domain. As in the former case of the optimisation of face sheets, one must add the constraints representing the equilibrium and the updating from the simplified model of (16) to the model of (1). As a final result, the following condition is obtained, that defines the core properties distribution that makes the energy of transverse shears extremal:

$$\int Q_{ij}(z)F dz = \text{constant}, \quad (21)$$

where $F = A + Bz$, with A and B representing integrals of the spatial derivatives of the displacements in (x, y) . Similar considerations hold for the membrane energy contributions. In this case, the extremal conditions correspond to

$$F = Az^2 + Bz. \quad (22)$$

This equation holds for the elastic coefficients Q_{11} , Q_{12} , Q_{22} , Q_{16} , Q_{26} and Q_{66} , while in the case of Q_{44} , Q_{45} and Q_{55} , the quantity F has to be set equal to 1. Accordingly, the stiffness properties Q_{11} to Q_{66} have to vary across the thickness according to $(Az^2 + Bz)^{-1}$, while Q_{44} , Q_{45} and Q_{55} have to be constant.

If we assume the foam constituting the core to be an isotropic material with properties E , G and ν and represent its stiffness coefficients as $Q_{11} = K_1/(z^2 + C_1z)$, $Q_{12} = K_2/(z^2 + C_2z)$, we find the following relation after enforcement of thermodynamic and isotropy constraints:

$$-2K_1 < K_2 < K_1. \quad (23)$$

In the numerical applications, the properties of the core will be assumed to vary according to the former relations (19) to (23) considering as upper and lower limits those of the ROHACELL foam.

5. Numerical results

The accuracy of the present structural model with energy updating was extensively assessed in a number of previously published papers. The reader is referred, among other recent papers by the authors not cited for brevity, to [Icardi 2007] for laminates and to [Icardi and Ferrero 2009] for sandwich plates with or without damage. In all these assessments, the result of the simulation in terms of stress fields, damage and impact force time history were compared to the exact 3D elasticity solution, where available, and to experiments. The model always appeared accurate with a low computational effort (less than two minutes

on a PC with a 1.9 GHz dual core processor); therefore no further assessments will be presented in this paper.

Our purpose is to test whether the optimisation of layers and core can relax the critical interlaminar stress concentrations and then improve the strength at the onset of delamination (without any loss of bending stiffness or decay of the response properties).

As a necessary premise, comparisons by the results of the present simulation to the results by Librescu and co-workers will be presented for sample cases taken from [Librescu and Nosier 1990; Hause and Librescu 2005], with the purpose to assess whether the higher-order effects by the present model (necessary for capturing the 3D stress fields) improve the accuracy of the dynamic response. To this purpose, also the results of a closed-form approach based on the model of Section 2.1 and solution of the governing equations by the Galerkin method will be presented for comparisons. The reader can find details in [Icardi 2007], where this approach was used for computing the contact force time history. Note that while in the impact study of [Icardi 2007] up to 15 terms were required to represent the waves that reach the edges and reflect off during the contact time, in the current case no change in the results was seen up to 11 terms. Since the FSDPT model can be particularised from the zigzag model of (1)–(5), the response of this model will also be used for comparisons.

It will be shown that the results by Librescu and co-workers agree with those obtained by the FSDPT model using a single term, while using more terms high-order effects will be evidenced as little larger deflections and lower frequencies. This behaviour is believed to be correct, since the improved description of the shear deformation and the inclusion of the energy associated to the transverse normal stress and strain modes make the structural model a little less stiff.

Hereafter results will be presented for laminated and sandwich panels with laminated faces under blast loading. Note that sandwich composites represent much more severe test cases from the viewpoint of modelling, since they require a refined modelling that accounts for large transverse shear and normal deformations.

5.1. Laminated plates. Consider a pinned $[0/90/90/0]$ laminated square plate with a length-to-thickness ratio of 30, undergoing a pressure pulse characterised by $a'/t_p = 0$ in (14), $P_m = 3.447$ MPa and $t_p = 0.1$ s, according to [Librescu and Nosier 1990, Figure 3], which is here referred as the classical case. The deflection will be presented for all the studied cases in a non-dimensional form, as the ratio between the dynamic displacement and the static one. The non-dimensional deflection predicted by the present finite element model with energy updating (in-plane discretization into 10×10 elements) is represented in Figure 1, left, where it is compared with the predictions of the closed-form approach based on the Galerkin's method for 11 terms in both x and y directions, as predicted by the zigzag model of Section 2.1 and by the CLPT (classical laminated plate theory) and FSDPT models with only one term in both directions. Figure 1, right, shows the response when the effects of damage are assessed while time unfolds.

According to [Librescu and Nosier 1990], the normalisation of results is carried out with respect to the deflection of the static case. In the damaged case, this reference deflection is computed when the delaminated area at the most critical interface (the one next to the impacted face) is 50%.

Figure 1, left, also depicts the time response when the external layers oriented at 0° are replaced with optimised layers having the stiffness distributions of Figure 2 (corresponding to the variable orientation

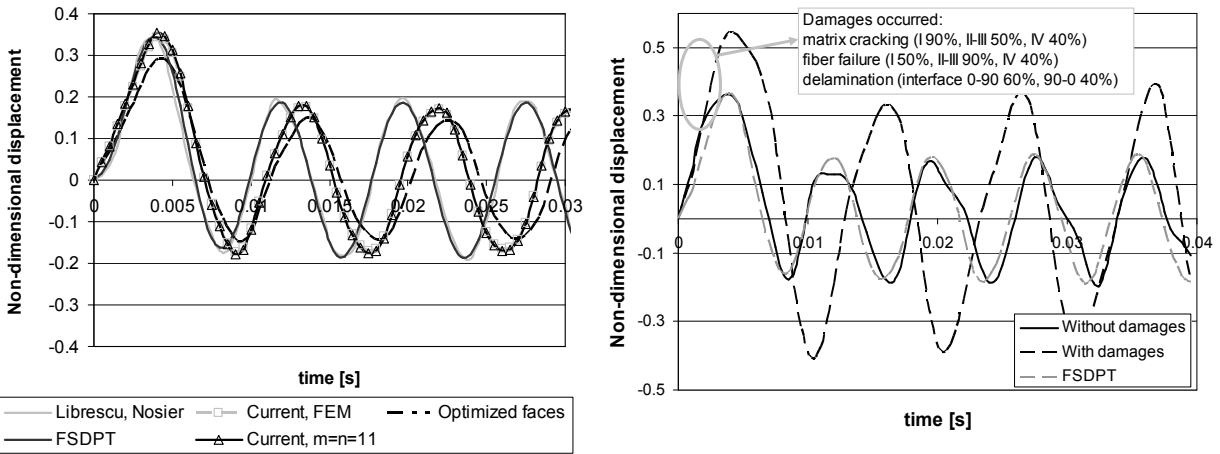


Figure 1. Triangular blast pulse loading: nondimensional deflection time history for a [0/90/90/0] laminate.

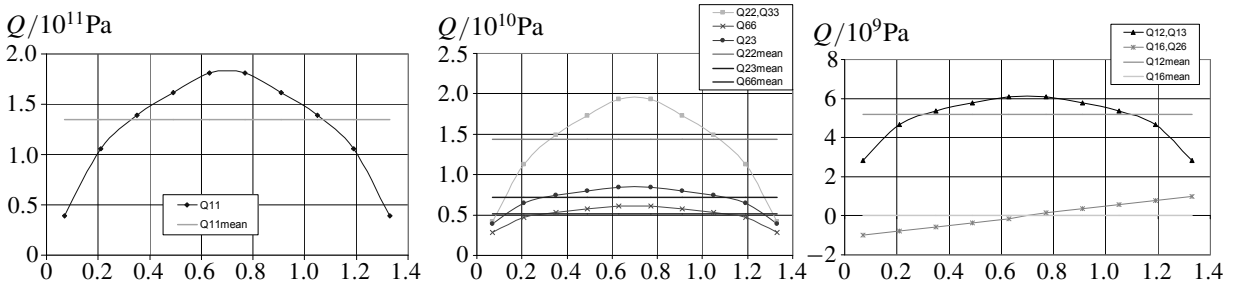


Figure 2. Stiffness distribution for the optimised layers. The horizontal coordinate is the in-plane direction x , in meters.

of reinforcement fibres presented in [Icardi and Ferrero 2008, Figure 3], here referred as OPT1). In this figure we regard the material as undamaged, although the hypothesis of mild loading is not consistent with the magnitude of the pressure pulse considered by Librescu and Nosier, the stresses being very large (that is, failure has already occurred at the loading level they consider). To be consistent with [Librescu and Nosier 1990], we will compare the stress fields without considering the degradation of the properties also in the remaining cases.

In Section 2.3 we analyse Figure 1, right, considering the effects of damage, and showing that at the first peak, after about 0.005 sec, the matrix damage is extended to 90% of first layer, 50% of second and third layers and 40% in the last layer. The area where the fibres have failed is 50% in the first layers, 90% in the subsequent two layers and 40% in the last layer. Delamination occurs at the 0°/90° and 90°/0° interfaces. In the first case, the delaminated area is 60% of the whole interface area, while in the last case it has an extension of 40%.

It appears by the comparison with the response predicted by the FSDPT model in Figure 1, left, that the high-order effects brought by the zigzag model have an increasing importance while the time unfolds. Also evident from the same figure is the beneficial effect of optimised layers in terms of motion amplitude

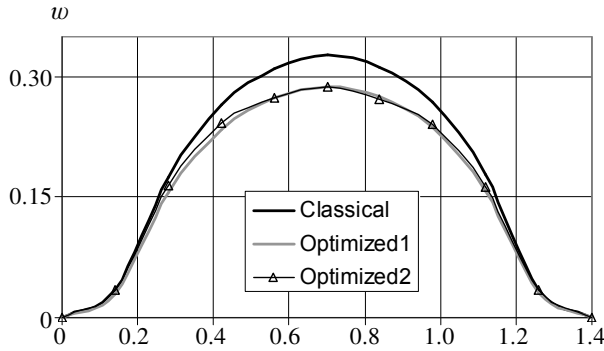


Figure 3. Transverse displacement (vertical axis, in meters) versus spanwise coordinate (horizontal axis, in meters) for the laminate with classical layers and the two laminates with optimised layers.

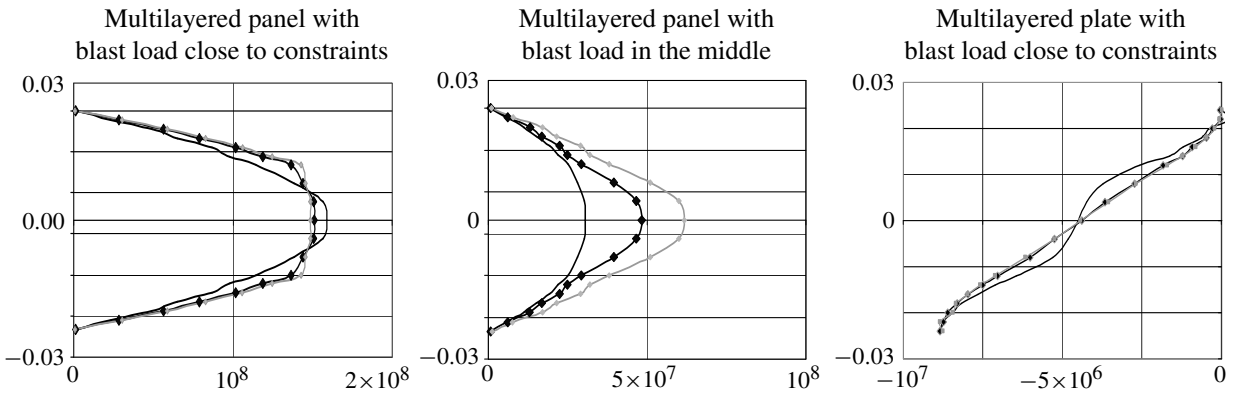


Figure 4. Normalized transversal shear stress (horizontal axis) versus thickness coordinate (vertical axis, in meters) for the laminate with classical layers (black curve with markers) and the two with optimised layers (smooth black curve = OPT1; grey curve = OPT2).

reduction (mean properties equal to those of the replaced layers). The effect on interlaminar stress fields of optimised layers is shown in [Figure 4](#), which reports the stresses at the interfaces. A comparison is presented with the reference configuration and also with another optimised case having in plane shear stiffness with a maximum value close to the constraints and Q_{16} and Q_{26} with a double slope, here referred as OPT2.

These results are those corresponding to 3 msec after application of the pressure pulse. One can see in [Figures 3](#) and [4](#) how the optimised layers that have limited deflections also can limit the magnitude of interlaminar stresses and oppose the spreading of the stress peaks at the inner interfaces. Application of the delamination criterion by Chang and Springer shows that the loading magnitude considered corresponds to a fully delaminated area at the first interface (starting from the bottom layer), as shown by the left column of [Figure 5](#), while at the next interfaces the central region remain undamaged. When an optimised layer OPT2 is incorporated, these regions enlarge to the whole plate and at the first interface there is a central region where delamination does not take place; see middle column of [Figure 5](#). Thus, it appears

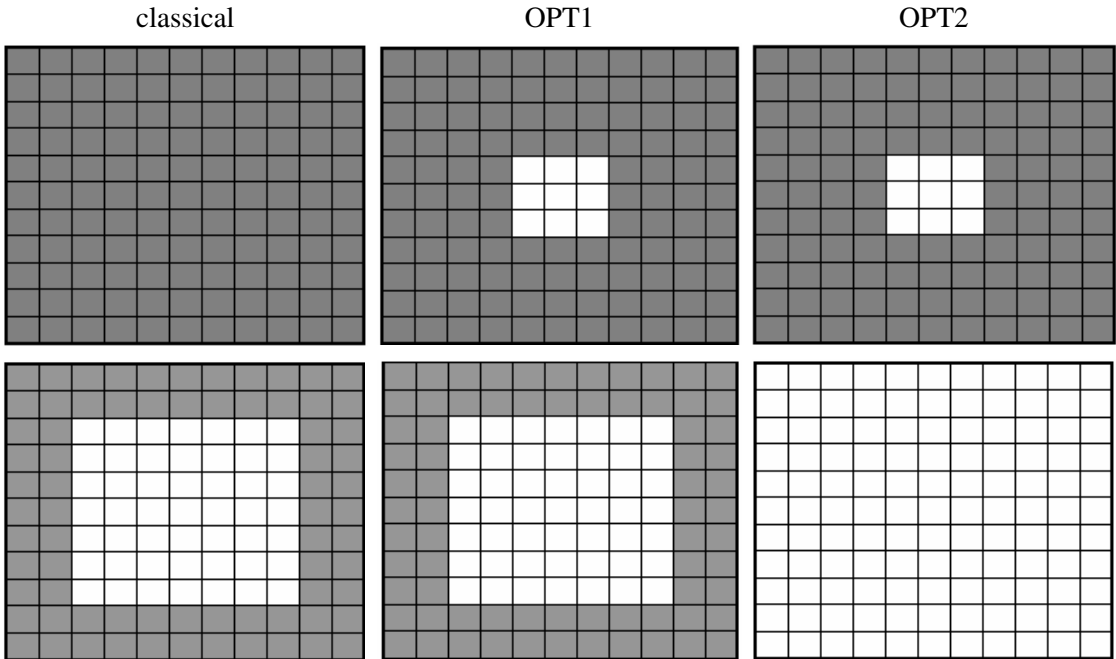


Figure 5. Delaminated area (shown in grey) at the first interface (0/90, top row) and at the third (90/0, bottom row). Left column, classical laminate; middle column, OPT1; right column, OPT2.

that the present optimisation technique can both improve the response and the strength. Obviously, orienting the reinforcement fibres in a complementary way, the opposite result could be found.

5.2. Sandwich plates. Now consider cases of sandwich panels subjected to different blast pulse loading, with the purpose to assess the accuracy of the structural model when it predicts their transient motions and discuss the implications of the optimisation. Cases with optimised face sheets, i.e. incorporating optimised layers with the features discussed above, and with or without an optimised distribution of the core properties across the thickness will be considered. The reference configurations are chosen among the sample cases presented in [Hause and Librescu 2005, Figure 7 and 12].

The first of these refers to a pulse step of 0.005 sec, using the same 10×10 in-plane discretization than in the former case. The time response for this case as predicted by Hause and Librescu, by the present structural finite element model with energy updating, by the CLPT and FSDPT models using the Galerkin method (with only one term in both directions) and by the present model varying the core properties across the thickness is represented in Figure 6. The stacking sequence for this case is $[45/-45/45/-45/45/\text{core}/45/-45/45/-45/45]$; the length-to-thickness ratio is 20.97. It appears again that the high-order effects incorporated in the current model results in little larger deflections, while frequencies remain unchanged. This result is consequent to the large deformation in the transverse direction and to the very high bending stiffness peculiar of sandwich panels. The four core configurations considered produce a different response, but the variation is not large. All have the same mean properties that correspond to those of the reference case and all produce a reduction in the amplitude of motions. The

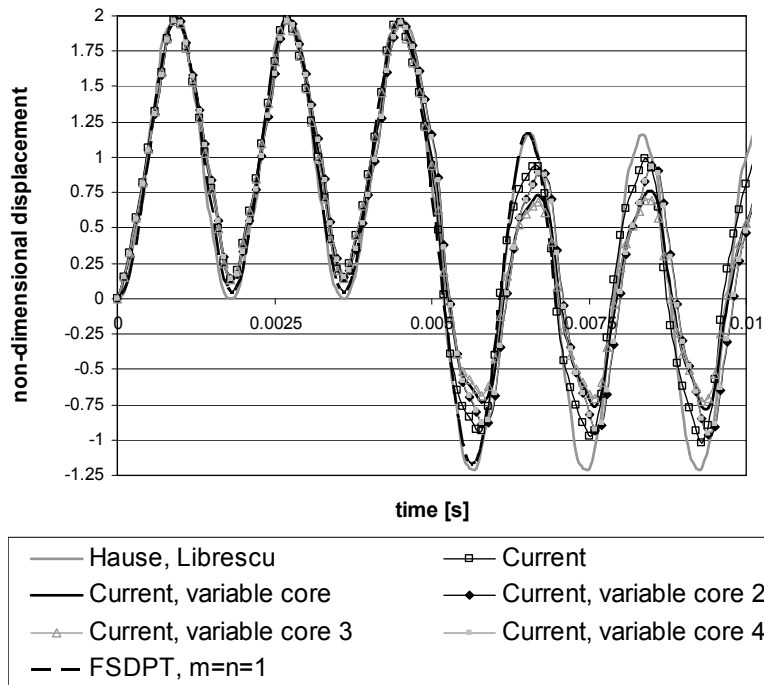


Figure 6. Step blast pulse loading: non-dimensional deflection time history for the sandwich plates with $[45/-45/45/-45/45/\text{core}/45/-45/45/-45/45]$ lay-up.

first case OPT-S1 corresponds to a V variation of the core properties across the thickness increasing at the midplane; it represents a simplified suboptimal variation that simulates in a rough way the optimised variation of (21)–(23), here referred to as OPT-S2 (where the property variation on the thickness has an hyperbolic shape). The case OPT-S3 is similar to OPT-S1 but has properties that decrease from the interfaces with the face sheets to the midplane. The last case OPT-S4 is similar to OPT-S2, but has the minimum value at the midplane.

Consider now the sample case treated in [Hause and Librescu 2005, Figure 12] with the purpose to show the high sensitivity of the response to the lay-up variation of the faces, for a sonic boom pressure pulse. The lay-up considered in by Hause and Librescu was $(t/-t/t/-t/t/\text{core}/t/-t/t/-t/t)$, with t respectively equal to 45° , 30° , 0° . The response predicted by the present model for these three cases is reported in Figure 7. It appears that also for this sample case, the FSDPT model and the Galerkin's solution with just one term in both the directions x and y is equivalent to that of Hause and Librescu, as shown by the results for $t = 0^\circ$ and $t = 45^\circ$. A similar result, not shown in the figure for readability, was also obtained for $t = 30^\circ$.

The effect of incorporation of cores with variable properties across the thickness is shown in Figure 8. The sample cases considered in this figure pertains to the case $t = 0^\circ$ and the core variations OPT-S2 and OPT-S3. Besides the beneficial effect of the core property variation across the thickness that is shown by both the configurations considered, it has to be noted that a different behaviour is presented for different boundary conditions. Numerical tests show that for pinned edges better results are obtained in terms

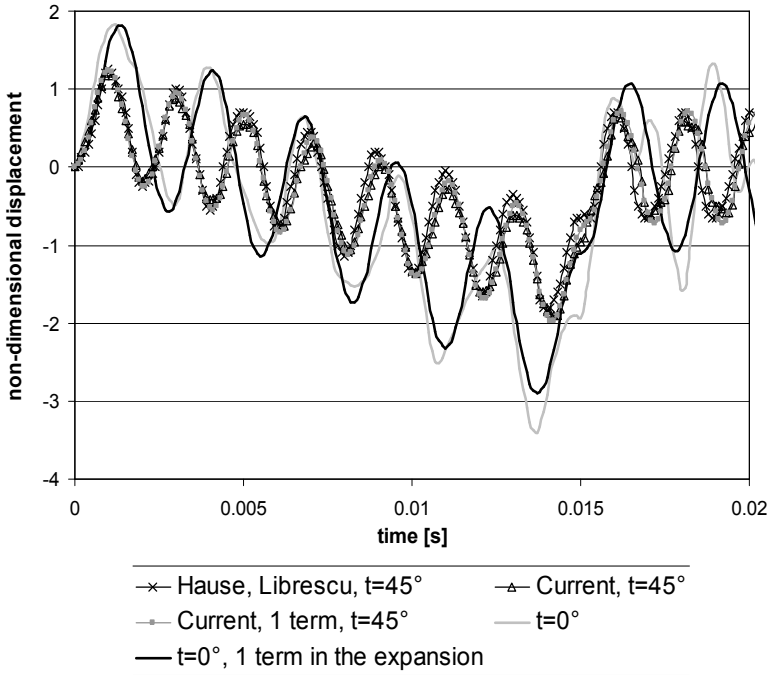


Figure 7. Sonic boom blast pulse loading: nondimensional deflection time history for sandwich plates with $[t/-t/t/-t/t/core/t/-t/t/-t/t]$ lay-up.

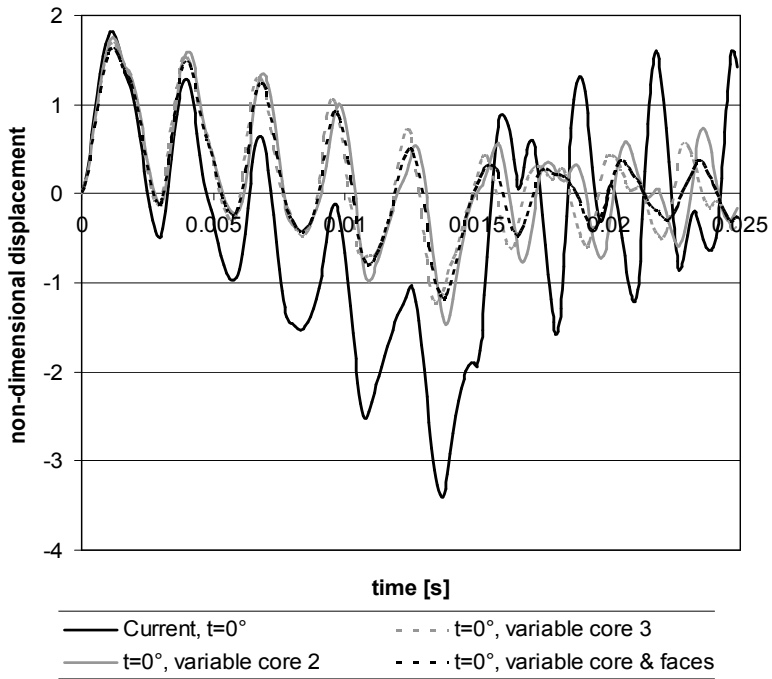


Figure 8. Sonic boom blast pulse loading: nondimensional deflection time history for optimised sandwich plates.

of vibrations suppression when the elastic coefficients of the core are decreasing from the face sheets interfaces to the midplane, as in OPT-S3, while the opposite occurs for simply supported edges: OPT-S2 is more efficient.

To assess whether the incorporation of optimised faces in sandwich panels with optimised core can consistently decrease the amplitude of motions, the sample case of a sandwich panel with core of type OPT-S2 (i.e., not the most efficient case) and faces with a $[0/90/90/0]$ lay-up was considered. To be self-contained, the motions for this case are not reported; it is just reported that if the 0° layers are substituted with optimised layers, as described in Section 5.1, a reduction of the amplitude to 1/6 is obtained already in the first instants of motion with respect to the reference case with constant properties of the 0° layers (equivalent to the mean value of optimised layers) and this ratio is kept while the time unfolds.

The interlaminar stress fields for the case $t = 0^\circ$ and cores with variable properties OPT-S2 and OPT-S3 are reported in Figure 9, which refers to 0.11 sec after application of the pressure pulse. Their magnitude being large, the pressure pulse considered in [Hause and Librescu 2005] for this sample case does not reflect the hypothesis of mild loading, therefore failures occurred during the motions that also in the present paper have not been considered. Just comparing the stress fields without considering the degradation of properties, it appears that the variable core properties reduce the critical stress concentration of shear stresses at the interface with the core and spread these stresses across the core. Beneficial effects are seen also for the transverse normal stress, since in the region close to the lower interface where they are peeling, i.e., tensile, the magnitude consistently decreases, and they also decrease at the upper interface where they are compressive; since they are spread across the core. This reduction of the critical interfacial concentration by spreading the stresses was also the objective pursued by the former studies on functionally graded materials. While in such studies the core property variation was postulated, in the present paper it is grounded on energy considerations and still appears successful.

Applying the Chang–Springer criterion for delamination it appears that in the reference case the upper interface with the core is fully delaminated, while the lower one is undamaged, as shown by Figure 10. The situation is different in the optimised cases; for example in the case OPT-S1 some regions are

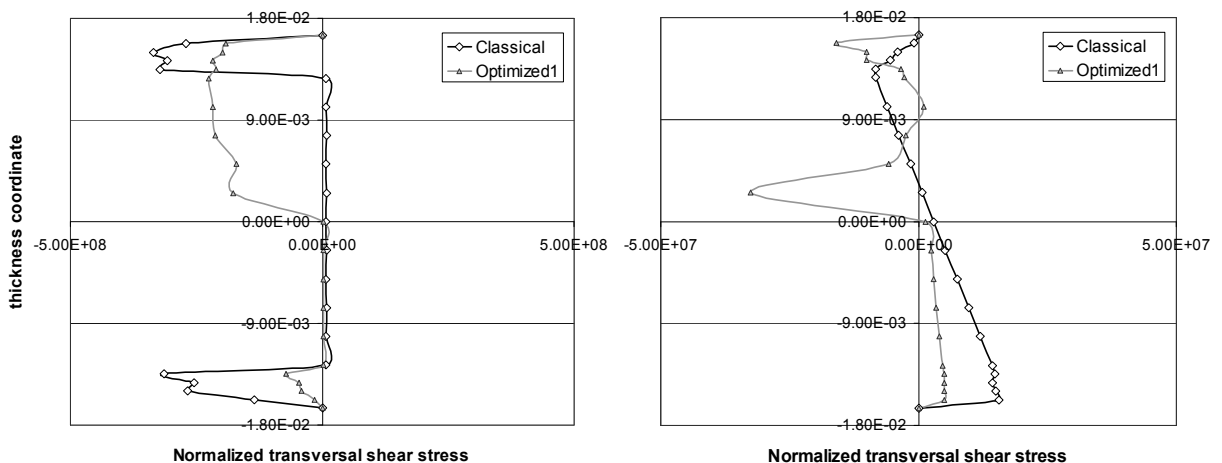


Figure 9. Transverse shear (left) and normal (right) stresses across the thickness for the sandwich plate with classical and optimised configuration.

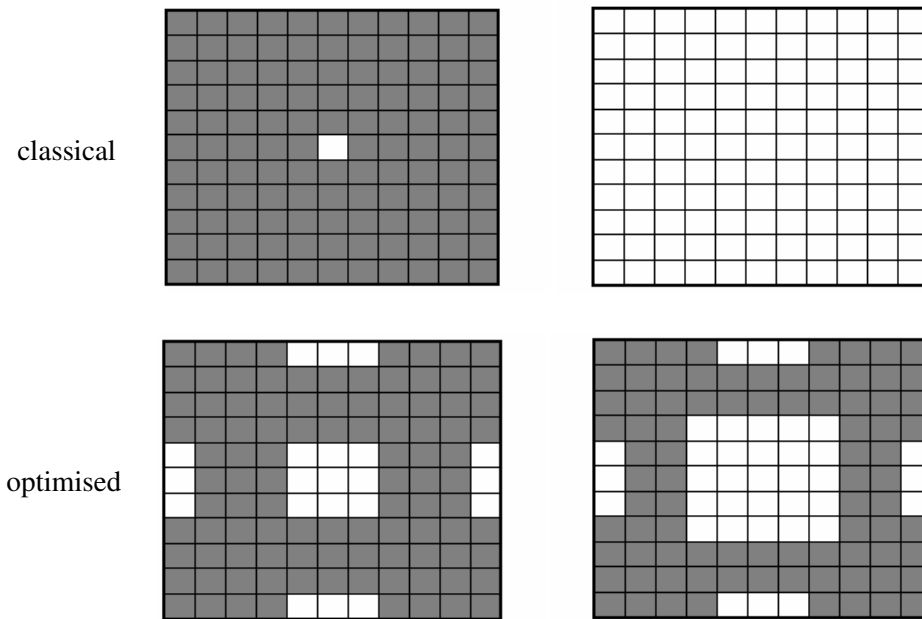


Figure 10. Delaminated area (shown in grey) at the two core-face interfaces for the sandwich plate with classical (top row) and optimised (bottom row) configurations.

preserved from delamination at the upper interface, while the lower interface present a delamination damage distributed in a similar way because the stress peak are spread across the thickness. This means that all the constituent materials contribute to the absorption of the incoming energy due to the pulse pressure, with evident practical advantages.

Concluding remarks

The dynamic response and the stress fields of laminated and sandwich flat panels undergoing impulsive pressure loading have been investigated for different pulse pressure time histories. A refined zigzag model with a piecewise high-order variation of in-plane and transverse displacements is employed as structural model, which is incorporated through a strain energy updating into a conventional shear deformable plate element. The reason is that the direct implementation of the zigzag model involves displacement derivatives as nodal DOFs, which makes the elements inefficient from the computational viewpoint. The current model represents a good compromise because it requires a lower computational effort than discrete-layer models for providing a lower, but still rather good accuracy of predictions.

A recently developed technique is employed for relaxing the critical interlaminar stress concentrations at the interfaces of constituent layers. With this technique, the optimal through-the-thickness distribution of the core properties and the in-plane distribution of the stiffness properties of the face sheets (and of the constituent layers of laminates) are found maximising the strain energy absorbed through membrane and bending modes and minimizing that absorbed by out-of-plane modes involving the interlaminar stresses. While in the former studies on functionally graded materials the core property variation was postulated, in the present paper it results from energy considerations.

It appears that the current technique reduces the critical interlaminar stress concentrations (that is, it spreads them across the thickness), with beneficial effects on the strength at the onset of damage. It also improves the dynamic response, since it limits deflections while time unfolds. Even simple suboptimal distributions that approximate in a rough way the optimised variation of stiffness properties appear effective in the numerical applications.

References

- [Apetre et al. 2006] N. A. Apetre, B. V. Sankar, and D. R. Ambur, “Low-velocity impact response of sandwich beams with functionally graded core”, *Int. J. Solids Struct.* **43**:9 (2006), 2479–2496.
- [Birman and Bert 1987] V. Birman and C. W. Bert, “Behaviour of laminated plates subjected to conventional blast”, *Int. J. Impact Eng.* **63**:3 (1987), 145–155.
- [CAA 2001] “Aircraft hardening research programme: final overview report”, CAA Paper 2001/9, Civil Aviation Authority, London, 2001, Available at <http://www.caa.co.uk/docs/33/CAPAP200109.PDF>.
- [Cederbaum et al. 1988] G. Cederbaum, L. Librescu, and I. Elishakoff, “Random vibration of laminated plates modeled within a high-order shear deformation theory”, *J. Acoust. Soc. Am.* **84**:2 (1988), 660–666.
- [Cederbaum et al. 1989] G. Cederbaum, L. Librescu, and I. Elishakoff, “Response of laminated plates to non-stationary random excitation”, *Struct. Safety* **6**:2–4 (1989), 99–113.
- [Cheng and Benveniste 1968] D. H. Cheng and J. E. Benveniste, “Sonic boom effects on structures: a simplified approach”, *Trans. New York Acad. Sci., Ser. II* **30** (1968), 457–478.
- [Crocker and Hudson 1969] M. J. Crocker and R. R. Hudson, “Structural response to sonic booms”, *J. Sound Vib.* **9**:3 (1969), 454–468.
- [Dobyns 1981] A. L. Dobyns, “Analysis of simply-supported orthotropic plates subjected to static and dynamic loads”, *AIAA J.* **19**:5 (1981), 642–650.
- [Gupta 1985] A. D. Gupta, “Dynamic analysis of a flat plate subjected to an explosive blast”, pp. 491–496 in *Computers in engineering, 1985: proceedings of the 1985 ASME International Computers in Engineering Conference and Exhibition* (Boston, 1985), vol. 1, edited by R. Raghavan and S. M. Rohde, ASME, New York, 1985.
- [Gupta et al. 1986] A. D. Gupta, F. H. Gregory, and R. L. Bitting, “Dynamic response of a simply-supported rectangular plate to an explosive blast”, pp. 385–390 in *SECTAM XIII proceedings: the Southeastern Conference on Theoretical and Applied Mechanics* (Columbia, SC, 1986), vol. 1, edited by W. F. Ranson and J. H. Biedenbach, College of Engineering, University of South Carolina, Columbia, SC, 1986.
- [Hause and Librescu 2005] T. Hause and L. Librescu, “Dynamic response of anisotropic sandwich flat panels to explosive pressure pulses”, *Int. J. Impact Eng.* **31**:5 (2005), 607–628.
- [Hause and Librescu 2007] T. Hause and L. Librescu, “Dynamic response of doubly-curved anisotropic sandwich panels impacted by blast loadings”, *Int. J. Solids Struct.* **44**:20 (2007), 6678–6700.
- [Hayman 1996] B. Hayman, “Underwater explosion loadings on foam-cored sandwich panels”, in *Sandwich construction 3: proceedings of the Third International Conference on Sandwich Construction* (Southampton, 1995), vol. 2, edited by H. G. Allen, Engineering Materials Advisory Service, Cradley Heath, 1996.
- [Houlston et al. 1985] R. Houlston, J. E. Slater, N. Pegg, and C. G. DesRochers, “On analysis of structural response of ship panels subjected to air blast loading”, *Comput. Struct.* **21**:1–2 (1985), 273–289.
- [Icardi 2001] U. Icardi, “Higher-order zig-zag model for analysis of thick composite beams with inclusion of transverse normal stress and sublaminate approximations”, *Compos. B Eng.* **32**:4 (2001), 343–354.
- [Icardi 2007] U. Icardi, “ C^0 plate element based on strain energy updating and spline interpolation, for analysis of impact damage in laminated composites”, *Int. J. Impact Eng.* **34**:11 (2007), 1835–1868.
- [Icardi and Ferrero 2008] U. Icardi and L. Ferrero, “A new tailoring optimization approach for improving structural response and energy absorption capability of laminated and sandwich composites”, *J. Mech. Mater. Struct.* **3**:4 (2008), 729–760.

- [Icardi and Ferrero 2009] U. Icardi and L. Ferrero, “Impact analysis of sandwich composites based on a refined plate element with strain energy updating”, *Compos. Struct.* **89**:1 (2009), 35–51.
- [Jiang and Olson 1994] J. Jiang and M. D. Olson, “Modelling of underwater shock-induced response of thin plate structures”, Technical Report 39, Department of Civil Engineering, University of British Columbia, Vancouver, 1994.
- [Kim and Han 2006] D.-K. Kim and J.-H. Han, “Establishment of gun blast wave model and structural analysis for blast load”, *J. Aircraft* **43**:4 (2006), 1159–1168.
- [Langdon and Schleyer 2006] G. S. Langdon and G. K. Schleyer, “Deformation and failure of profiled stainless steel blast wall panels, III: Finite element simulations and overall summary”, *Int. J. Impact Eng.* **32**:6 (2006), 988–1012.
- [Librescu and Na 1998] L. Librescu and S. Na, “Dynamic response of cantilevered thin-walled beams to blast and sonic-boom loadings”, *Shock Vib.* **5**:1 (1998), 23–33.
- [Librescu and Nosier 1990] L. Librescu and A. Nosier, “Response of laminated composite flat panels to sonic boom and explosive blast loadings”, *AIAA J.* **28**:2 (1990), 345–352.
- [Librescu et al. 2004] L. Librescu, S.-Y. Oh, and J. Hohe, “Linear and non-linear dynamic response of sandwich panels to blast loading”, *Compos. B Eng.* **35**:6–8 (2004), 673–683.
- [Librescu et al. 2005] L. Librescu, S. Na, P. Marzocca, C. Chung, and M. K. Kwak, “Active aeroelastic control of 2-D wing-flap systems operating in an incompressible flowfield and impacted by a blast pulse”, *J. Sound Vib.* **283**:3–5 (2005), 685–706.
- [Librescu et al. 2006] L. Librescu, S.-Y. Oh, and J. Hohe, “Dynamic response of anisotropic sandwich flat panels to underwater and in-air explosions”, *Int. J. Solids Struct.* **43**:13 (2006), 3794–3816.
- [Makinen 1999] K. Makinen, “Underwater shock loaded sandwich structures”, Report 99-01, Department of Aeronautics, Royal Institute of Technology, Stockholm, 1999.
- [Proctor 1972] J. F. Proctor, “Internal blast damage mechanisms computer program”, Technical Report NOLTR 72-231, Naval Ordnance Laboratory, Silver Spring, MD, 1972.
- [Rajamani and Prabhakaran 1980] A. Rajamani and R. Prabhakaran, “Response of composite plates to blast loading”, *Exp. Mech.* **20**:7 (1980), 245–250.
- [Rudrapatna et al. 2000] N. S. Rudrapatna, R. Vaziri, and M. D. Olson, “Deformation and failure of blast-loaded stiffened plates”, *Int. J. Impact Eng.* **24**:5 (2000), 457–474.
- [Shin and Geers 1994] Y. S. Shin and T. L. Geers, *Response of marine structures to underwater explosions*, Shock and Vibration Research, Monterey, CA, 1994.
- [Simmons and Schleyer 2006] M. C. Simmons and G. K. Schleyer, “Pulse pressure loading of aircraft structural panels”, *Thin-Walled Struct.* **44**:5 (2006), 496–506.
- [Song et al. 1998] O. Song, J.-S. Ju, and L. Librescu, “Dynamic response of anisotropic thin-walled beams to blast and harmonically oscillating loads”, *Int. J. Impact Eng.* **21**:8 (1998), 663–682.
- [Xue and Hutchinson 2004] Z. Xue and J. W. Hutchinson, “A comparative study of impulse-resistant metal sandwich plates”, *Int. J. Impact Eng.* **30**:10 (2004), 1283–1305.
- [Zhu 1996] L. Zhu, “Transient deformation modes of square plates subjected to explosive loadings”, *Int. J. Solids Struct.* **33**:3 (1996), 301–314.

Received 15 Jan 2009. Revised 18 Mar 2009. Accepted 2 Jun 2009.

UGO ICARDI: ugo.icardi@polito.it

Dipartimento di Ingegneria Aeronautica e Spaziale, Politecnico di Torino, Corso Duca degli Abruzzi 24, 10129 Torino, Italy

LAURA FERRERO: laura.ferrero@polito.it

Dipartimento di Ingegneria Aeronautica e Spaziale, Politecnico di Torino, Corso Duca degli Abruzzi 24, 10129 Torino, Italy

UNIFORMITY OF STRESSES INSIDE AN ANISOTROPIC ELLIPTICAL INHOMOGENEITY WITH AN IMPERFECT INTERFACE

XU WANG

By employing the Stroh formalism for two-dimensional anisotropic elasticity, we find that a uniform stress field exists inside an anisotropic elliptical inhomogeneity imperfectly bonded to an infinite anisotropic matrix subject to uniform stresses and strains at infinity. Here, the behavior of the imperfect interface between the inhomogeneity and the matrix is characterized by the linear spring model with vanishing thickness. The degree of imperfections, both normal and in-plane tangential to the interface, are assumed to be equal. A particular form of the interface function that leads to a uniform stress field within the anisotropic elliptical inhomogeneity is identified. Also presented are real form expressions for the stress field inside the inhomogeneity that are shown to be valid for mathematically degenerate (isotropic) material as well. We note that the interpenetration issue that arises from application of the linear spring model to the imperfect interface is not discussed here.

1. Introduction

Eshelby's celebrated results [1957; 1959; 1961] demonstrated that the stress field inside an anisotropic ellipsoidal inhomogeneity is uniform when the infinite matrix is subject to remote uniform stresses. The corresponding two-dimensional anisotropic elliptical inhomogeneity was discussed by Hwu and Ting [1989]. These authors also found that the stress field inside an anisotropic elliptical inhomogeneity is uniform when the infinite matrix is subject to remote uniform stresses. In [Eshelby 1957; 1959; 1961; Hwu and Ting 1989], the inhomogeneity-matrix interface was assumed to be perfect, such that tractions and displacements across the interface are continuous. In recent years, problems involving inhomogeneities with imperfect bonding at the inhomogeneity-matrix interface have attracted great interest [Achenbach and Zhu 1989; Hashin 1991; Gao 1995; Ru and Schiavone 1997; Shen et al. 2001; Antipov and Schiavone 2003]. The behavior of the imperfect interface is commonly simulated by the spring layer model with vanishing thickness. In this model, tractions are continuous but displacements are discontinuous across the interface. More precisely, the jumps in displacement components are proportional (in terms of the 'spring-factor-type' interface functions or interface parameters) to the respective traction components. Hashin [1991] found that the stress field inside a spherical inhomogeneity imperfectly bonded to a three-dimensional matrix is intrinsically *nonuniform* under a remote uniform stress field. The results of [Gao 1995; Shen et al. 2001] also demonstrated that the stress field inside a circular or elliptical inhomogeneity imperfectly bonded to a matrix is nonuniform under a remote uniform stress field.

Keywords: Stroh formalism, uniform stress field, anisotropy, imperfect interface, generalized plane strain.

This research was supported by the United States Army Research Laboratory through the Composite Materials Technology cooperative agreement with the Center for Composite Materials at the University of Delaware.

More recently, it was found that the stress field inside an elliptical inhomogeneity imperfectly bonded to a matrix can still be uniform under a remote uniform antiplane stress field [Antipov and Schiavone 2003] or a remote uniform in-plane stress field [Wang et al. 2008] for a special form of the interface function. In these investigations, the elastic properties of the inhomogeneity and the matrix were assumed to be *isotropic*. The purpose of the research presented here is to address whether a uniform stress field exists inside a generally anisotropic elliptical inhomogeneity imperfectly bonded to an infinite anisotropic matrix subject to uniform stresses and strains at infinity.

In this research, the Stroh formalism [Stroh 1958; Ting 1996] is employed to investigate the two-dimensional problem associated with an anisotropic elliptical inhomogeneity imperfectly bonded to an infinite matrix under a remote uniform stress field. We find a particular type of interface function that leads to a uniform stress field inside the anisotropic elliptical inhomogeneity. We also present the real-form expressions of the uniform stress field by using the identities established in [Ting 1996].

2. Stroh formalism for two-dimensional anisotropic elasticity

The basic equations for a linear anisotropic elastic material are

$$\sigma_{ij,j} = 0, \quad \varepsilon_{ij} = \frac{1}{2}(u_{i,j} + u_{j,i}), \quad \sigma_{ij} = C_{ijkl}\varepsilon_{kl}, \tag{1}$$

where u_i are displacement components, σ_{ij} and ε_{ij} are the stresses and strains, and C_{ijkl} are the elastic constants. For a two-dimensional problem, a solution exists of the form

$$\mathbf{u} = [u_1 \ u_2 \ u_3]^T = \mathbf{a}f(x_1 + px_2), \tag{2}$$

where \mathbf{a} is a 3×1 column, p is a complex number, and $f(*)$ is an analytic function. (The justification for this and for many of the assertions in this section can be found in [Ting 1996].)

Thus equations (1) are satisfied for an arbitrary function $f(*)$ if

$$(\mathbf{Q} + p(\mathbf{R} + \mathbf{R}^T) + p^2\mathbf{T})\mathbf{a} = \mathbf{0}, \tag{3}$$

where the 3×3 real matrix \mathbf{R} and the two 3×3 symmetric matrices \mathbf{Q} and \mathbf{T} are defined by

$$Q_{ik} = C_{i1k1}, \quad R_{ik} = C_{i1k2}, \quad T_{ik} = C_{i2k2}. \tag{4}$$

For a stable material with positive-definite energy density, the six roots of (3) form three distinct conjugate pairs with nonzero imaginary parts. If p_i (where $i = 1, 2, 3$) are the three distinct roots with positive imaginary parts, and \mathbf{a}_i are the associated eigenvectors, then the general solution is given by

$$\mathbf{u} = [u_1 \ u_2 \ u_3]^T = \mathbf{A}\mathbf{f}(z) + \bar{\mathbf{A}}\bar{\mathbf{f}}(\bar{z}), \quad \Phi = [\Phi_1 \ \Phi_2 \ \Phi_3]^T = \mathbf{A}\mathbf{f}(z) + \bar{\mathbf{B}}\bar{\mathbf{f}}(\bar{z}), \tag{5}$$

where

$$\begin{aligned} \mathbf{b}_i &= (\mathbf{R}^T + p_i\mathbf{T})\mathbf{a}_i = -p_i^{-1}(\mathbf{Q} + p_i\mathbf{R})\mathbf{a}_i, \quad (i = 1, 2, 3), \\ \mathbf{A} &= [\mathbf{a}_1 \ \mathbf{a}_2 \ \mathbf{a}_3], \quad \mathbf{B} = [\mathbf{b}_1 \ \mathbf{b}_2 \ \mathbf{b}_3], \\ \mathbf{f}(z) &= [f_1(z_1) \ f_2(z_2) \ f_3(z_3)]^T, \\ z_i &= x_1 + p_ix_2, \quad \text{Im}\{p_i\} > 0, \quad (i = 1, 2, 3). \end{aligned} \tag{6}$$

Thus, the stresses are given by

$$\sigma_{i1} = -\Phi_{i,2}, \quad \sigma_{i2} = \Phi_{i,1}, \quad (i = 1, 2, 3). \tag{7}$$

The second-order eigenvalue problem (3) can also be recast into the standard first-order eigenvalue problem,

$$N \begin{bmatrix} a \\ b \end{bmatrix} = p \begin{bmatrix} a \\ b \end{bmatrix}, \tag{8}$$

where

$$N = \begin{bmatrix} N_1 & N_2 \\ N_3 & N_1^T \end{bmatrix} = \begin{bmatrix} -T^{-1}R^T & T^{-1} \\ RT^{-1}R^T - Q & -RT^{-1} \end{bmatrix}. \tag{9}$$

Due to the fact that the matrices A and B satisfy the normalized orthogonal relationship

$$\begin{bmatrix} B^T & A^T \\ \bar{B}^T & \bar{A}^T \end{bmatrix} \begin{bmatrix} A & \bar{A} \\ B & \bar{B} \end{bmatrix} = I, \tag{10}$$

the real matrices S , H , and L can be introduced,

$$S = i(2AB^T - I), \quad H = 2iAA^T, \quad L = -2iBB^T, \tag{11}$$

Furthermore, H and L are symmetric, while SH , LS , $H^{-1}S$, and SL^{-1} are antisymmetric. The development presented here uses the identities

$$\begin{aligned} 2A\langle p_\alpha \rangle A^T &= N_2 - i(N_1H + N_2S^T), \\ 2A\langle p_\alpha \rangle B^T &= N_1 + i(N_2L - N_1S), \\ 2B\langle p_\alpha \rangle B^T &= N_3 + i(N_1^T L - N_3S), \end{aligned} \tag{12}$$

where $\langle * \rangle$ is a 3×3 diagonal matrix in which each component is varied according to the index α .

Let t be the surface traction on a boundary Γ . If s is the arc-length measured along Γ so that, when facing the direction of increasing s , the material is on the right-hand side, it can be shown that [Stroh 1958; Ting 1996]

$$t = \frac{d\Phi}{ds}. \tag{13}$$

To simplify the analysis, we set $x = x_1$, $y = x_2$, and $z = x_3$.

3. Uniform stress field inside the anisotropic elliptical inhomogeneity

Consider an infinite domain in R^2 that contains a single internal anisotropic elastic inhomogeneity with elastic properties that are different from those of the surrounding anisotropic matrix, as shown in Figure 1. The elastic constants are $C_{ijkl}^{(1)}$ for the inhomogeneity and $C_{ijkl}^{(2)}$ for the surrounding matrix. The inhomogeneity occupies the elliptical region

$$S_1 : \frac{x^2}{a^2} + \frac{y^2}{b^2} \leq 1,$$

and the matrix domain is given by

$$S_2 : \frac{x^2}{a^2} + \frac{y^2}{b^2} \geq 1.$$

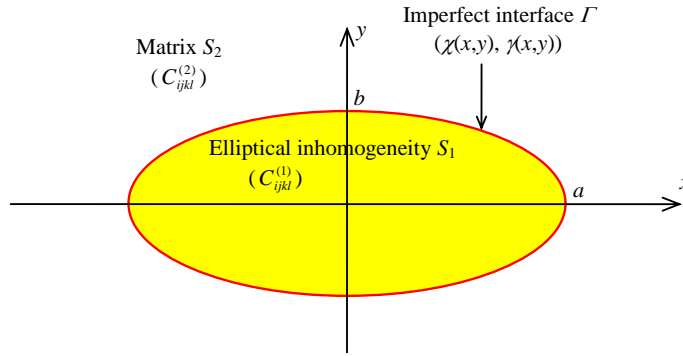


Figure 1. An anisotropic elliptical inhomogeneity imperfectly bonded to an infinite matrix.

The ellipse Γ , whose semimajor and semiminor axes are a and b , respectively, denotes the interface between the inhomogeneity and matrix. In the following discussion, the subscripts or superscripts 1 and 2 refer to the regions S_1 and S_2 , respectively. At infinity, the matrix is subject to remote uniform stresses

$$\mathbf{t}_2^\infty = [\sigma_{12}^\infty \ \sigma_{22}^\infty \ \sigma_{32}^\infty]^T,$$

and remote uniform strains

$$\mathbf{e}_1^\infty = [\varepsilon_{11}^\infty \ \varepsilon_{12}^\infty \ 2\varepsilon_{31}^\infty]^T.$$

Without losing generality, the rigid body rotation at infinity is assumed to be zero. The inhomogeneity is imperfectly bonded to the matrix. The boundary conditions on the imperfect interface Γ are given by

$$\begin{aligned} \sigma_{rr}^{(1)} &= \sigma_{rr}^{(2)} = \chi(x, y)(u_r^{(2)} - u_r^{(1)}), \\ \sigma_{r\theta}^{(1)} &= \sigma_{r\theta}^{(2)} = \chi(x, y)(u_\theta^{(2)} - u_\theta^{(1)}), \\ \sigma_{r3}^{(1)} &= \sigma_{r3}^{(2)} = \gamma(x, y)(u_3^{(2)} - u_3^{(1)}), \end{aligned} \tag{14}$$

where $\chi(x, y)$ and $\gamma(x, y)$ are nonnegative imperfect interface functions whose values depend on the coordinates x and y of Γ ; $\sigma_{rr}^{(k)}$, $\sigma_{r\theta}^{(k)}$, and $\sigma_{r3}^{(k)}$ ($k = 1, 2$) denote the traction components along the normal, in-plane tangential, and antiplane directions of the interface, respectively; and $u_r^{(k)}$, $u_\theta^{(k)}$, and $u_3^{(k)}$ ($k = 1, 2$) denote the displacement components along the normal, in-plane tangential, and antiplane directions of the interface, respectively. Equation (14) demonstrates that the same degree of imperfection is realized in both the normal and in-plane tangential directions. A perfectly bonded interface is achieved for $\chi \rightarrow \infty$, $\gamma \rightarrow \infty$, while a traction-free surface is achieved for $\chi \rightarrow 0$, $\gamma \rightarrow 0$. Note that a jump in the normal displacement may give rise to interpenetration of the inhomogeneity and the matrix in some regions of the interface. This issue will not be discussed here.

Combining (13) and (14), we can equivalently write the boundary conditions on Γ as

$$\Phi_1 = \Phi_2, \quad -\frac{d\Phi_1}{ds} = \mathbf{t} = \mathbf{\Omega}(x, y)(\mathbf{u}_2 - \mathbf{u}_1), \tag{15}$$

where the increasing s is in the counterclockwise direction of the interface, and

$$\mathbf{\Omega}(x, y) = \begin{bmatrix} \chi(x, y) & 0 & 0 \\ 0 & \chi(x, y) & 0 \\ 0 & 0 & \gamma(x, y) \end{bmatrix}. \tag{16}$$

In order to address the boundary value problem, we first consider the mapping functions

$$z_\alpha = x + p_\alpha y = m_\alpha(\zeta_\alpha) = \frac{1}{2}(a - ip_\alpha b)\zeta_\alpha + \frac{1}{2}(a + ip_\alpha b)\zeta_\alpha^{-1} \quad (\alpha = 1, 2, 3), \tag{17}$$

which map the elliptical region with a cut in the z_α -plane onto the annulus

$$\sqrt{\left| \frac{a + ip_\alpha b}{a - ip_\alpha b} \right|} \leq |\zeta_\alpha| \leq 1,$$

in the ζ_α -plane. p_α ($\alpha = 1, 2, 3$) are the three Stroh eigenvalues pertaining to the inhomogeneity.

Second, we consider the mapping functions

$$z_\alpha^* = x + p_\alpha^* y = m_\alpha^*(\zeta_\alpha^*) = \frac{1}{2}(a - ip_\alpha^* b)\zeta_\alpha^* + \frac{1}{2}(a + ip_\alpha^* b)\zeta_\alpha^{*-1} \quad (\alpha = 1, 2, 3), \tag{18}$$

which map the outside of an elliptical region in the z_α^* -plane onto the outside of unit circle, $|\zeta_\alpha^*| \geq 1$, in the ζ_α^* -plane. p_α^* , ($\alpha = 1, 2, 3$) are the three Stroh eigenvalues pertaining to the matrix.

Third, we consider the mapping function [Muskhelishvili 1953]

$$z = x + iy = m(\zeta) = \frac{1}{2}(a + b)\zeta + \frac{1}{2}(a - b)\zeta^{-1}, \tag{19}$$

which maps the region $S_2 : \frac{x^2}{a^2} + \frac{y^2}{b^2} \geq 1$ onto $|\zeta| \geq 1$ in the ζ -plane.

Given that $\zeta_1 = \zeta_2 = \zeta_3 = \zeta_1^* = \zeta_2^* = \zeta_3^* = \zeta$ on Γ , we can replace ζ_α and ζ_α^* by ζ . The variable ζ can be easily substituted with ζ_α or ζ_α^* at the end of the analysis.

Extending the developments outlined in [Antipov and Schiavone 2003] and [Wang et al. 2008], the two interface functions $\chi(x, y)$ and $\gamma(x, y)$ are chosen to be

$$\chi(x, y) = \frac{1}{\lambda_1 |m'(\zeta)|}, \quad \gamma(x, y) = \frac{1}{\lambda_2 |m'(\zeta)|} \quad (|\zeta| = 1), \tag{20}$$

where λ_1 and λ_2 are two nonnegative constants, and $|m'(\zeta)|$ is explicitly given by

$$|m'(\zeta)| = \frac{1}{2}|(a + b) - (a - b)\zeta^{-2}| = b\sqrt{1 + b^* \sin^2 \theta}, \quad \zeta = e^{i\theta} \text{ on } \Gamma, \tag{21}$$

with $b^* = (a^2 - b^2)/b^2$.

In this case, $\mathbf{\Omega}(x, y)$ in (16) can also be expressed as

$$\mathbf{\Omega}(x, y) = \frac{\mathbf{\Lambda}^{-1}}{|m'(\zeta)|}, \quad \text{where } \mathbf{\Lambda} = \text{diag}[\lambda_1 \ \lambda_1 \ \lambda_2]. \tag{22}$$

The boundary conditions in (15) on the imperfect interface can also be expressed in terms of the analytic function vectors $\mathbf{f}_1(\zeta)$ and $\mathbf{f}_2(\zeta)$, for $|\zeta| = 1$, as

$$\begin{aligned} \mathbf{B}_2 \mathbf{f}_2^-(\zeta) + \bar{\mathbf{B}}_2 \bar{\mathbf{f}}_2^+(1/\zeta) &= \mathbf{B}_1 \mathbf{f}_1^+(\zeta) + \bar{\mathbf{B}}_1 \bar{\mathbf{f}}_1^-(1/\zeta), \\ \mathbf{A}_2 \mathbf{f}_2^-(\zeta) + \bar{\mathbf{A}}_2 \bar{\mathbf{f}}_2^+(1/\zeta) - \mathbf{A}_1 \mathbf{f}_1^+(\zeta) - \bar{\mathbf{A}}_1 \bar{\mathbf{f}}_1^-(1/\zeta) &= -i\mathbf{\Lambda}(\zeta \mathbf{B}_1 \mathbf{f}_1^+(\zeta) - \zeta^{-1} \bar{\mathbf{B}}_1 \bar{\mathbf{f}}_1^-(1/\zeta)). \end{aligned} \tag{23}$$

To ensure that the stress field inside the elliptical inhomogeneity is uniform, assume that

$$f_1(\zeta) = \frac{1}{2} \langle (a - ip_\alpha b)\zeta + (a + ip_\alpha b)\zeta^{-1} \rangle \mathbf{k}, \tag{24}$$

where \mathbf{k} is a 3×1 vector to be determined.

Substituting (24) into (23), we obtain, for $|\zeta| = 1$,

$$\begin{aligned} \mathbf{B}_2 f_2^-(\zeta) + \bar{\mathbf{B}}_2 \bar{f}_2^+(1/\zeta) &= \frac{1}{2} \zeta (\mathbf{B}_1 \langle a - ip_\alpha b \rangle \mathbf{k} + \bar{\mathbf{B}}_1 \langle a - i\bar{p}_\alpha b \rangle \bar{\mathbf{k}}) \\ &\quad + \frac{1}{2} \zeta^{-1} (\mathbf{B}_1 \langle a + ip_\alpha b \rangle \mathbf{k} + \bar{\mathbf{B}}_1 \langle a + i\bar{p}_\alpha b \rangle \bar{\mathbf{k}}), \\ \mathbf{A}_2 f_2^-(\zeta) + \bar{\mathbf{A}}_2 \bar{f}_2^+(1/\zeta) &= \frac{1}{2} \zeta ((\mathbf{A}_1 - i\Lambda \mathbf{B}_1) \langle a - ip_\alpha b \rangle \mathbf{k} + (\bar{\mathbf{A}}_1 - i\Lambda \bar{\mathbf{B}}_1) \langle a - i\bar{p}_\alpha b \rangle \bar{\mathbf{k}}) \\ &\quad + \frac{1}{2} \zeta^{-1} ((\mathbf{A}_1 + i\Lambda \mathbf{B}_1) \langle a + ip_\alpha b \rangle \mathbf{k} + (\bar{\mathbf{A}}_1 + i\Lambda \bar{\mathbf{B}}_1) \langle a + i\bar{p}_\alpha b \rangle \bar{\mathbf{k}}). \end{aligned} \tag{25}$$

Given that $f_2(\zeta) \cong \frac{1}{2} \zeta \langle a - ip_\alpha^* b \rangle (\mathbf{B}_2^T \mathbf{e}_1^\infty + \mathbf{A}_2^T \mathbf{t}_2^\infty)$ as $\zeta \rightarrow \infty$, it follows from (25)₁ that, for $|\zeta| \geq 1$,

$$\begin{aligned} f_2(\zeta) &= \frac{1}{2} \zeta^{-1} (\mathbf{B}_2^{-1} \mathbf{B}_1 \langle a + ip_\alpha b \rangle \mathbf{k} + \mathbf{B}_2^{-1} \bar{\mathbf{B}}_1 \langle a + i\bar{p}_\alpha b \rangle \bar{\mathbf{k}} \\ &\quad - \mathbf{B}_2^{-1} \bar{\mathbf{B}}_2 \langle a + i\bar{p}_\alpha^* b \rangle (\bar{\mathbf{B}}_2^T \mathbf{e}_1^\infty + \bar{\mathbf{A}}_2^T \mathbf{t}_2^\infty)) + \frac{1}{2} \zeta \langle a - ip_\alpha^* b \rangle (\mathbf{B}_2^T \mathbf{e}_1^\infty + \mathbf{A}_2^T \mathbf{t}_2^\infty), \end{aligned} \tag{26}$$

Similarly, it follows from (25)₂ that, for $|\zeta| \geq 1$,

$$\begin{aligned} f_2(\zeta) &= \frac{1}{2} \zeta^{-1} (\mathbf{A}_2^{-1} (\mathbf{A}_1 + i\Lambda \mathbf{B}_1) \langle a + ip_\alpha b \rangle \mathbf{k} + \mathbf{A}_2^{-1} (\bar{\mathbf{A}}_1 + i\Lambda \bar{\mathbf{B}}_1) \langle a + i\bar{p}_\alpha b \rangle \bar{\mathbf{k}} \\ &\quad - \mathbf{A}_2^{-1} \bar{\mathbf{A}}_2 \langle a + i\bar{p}_\alpha^* b \rangle (\bar{\mathbf{B}}_2^T \mathbf{e}_1^\infty + \bar{\mathbf{A}}_2^T \mathbf{t}_2^\infty)) + \frac{1}{2} \zeta \langle a - ip_\alpha^* b \rangle (\mathbf{B}_2^T \mathbf{e}_1^\infty + \mathbf{A}_2^T \mathbf{t}_2^\infty). \end{aligned} \tag{27}$$

The obtained expressions for $f_2(\zeta)$ must be compatible with each other (or must be equal), and the following set of linear algebraic equations can be obtained

$$\begin{aligned} (\mathbf{B}_1 \langle a + ip_\alpha b \rangle - \mathbf{B}_2 \mathbf{A}_2^{-1} (\mathbf{A}_1 + i\Lambda \mathbf{B}_1) \langle a + ip_\alpha b \rangle) \mathbf{k} + (\bar{\mathbf{B}}_1 \langle a + i\bar{p}_\alpha b \rangle - \mathbf{B}_2 \mathbf{A}_2^{-1} (\bar{\mathbf{A}}_1 + i\Lambda \bar{\mathbf{B}}_1) \langle a + i\bar{p}_\alpha b \rangle) \bar{\mathbf{k}} \\ = (\bar{\mathbf{B}}_2 - \mathbf{B}_2 \mathbf{A}_2^{-1} \bar{\mathbf{A}}_2) \langle a + i\bar{p}_\alpha^* b \rangle (\bar{\mathbf{B}}_2^T \mathbf{e}_1^\infty + \bar{\mathbf{A}}_2^T \mathbf{t}_2^\infty). \end{aligned} \tag{28}$$

Consequently, the unknown vector \mathbf{k} can be uniquely determined,

$$\mathbf{k} = \mathbf{B}_1^{-1} (\mathbf{E}_2^{-1} \mathbf{E}_1 - \bar{\mathbf{E}}_1^{-1} \bar{\mathbf{E}}_2)^{-1} (\mathbf{E}_2^{-1} \mathbf{g} - \bar{\mathbf{E}}_1^{-1} \bar{\mathbf{g}}), \tag{29}$$

where the 3×3 matrices $\mathbf{E}_1, \mathbf{E}_2$, and the 3×1 vector \mathbf{g} are given by

$$\begin{aligned} \mathbf{E}_1 &= a\mathbf{I} - a\mathbf{M}_2(\mathbf{M}_1^{-1} - \Lambda) + b(\mathbf{I} + \mathbf{M}_2\Lambda)(N_3\mathbf{L}_1^{-1} + i(N_1^T - N_3\mathbf{S}_1\mathbf{L}_1^{-1})) \\ &\quad + b\mathbf{M}_2((N_2 - N_1\mathbf{S}_1\mathbf{L}_1^{-1}) - iN_1\mathbf{L}_1^{-1}), \\ \mathbf{E}_2 &= a\mathbf{I} + a\mathbf{M}_2(\bar{\mathbf{M}}_1^{-1} + \Lambda) - b(\mathbf{I} + \mathbf{M}_2\Lambda)(N_3\mathbf{L}_1^{-1} + i(N_3\mathbf{S}_1\mathbf{L}_1^{-1} - N_1^T)) \\ &\quad + b\mathbf{M}_2((N_2 - N_1\mathbf{S}_1\mathbf{L}_1^{-1}) + iN_1\mathbf{L}_1^{-1}), \\ \mathbf{g} &= (\mathbf{H}_2^{-1}(bN_1^*\mathbf{S}_2 + a\mathbf{S}_2) + i\mathbf{H}_2^{-1}(bN_1^*\mathbf{S}_2 - bN_2^*\mathbf{L}_2 - a\mathbf{I}))\mathbf{e}_1^\infty \\ &\quad + ((a\mathbf{I} + b\mathbf{H}_2^{-1}N_2^*) + ib\mathbf{H}_2^{-1}(N_1^*\mathbf{H}_2 + N_2^*\mathbf{S}_2^T))\mathbf{t}_2^\infty, \end{aligned} \tag{30}$$

with

$$\mathbf{M}_k = -i\mathbf{B}_k\mathbf{A}_k^{-1} = \mathbf{H}_k^{-1}(\mathbf{I} + i\mathbf{S}_k) = \mathbf{L}_k(\mathbf{I} - i\mathbf{S}_k)^{-1} \quad (k = 1, 2). \tag{31}$$

In (30), N_1, N_2, N_3 are the real matrices defined in (9) for the inhomogeneity, and N_1^*, N_2^*, N_3^* are those for the surrounding matrix. Note that in the course of this derivation, we have utilized the identities (11) and (12).

The uniform stress field within the elliptical inhomogeneity can now be given by

$$\begin{bmatrix} \sigma_{12} \\ \sigma_{22} \\ \sigma_{32} \end{bmatrix} = 2 \operatorname{Re}\{\mathbf{B}_1\mathbf{k}\} = 2 \operatorname{Re}\{(\mathbf{E}_2^{-1}\mathbf{E}_1 - \bar{\mathbf{E}}_1^{-1}\bar{\mathbf{E}}_2)^{-1}(\mathbf{E}_2^{-1}\mathbf{g} - \bar{\mathbf{E}}_1^{-1}\bar{\mathbf{g}})\}, \tag{32}$$

$$\begin{bmatrix} \sigma_{11} \\ \sigma_{21} \\ \sigma_{31} \end{bmatrix} = -2 \operatorname{Re}\{\mathbf{B}_1\langle p_\alpha \rangle\mathbf{k}\} \\ = 2 \operatorname{Re}\{(\mathbf{N}_3\mathbf{S}_1\mathbf{L}_1^{-1} - \mathbf{N}_1^T + i\mathbf{N}_3\mathbf{L}_1^{-1})(\mathbf{E}_2^{-1}\mathbf{E}_1 - \bar{\mathbf{E}}_1^{-1}\bar{\mathbf{E}}_2)^{-1}(\mathbf{E}_2^{-1}\mathbf{g} - \bar{\mathbf{E}}_1^{-1}\bar{\mathbf{g}})\}. \tag{33}$$

We note that $\mathbf{E}_1, \mathbf{E}_2, \mathbf{g}$, defined in (30), are expressed in terms of the real Barnett–Lothe tensors $\mathbf{H}_k, \mathbf{L}_k, \mathbf{S}_k$ ($k = 1, 2$), whose explicit expressions are given in [Dongye and Ting 1989; Ting 1997], and (ii) the three 3×3 real matrices N_i ($i = 1, 2, 3$) for the inhomogeneity, and the three 3×3 real matrices N_i^* ($i = 1, 2, 3$) for the matrix. In other words, the expressions of $\mathbf{E}_1, \mathbf{E}_2, \mathbf{g}$ do not contain the Stroh eigenvalues or eigenvectors, thus the expressions of stresses (and also strains and rigid-body rotation) within the elliptical inhomogeneity are also valid for (mathematically) degenerate materials, such as an isotropic material. Note from (29) that the internal stress field depends on the imperfection of the interface characterized by the two nonnegative interface constants λ_1 and λ_2 . Finally, the full field expression of $f_2(\zeta)$ can be easily obtained,

$$f_2(\zeta) = \frac{1}{2}\langle \zeta_\alpha^{*-1} \rangle (\mathbf{B}_2^{-1}\mathbf{B}_1\langle a + ip_\alpha b \rangle\mathbf{k} + \mathbf{B}_2^{-1}\bar{\mathbf{B}}_1\langle a + i\bar{p}_\alpha b \rangle\bar{\mathbf{k}} - \mathbf{B}_2^{-1}\bar{\mathbf{B}}_2\langle a + i\bar{p}_\alpha^* b \rangle(\bar{\mathbf{B}}_2^T\mathbf{e}_1^\infty + \bar{\mathbf{A}}_2^T\mathbf{t}_2^\infty)) \\ + \frac{1}{2}\langle \zeta_\alpha^* \rangle \langle a - ip_\alpha^* b \rangle (\mathbf{B}_2^T\mathbf{e}_1^\infty + \mathbf{A}_2^T\mathbf{t}_2^\infty), \tag{34}$$

for $|\zeta_\alpha^*| \geq 1$, which clearly indicates that the remote uniform stresses and strains are disturbed by the imperfectly bonded elliptical inhomogeneity.

4. Conclusions

In this investigation, we found that a uniform stress field exists inside an anisotropic elliptical inhomogeneity imperfectly bonded to an infinite matrix provided that: (i) the same degree of imperfection on the interface is realized in both the normal and the in-plane tangential directions; and (ii) the interface functions satisfy equation (20). Condition (i) has been adopted in previous studies of isotropic materials [Wang et al. 2005; Wang et al. 2008], while the circumferential inhomogeneity of the imperfect interface reflects a realistic scenario of inhomogeneous interface damage in which the extent of bonding varies along the interface [Ru and Schiavone 1997]. The interface functions given by equation (20), which lead to a uniform stress field inside the inhomogeneity, depend only on the shape of the ellipse Γ , that is, the semimajor and semiminor axes a and b are independent of the material properties of both inhomogeneity and matrix. For a circular inhomogeneity $a = b$, it follows from (20) and (21) that $\chi(x, y) = 1/(\lambda_1 a)$

and $\gamma(x, y) = 1/(\lambda_2 a)$ are constant. In other words, the stress field inside an anisotropic circular inhomogeneity will be uniform when the interface is homogeneously imperfect and when the same degree of imperfection on the circular interface is realized in both the normal and the in-plane tangential directions. The interpenetration issue due to the introduction of the imperfect interface is not discussed here. Finally, our work poses an interesting question: Can the stress field inside an imperfectly bonded anisotropic ellipsoidal inhomogeneity still remain uniform when the infinite anisotropic matrix is subject to remote uniform stresses?

Acknowledgement

The author is greatly indebted to the referees for their very helpful comments and suggestions.

References

- [Achenbach and Zhu 1989] J. D. Achenbach and H. Zhu, “Effect of interfacial zone on mechanical behavior and failure of fiber-reinforced composites”, *J. Mech. Phys. Solids* **37**:3 (1989), 381–393.
- [Antipov and Schiavone 2003] Y. A. Antipov and P. Schiavone, “On the uniformity of stresses inside an inhomogeneity of arbitrary shape”, *IMA J. Appl. Math.* **68**:3 (2003), 299–311.
- [Dongye and Ting 1989] C. Dongye and T. C. T. Ting, “Explicit expressions of Barnett–Lothe tensors and their associated tensors for orthotropic materials”, *Quart. Appl. Math.* **47** (1989), 723–734.
- [Eshelby 1957] J. D. Eshelby, “The determination of the elastic field of an ellipsoidal inclusion, and related problems”, *Proc. R. Soc. Lond. A* **241**:1226 (1957), 376–396.
- [Eshelby 1959] J. D. Eshelby, “The elastic field outside an ellipsoidal inclusion”, *Proc. R. Soc. Lond. A* **252**:1271 (1959), 561–569.
- [Eshelby 1961] J. D. Eshelby, “Elastic inclusion and inhomogeneities”, pp. 222–246 in *Progress in solid mechanics*, vol. 2, edited by I. N. Sneddon and R. Hill, North-Holland, Amsterdam, 1961.
- [Gao 1995] J. Gao, “A circular inclusion with imperfect interface: Eshelby’s tensor and related problems”, *J. Appl. Mech. (ASME)* **62**:4 (1995), 860–866.
- [Hashin 1991] Z. Hashin, “The spherical inclusion with imperfect interface”, *J. Appl. Mech. (ASME)* **58**:2 (1991), 444–449.
- [Hwu and Ting 1989] C. Hwu and T. C. T. Ting, “Two-dimensional problems of the anisotropic elastic solid with an elliptic inclusion”, *Q. J. Mech. Appl. Math.* **42**:4 (1989), 553–572.
- [Muskhelishvili 1953] N. I. Muskhelishvili, *Some basic problems of the mathematical theory of elasticity*, Noordhoff, Groningen, 1953.
- [Ru and Schiavone 1997] C. Q. Ru and P. Schiavone, “A circular inclusion with circumferentially inhomogeneous interface in antiplane shear”, *Proc. R. Soc. Lond. A* **453**:1967 (1997), 2551–2572.
- [Shen et al. 2001] H. Shen, P. Schiavone, C. Q. Ru, and A. Mioduchowski, “Stress analysis of an elliptic inclusion with imperfect interface in plane elasticity”, *J. Elasticity* **62**:1 (2001), 25–46.
- [Stroh 1958] A. N. Stroh, “Dislocations and cracks in anisotropic elasticity”, *Philos. Mag.* **3**:30 (1958), 625–646.
- [Ting 1996] T. C. T. Ting, *Anisotropic elasticity: theory and applications*, Oxford University Press, New York, 1996.
- [Ting 1997] T. C. T. Ting, “New explicit expression of the Barnett–Lothe tensors for anisotropic linear elastic materials”, *J. Elasticity* **47**:1 (1997), 23–50.
- [Wang et al. 2005] X. Wang, J. Q. Zhang, and X. M. Guo, “Two circular inclusions with inhomogeneously imperfect interfaces in plane elasticity”, *Int. J. Solids Struct.* **42**:9–10 (2005), 2601–2623.
- [Wang et al. 2008] X. Wang, E. Pan, and L. J. Sudak, “Uniform stresses inside an elliptical inhomogeneity with an imperfect interface in plane elasticity”, *J. Appl. Mech. (ASME)* **75**:5 (2008), 054501.

Received 10 Oct 2008. Accepted 11 May 2009.

XU WANG: xuwang@uakron.edu

Center for Composite Materials, 202 Composites Manufacturing Science Laboratory, University of Delaware, Newark DE, 19716, United States

MODELING DISLOCATION SOURCES AND SIZE EFFECTS AT INITIAL YIELD IN CONTINUUM PLASTICITY

SAURABH PURI, ANISH ROY, AMIT ACHARYA AND DENNIS DIMIDUK

Size effects at initial yield (prior to stage II) of idealized micron-sized specimens are modeled within a continuum model of plasticity. Two different aspects are considered: specification of a density of dislocation sources that represent the emission of dislocation dipoles, and the presence of an initial, spatially inhomogeneous excess dislocation content. Discreteness of the source distribution appears to lead to a stochastic response in stress-strain curves, with the stochasticity diminishing as the number of sources increases. Variability in stress-strain response due to variations of source distribution is also shown. These size effects at initial yield are inferred to be due to physical length scales in dislocation mobility and the discrete description of sources that induce internal-stress-related effects, and not due to length-scale effects in the mean-field strain-hardening response (as represented through a constitutive equation).

1. Introduction

There is a considerable body of experimental evidence that demonstrates that plastic deformation in FCC and other crystalline solids is size dependent at length scales of the order of tens of microns and smaller [Fleck et al. 1994; Ma and Clarke 1995; Stölken and Evans 1998]. Research has suggested that this behavior can be either an effect of constraint imposed on dislocation motion from grain boundaries or internal interfaces or an effect of excess dislocation density resulting from similar externally imposed constraints. However, recently, experiments performed on unconstrained single crystals demonstrated strong size effects at initial yield (including a hardening phenomenon at small strains) as well [Uchic et al. 2004; Dimiduk et al. 2005; Greer et al. 2005; Frick et al. 2008]. This observed phenomenon was modeled within a two-dimensional discrete dislocation (DD) framework [Benzerga et al. 2005; Deshpande et al. 2005; Balint et al. 2006; Benzerga and Shaver 2006] and, more recently using three-dimensional DD techniques [Rao et al. 2008; Tang et al. 2008]. While those studies showed via selected DD frameworks that size effects may arise from aspects of dislocation source properties and source availability, they did not consider that related size effects may arise simply from the dislocation source attributes and heterogeneous spatial arrangement coupling to the boundary constraints when considered completely within a continuum theory for the flow kinematics.

In this paper we examine the question of how dislocation sources may be modeled in continuum plasticity and if the nature of sources contributes to size effects within a continuum representation of idealized simulation cells. We find the answer to be affirmative and use the strategy to demonstrate size effects at initial yield within the context of a recently proposed continuum theory; namely, phenomenological mesoscopic field dislocation mechanics (PMFDM) [Acharya and Roy 2006]. Results obtained from a

Keywords: continuum plasticity, dislocations, finite elements.

finite-element implementation of the theory reasonably accounted for plasticity at mesoscopic scales. Physical length scales exist in the theory and size-affected strain hardening has been demonstrated successfully [Roy and Acharya 2006]. In this paper we specifically discuss size effects at initial yield based on two continuum-level mechanisms. First, size effects are demonstrated in idealized simulation cells having a predefined pattern of statistical dislocation (SD) sources. For the second mechanism, simulations are performed on cells having an initial, spatially inhomogeneous excess dislocation (ED) distribution. Note that the present study is not intended to provide a direct quantitative rationalization of the widely reported experimental findings. Any such attempt would require more advanced quantitative treatments of selected constitutive assumptions, as well as further advances to the computation framework.

In Section 2, a brief description of the governing equations of PMFDM is presented. Section 3 involves discussion of modeling strategy and results so obtained. The paper ends with some concluding remarks in Section 4.

A note regarding terminology: henceforth, given a scale of resolution, l , we refer to the spatial average of Nye's dislocation-density tensor [Nye 1953] over a volume l^3 around a point as the excess dislocation (ED) density tensor at that point. Nye's tensor being a tensorial quantity, the dislocations that on average make no contribution to the net density of Burgers vectors in this process, due to cancellation in sign, form a density that we refer to as the statistically distributed dislocation (SD) density. Thus, the difference of local value of Nye's tensor field and its spatial average (ED) is referred to as SD.

2. Theory

The phenomenological mesoscopic field dislocation mechanics (PMFDM) theory [Acharya and Roy 2006] results from an elementary space-time averaging of the equations of field dislocation mechanics [Acharya 2001; 2003; 2004]. It admits constitutive hypotheses on elasticity, the mean (that is, the space-time average) of signed velocity of dislocation segments (that may be associated with the velocity of mean ED), and the mean slip rate produced by SD. The phenomenology introduced in the model beyond conventional plasticity is meager, with the qualitative predictions of the model not depending upon the phenomenological assumptions. The essential equations of PMFDM are summarized below¹.

The (symmetric) stress tensor \mathbf{T} satisfies

$$\mathbf{T} = \mathbf{C} : \mathbf{U}^e, \quad \text{div } \mathbf{T} = \mathbf{0}, \quad (1)$$

along with standard traction/displacement boundary conditions. \mathbf{C} is the possibly anisotropic fourth order tensor of linear elastic moduli and \mathbf{U}^e is the elastic distortion tensor defined as

$$\mathbf{U}^e = \text{grad } \mathbf{u} - \mathbf{U}^p. \quad (2)$$

In this equation, \mathbf{u} is the total displacement field and \mathbf{U}^p is the plastic distortion tensor which is decomposed uniquely into compatible and incompatible parts as

$$\mathbf{U}^p = \text{grad } \mathbf{z} - \boldsymbol{\chi}. \quad (3)$$

¹For motivation behind the formulation the reader is referred to the work of Acharya and Roy [2006].

Thus, the elastic distortion tensor may be rewritten as,

$$\mathbf{U}^e = \text{grad}(\mathbf{u} - \mathbf{z}) + \chi, \quad (4)$$

where the field χ cannot be written as a nontrivial gradient. The incompatible part, χ , is given by

$$\text{curl } \chi = \boldsymbol{\alpha}, \quad \text{div } \chi = \mathbf{0}, \quad \chi \mathbf{n} = \mathbf{0} \text{ on } \partial B, \quad (5)$$

where $\boldsymbol{\alpha}$ is the space-time averaged excess dislocation density tensor field and \mathbf{n} is the unit normal on the boundary ∂B of the body. The vector field \mathbf{z} whose gradient represents the compatible part of \mathbf{U}^p obeys the relation

$$\text{div}(\text{grad } \dot{\mathbf{z}}) = \text{div}(\boldsymbol{\alpha} \times \mathbf{V} + \mathbf{L}^p), \quad (\text{grad } \dot{\mathbf{z}})\mathbf{n} = (\boldsymbol{\alpha} \times \mathbf{V} + \mathbf{L}^p)\mathbf{n} \text{ on } \partial B, \quad (6)$$

where \mathbf{V} and \mathbf{L}^p need to be specified constitutively. \mathbf{V} represents the velocity of the ED and \mathbf{L}^p represents that part of the total slip strain rate which is not represented by the slipping produced by the averaged signed dislocation density (ED). The value of $\dot{\mathbf{z}}$ is prescribed at an arbitrarily chosen point of the body and in our case is assumed to vanish without loss of generality. Finally the temporal evolution of the ED density tensor field is prescribed as

$$\dot{\boldsymbol{\alpha}} = -\text{curl } \mathbf{S}, \quad (7)$$

where \mathbf{S} is the averaged slipping distortion (slip rate) defined as

$$\mathbf{S} := \boldsymbol{\alpha} \times \mathbf{V} + \mathbf{L}^p. \quad (8)$$

2.1. Boundary condition on surface flow. Equation (7) admits boundary conditions on the dislocation flow [Acharya and Roy 2006]. In general, a natural boundary condition of the form $\mathbf{S} \times \mathbf{n} = \boldsymbol{\Phi}$, where $\boldsymbol{\Phi}$ is a (second-order tensor valued) specified function of time and position along the boundary satisfying the constraint $\boldsymbol{\Phi} \mathbf{n} = \mathbf{0}$, is appropriate to model controlled flow at the boundary. A rigid boundary with respect to slipping may be represented with a zero flow boundary condition $\mathbf{S} \times \mathbf{n} = \mathbf{0}$ on the entire boundary. Imposing such a boundary condition can lead to the development of shocks or discontinuities. A less restrictive boundary condition is the imposition of the dislocation flux, $\boldsymbol{\alpha}(\mathbf{V} \cdot \mathbf{n})$, on inflow points of the boundary (where $\mathbf{V} \cdot \mathbf{n} < 0$), along with a specification of $\mathbf{L}^p \times \mathbf{n}$ on the entire boundary. This condition allows free exit of dislocations without any added specification.

2.2. Constitutive specification. Constitutive specifications for the dislocation-velocity vector, \mathbf{V} , and the slip-distortion rate due to SDs, \mathbf{L}^p , are required. Simple choices motivated by conventional plasticity and the thermodynamics of PMFDM (ibid.) are

$$\mathbf{L}^p = \dot{\gamma} \frac{\mathbf{T}'}{|\mathbf{T}'|}, \quad \dot{\gamma} \geq 0, \quad \mathbf{V} = v \frac{\mathbf{d}}{|\mathbf{d}|}, \quad v \geq 0, \quad (9)$$

where \mathbf{T}' is the stress deviator, $\dot{\gamma}$ and v are nonnegative functions of state representing the magnitudes of the SD slipping rate and the averaged ED velocity, respectively. The direction of the dislocation velocity is defined by

$$\begin{aligned} \mathbf{d} &:= \mathbf{b} - \left(\mathbf{b} \cdot \frac{\mathbf{a}}{|\mathbf{a}|} \right) \frac{\mathbf{a}}{|\mathbf{a}|}, & \mathbf{b} &:= \mathbf{X}(\mathbf{T}'\boldsymbol{\alpha}), & b_i &= e_{ijk} T'_{jr} \alpha_{rk}, \\ \mathbf{a} &:= \mathbf{X}(\text{tr}(\mathbf{T})\boldsymbol{\alpha}), & a_i &= \left(\frac{1}{3} T_{mm} \right) e_{ijk} \alpha_{jk}. \end{aligned} \quad (10)$$

Thermodynamics indicates \mathbf{b} as the driving force for \mathbf{V} ; the definition of \mathbf{d} is to ensure pressure independence of plastic straining in the model. We choose a power law relation for $\dot{\gamma}$ as

$$\dot{\gamma} = \dot{\gamma}_0 \left(\frac{|\mathbf{T}'|}{\sqrt{2g}} \right)^{1/m}, \quad (11)$$

where m is the rate sensitivity of the material, g is the strength of the material, and $\dot{\gamma}_0$ is a reference strain rate. The expression for v is assumed to be

$$v(\text{state}) = \eta^2 b \left(\frac{\mu}{g} \right)^2 \dot{\gamma}(\mathbf{T}', g), \quad (12)$$

where μ is the shear modulus, b the Burgers vector magnitude and $\eta = 1/3$ a material parameter.

The strength of the material is assumed to evolve according to

$$\dot{g} = \left[\frac{\eta^2 \mu^2 b}{2(g - g_0)} k_0 |\boldsymbol{\alpha}| + \theta_0 \left(\frac{g_s - g}{g_s - g_0} \right) \right] \{ |\boldsymbol{\alpha} \times \mathbf{V}| + \dot{\gamma} \}, \quad (13)$$

where g_s is the saturation stress, g_0 is the yield stress, and θ_0 is the stage II hardening rate. The material parameters g_s , g_0 , μ , b , $\dot{\gamma}_0$, and m are known from conventional plasticity (Voce law and power-law hardening). Consequently, k_0 is the only extra parameter that needs to be fitted and can be obtained from experimental grain-size dependence of flow stress results, as shown in [Acharya and Beaudoin 2000; Beaudoin et al. 2000].

The finite-element discretization for the system of equations above is discussed in [Roy and Acharya 2006]. Here we only summarize the finite-element discretization of (7), which has an extra term in the weak formulation corresponding to the least-squares finite-element discretization of the inflow boundary condition on $\boldsymbol{\alpha}$ [Varadhan et al. 2006].

In the following expression, the symbol $\delta(\cdot)$ represents a variation (or test function) associated with the field (\cdot) in a suitable class of functions. An increment of time $[t, t + \Delta t]$ is considered, and fields without any superscripts refer to values at $t + \Delta t$ and those with the superscript t refer to values at time t . All spatial fields are discretized by first-order, 8-node (three-dimensional), isoparametric brick elements. A mixed forward-backward Euler scheme is adopted as

$$\begin{aligned} & \int_B \delta \alpha_{ij} (\alpha_{ij} - \alpha_{ij}^t) dv - \Delta t \int_B [\delta \alpha_{ij,k} \alpha_{ij} v_k^t - \delta \alpha_{ij,k} \alpha_{ik} v_j^t] dv - \Delta t \int_B \delta \alpha_{ij} s_{ij}^t dv + \Delta t \int_{\partial B_i} \delta \alpha_{ij} F_{ij} da \\ & + \Delta t \int_{\partial B_o} \delta \alpha_{ij} \alpha_{ij}^t (v_k^t n_k) da - \Delta t \int_{\partial B} \delta \alpha_{ij} \alpha_{ik}^t n_k v_j^t da - \Delta t \int_B \delta \alpha_{ij,k} e_{jkl} L_{il}^p dv \\ & + \Delta t \int_{\partial B} \delta \alpha_{ij} e_{jkl} L_{il}^p n_k da + \int_{B_{\text{interiors}}} A_{ri} (\delta \alpha_{ri} + \Delta t [\delta \alpha_{ri,j} v_j^t + \delta \alpha_{ri} v_{j,j}^t - \delta \alpha_{rj,j} v_i^t - \delta \alpha_{rj} v_{i,j}^t]) dv \\ & + \Delta t \int_{\partial B_i} \delta \alpha_{ij} (F_{ij} - \alpha_{ij}^t (v_k^t n_k)) da = 0, \quad (14) \end{aligned}$$

where

$$A_{ri} = \alpha_{ri} - \alpha_{ri}^t + \Delta t [\alpha_{ri,j}^t v_j^t + \alpha_{ri}^t v_{j,j}^t - \alpha_{rj,j}^t v_i^t - \alpha_{rj}^t v_{i,j}^t - s_{ri}^t + e_{ijk} L_{rk,j}^p]. \quad (15)$$

\mathbf{F} is the prescribed flux on the inflow boundary (∂B_i), ∂B_o is the set of outflow/neutral points of the boundary where $\mathbf{V} \cdot \mathbf{n} \geq 0$, and $B_{\text{interiors}}$ refers to the union of the element interiors. $\delta \alpha_{ij}$ is arbitrary up to

satisfying any prescribed essential boundary conditions. The term on the last line of (14) is an additional term that enters the discretization for excess dislocation density evolution for all the computations in this paper over those described in [Roy and Acharya 2006]. The scheme is consistent even without the addition of this term; numerical experiments show a better imposition of inflow boundary conditions with its inclusion.

3. Results and discussion

Unless otherwise mentioned, material parameters used for all the computational experiments are

$$b = 4.05 \times 10^{-4} \mu\text{m}, \quad m = 1.0, \quad g_s = 161 \text{ MPa}, \quad g_0 = 17.3 \text{ MPa}, \quad \theta_0 = 392.5 \text{ MPa}, \quad k_0 = 20.0.$$

The reference strain rate is $\dot{\gamma}_0 = 1 \text{ sec}^{-1}$. Isotropic elastic constants of the representative material, aluminum, are $E = 62.78 \text{ GPa}$, $\nu = 0.3647$, where E is the Young's modulus and ν is the Poisson's ratio.

A comment on the rate sensitivity value is in order. Our intent here is to model a situation where dislocations move in unobstructed, free-flight mode in large parts of the body. Under these circumstances, and with the understanding that rate insensitivity is a manifestation of very fast motions homogenized in time with near stationary events, it is only reasonable to utilize a rate sensitivity parameter value representative of linear drag in our simulations.

The initial conditions corresponding to the field equations mentioned in Section 2 are as follows. For the \mathbf{u} field we assume $\mathbf{u}|_{t=0} \equiv \mathbf{0}$, which is a physically natural initial condition on the displacement field. Unless otherwise mentioned, we assume that the body is initially ED-free which translates to $\boldsymbol{\alpha}|_{t=0} \equiv \mathbf{0}$. The initial condition on the grad z field is obtained from solving (1) and (5) with $\mathbf{u}|_{t=0} \equiv \mathbf{0}$ and the value of z set to zero at a single arbitrary point in the body.

Time-dependent simple-shearing solutions are studied numerically. The imposed boundary conditions corresponding to such a loading are as follows: displacements on the bottom face are constrained in all three directions while those on the top, left and right faces are constrained in the x_2 and x_3 directions only (see Figure 1). The front and back faces are displacement-constrained in the x_3 direction and traction free in the x_1 and x_2 directions. The displacements corresponding to a simple shear strain are prescribed

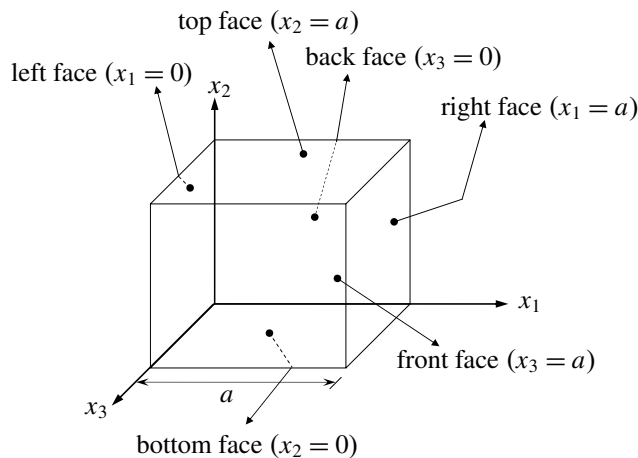


Figure 1. Schematic layout of a typical model geometry.

through the kinematic boundary condition

$$u_1(x_1, x_2, x_3, t) = d(x_2)\dot{\Gamma}t \quad (16)$$

on the nodes of the left, right, top, and bottom faces. Here, $d(x_2)$ is the height, from the bottom of the cube, of the point with coordinates (x_1, x_2, x_3) . Γ is the average engineering shear strain given by the ratio of the applied horizontal displacement of the top surface to the cube height, $\dot{\Gamma}$ is an applied shear strain rate of 1 sec^{-1} , and t is time.

All computations are performed on one of two desktop machines with 2 GB and 8 GB RAM, respectively. In the interpretation of results, the symbol τ refers to the nominal (reaction) shear traction on the top surface of the simulation cell.

3.1. Dislocation source distribution. The effect of physical dimensions of the simulation cell (having a predefined distribution of SD sources) on the initial yield strength is described in this section. First we discuss how a Frank–Read source is grossly represented in our framework. In general, a Frank–Read source produces dislocation loops that cannot be sensed if their size is less than the scale of resolution. However, once the loop expands up to the scale of resolution, it can be sensed as demonstrated in Figure 2a. In order to numerically simulate (SD) dislocation sources in the framework of PMFDM, the size of the region representing a source is assumed to be greater than or equal to the scale of resolution (see Figure 2b). In the interior of the source region there are no EDs due to cancellation in signs during

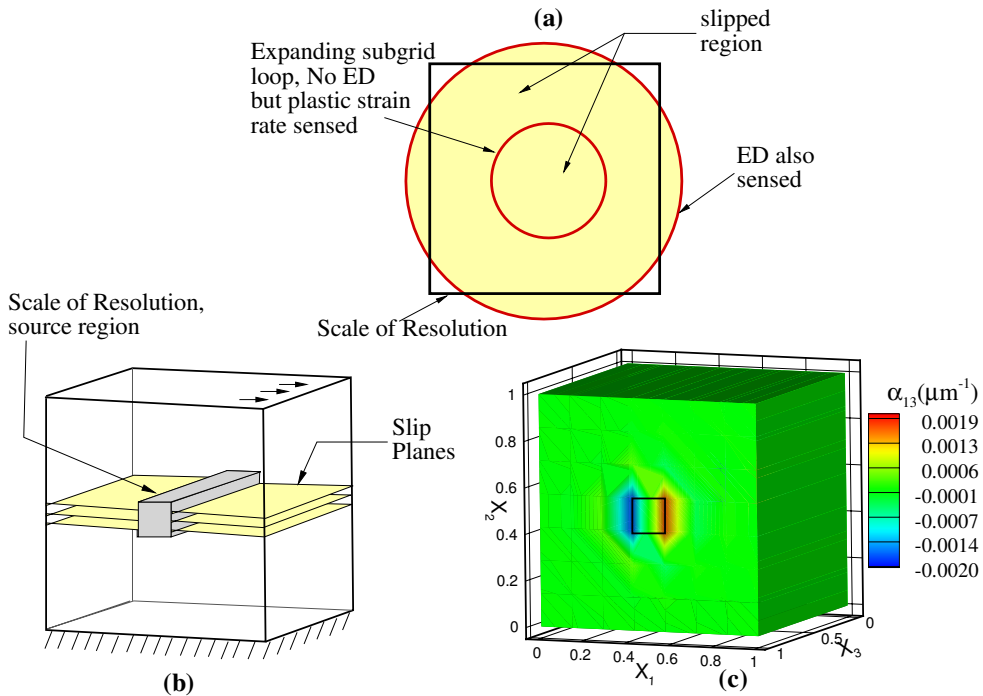


Figure 2. Top: physical representation of a Frank–Read source. Bottom left: representation of a numerically simulated Frank–Read Source. Bottom right: excess dislocation density at $\Gamma = 0.1\%$ for pattern (a).

averaging. This corresponds to the physical situation of the dislocation loop not being sensed when its size is smaller than the scale of resolution. The plastic strain rate corresponding to the motion of these unresolved dislocations, however, is sensed, and is taken into account through L^p . At the interface between the slipped and unslipped regions, EDs are observed due to the gradient in plastic strain rate (7) and (8). This observation corresponds to the physical definition of a dislocation loop being sensed when its size equals or exceeds the scale of resolution. A simple test is performed to demonstrate this idea. Consider a cubical cell of edge length of $1.0 \mu\text{m}$ and discretized into a finite element grid. The element at the center is the dislocation source region, as shown in Figure 2b. The cell is unstressed and ED free initially, with some SD content in the source region. Displacement boundary conditions corresponding to a simple shear strain of 0.1% are imposed. With the onset of plasticity in the source region, excess edge dislocations (α_{13}) of opposite signs generated at the subgrid scale of resolution cancel each other, resulting in zero ED density inside the source region, though a change in the magnitude of L_{12}^p values corresponding to these cancelled dislocations is observed. Since L^p is zero in nonslipped regions, a gradient in L_{12}^p develops at the interfaces of the slipped and nonslipped regions which in turn leads to the generation of α_{13} through (7), as shown in Figure 2c. The α_{13} density generated contributes to flow in the grid elements not containing sources.

Now we discuss size effects at initial yield in cells having a predefined distribution of dislocation sources. Two cubical samples with edge lengths of $0.6 \mu\text{m}$ and $3.0 \mu\text{m}$ are considered. The spatial distribution of dislocation sources is shown in Figure 3. Both cells are discretized into a finite element grid with equal element size and are equal to the size of a dislocation source region, in order to avoid any size effect due to the scale of resolution. Displacement boundary conditions corresponding to an engineering simple shearing strain of 0.3% are imposed on the cells as in (16). First, experiments were performed in the context of conventional plasticity theory. Conventional plasticity may be recovered from PMFDM by setting $\alpha = \mathbf{0}$ for all times and replacing (2) with

$$U^e = \text{grad } \mathbf{u} - U^p, \quad \dot{U}^p = L^p. \tag{17}$$

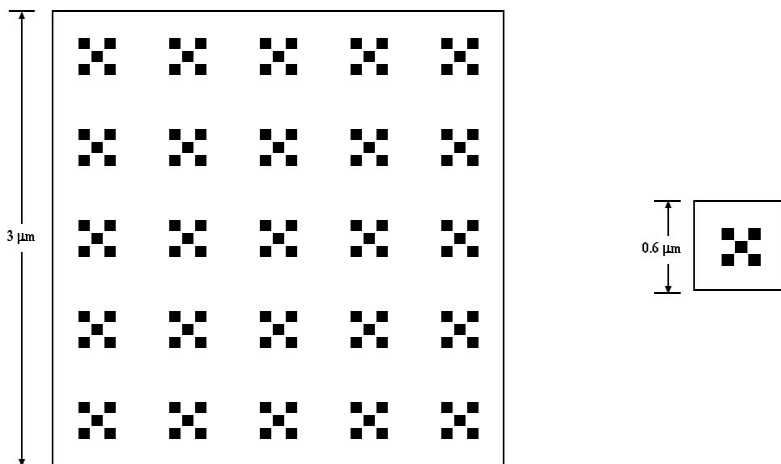


Figure 3. Schematic layout of position of sources (black spots represents the dislocation sources).

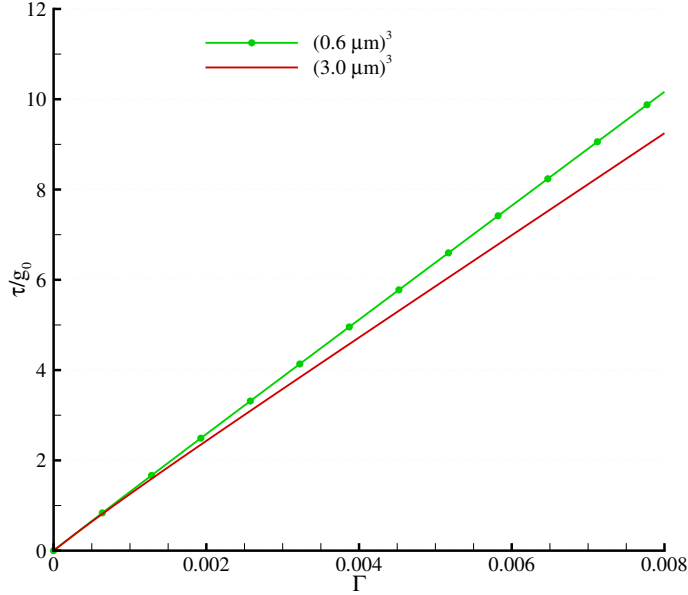


Figure 4. Size effect in simple shear with a predefined spatial distribution of dislocation sources, within a conventional plasticity framework.

Since $\alpha = \mathbf{0}$ in the conventional plasticity framework, nonsource regions are elastic in nature. A size effect is observed for this case as shown in Figure 4, with smaller being harder. It can be inferred from dimensional analysis that in the case of a homogeneous material, there is no length scale in the classical plasticity theory and hence it is not possible to predict size effects in this framework. However, a length scale emerges when a body consisting of discrete dislocation sources is considered. Dimensional analysis of τ yields

$$\tau = \mu \Phi \left(\frac{\theta_0}{\mu}, \frac{g_s}{\mu}, \frac{g_0}{\mu}, \frac{\dot{\Gamma}}{\dot{\gamma}_0}, m, \Gamma, \frac{s}{H} \right), \tag{18}$$

where H denotes the dimension of the body, s is a representative measure of the distance between the sources (strictly speaking, the size of the sources should also enter as another length-scale parameter), and Φ is a dimensionless function of the arguments shown. It can be deduced from the relation above that if s is kept the same and H is changed, a difference in average response is expected. Thus, it is the spatial layout of dislocation sources that introduces a physical length scale in classical plasticity theory which is otherwise absent. However, the magnitude of that size effect on an average response utilizing discrete sources in an otherwise conventional elastoplastic material falls short of what is qualitatively observed in experiment, indicating the existence of other scale effects and the need for better theory. Nonetheless, this same phenomenology of dislocation sources carries in PMFDM, but now with a greater effect because of the generation of ED at all spatial discontinuities of flow (such as source and nonsource grid elements) and its transport, as well as its accurate accounting in stress response via (1)–(5).

The same numerical experiment is now performed with PMFDM. Accordingly, two cubical cells having edge lengths of $0.6 \mu\text{m}$ and $3.0 \mu\text{m}$ and a spatial distribution of dislocation sources as shown in Figure 3, are considered. The area density of sources is identical (0.1) in both cells. The displacement boundary conditions corresponding to a simple shear strain of 0.8% are applied through (16). The

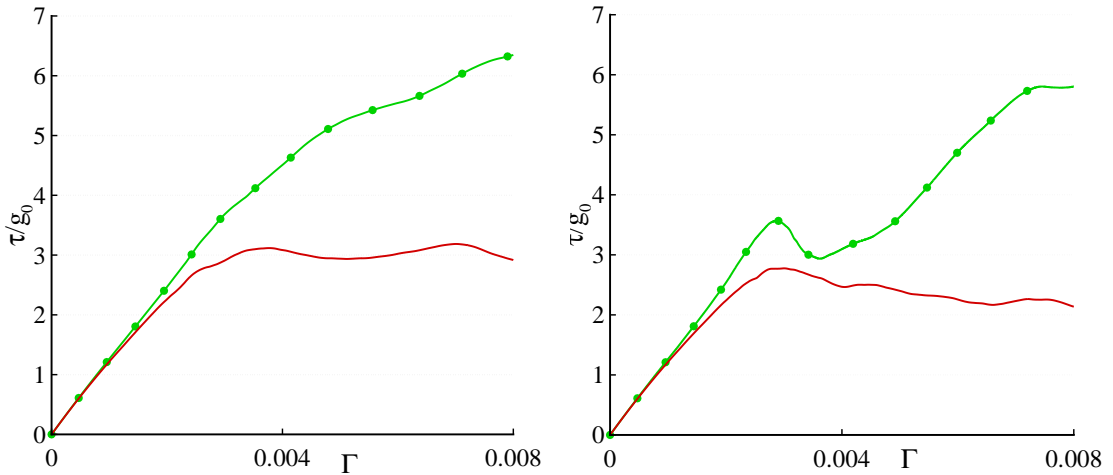


Figure 5. Size effect in simple shear with a predefined source pattern, with hardening rate based on Equation (13) (left) and on Equation (20) (right). The green curves with knots correspond to the $0.6 \mu\text{m}$ cubes, and the smooth brown curves to the $3.0 \mu\text{m}$ cubes.

nonsource regions can behave in a plastic manner when ED content is transported through them; however, there is no SD slip rate in these regions.

The average shear stress-strain response, graphed on the left in Figure 5, shows that initial yield strength strongly depends on the cell size with smaller being harder. The size effect is maintained throughout the process of deformation in qualitative agreement with experimentally observed trends [Dimiduk et al. 2005; Greer et al. 2005]. A significant stress drop corresponding to the dislocation activity developing bursts of plastic strain rate is observed in our results which is absent in the experimental results of [Uchic et al. 2004] but may be present in the results from [Greer et al. 2005]. This is due to the fact that numerical experiments performed here correspond to displacement control (similar to those by Greer et al. [2005]) whereas the experimental results presented in [Uchic et al. 2004; Dimiduk et al. 2005] involved mixed (load and displacement) control. The applied load was not allowed to decrease during the experiments performed by Uchic et al. [2004] and Dimiduk et al. [2005] and thus, stress drops are not observed in those studies. The other serrations observed in the experimental results can be obtained in this setup by incorporating a stochastic constitutive response for the plastic strain rate and the ED velocity. We have intentionally stayed away from doing so to demonstrate size effects with the least constitutive input.

In order to understand the cause of size effects in the current framework, dimensional analysis of the applied, (reaction) nominal stress τ is performed which implies the relation

$$\tau = \mu \Phi \left(\frac{\theta_0}{\mu}, \frac{g_s}{\mu}, \frac{g_0}{\mu}, \frac{\dot{\Gamma}}{\dot{\gamma}_0}, \frac{b}{H}, \alpha_0 H, m, \Gamma, k_0, \eta, \frac{s}{H} \right), \quad (19)$$

where α_0 is a representative measure of the magnitude of the initial ED density field, s is a representative measure of the distance between sources, and Φ is a dimensionless function of the arguments shown. The dimensionless arguments b/H , $\alpha_0 H$, s/H introduce a dependence of average response on the Burgers vector of the material, the geometric proportion of the body, the initial ED density, and the layout of

sources. In these series of tests, the response is independent of $\alpha_0 H$ as the specimens were initially ED-free. Due to the change in spatial distribution of dislocation sources (with associated changes in ED generation), internal stresses may change. Thus, s/H corresponds to the effect of internal stresses of dislocation distributions on average response. The argument (b/H) corresponds to the size effects due to dislocation mobility (12) and strain hardening (13). To evaluate the dependence of the response on internal length scale in strain hardening, the following equation is used for strength rate instead of (13):

$$\dot{g} = \theta_0 \left(\frac{g_s - g}{g_s - g_0} \right) \{ |\boldsymbol{\alpha} \times \mathbf{V}| + \dot{\gamma} \}. \quad (20)$$

Use of such an equation removes all excess hardening by the ED evolution and interactions as can be seen from the following expression:

$$h = \frac{dg}{dP} = \theta_0 \left(\frac{g_s - g}{g_s - g_0} \right), \quad P = \int \{ |\boldsymbol{\alpha} \times \mathbf{V}| + \dot{\gamma} \} dt. \quad (21)$$

Nonetheless, significant size effects are observed as shown in Figure 5, right. Thus, from these sets of computational experiments it may be inferred that a strong size effect at initial yield in PMFDM is primarily due to length scales induced by a discrete SD source distribution and the ED mobility, but not due to strain hardening in the mean-field or stage II sense. This finding is qualitatively consistent with the recent reports by Norfleet et al. [2008] and Rao et al. [2008], both of which show a potent size effect in microcrystal deformation that is associated with the instantaneous mobile dislocation density relative to the imposed loading conditions. Further, the result does not preclude other hardening phenomena, such as the absence of sources as suggested by Greer et al. [2005], or the hardening of sources as suggested by Parthasarathy et al. [2006], from providing alternate or additional hardening mechanisms, respectively. Those effects, while not investigated in the present study, may be represented via alternative selections of the constitutive assumptions of (11)–(13).

Effect of dynamic instability. To study the possibility of dynamical sensitivity of the stress-strain response at initial yield, additional numerical experiments were performed, each corresponding to a small perturbation of the order of machine precision in the boundary condition for displacement. The spatial distribution of sources is assumed to be similar to that used in Section 3.1. It is observed that this small magnitude of perturbation in boundary condition results in a significant difference in the stress-strain response as shown in the top row of Figure 6. There is about 34% variation in the shear stress at 0.8% applied strain for the cell having an edge length of $0.6 \mu\text{m}$ and 16% for the cell having an edge length of $3.0 \mu\text{m}$. The mean shear stress-strain response for each cell size is shown in Figure 6, bottom. The mean values show a cell-size dependence with smaller being harder.

The mechanical response at the macroscopic scale is insensitive to minor perturbations. At the macroscopic scale, sources are considered to be present everywhere in the body. Motivated by this fact, numerical experiments were performed with sources present everywhere in the body, that is, \mathbf{L}^p is set active in the entire cell. The four simple shear experiments with varying boundary condition perturbations were performed on the small and big cells. It was observed that in the case of plastically unconstrained cells the stress-strain response up to 0.8% simple shear strain is insensitive to such perturbation in the boundary conditions.

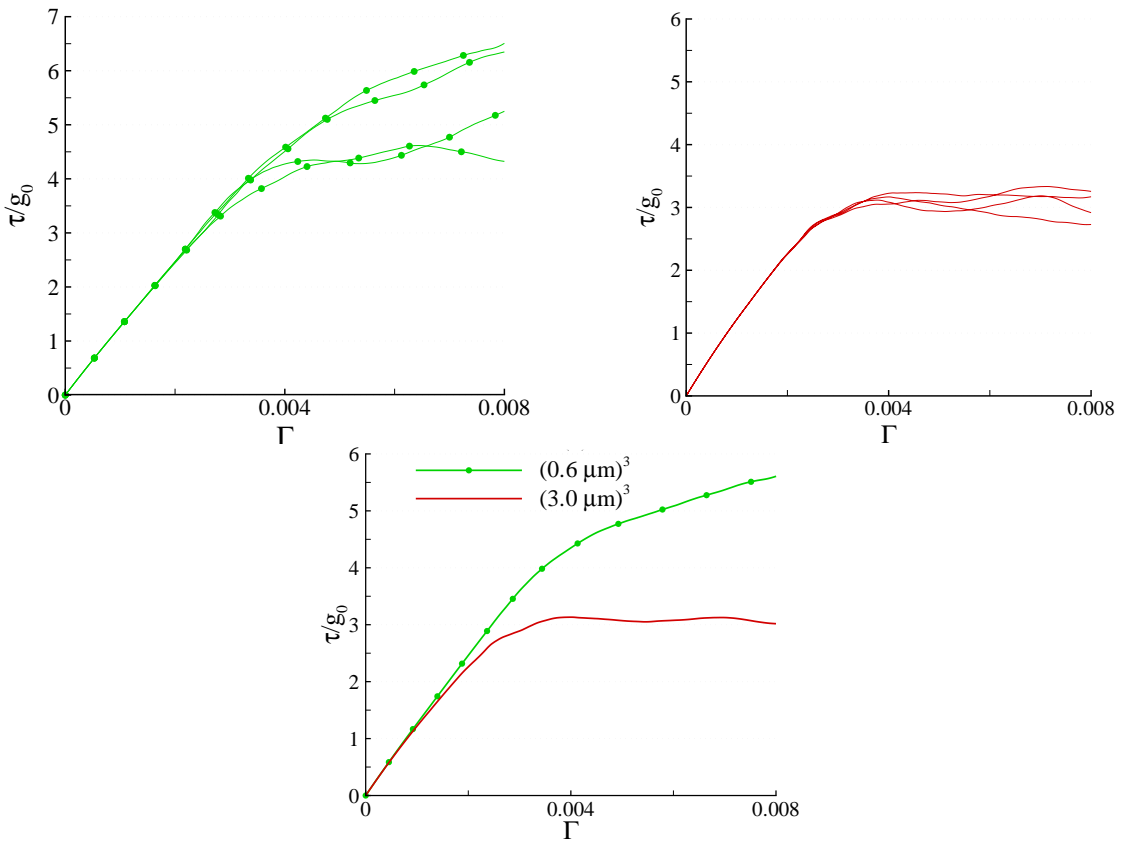


Figure 6. Variability in stress-strain response in simple shear with perturbation in boundary conditions. Top left: $0.6 \mu\text{m}$, Top right: $3.0 \mu\text{m}$, Bottom: mean response for each of the two sizes.

From these experiments and results presented in [Roy and Acharya 2006] pertaining to the effect of size on stability of stress-strain response in PMFDM, one may infer that discreteness in source distribution and decreasing cell size lead to dynamical sensitivity to perturbations in this model. Note that a qualitatively similar sensitivity to perturbations was found in DD simulations by Deshpande et al. [2001]. Interestingly, there are experimental observations of drastically different responses in samples of the same size when subjected to a prescribed deformation [Uchic et al. 2004]. However, it is not yet possible to deduce from those experiments the degree to which such variation results from differences in initial dislocation configurations and how much may result from small perturbations in the testing. The existence of such intrinsic instability in flow response also emphasizes the importance of the stochastic nature of the material response and the need to average over large numbers of samples to glean the typical material behavior at small scales.

Variation of microstructure. It was deduced from dimensional analysis performed in Section 3.1 that the stress-strain response of PMFDM material depends upon the dimensionless argument s/H . Here we investigate the effect of changes in the spatial distribution of sources in a cell of fixed size containing a fixed source density. Calculations for a cubic cell having an edge length of $3 \mu\text{m}$ were performed with

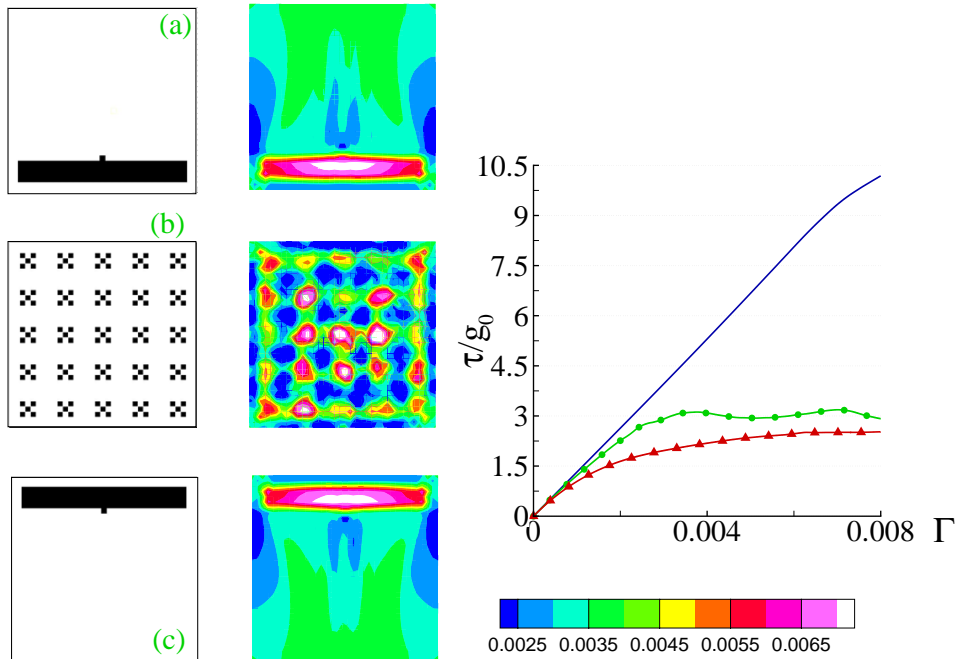


Figure 7. Variability in stress-strain response with change in the source pattern.

three patterns of source distribution, as shown in [Figure 7](#). No perturbations were imposed in this case. The figure shows that average stress at 0.8% applied strain varies approximately from 43 MPa to 180 MPa with varying source pattern. This demonstrates the variation of mechanical response of same-sized cells with a change in microstructure.

Since cells (a) and (c) in [Figure 7](#) are geometrically equivalent (by a 180 degree rotation about the x_3 direction, so the top face of (a) corresponds to the bottom face of (c)), the intuitive expectation is to get the same response in these cases. Reaction forces, however, are measured at the top faces of all cells. The cause for this difference in the reaction force for the two different source patterns is due to the presence of nonzero tractions in the x_1 -direction on the left and right faces of the cube due to the imposed displacement boundary conditions for simple shear. Accordingly, the reaction forces on the top need not be equal in magnitude to the reaction forces at the bottom of the cell. The horizontal reaction force on the top face of (a) was indeed identical to the horizontal reaction at the bottom face of (c) as required by symmetry, and likewise for the bottom face of (a) and the top face of (c). The top and bottom face reactions would have to be equal in magnitude from statics for both (a) and (c) if the side faces of the cube were traction free in the 1-direction; this was verified in our numerical experiments.

3.2. Size effects due to initial ED distribution. Low energy dislocation microstructures are observed in materials. Such structures frequently consist of an array of like-signed dislocations having a low energy arrangement, such as a tilt or twist boundary. Here we investigate the variation of initial yield strength in cells having a predefined spatial distribution of initial ED density of a common sign. Two cubical cells having edge lengths of $0.6 \mu\text{m}$ and $3 \mu\text{m}$ are considered. The spatial distribution of initial ED density is shown in [Figure 3](#) for an excess edge-dislocation density of $\alpha_{23} = -2.025 \times 10^{-3} \mu\text{m}^{-1}$ prescribed on

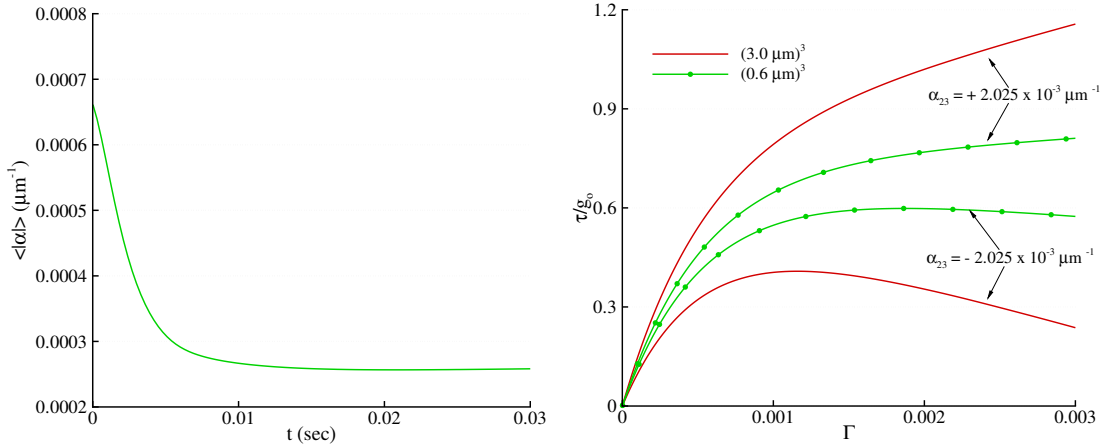


Figure 8. Left: variation in average of $|\alpha|$ over the whole domain with time. Right: size effect in simple shear with a nonzero initial excess dislocation density.

the nodes of shaded elements. In order to obtain an equilibrium state of initial ED density distribution, cells are relaxed in time without any external load. The volume average of $|\alpha|$ is used as a measure of ED content in the cell. Equilibrium is considered to be attained at $t = 0.03$ sec when this measure attains a constant value with respect to time, as shown in Figure 8, left. The strength of the material is assumed to be constant throughout the deformation process, that is, $\dot{g} = 0$ in (13). Once equilibrium is attained, simple shear boundary conditions corresponding to a strain of 0.3% are imposed on the cells. The average shear stress at 0.3% strain for the cell having an edge length of $0.6 \mu\text{m}$ is 2.5 times higher than that of cell having a $3 \mu\text{m}$ edge length, as shown in Figure 8, right. Next, a similar test was performed with an initially-prescribed ED density of the same magnitude and opposite in sign. A reversed size effect is observed in this test wherein the larger cell shows a harder response (see again Figure 8b). One can infer from the dimensional analysis performed in (19), that the average response of the material depends upon $\alpha_0 H$ for these cases. With a prescribed α_0 among different sized cells a size effect is expected but it is not possible to predict the sense of size effect based on dimensional analysis alone. Due to the complexity and difference in initial ED distribution in these examples, a simpler problem is studied to understand the variation in the sense of size effect depending on the sign of initial ED density. For this simpler case, an initial excess edge-dislocation density $\alpha_{23} = 2.025 \times 10^{-3} \mu\text{m}^{-1}$ is prescribed at the center of two cubic cells having edge lengths of $0.6 \mu\text{m}$ and $3 \mu\text{m}$, as shown in Figure 9. The cells are relaxed in time to obtain corresponding equilibrated ED arrangements. Then, displacement boundary conditions corresponding to an engineering simple shearing strain of 0.3% are imposed on the cell. The average shear stress-strain response demonstrates that the smaller cell is indeed harder than the large one. However, a reversed size effect is observed with a change in sign of initial excess dislocation density (see Figure 9). This phenomenon is explained as follows.

Consider a traction free finite cubical block containing a dislocation. In order to understand the resulting stress distribution in the block, we first note that the equations for determining the stress field of a specified ED field in PMFDM are linear; thus supersposition applies. Consider now the stress field of a dislocation in an infinite medium, situated as in Figure 9. This infinite medium stress field

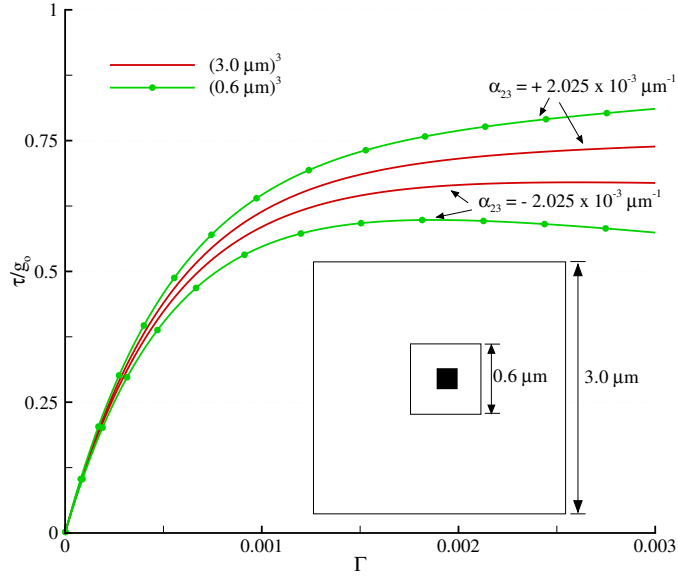


Figure 9. Size effect in simple shear with a nonzero initial excess dislocation density and the new pattern as shown in the inset.

naturally induces tractions on the surface of the finite crystal. Thus, image tractions equal in magnitude and opposite in sign of those induced by the dislocation need to be present on the external surface of the block to satisfy the traction free boundary conditions. Therefore, the *initial stress* field of a traction free finite crystal in equilibrium can be considered as a superposition of the internal stress due to initial ED distribution in the linear elastic infinite medium and the image stress required to satisfy the traction-free boundary conditions. When an external stress is applied, the stress at any point in the finite body is a sum of the initial stress and the applied stress due to boundary conditions (again using superposition) at that point. In the regions having an initially prescribed ED density, less applied stress is required to cause flow if both the initial stress and the applied stress are of the same sign as compared to the case when both are of opposite sign. Now, consider two cubic blocks of different sizes and same initial ED distribution. The magnitude of image stress corresponding to the $(1/r)$ fundamental stress field of a dislocation is higher for the smaller block than the larger block. Accordingly, in the case of the external applied stress being the same sign as the initial stress in the dislocation core region, the smaller cell yields before the large cell (for a constant yield stress). If the sign of the initial ED density is now changed with the direction of applied stressing remaining the same, the initial stress changes sign, the larger cell has a smaller-in-magnitude initial stress that *subtracts* from the applied stress and consequently yields later than the smaller cell.

4. Conclusions

A finite element implementation of PMFDM has been shown to predict size effects at initial yield in plasticity of micron-scale simulation cells. The results are qualitatively consistent with experimental observation in [Uchic et al. 2004; Dimiduk et al. 2005; Greer et al. 2005], as well as with recent discrete dislocation simulations of Weygand et al. [2007], Senger et al. [2008], Tang et al. [2007; 2008], and Rao

et al. [2008]. In the PMFDM framework, size effects are caused by the internal stress of the dislocation distribution, its coupling to the imposed deformation conditions including deformation rate, and natural length scales that enter the theory through strain hardening and the ED velocity. However, an important observation from the computational experiments presented in this paper is that length scales associated with the internal stress due to discrete source patterns and those associated with the plastic strain rate of ED, are solely sufficient for size effects at initial yield within this model. We observe a sensitivity of the overall mechanical response to the presence of discrete source volumes or regions. Size-effect reversals under appropriate circumstances are also observed and explained. For the most part, such sample-scale kinematical size effects have not been treated in discrete dislocation (DD) simulations (notable exceptions being those following the Needleman–Van der Giessen formulation of discrete DD), and have only been peripherally considered in explanations of the widening set of size-effect experiments.

Acknowledgments

We thank Armand Beaudoin for discussions on dynamical sensitivity. Support for this work from the National Science Foundation (Grant number: DMI-0423304), the Dowd-ICES Fellowship at CMU to Saurabh Puri, and the Metallic Materials Division of the AFRL at WPAFB is gratefully acknowledged.

References

- [Acharya 2001] A. Acharya, “A model of crystal plasticity based on the theory of continuously distributed dislocations”, *J. Mech. Phys. Solids* **49** (2001), 761–785.
- [Acharya 2003] A. Acharya, “Driving forces and boundary conditions in continuum dislocation mechanics”, *Proc. Royal Soc. A* **459** (2003), 1343–1363.
- [Acharya 2004] A. Acharya, “Constitutive analysis of finite deformation field dislocation mechanics”, *J. Mech. Phys. Solids* **52** (2004), 301–316.
- [Acharya and Beaudoin 2000] A. Acharya and A. J. Beaudoin, “Grain size effect in viscoplastic polycrystals at moderate strains”, *J. Mech. Phys. Solids* **48** (2000), 2213–2230.
- [Acharya and Roy 2006] A. Acharya and A. Roy, “Size effects and idealized dislocation microstructure at small scales: predictions of a phenomenological model of mesoscopic field dislocation mechanics: Part I”, *J. Mech. Phys. Solids* **54** (2006), 1687–1710.
- [Balint et al. 2006] D. S. Balint, V. S. Deshpande, N. A., and E. Van der Giessen, “Size effects in uniaxial deformation of single and polycrystals: a discrete dislocation plasticity analysis”, *Modelling Simulation Mater. Sci. Eng.* **14** (2006), 409–422.
- [Beaudoin et al. 2000] A. J. Beaudoin, A. Acharya, S. R. Chen, D. A. Korzekwa, and M. G. Stout, “Consideration of grain-size effect and kinetics in the plastic deformation of metal polycrystals”, *Acta Metallurgica* **48** (2000), 3409–3423.
- [Benzerga and Shaver 2006] A. A. Benzerga and N. F. Shaver, “Scale dependence of mechanical properties of single crystals under uniform deformation”, *Scripta Mater.* **54** (2006), 1937–1941.
- [Benzerga et al. 2005] A. A. Benzerga, Y. Brechet, A. Needleman, and E. Van der Giessen, “The stored energy of cold work: Predictions from discrete dislocation plasticity”, *Acta Materialia* **53** (2005), 4765–4779.
- [Deshpande et al. 2001] V. S. Deshpande, A. Needleman, and E. Van der Giessen, “Dislocation dynamics is chaotic”, *Scripta Mater.* **45** (2001), 1047–1053.
- [Deshpande et al. 2005] V. S. Deshpande, A. Needleman, and E. Van der Giessen, “Plasticity Size effects in tension and compression of single crystals”, *J. Mech. Phys. Solids* **53** (2005), 2661–2691.
- [Dimiduk et al. 2005] D. Dimiduk, M., M. D. Uchic, and T. A. Parthasarathy, “Size-affected single-slip behavior of pure nickel microcrystals”, *Acta Materialia* **53** (2005), 4065–4077.

- [Fleck et al. 1994] N. A. Fleck, G. M. Muller, M. F. Ashby, and J. W. Hutchinson, “Strain gradient plasticity: theory and experiment”, *Acta Metallurgica et Materialia* **42** (1994), 475–487.
- [Frick et al. 2008] C. P. Frick, B. G. Clark, S. Orso, A. S. Schneider, and E. Arzt, “Size effect on strength and strain hardening of small-scale [1 1 1] nickel compression pillars”, *Mater. Sci. Eng. A* **489** (2008), 319–329.
- [Greer et al. 2005] J. R. Greer, W. C. Oliver, and W. D. Nix, “Size dependence of mechanical properties of gold at the micron scale in the absence of strain gradients”, *Acta Materialia* **53** (2005), 1821–1830.
- [Ma and Clarke 1995] Q. Ma and D. R. Clarke, “Size-dependent hardness of silver single-crystals”, *J. Mater. Res.* **10**:4 (1995), 853–863.
- [Norfleet et al. 2008] D. M. Norfleet, D. M. Dimiduk, S. J. Polasik, M. D. Uchic, and M. J. Mills, “Examination of dislocation structures and their relationship to strength of pure nickel microcrystals”, *Acta Materialia* **56** (2008), 2988–3001.
- [Nye 1953] J. F. Nye, “Some geometrical relations in dislocated crystals”, *Acta Metallurgica* **1** (1953), 153–162.
- [Parthasarathy et al. 2006] T. A. Parthasarathy, S. I. Rao, D. M. Dimiduk, M. D. Uchic, and D. R. Trinkle, “Contribution to size effect of yield strength from the stochastics of dislocation source lengths in finite samples”, *Scripta Mater.* **56** (2006), 313–316.
- [Rao et al. 2008] S. I. Rao, D. M. Dimiduk, T. A. Parthasarathy, M. D. Uchic, M. Tang, and C. Woodward, “Athermal mechanisms of size-dependent crystal flow gleaned from three dimensional discrete dislocation simulations”, *Acta Materialia* **56** (2008), 3245–3259.
- [Roy and Acharya 2006] A. Roy and A. Acharya, “Size effects and idealized dislocation microstructure at small scales: predictions of a phenomenological model of mesoscopic field dislocation mechanics: Part II”, *J. Mech. Phys. Solids* **54** (2006), 1711–1743.
- [Senger et al. 2008] J. Senger, D. Weygand, P. Gumbsch, and O. Kraft, “Discrete dislocation simulations of the plasticity of micro-pillars under uniaxial loading”, *Scripta Mater.* **58** (2008), 587–590.
- [Stölken and Evans 1998] J. S. Stölken and A. G. Evans, “A microbend test method for measuring the plasticity length scale”, *Acta Materialia* **46**:14 (1998), 5109–5115.
- [Tang et al. 2007] H. Tang, K. W. Schwarz, and H. D. Espinosa, “Dislocation escape-related size effects in single-crystal micropillars under uniaxial compression”, *Acta Materialia* **55** (2007), 1607–1616.
- [Tang et al. 2008] H. Tang, K. W. Schwarz, and H. D. Espinosa, “Dislocation-source shutdown and the plastic behavior of single-crystal micropillars”, *Phys. Rev. Letters* **100** (2008), 185503–1–4.
- [Uchic et al. 2004] M. D. Uchic, D. M. Dimiduk, J. N. Florando, and W. D. Nix, “Sample dimensions influence strength and crystal plasticity”, *Science* **305** (2004), 986–989.
- [Varadhan et al. 2006] S. N. Varadhan, A. J. Beaudoin, A. A., and C. Fressengeas, “Dislocation transport using an explicit Galerkin/least-squares formulation”, *Modelling Simulation Mater. Sci. Eng.* **14** (2006), 1245–1270.
- [Weygand et al. 2007] D. Weygand, M. Poignant, P. Gumbsch, and O. Kraft, “Three-dimensional dislocation dynamics simulation of the influence of sample size on the stress–strain behavior of fcc single-crystalline pillars”, *Mater. Sci. Eng. A* (2007), in press.

Received 16 Jul 2008. Revised 14 Mar 2009. Accepted 4 Jun 2009.

SAURABH PURI: saurabhp@caltech.edu

Department of Mechanical Engineering, California Institute of Technology, Pasadena, CA 91125, United States

ANISH ROY: A.Roy3@lboro.ac.uk

Wolfson School of Mechanical and Manufacturing Engineering, Loughborough University, Leicestershire, LE11 3TU, United Kingdom

AMIT ACHARYA: acharyaamit@cmu.edu

Department of Civil and Environmental Engineering, Carnegie Mellon University, Pittsburgh, PA 15213, United States

DENNIS DIMIDUK: dennis.dimiduk@wpafb.af.mil

Air Force Research Laboratory, Materials and Manufacturing Directorate, AFRL/MLLM Bldg. 655, 2230 Tenth Street, Wright-Patterson AFB, OH 45433-7817, United States

FORCED VIBRATIONS OF A NONLINEAR OSCILLATOR WITH WEAK FRACTIONAL DAMPING

YURIY A. ROSSIKHIN, MARINA V. SHITIKOVA AND TATIANA SHCHEGLOVA

This article deals with force-driven vibrations of nonlinear mechanical oscillators whose constitutive equations involve fractional derivatives, defined as fractional powers of the conventional time-derivative operator. This definition of fractional derivatives enables one to analyze approximately the vibratory regimes of the oscillator. The assumption of small fractional derivative terms allows one to use the method of multiple time scales, whereby a comparative analysis of the solutions obtained for different orders of low-level fractional derivatives and disturbing force terms can be carried out. The relationship between the fractional parameter (order of the fractional operator) and nonlinearity manifests itself in full measure when the orders of the small fractional derivative term and of the cubic nonlinearity appearing in the oscillator's constitutive equation coincide.

1. Introduction

Fractional derivatives have been useful in describing, among other things, the frequency-dependent damping behavior of nonlinear structural systems [Padovan and Sawicki 1998; Rossikhin and Shitikova 1997a; 1998; 2000; 2003; 2006; Li et al. 2003; Sereďyńska and Hanyga 2005; Nasuno et al. 2006]. Since the methods of integral transformations are unusable in nonlinear problems, different perturbation techniques or numerical methods must be used for investigating vibrations of such nonlinear structures.

The dynamics of the fractionally damped Duffing oscillator has been examined by several authors [Padovan and Sawicki 1998; He 1998; Sheu et al. 2007; Sereďyńska and Hanyga 2000; Gao and Yu 2005; Singh and Chatterjee 2006; Wahi and Chatterjee 2004; Chen and Zhu 2009; Atanackovic and Stankovic 2008]. In particular, a Duffing-like oscillator with positive linear stiffness and weak damping defined by a fractional derivative has been studied in [Padovan and Sawicki 1998] using an energy-constrained Lindstedt–Poincaré perturbation procedure that involves a diophantine version of the fractional operator powers. The influence of fractional damping on the frequency amplitude response has been examined when the oscillator is subjected to the action of an external harmonic force.

The case of free vibrations with a half-order Riemann–Liouville fractional derivative was analyzed in [He 1998] using variational iteration method, allowing the author to obtain an approximate analytical solution.

The occurrence and nature of chaotic motion in a single-degree-of-freedom system described by a Duffing-like equation with negative linear stiffness have been studied using different numerical methods in [Sheu et al. 2007], including the use of Caputo-type fractional derivatives. The Galerkin projection

Keywords: fractionally damped oscillator, nonlinear fractional oscillator, method of multiple time scales.

This research has been made possible in part by a joint Grant from the Russian Foundation for Basic Research No. 07-01-92002-HHC-a and the National Science Council of Taiwan No. 96WFA2500005.

method and the finite element method were adopted in [Singh and Chatterjee 2006] for solving a similar equation but with the dissipative force modeled via Riemann–Liouville fractional derivatives of half-order, while the possibilities of using other values of the fractional parameter were also discussed.

The method of averaging was applied in [Wahi and Chatterjee 2004] for investigating the equations with a different type of small damping including Riemann–Liouville half-order fractional derivative terms and delayed terms, as well as in [Chen and Zhu 2009] for treating the case of combined external harmonic and parametric white noise excitations.

In [Rossikhin and Shitikova 2009], departing from earlier practice in the literature, we suggested an approximate approach to the analysis of free vibrations of mechanical oscillators whose constitutive equations involve fractional derivatives. The approach is based on the representation of the fractional derivative as a fractional power of the ordinary time derivative operator d/dt , a representation typically given by the equality

$$\left(\frac{d}{dt}\right)^\gamma x(t) = D_+^\gamma x(t) \quad (1-1)$$

(see formula (5.82) of [Samko et al. 1993]), where

$$D_+^\gamma x(t) = \frac{d}{dt} \int_{-\infty}^t \frac{x(t-t') dt'}{\Gamma(1-\gamma)t'^\gamma} \quad (1-2)$$

is the Riemann–Liouville fractional time-derivative. Since the lower limit of the integral here is $-\infty$, the equality in (1-1) allows one to use the Liouville representation of the fractional derivative applied to the exponential function:

$$D_+^\gamma e^{i\omega t} = (i\omega)^\gamma e^{i\omega t}. \quad (1-3)$$

This latter formula is no longer valid when the lower limit of integration is 0. For this case there exists another formula (see Appendix for details) based on the Riemann–Liouville fractional derivative

$$D_{0+}^\gamma e^{i\omega t} = \frac{d}{dt} \int_0^t \frac{e^{i\omega(t-t')} dt'}{\Gamma(1-\gamma)t'^\gamma} = (i\omega)^\gamma e^{i\omega t} + \frac{\sin \gamma\pi}{\pi} \int_0^\infty \frac{u^\gamma e^{-ut} du}{u + i\omega}, \quad (1-4)$$

which turns into (1-3) when $t \rightarrow +\infty$.

If one uses the exact formula (1-4) for the fractional differentiation of the exponent, in many cases the integral appearing in (1-4) can also be neglected compared with the first term in the same formula [Rossikhin and Shitikova 1997a; 1997b; 1998; 2000; 2003], since this integral decays rapidly with time. For example, if γ is small, while the frequency ω lies within the range of interest in engineering, the integral on the right-hand side of (1-4) can be ignored, what allows one to use formula (1-3).

Calculations of the magnitude of the fractional parameters carried out on the basis of experimental data [Abdel-Ghaffar and Scanlan 1985] show that this value for suspension bridges is of the order of 0.05–0.1 [Rossikhin and Shitikova 1998; 2008]. The value $\gamma = 0.118$ was reported in [Giovagnoni and Berti 1992] when studying the experimental response of a deformable single-link mechanism, which was realized by means of a brass bar fixed onto a vertical shaft. The fractional parameters $\gamma_1 = 0.1991$ and $\gamma_2 = 0.2499$ were identified in [Schmidt and Gaul 2006] from experimental measurements of a cantilever made of DelrinTM. The value $\gamma = 0.28$ was obtained in [Cooke and Keltie 1987] in a beam impact experiment. A series of experiments measuring the frequency responses of viscoelastic rods of materials like teflon, polyamide, polyurethane, polyvinyl chloride, and polyethylene was reported in

[Schäfer 2000; Schäfer and Seifert 2002], where it was found that the fractional parameter lies in the range of 0.086–0.11. During flexible polyurethane foam modeling via a nonlinear fractional oscillator in [Deng et al. 2003], viscoelastic parameters for automotive seating applications were identified with a fractional parameter equal to 0.019.

The evaluation of the second term in (1-4) is of great importance only during the consideration of linear vibrations, since ignoring this term allows one to solve the equation of linear vibrations of a fractionally damped oscillator

$$\ddot{x} + \omega_0^2 \tau_\sigma^\gamma \left(\frac{d}{dt} \right)^\gamma x(t) + \omega_0^2 x = 0, \quad (1-5)$$

where $\omega_0^2 = E_0 m^{-1}$, E_0 is the spring rigidity, m is the oscillator's mass, and τ_σ is the relaxation time, with the help of the Euler substitution as done in [Rossikhin and Shitikova 2009]:

$$x(t) = C e^{\lambda T}. \quad (1-6)$$

Indeed, substituting (1-6) into (1-5) we obtain the characteristic equation

$$\lambda^2 + \omega_0^2 \tau_\sigma^\gamma \lambda^\gamma + \omega_0^2 = 0, \quad (1-7)$$

which possesses two complex conjugate roots [Rossikhin and Shitikova 1997b]

$$\lambda_{1,2} = -\alpha \pm i\omega, \quad (1-8)$$

where α and ω are the damping coefficient and the frequency of vibrations, respectively.

The solution of (1-5) with due account for (1-8) can be written as [Rossikhin and Shitikova 2009]

$$x(t) = A e^{-\alpha t} \cos(\omega t + \varphi), \quad (1-9)$$

where A and φ are arbitrary constants to be determined from the initial conditions.

The Green's function for (1-5) with the second term of (1-4) taken into consideration is written in the form [Rossikhin and Shitikova 1997b]

$$x(t) = A_0(t) + A e^{-\alpha t} \cos(\omega t + \varphi), \quad (1-10)$$

where $A_0(t)$ is the term governing the drift of the position of equilibrium.

In the present paper, the approach suggested in [Rossikhin and Shitikova 2009] for the analysis of free vibrations of nonlinear mechanical oscillators is generalized to the case of forced vibrations. It will be shown that the second term in (1-4) can altogether be ignored in nonlinear problems, since it does not affect the first approximations to be constructed here using the method of multiple time scales.

The need for studying fractional oscillators is motivated by two reasons: first, engineers often use one-degree-of-freedom models as a first approximation or as a benchmark before preceding to more intricate models or multi-degree-of-freedom structural systems (for example, as the simplest model of a vibration-isolation system [Koh and Kelly 1990; Makris and Constantinou 1991; Hwang and Ku 1997; Aprile et al. 1997; Munshi 1997; Hwang and Hsu 2001; Gusella and Terenzi 2001; Sjöberg and Kari 2003]), and second, the study of vibrations of more complex structures can be reduced to vibrations of a set of fractional oscillators [Giovagnoni and Berti 1992; Rossikhin and Shitikova 2001; 2004; Agrawal 2004; Schäfer and Kempfle 2004].

In all the examples considered below the emphasis will be on investigating the influence of a small external force on vibratory motion, because many of our recent publications have already examined the influence of the order γ of the fractional derivative on nonlinear free damped vibrations of such fractionally damped structures as oscillators [Rossikhin and Shitikova 2009], two-degree-of-freedom mechanical systems [2000], plates [2003; 2006], and suspension bridges [1998; 2008]. We have shown that the fractional parameter plays the role of a structural parameter of the whole system and influences the character of the system's damping coefficient as a function of the natural frequencies of linear vibrations. For example, the power relationships obtained in [Rossikhin and Shitikova 1998; 2008] between the damping coefficient of the system and its natural frequencies of linear vibration correlate well with the experimental data describing the natural frequency dependence of the damping ratio for the Golden Gate suspension bridge [Abdel-Ghaffar and Scanlan 1985]. When the fractional parameter tends to one, i.e., when the fractional derivative transforms into the common derivative with respect to time, the system's damping coefficient does not depend on the natural frequencies of linear vibrations, which is in contradiction with experimental data. Thus, nonlinear viscoelastic models with fractional derivatives with respect to time are to be preferred over models with integral derivatives for describing the damping features of a combined suspension system.

2. Problem formulation

We will consider force-driven vibrations of the Duffing-like oscillator with positive linear stiffness and damping defined by a fractional derivative (1-1):

$$m\ddot{x}(t) + \beta\left(\frac{d}{dt}\right)^\gamma x(t) + k_1x(t) + k_2x(t)^3 = f \cos(\omega t), \quad (2-1)$$

where x , β , k_1 , and k_2 are, respectively, the oscillator's displacement, damping coefficient, linear stiffness, and small parameter of nonlinear stiffness, f is the force amplitude, and ω is its frequency.

Dividing (2-1) by the mass and introducing dimensionless values

$$\tilde{t} = t\Omega_0, \quad \tilde{x} = \frac{x}{x_0}, \quad \tilde{\omega} = \frac{\omega}{\Omega_0}, \quad \tilde{\omega}_0^2 = \frac{\omega_0^2}{\Omega_0^2}, \quad (2-2)$$

where

$$\omega_0^2 = \frac{k_1}{m}, \quad \Omega_0 = \sqrt{\frac{g}{l_0}}, \quad x_0 = \frac{mg}{k_1} = \frac{g}{\omega_0^2}$$

(g being the acceleration of gravity and l_0 the undeformed spring length) yields

$$\ddot{\tilde{x}} + \frac{\beta}{m} \Omega_0^{\gamma-2} \left(\frac{d}{d\tilde{t}}\right)^\gamma \tilde{x} + \tilde{\omega}_0^2 \tilde{x} + \frac{k_2}{m} x_0^2 \Omega_0^{-2} \tilde{x}^3 = \frac{f}{m} \Omega_0^{-2} x_0^{-1} \cos(\tilde{\omega}\tilde{t}), \quad (2-3)$$

which we then turn into the dimensionless form of Equation (2-1):

$$\ddot{\tilde{x}} + \varepsilon^k \mu \left(\frac{d}{d\tilde{t}}\right)^\gamma \tilde{x} + \tilde{\omega}_0^2 \tilde{x} + \tilde{k}_2 \tilde{x}^3 = \varepsilon^{k+1} F \cos(\tilde{\omega}\tilde{t}) \quad (k = 1 \text{ or } 2), \quad (2-4)$$

where

$$\varepsilon^k \mu = \frac{\beta}{m} \Omega_0^{\gamma-2}, \quad \tilde{k}_2 = \frac{k_2}{m} x_0^2 \Omega_0^{-2}, \quad \varepsilon^{k+1} F = \frac{f}{m} \Omega_0^{-2} x_0^{-1}.$$

Here ε is a small parameter which is of the same order of magnitude as the amplitudes, and μ and F are finite values. The choice of k in (2-4) depends on the order of smallness of the exciting force amplitude and viscosity coefficient.

To lighten the notation, tildes over dimensionless values will be omitted henceforth.

We will assume that the linear natural frequency ω_0 is approximately equal to the frequency of the external excitation ω , i.e.,

$$\omega_0 \approx \omega. \tag{2-5}$$

3. Method of solution

An approximate solution of (2-4) for small amplitudes varying weakly with time can be represented by an expansion in terms of different time scales in the following form [Nayfeh 1973]:

$$x(t) = \varepsilon x_1(T_0, T_1, T_2, \dots) + \varepsilon^2 x_2(T_0, T_1, T_2, \dots) + \varepsilon^3 x_3(T_0, T_1, T_2, \dots) + \dots \tag{3-1}$$

Here, $T_n = \varepsilon^n t$ ($n = 0, 1, 2, \dots$) are new independent variables, among them: $T_0 = t$ is a fast scale, characterizing motions with ω and the natural frequency ω_0 , and $T_1 = \varepsilon t$ and $T_2 = \varepsilon^2 t$ are slow scales characterizing the modulations of the amplitude and phase.

Recall that the first, the second and fractional derivatives are defined by

$$\begin{aligned} \frac{d}{dt} &= D_0 + \varepsilon D_1 + \varepsilon^2 D_2 + \dots, & \frac{d^2}{dt^2} &= D_0^2 + 2\varepsilon D_0 D_1 + \varepsilon^2 (D_1^2 + 2D_0 D_2) + \dots, \\ \left(\frac{d}{dt}\right)^\gamma &= (D_0 + \varepsilon D_1 + \varepsilon^2 D_2 + \dots)^\gamma = D_+^\gamma + \varepsilon \gamma D_+^{\gamma-1} D_1 + \frac{1}{2} \varepsilon^2 \gamma (\gamma - 1) D_+^{\gamma-2} D_1^2 + 2D_+^{\gamma-1} D_2 + \dots, \end{aligned}$$

where $D_n = \partial/\partial T_n$, and $D_+^\gamma, D_+^{\gamma-1}, D_+^{\gamma-2}, \dots$ are the Riemann–Liouville fractional time derivatives:

$$D_+^{\gamma-n} x = \frac{d}{dt} \int_{-\infty}^t \frac{x(t-t') dt'}{\Gamma(1-\gamma+n) t'^{\gamma-n}} \quad (n = 0, 1, 2, \dots).$$

Using this and substituting (3-1) into (2-4), after equating the coefficients at equal powers of ε , we are led to a set of recurrence equations to various orders:

to order ε :

$$D_0^2 x_1 + \omega_0^2 x_1 = 0, \tag{3-2}$$

to order ε^2 :

$$D_0^2 x_2 + \omega_0^2 x_2 = -2D_0 D_1 x_1 - \mu(2-k) D_+^\gamma x_1 + (2-k) F \cos \omega T_0 \tag{3-3}$$

to order ε^3 :

$$\begin{aligned} D_0^2 x_3 + \omega_0^2 x_3 &= -2D_0 D_1 x_2 - (D_1^2 + 2D_0 D_2) x_1 - \mu(2-k) D_+^\gamma x_2 \\ &\quad - \mu \gamma (2-k) D_+^{\gamma-1} D_1 x_1 - \mu(k-1) D_+^\gamma x_1 - k_2 x_1^3 + (k-1) F \cos \omega T_0. \end{aligned} \tag{3-4}$$

The general solution of (3-2) has the form

$$x_1 = A_1(T_1, T_2) e^{i\omega_0 T_0} + \bar{A}_1(T_1, T_2) e^{-i\omega_0 T_0}, \tag{3-5}$$

where A_1 and \bar{A}_1 are yet unknown complex conjugate functions.

For further analysis we need to specify the order of weak damping and external excitation.

3A. Viscosity of the order of ϵ . Consider first the case where the viscosity is of the order of ϵ . Then (2-4) reduces to

$$\ddot{x} + \epsilon\mu \left(\frac{d}{dt}\right)^\gamma x + \omega_0^2 x + k_2 x^3 = \epsilon^2 F \cos(\omega t). \tag{3-6}$$

Substituting (3-5) in the right-hand side of (3-3) with $k = 1$ and taking (1-4) into account, we obtain $D_0^2 x_2 + \omega_0^2 x_2 = -2i\omega_0 \left(\frac{1}{2}(i\omega_0)^{\gamma-1} \mu A_1 + D_1 A_1\right) e^{i\omega_0 T_0} + 2i\omega_0 \left(\frac{1}{2}(-i\omega_0)^{\gamma-1} \mu \bar{A}_1 + D_1 \bar{A}_1\right) e^{-i\omega_0 T_0} + \frac{1}{2} F (e^{i\omega T_0} + e^{-i\omega T_0}) - \mu A_1 \frac{\sin \gamma\pi}{\pi} \int_0^\infty \frac{u^\gamma e^{-uT_0} du}{u + i\omega_0} - \mu \bar{A}_1 \frac{\sin \gamma\pi}{\pi} \int_0^\infty \frac{u^\gamma e^{-uT_0} du}{u - i\omega_0}$. (3-7)

The functions $\exp(\pm i\omega_0 T_0)$ on the right-hand side of (3-7) produce secular terms, so the coefficients affecting these functions must be made to vanish. Taking (2-5) into account, we have as a result

$$D_1 A_1 + \frac{1}{2}(i\omega_0)^{\gamma-1} \mu A_1 - \frac{F}{4i\omega_0} = 0, \tag{3-8}$$

whence it follows that

$$A_1(T_1, T_2) = a_1(T_2) \exp\left(-\frac{1}{2}(i\omega_0)^{\gamma-1} \mu T_1\right) + \frac{F}{2\mu(i\omega_0)^\gamma}, \tag{3-9}$$

where $a_1(T_2)$ is yet unknown function.

In view of (3-9), Equation (3-7) takes on the form

$$D_0^2 x_2 + \omega_0^2 x_2 = -\mu \frac{\sin \gamma\pi}{\pi} \int_0^\infty u^\gamma e^{-uT_0} \left(A_1 \frac{u - i\omega_0}{u^2 + \omega_0^2} + \bar{A}_1 \frac{u + i\omega_0}{u^2 + \omega_0^2} \right) du. \tag{3-10}$$

Writing the function $A_1(T_1, T_2)$ defined by (3-9) and its complex conjugate $\bar{A}_1(T_1, T_2)$ as

$$A_1 = a + ib, \quad \bar{A}_1 = a - ib \tag{3-11}$$

and substituting (3-11) into (3-10) yields

$$D_0^2 x_2 + \omega_0^2 x_2 = -2\mu \frac{\sin \gamma\pi}{\pi} f(T_0, T_1, T_2), \tag{3-12}$$

where

$$f(T_0, T_1, T_2) = \int_0^\infty \frac{u^\gamma (au + b\omega_0)}{u^2 + \omega_0^2} e^{-uT_0} du. \tag{3-13}$$

Then the solution of (3-12) has the form

$$x_2 = A_2(T_1, T_2)e^{i\omega_0 T_0} + \bar{A}_2(T_1, T_2)e^{-i\omega_0 T_0} + C(T_0, T_1, T_2)e^{i\omega_0 T_0} + \bar{C}(T_0, T_1, T_2)e^{-i\omega_0 T_0}, \tag{3-14}$$

where A_2 and \bar{A}_2 , and C and \bar{C} are yet unknown complex conjugate functions. The first two terms of (3-14) represent the general solution of the homogeneous part of (3-12), while the second pair of terms is the particular solution of the inhomogeneous equation (3-12).

Substituting the particular solution from (3-14) in (3-12), we find

$$C(T_0, T_1, T_2) = -2\mu \frac{\sin \gamma\pi}{\pi} \int_0^{T_0} e^{-2i\omega_0 T_0'} dT_0' \int_0^{T_0'} f(T_0'', T_1, T_2) e^{i\omega_0 T_0''} dT_0''. \tag{3-15}$$

Substituting (3-5), (3-9), (3-14), and (3-15) in the right-hand side of (3-4) with $k = 1$, we are led to the equation for determining x_3 . Eliminating the terms that produce secular terms, we obtain the solvability condition

$$D_2 a_1(T_2) + a_1 \left(\frac{1}{8} \mu^2 (1 - 2\gamma) (i\omega_0)^{2\gamma-3} - \kappa \frac{3k_2 F^2}{4\mu^2 \omega_0^{2\gamma+1}} \right) = 0,$$

whence it follows that

$$a_1 = a_{11} \exp \left(-\frac{1}{8} \mu^2 (1 - 2\gamma) (i\omega_0)^{2\gamma-3} + \kappa \frac{3k_2 F^2}{4\mu^2 \omega_0^{2\gamma+1}} \right) T_2, \tag{3-16}$$

where a_{11} is a constant to be determined from the initial conditions and $\kappa = i \cos 2\gamma\pi + \sin 2\gamma\pi$.

Considering (3-16), the coefficients a and b appearing in the expression (3-13) of $f(T_0, T_1, T_2)$ take the form

$$\begin{aligned} a(T_1, T_2) = & a_{11} \exp \left(-\frac{1}{2} \mu T_1 \omega_0^{\gamma-1} \sin \left(\frac{1}{2} \gamma \pi \right) + \frac{1}{8} \mu^2 T_2 (1 - 2\gamma) \omega_0^{2\gamma-3} \sin \gamma \pi \right) \\ & \times \cos \left(\frac{1}{2} \mu T_1 \omega_0^{\gamma-1} \sin \left(\frac{1}{2} \gamma \pi \right) + \frac{1}{8} \mu^2 T_2 (2\gamma - 1) \omega_0^{2\gamma-3} \cos \gamma \pi + \frac{3k_2 F^2}{4\mu^2 \omega_0^{2\gamma+1}} T_2 \cos 2\gamma \pi \right) \\ & + \frac{F}{\mu \omega_0^\gamma} \cos \frac{\gamma \pi}{2}, \end{aligned} \tag{3-17}$$

$$\begin{aligned} b(T_1, T_2) = & a_{11} \exp \left(-\frac{1}{2} \mu T_1 \omega_0^{\gamma-1} \sin \left(\frac{1}{2} \gamma \pi \right) + \frac{1}{8} \mu^2 T_2 (1 - 2\gamma) \omega_0^{2\gamma-3} \sin \gamma \pi \right) \\ & \times \sin \left(\frac{1}{2} \mu T_1 \omega_0^{\gamma-1} \sin \left(\frac{1}{2} \gamma \pi \right) + \frac{1}{8} \mu^2 T_2 (2\gamma - 1) \omega_0^{2\gamma-3} \cos \gamma \pi + \frac{3k_2 F^2}{4\mu^2 \omega_0^{2\gamma+1}} T_2 \cos 2\gamma \pi \right) \\ & - \frac{F}{\mu \omega_0^\gamma} \sin \frac{\gamma \pi}{2}, \end{aligned} \tag{3-18}$$

Combining (3-9) and (3-16) with (3-5) yields

$$\begin{aligned} x_1 = & \left[a_{11} \exp \left(-\frac{1}{8} \mu^2 (1 - 2\gamma) (i\omega_0)^{2\gamma-3} + \kappa \frac{3k_2 F^2}{4\mu^2 \omega_0^{2\gamma+1}} \right) T_2 \exp \left(-\frac{1}{2} (i\omega_0)^{\gamma-1} \mu T_1 \right) + \frac{F}{2\mu (i\omega_0)^\gamma} \right] \\ & \times \exp(i\omega_0 T_0) + \text{c.c.}, \end{aligned} \tag{3-19}$$

where c.c. stands for the complex conjugate to the preceding terms.

Reference to (3-19) shows that the second term of formula (1-4) does not affect the solution within the limits of this approximation.

Limiting ourselves to the first term in (3-1) with due account for (3-19), we find the solution of (3-6) in the form

$$x = \varepsilon \left(a_0 e^{-\alpha t} \cos \Omega t + \frac{F}{\mu \omega_0^\gamma} \cos \left(\omega_0 t - \frac{1}{2} \gamma \pi \right) \right), \tag{3-20}$$

where we have introduced the quantities $a_0 = 2a_{11}$,

$$\alpha = \frac{1}{2} \varepsilon \mu \omega_0^{\gamma-1} \sin \frac{1}{2} \gamma \pi \left(1 + \frac{1}{2} \varepsilon \mu (2\gamma - 1) \omega_0^{\gamma-2} \cos \frac{1}{2} \gamma \pi \right) - \varepsilon^2 \frac{3k_2 F^2}{4\mu^2 \omega_0^{2\gamma+1}} \sin 2\gamma \pi, \tag{3-21}$$

and

$$\Omega = \omega_0 \left(1 + \frac{1}{2} \varepsilon \mu \omega_0^{\gamma-2} \cos \frac{1}{2} \gamma \pi + \frac{1}{8} \varepsilon^2 \mu^2 (2\gamma - 1) \omega_0^{2(\gamma-2)} \cos \gamma \pi + \varepsilon^2 \frac{3k_2 F^2}{4\mu^2 \omega_0^{2(\gamma+1)}} \cos 2\gamma \pi \right). \quad (3-22)$$

Reference to (3-20) shows that the solution involves two parts: the first corresponds to the damping vibrations and describes the transient process, while the second one is nondamping in character and describes forced vibrations with the frequency of the exciting force and with the phase difference depending on the fractional parameter γ . Note that in the first term of (3-20) the amplitude of the external force F does not affect the damping coefficient α (3-21), while it weakly influences the nonlinear frequency Ω of vibrations (3-22).

When $\gamma = 1$, Equation (3-20) goes over into the equation describing vibrations of the viscoelastic Duffing oscillator with ordinary Kelvin–Voigt constitutive relations, i.e.,

$$x = \varepsilon \left\{ a_0 e^{-\varepsilon \mu t/2} \cos \omega_0 \left[1 - \frac{\varepsilon^2 \mu^2}{4\omega_0^2} \left(\frac{1}{2} - \frac{3k_2 F^2}{\mu^4 \omega_0^2} \right) \right] t + \frac{F}{\mu \omega_0} \cos \left(\omega_0 t - \frac{\pi}{2} \right) \right\}. \quad (3-23)$$

It can be noted that if in the right-hand part of (3-6) one takes $\sin \omega t$ instead of the cosine function, then the first term in the solution remains unchanged, while in the second term of (3-20) or (3-23) the cosine function should be simply substituted with the sine function.

3B. Viscosity of the order of ε^2 . Now let us consider vibrations of a nonlinear oscillator putting $k = 2$ in the equation of motion (2-4):

$$\ddot{x} + \varepsilon^2 \mu \left(\frac{d}{dt} \right)^\gamma x + \omega_0^2 x + k_2 x^3 = \varepsilon^3 F \cos \omega t. \quad (3-24)$$

Substituting (3-5) into the right-hand side of (3-3) with $k = 2$, we obtain

$$D_0^2 x_2 + \omega_0^2 x_2 = -2i\omega_0 D_1 A_1 \exp(i\omega_0 T_0) + \text{c.c.} \quad (3-25)$$

To eliminate circular terms in (3-25), it is necessary to vanish to zero the coefficient standing at $\exp(i\omega_0 T_0)$, i.e.,

$$D_1 A_1(T_1, T_2) = 0,$$

whence it follows that A_1 is T_1 -independent.

Then the general solution of (3-25) has the form

$$x_2 = A_2(T_1, T_2) e^{i\omega_0 T_0} + \bar{A}_2(T_1, T_2) e^{-i\omega_0 T_0}. \quad (3-26)$$

Substituting (3-5) and (3-26) in the right-hand side of (3-4) with $k = 2$ and considering formula (1-4) and condition (2-5), we are led to this equation for determining x_3 :

$$D_0^2 x_3 + \omega_0^2 x_3 = -2i\omega_0 D_1 A_2 \exp(i\omega_0 T_0) - k_2 A_1^3 \exp(3i\omega_0 T_0) - (2i\omega_0 D_2 A_1 + \mu(i\omega_0)^\gamma A_1 + 3k_2 A_1^2 \bar{A}_1 - \frac{1}{2} F) \exp(i\omega_0 T_0) - \mu A_1 \frac{\sin \gamma \pi}{\pi} \int_0^\infty \frac{u^\gamma e^{-u T_0} du}{u + i\omega_0} + \text{c.c.} \quad (3-27)$$

From (3-27) it is evident that its last term does not generate secular terms and thus does not affect the solution constructed thereafter.

Eliminating secular terms in (3-27), we obtain the solvability conditions

$$D_1 A_2(T_1, T_2) = 0, \tag{3-28}$$

$$2i\omega_0 D_2 A_1 + \mu(i\omega_0)^\gamma A_1 + 3k_2 A_1^2 \bar{A}_1 - \frac{1}{2} F = 0. \tag{3-29}$$

From (3-28) it follows that A_2 is independent of T_1 .

We multiply (3-29) by \bar{A}_1 and write its complex conjugate. Separately adding and subtracting together the two conjugate equations, we find

$$3k_2\omega_0^{-1} A_1^2 \bar{A}_1^2 + i(\bar{A}_1 D_2 A_1 - A_1 D_2 \bar{A}_1) + 2\mu\omega_0^{\gamma-1} A_1 \bar{A}_1 \cos \frac{\pi}{2} \gamma - \frac{F}{4\omega_0} (A_1 + \bar{A}_1) = 0, \tag{3-30}$$

$$i(\bar{A}_1 D_2 A_1 + A_1 D_2 \bar{A}_1) + 2\mu i\omega_0^{\gamma-1} A_1 \bar{A}_1 \sin \frac{\pi}{2} \gamma + \frac{F}{4\omega_0} (A_1 - \bar{A}_1) = 0. \tag{3-31}$$

Representing the function $A_1(T_2)$ in the polar form

$$A_1 = a \exp(i\varphi),$$

we obtain from (3-30) and (3-31)

$$\dot{\varphi} - \frac{1}{2} \delta - \frac{3k_2}{2\omega_0} a^2 + \frac{1}{4\omega_0} F a^{-1} \cos \varphi = 0, \quad (a^2)^\cdot + s a^2 + \frac{1}{2\omega_0} F a \sin \varphi = 0, \tag{3-32}$$

where the superscript dot denotes the T_2 -derivative, $\delta = \mu\omega_0^{\gamma-1} \cos \frac{\pi}{2} \gamma$, and $s = \mu\omega_0^{\gamma-1} \sin \frac{\pi}{2} \gamma$.

Dividing the second equation in (3-32) by a we obtain

$$\dot{a} + \frac{1}{2} s a + \frac{1}{4\omega_0} F \sin \varphi = 0 \tag{3-33}$$

and then integrating (3-33), we obtain

$$a = \left(a_0 - \frac{F}{4\omega_0} \int_0^{T_2} e^{sT_2/2} \sin(\varphi(T_2)) dT_2 \right) e^{-sT_2/2} \tag{3-34}$$

To obtain the equation for determining the function $\varphi(T_2)$, rewrite (3-32)₂ as

$$(\ln a^2)^\cdot = -s - \frac{F}{2\omega_0} a^{-1} \sin \varphi, \tag{3-35}$$

multiply it by $\cos \varphi$ and add it to (3-32)₁ multiplied by $-\sin \varphi$. Considering (3-35), as a result we obtain

$$\begin{aligned} (\cos \varphi)^\cdot - \left(a_0 - \frac{F}{4\omega_0} \int_0^{T_2} e^{sT_2/2} \sqrt{1 - \cos^2 \varphi} dT_2 \right)^{-1} \frac{F}{4\omega_0} e^{sT_2/2} \cos \varphi \sqrt{1 - \cos^2 \varphi} \\ + \left(a_0 - \frac{F}{4\omega_0} \int_0^{T_2} e^{sT_2/2} \sqrt{1 - \cos^2 \varphi} dT_2 \right)^2 \frac{3k_2}{2\omega_0} e^{-sT_2} \sqrt{1 - \cos^2 \varphi} + \frac{1}{2} \delta \sqrt{1 - \cos^2 \varphi} = 0. \end{aligned} \tag{3-36}$$

Integrating (3-36), we find the T_2 -dependence of $\cos \varphi$, and then substituting the function $\sin \varphi(T_2)$ thus found in (3-35), we can obtain T_2 -dependence of a .

To find the functions $\varphi(T_2)$ and $a(T_2)$, we use another approach. Dividing (3-32)₁ by (3-33), we get

$$\frac{d\varphi}{da} = \frac{F(4\omega_0)^{-1}a^{-1} \cos \varphi - 3k_2(2\omega_0)^{-1}a^2 - 2^{-1}\delta}{2^{-1}sa + F(4\omega_0)^{-1} \sin \varphi} \tag{3-37}$$

or

$$\tan \chi(F) = \frac{d\varphi}{d(\ln a)} = \frac{F(4\omega_0)^{-1} \exp(-\ln a) \cos \varphi - 3k_2(2\omega_0)^{-1} \exp(2 \ln a) - 2^{-1}\delta}{2^{-1}s + F(4\omega_0)^{-1} \exp(-\ln a) \sin \varphi} \tag{3-38}$$

From (3-38) first we find the function $\varphi(a)$ and substituting it in (3-33), we can determine the function $a(T_2)$, hence, $\varphi[a(T_2)] = \varphi(T_2)$.

If on the right-hand part of (3-24) one takes $\sin \omega t$ instead of the cosine function, (3-38) takes on the form

$$\tan \chi(F) = \frac{d\varphi}{d(\ln a)} = \frac{F(4\omega_0)^{-1} \exp(-\ln a) \sin \varphi - 3k_2(2\omega_0)^{-1} \exp(2 \ln a) - 2^{-1}\delta}{2^{-1}s + F(4\omega_0)^{-1} \exp(-\ln a) \cos \varphi} \tag{3-39}$$

3B1. *The case of free vibrations.* At $F = 0$, the system (3-32) is reduced to the form

$$\dot{\varphi} - \frac{1}{2}\delta - \frac{3k_2}{2\omega_0} a^2 = 0, \quad (a^2)' + sa^2 = 0. \tag{3-40}$$

Integration yields

$$a^2 = a_0^2 e^{-sT_2}, \quad \varphi = \frac{1}{2} \delta T_2 - \frac{3k_2}{2\omega_0 s} a_0^2 e^{-sT_2} + \varphi_0, \tag{3-41}$$

where a_0 and φ_0 are the initial magnitudes of a and φ , respectively. Eliminating T_2 from (3-41), we find

$$\varphi = -\frac{\delta}{s} \ln \frac{a}{a_0} - \frac{3k_2}{2\omega_0 s} (a^2 - a_0^2) + \varphi_0, \tag{3-42}$$

or

$$G(\ln a, \varphi) = \frac{1}{2}\varphi s + \frac{1}{2}\delta \ln a + \frac{3k_2}{4\omega_0} \exp(2 \ln a) = G_0(\ln a_0, \varphi_0) \tag{3-43}$$

This relationship can be interpreted as the stream-function for the phase fluid moving in the plane with the coordinates $\ln a, \varphi$. Really, considering (3-40), it is followed from (3-43) that the components of the vector of the phase fluid motion $\vec{V} \{v_{\ln a} = (\ln a)', v_\varphi = \dot{\varphi}\}$ are determined by the formulas

$$(\ln a)' = -\frac{\partial G}{\partial \varphi}, \quad \dot{\varphi} = \frac{\partial G}{\partial (\ln a)}. \tag{3-44}$$

Since

$$dG = \frac{\partial G}{\partial \varphi} d\varphi + \frac{\partial G}{\partial (\ln a)} d(\ln a) = 0,$$

we obtain, taking into account (3-44),

$$-v_{\ln a} d\varphi + v_\varphi d(\ln a) = 0, \quad \text{or} \quad \frac{d\varphi}{v_\varphi} = \frac{d(\ln a)}{v_{\ln a}}. \tag{3-45}$$

This is the equation of the streamline.

In the case of free vibrations, it follows from (3-38) that $\tan \chi|_{F=0}$ defines the angle of inclination of the tangent to the streamline. If a is small, then

$$\tan \chi(0) = -\frac{\delta}{s} = -\cot \frac{\gamma\pi}{2} \quad \text{or} \quad \chi = \frac{\pi}{2} + \frac{\gamma\pi}{2}. \tag{3-46}$$

For large a from (3-38) it follows that

$$\tan \chi(0) \rightarrow -\infty \quad \text{or} \quad \chi \rightarrow \frac{\pi}{2} + . \tag{3-47}$$

The streamlines for the oscillator with natural frequency $\omega_0 = 1$ are presented in Figure 1 in the semilogarithmic coordinates $\ln a, \phi$. The top pane shows streamlines constructed for various G_0 and fixed $\gamma = 0.5$ and $k_2 = 0.1$. On the bottom left we have $G_0 = 0$ and $k_2 = 0.1$ fixed and varying γ . The bottom right pane presents the streamlines constructed for the fixed $G_0 = 0$ and $\gamma = 0.5$, while k_2 is used as the parameter.

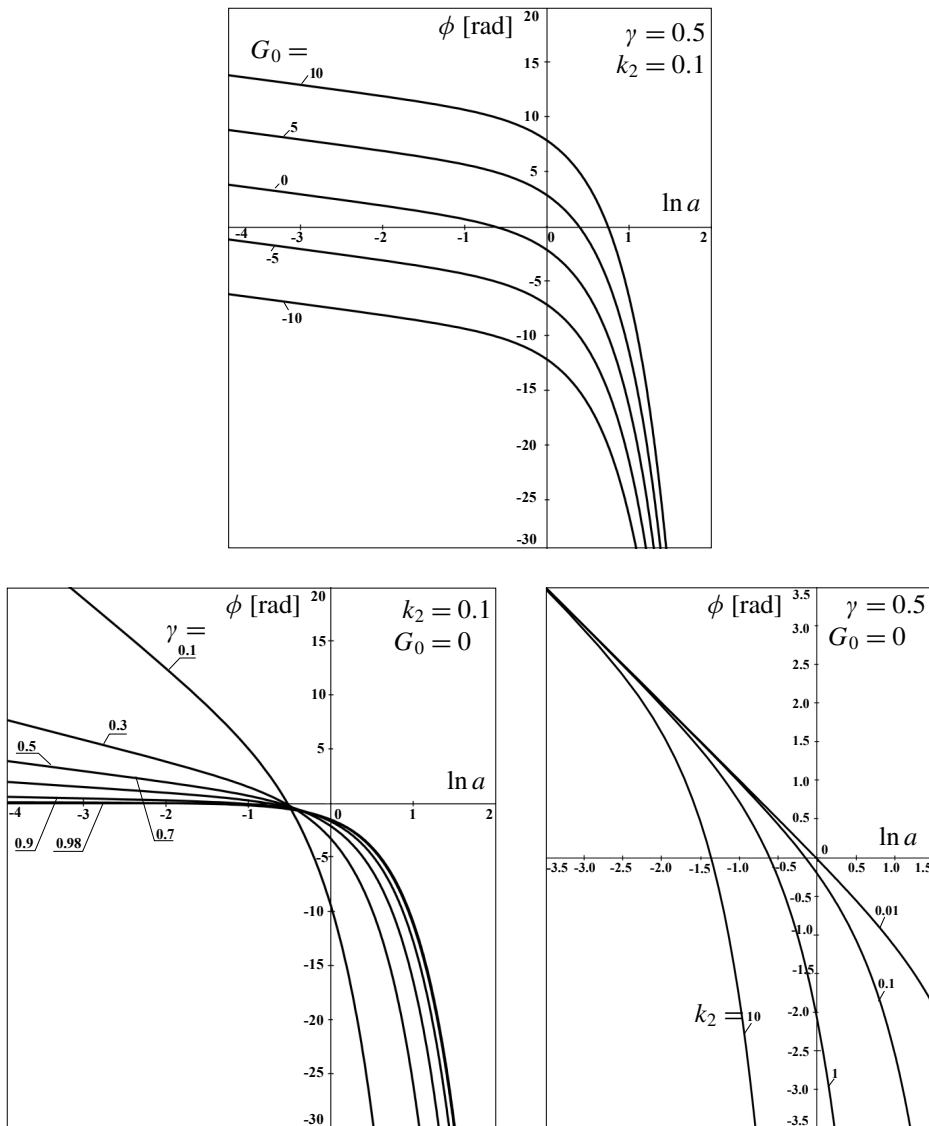


Figure 1. Streamlines of the phase fluid corresponding to different values of G_0 (top), fractional parameter γ (bottom left), and nonlinear stiffness coefficient k_2 (bottom right).

The asymptotic character of the curves in [Figure 1](#) is verified by relationships (3-46) and (3-47). In the first and last panes of the figure, the fractional parameter γ is fixed for all curves. Therefore their left branches are asymptotically parallel in the first case ([Figure 1](#), top) due to the different values of G_0 , and they tend to the same asymptote in the latter case ([Figure 1](#), bottom right) since the value of G_0 is shared. Further, from (3-46) and the bottom left pane of the figure it is seen that, for small values of a , the left branches of the curves approach infinitely close the vertical and horizontal axes as $\gamma \rightarrow 1$ and $\gamma \rightarrow 0$, respectively. Thus the curves in [Figure 1](#) show that the various parameters have different effects upon the behavior of the curves.

The solution for nonlinear free damped vibrations has the form

$$x = \varepsilon a_0 e^{-at/2} \cos(\Omega t + \varphi_0 - da_0^2 e^{-at}), \tag{3-48}$$

where

$$\alpha = \varepsilon^2 \mu \omega_0^{\gamma-1} \sin \frac{\pi}{2} \gamma, \quad d = \frac{3}{2} k_2 (\mu \omega_0^\gamma \sin \frac{\pi}{2} \gamma)^{-1}, \quad \Omega = \omega_0 (1 + \frac{1}{2} \varepsilon^2 \mu \omega_0^{\gamma-2} \cos \frac{\pi}{2} \gamma).$$

In the particular case when $\gamma = 1$, the solution takes the form

$$x = \varepsilon a_0 e^{-\varepsilon^2 \mu t/2} \cos\left(\omega_0 t + \varphi_0 - \frac{3k_2}{2\mu\omega_0} a_0^2 e^{-\varepsilon^2 \mu t}\right), \tag{3-49}$$

3B2. *The case of small force amplitude.* If the amplitude F of the external force is small, [Equation \(3-37\)](#) takes the form

$$\frac{d\varphi}{da} = -\frac{\delta}{s} a^{-1} - \frac{3k_2}{\omega_0 s} a + F f(a, \varphi), \tag{3-50}$$

where

$$f(a, \varphi) = \frac{\cos \varphi}{2\omega_0 s a^2} + \frac{\sin \varphi}{\omega_0 s^2 a^2} \left(\frac{3k_2 a^2}{2\omega_0} + \frac{1}{2} \delta \right).$$

Integrating (3-50) yields

$$\varphi = -\frac{\delta}{s} \ln \frac{a}{a_0} - \frac{3k_2}{2\omega_0 s} (a^2 - a_0^2) + \varphi_0 + F \int_{a_0}^a f[a, \varphi(a)] da, \tag{3-51}$$

or

$$\frac{1}{2} \varphi s + \frac{1}{2} \delta \ln a + \frac{3k_2}{4\omega_0} e^{2\ln a} = G_0 + \frac{1}{2} s F \int_{a_0}^a f[a, \varphi(a)] da. \tag{3-52}$$

From this relationship it is evident that the streamlines do not remain unchanged; they vary even for small external forces.

3B3. *The case of finite force amplitude.* To investigate the influence of a finite exciting force $F \cos \omega t$ (or $F \sin \omega t$) on the character of the oscillator’s vibratory motions, let us choose some streamline and assume that at $t = 0$ a phase fluid point lie somewhere on this line. If the external force $F \cos \omega t$ or $F \sin \omega t$ acts on the oscillator beginning from the moment $t = 0$, the phase fluid point under consideration moves, according to (3-38) or (3-39), respectively, along a trajectory that does not coincide with the chosen streamline. We can take another point on the same streamline and calculate the trajectory according to the same equations, and so on. If after some instant of time we connect with a curve the points thus found, lying on the different trajectories, and compare this curve to the reference streamline, we can judge by

the departure of one line from the other the character of the transient vibratory motion occurring in the mechanical system after the external force begins to act.

Relationships (3-38) and (3-39) define the angle of inclination of the tangent to the trajectory of the phase fluid point. For small a from (3-38) it follows that

$$\tan \chi = \cot \varphi \quad \text{or} \quad \chi = \frac{\pi}{2} - \varphi \quad \text{or} \quad \chi = \frac{3\pi}{2} - \varphi, \tag{3-53}$$

while from (3-39) for small a we have

$$\tan \chi = \tan \varphi \quad \text{or} \quad \chi = \varphi \quad \text{or} \quad \chi = \pi + \varphi. \tag{3-54}$$

The tangent vectors to the trajectories of motion for the phase fluid points (i.e., the polarization vector of motion of the given system) at different points of the streamline with the parameters $G_0 = 0$, $\gamma = 0.5$, and $k_2 = 0.1$ are presented in Figure 2, at the instant the force $F \cos \omega t$ or $F \sin \omega t$ begins to take effect ($T_2 = 0$).

Examination of the left half of the figure shows that under the action of the force $F \cos \omega t$ the polarization vector executes a vibrational motion with a decrease in $\ln a$: first it rotates counterclockwise until attaining the maximal angle $\chi = 164.5^\circ$ at the point with the coordinates $\ln a_0 = -1.18$, $\varphi_0 = 1.18$, and it then begins to rotate in a clockwise direction. From the right half of the figure it is seen that for the oscillator driven by the force $F \sin \omega t$ the polarization vector executes a counterclockwise rotational motion with the decrease in $\ln a$: the angle χ increases monotonically starting from 90° and tending to make a complete turn as $a_0 \rightarrow 0$.

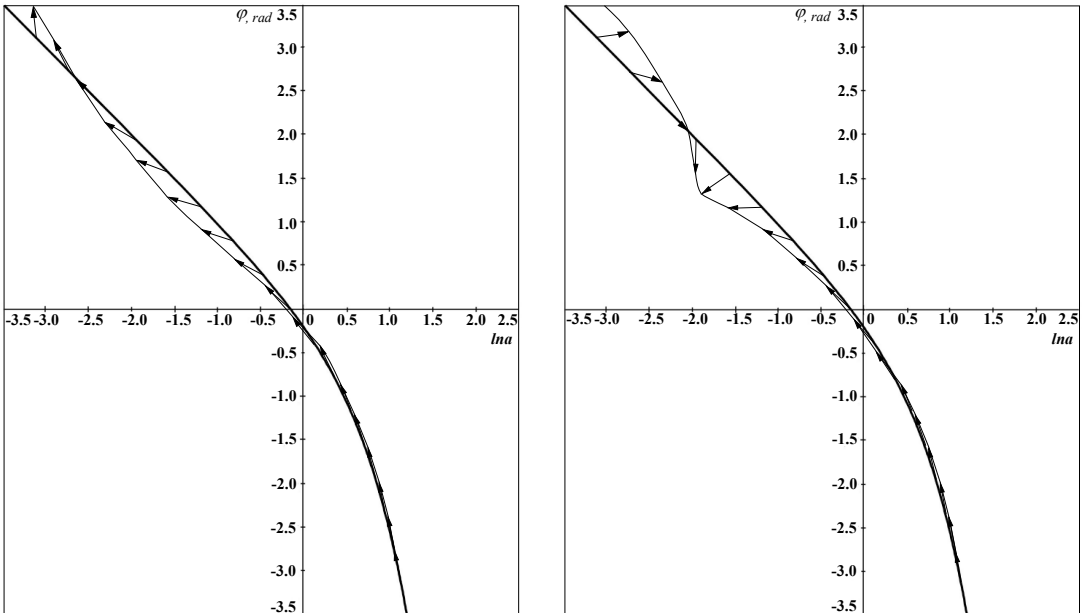


Figure 2. Directions of the polarization vectors of the system’s vibrational motions at the instant the force $F \cos \omega t$ (left) or $F \sin \omega t$ (right) takes effect, for $F = 0.5$.

Figure 2 makes it clear that at the instant the external exciting force begins to take effect on the system the points of the phase fluid leave the stream line either to the left or to the right of it and start to move along their own trajectories. In other words, the stream lines disappear the moment the force is applied.

4. Conclusion

The engineering analytical approach proposed in [Rossikhin and Shitikova 2009] for the approximate analysis of the dynamic behavior of linear and nonlinear fractional oscillators has been generalized to the case of forced vibrations. It allows the authors to analyze the force-driven vibrations of a fractional oscillator of Duffing type at different low-level orders of damping and external force terms using the method of multiple time scales.

In the case of viscosity of the order of ε and the external exciting force of the order of ε^2 , it has been shown that the solution involves two parts, where the first term corresponds to damping vibrations and describes the transient process, while the second one is nondamping in character and describes forced vibrations with the frequency of the exciting force and with a phase difference depending on the fractional parameter γ .

In the case of free vibrations with a weak damping term of the order of ε^2 , the nonlinear fractional oscillator performs steady-state vibrations, which are in compliance with the phase fluid motion in the phase plane along the streamlines in the direction of decreasing amplitude of vibrations. At the instant the small external force of the order of ε^3 begins to take effect, vibrations of the nonlinear fractional oscillator go over into transient ones, leading to the disappearance of the stream lines, while the phase fluid points lying on the streamlines at the moment of the force application start to follow their own phase trajectories.

It has been shown that the integral term in formula (1-4) does not affect the solution of either problem within the chosen approximation framework, so it is sufficient to use formula (1-3) regardless of the values of the driving frequency or the fractional parameter.

Appendix

It is well known [Janke et al. 1960; Abramowitz and Stegun 1964] that many special functions exist in two equivalent representations: as incomplete integrals and as infinite power series.

To show the validity of formula (1-4), we apply the Laplace transformation to the expression $x(t) = D_{0+}^\gamma e^{i\omega t}$, obtaining

$$\bar{x}(p) = \frac{p^\gamma}{p - i\omega}. \tag{4-1}$$

Applying the Mellin–Fourier inversion formula

$$x(t) = \frac{1}{2\pi i} \int_{c-i\infty}^{c+i\infty} \frac{p^\gamma e^{pt}}{p - i\omega} dp, \tag{4-2}$$

to go back to the time domain, and using the integration contour presented in Figure 3, we find

$$x(t) = \sum_k \text{res}(\bar{x}(p_k)e^{p_k t}) + \frac{1}{2\pi i} \int_0^\infty (\bar{x}(ue^{-i\pi}) - \bar{x}(ue^{i\pi}))e^{-ut} du. \tag{4-3}$$

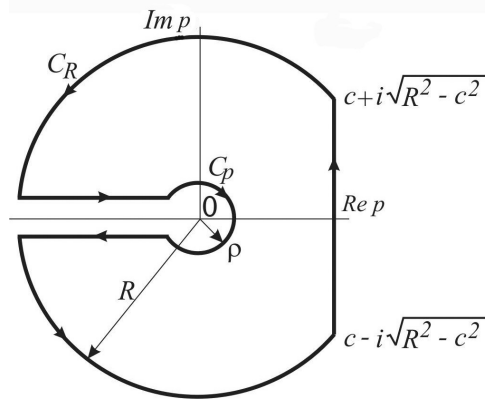


Figure 3. Integration contour used in the proof of (1-4).

Formula (1-4) follows immediately from (4-3).

For the function $x(t)$, it is possible to obtain another representation in the form of an infinite series. For this purpose, we rewrite formula (4-1) as

$$\bar{x}(p) = \frac{p^{\gamma-1} p}{p - i\omega} = \frac{p^{\gamma-1}}{1 - i\omega p^{-1}} \tag{4-4}$$

Now express this last fraction as the sum of an infinite descending geometric progression with initial term $p^{\gamma-1}$ and ratio $i\omega p^{-1}$:

$$\frac{p^{\gamma-1}}{1 - i\omega p^{-1}} = \sum_{n=1}^{\infty} (i\omega)^{n-1} p^{\gamma-n} = \sum_{n=0}^{\infty} (i\omega)^n p^{\gamma-n-1}. \tag{4-5}$$

The inversion of formula (4-5) gives

$$x(t) = t^\nu \sum_{n=0}^{\infty} \frac{Z^n}{\Gamma(n + 1 + \nu)} = \frac{t^\nu}{\Gamma(\nu)} \sum_{n=0}^{\infty} \frac{Z^n}{\nu(\nu + 1) \dots (\nu + n)}, \tag{4-6}$$

where $\nu = -\gamma$ and $Z = i\omega t$. We next use the equalities [Janke et al. 1960]

$$\sum_{n=0}^{\infty} \frac{Z^n}{\nu(\nu + 1) \dots (\nu + n)} = e^Z Z^{-\nu} \gamma(\nu, Z)$$

and

$$\gamma^*(\nu, Z) = \frac{Z^{-\nu}}{\Gamma(\nu)} \gamma(\nu, Z),$$

where $\gamma(\nu, Z)$ is the incomplete gamma function [Janke et al. 1960; Abramowitz and Stegun 1964], finally we obtain

$$x(t) = t^\nu e^Z \gamma^*(\nu, Z) = t^{-\gamma} e^{i\omega t} \gamma^*(-\gamma, i\omega t). \tag{4-7}$$

Formula (4-7) coincides (apart from notation) with that discussed in [Miller and Ross 1993].

In the present paper, the first representation for the function $x(t)$, resulting in formula (1-4), has been adopted, since it is more convenient and physically admissible for engineering applications.

Formulas (1-3) and (1-4) can also be easily obtained from the similar expressions for fractional integrals presented in [Samko et al. 1993, Tables 9.1 and 9.2].

Acknowledgements

The authors thank the reviewers for their valuable comments, which helped improved the manuscript.

References

- [Abdel-Ghaffar and Scanlan 1985] A. M. Abdel-Ghaffar and R. H. Scanlan, “Ambient vibration studies of Golden Gate Bridge, I: Suspended structure”, *J. Eng. Mech. (ASCE)* **111**:4 (1985), 463–482.
- [Abramowitz and Stegun 1964] M. Abramowitz and I. A. Stegun (editors), *Handbook of mathematical functions with formulas, graphs, and mathematical tables*, United States National Bureau of Standards Applied Mathematics Series **55**, U. S. Government Printing Office, Washington, DC, 1964.
- [Agrawal 2004] O. P. Agrawal, “Analytical solution for stochastic response of a fractionally damped beam”, *J. Vib. Acoust. (ASME)* **126**:4 (2004), 561–566.
- [Aprile et al. 1997] A. Aprile, J. A. Inaudi, and J. M. Kelly, “Evolutionary model of viscoelastic dampers for structural applications”, *J. Eng. Mech. (ASCE)* **123**:6 (1997), 551–560.
- [Atanackovic and Stankovic 2008] T. M. Atanackovic and B. Stankovic, “On a numerical scheme for solving differential equations of fractional order”, *Mech. Res. Commun.* **35**:7 (2008), 429–438.
- [Chen and Zhu 2009] L. C. Chen and W. Q. Zhu, “Stochastic averaging of strongly nonlinear oscillators with small fractional derivative damping under combined harmonic and white noise excitations”, *Nonlinear Dynam.* **56**:3 (2009), 231–241.
- [Cooke and Keltie 1987] J. A. Cooke and R. F. Keltie, “Determination of the impulse response of a viscoelastic beam using a fractional derivative constitutive model”, pp. 137–141 in *The role of damping in vibration and noise control* (Boston, 1987), edited by L. Rogers and J. C. Simonis, Design Engineering **5**, ASME, New York, 1987.
- [Deng et al. 2003] R. Deng, P. Davies, and A. K. Bajaj, “Flexible polyurethane foam modelling and identification of viscoelastic parameters for automotive seating applications”, *J. Sound Vib.* **262**:3 (2003), 391–417.
- [Gao and Yu 2005] X. Gao and J. Yu, “Chaos in the fractional order periodically forced complex Duffing’s oscillators”, *Chaos Solitons Fract.* **24**:4 (2005), 1097–1104.
- [Giovagnoni and Berti 1992] M. Giovagnoni and G. Berti, “A fractional derivative model for single-link mechanism vibration”, *Meccanica (Milano)* **27**:2 (1992), 131–138.
- [Gusella and Terenzi 2001] V. Gusella and G. Terenzi, “Time-domain analysis of structures with dampers modelled by fractional derivatives”, pp. 251–260 in *Earthquake resistant engineering structures III* (Malaga, 2001), edited by C. A. Brebbia and A. Corz, Advances in Earthquake Engineering **9**, WIT, Southampton, 2001.
- [He 1998] J.-H. He, “Approximate analytical solution for seepage flow with fractional derivatives in porous media”, *Comput. Methods Appl. Mech. Eng.* **167**:1-2 (1998), 57–68.
- [Hwang and Hsu 2001] J. S. Hwang and T. Y. Hsu, “A fractional derivative model to include effect of ambient temperature on HDR bearings”, *Eng. Struct.* **23**:5 (2001), 484–490.
- [Hwang and Ku 1997] J. S. Hwang and S. W. Ku, “Analytical modeling of high damping rubber bearings”, *J. Struct. Eng. (ASCE)* **123**:8 (1997), 1029–1036.
- [Janke et al. 1960] E. Janke, F. Emde, and F. Lösch, *Tafeln Höherer Funktionen*, 6th ed., Teubner, Stuttgart, 1960.
- [Koh and Kelly 1990] C. G. Koh and J. M. Kelly, “Application of fractional derivatives to seismic analysis of base-isolated models”, *Earthquake Eng. Struct. Dyn.* **19**:2 (1990), 229–241.
- [Li et al. 2003] G.-G. Li, Z.-Y. Zhu, and C.-J. Cheng, “Application of Galerkin method to dynamical behavior of viscoelastic Timoshenko beam with finite deformation”, *Mech. Time-Depend. Mater.* **7**:2 (2003), 175–188.
- [Makris and Constantinou 1991] N. Makris and M. Constantinou, “Fractional-derivative Maxwell model for viscous dampers”, *J. Struct. Eng. (ASCE)* **117**:9 (1991), 2708–2724.

- [Miller and Ross 1993] K. S. Miller and B. Ross, *An introduction to the fractional calculus and fractional differential equations*, Wiley, New York, 1993.
- [Munshi 1997] J. A. Munshi, “Effect of viscoelastic dampers on hysteretic response of reinforced concrete elements”, *Eng. Struct.* **19**:11 (1997), 921–935.
- [Nasuno et al. 2006] H. Nasuno, N. Shimizu, and T. Yasuno, “Geometrical nonlinear static and dynamical models of fractional derivative viscoelastic body”, *Trans. Jpn. Soc. Mech. Eng. C* **72**:4 (2006), 1041–1048. In Japanese.
- [Nayfeh 1973] A. H. Nayfeh, *Perturbation methods*, Wiley, New York, 1973.
- [Padovan and Sawicki 1998] J. Padovan and J. T. Sawicki, “Nonlinear vibrations of fractionally damped systems”, *Nonlinear Dynam.* **16**:4 (1998), 321–336.
- [Rossikhin and Shitikova 1997a] Y. A. Rossikhin and M. V. Shitikova, “Application of fractional derivatives for the analysis of nonlinear damped vibrations of suspension bridges”, pp. 541–544 in *Proceedings of the 1997 International Symposium on Nonlinear Theory and its Applications (NOLTA '97)* (Honolulu, HI, 1997), vol. 1, Research Society of NOLTA, IEICE, Tokyo, 1997.
- [Rossikhin and Shitikova 1997b] Y. A. Rossikhin and M. V. Shitikova, “Applications of fractional calculus to dynamic problems of linear and nonlinear hereditary mechanics of solids”, *Appl. Mech. Rev. (ASME)* **50**:1 (1997), 15–67.
- [Rossikhin and Shitikova 1998] Y. A. Rossikhin and M. V. Shitikova, “Application of fractional calculus for analysis of nonlinear damped vibrations of suspension bridges”, *J. Eng. Mech. (ASCE)* **124**:9 (1998), 1029–1036.
- [Rossikhin and Shitikova 2000] Y. A. Rossikhin and M. V. Shitikova, “Analysis of nonlinear vibrations of a two-degree-of-freedom mechanical system with damping modelled by a fractional derivative”, *J. Eng. Math.* **37**:4 (2000), 343–362.
- [Rossikhin and Shitikova 2001] Y. A. Rossikhin and M. V. Shitikova, “Analysis of dynamic behaviour of viscoelastic rods whose rheological models contain fractional derivatives of two different orders”, *Z. Angew. Math. Mech.* **81**:6 (2001), 363–376.
- [Rossikhin and Shitikova 2003] Y. A. Rossikhin and M. V. Shitikova, “Free damped nonlinear vibrations of a viscoelastic plate under two-to-one internal resonance”, *Mater. Sci. Forum* **440-441** (2003), 29–36.
- [Rossikhin and Shitikova 2004] Y. A. Rossikhin and M. V. Shitikova, “Analysis of the viscoelastic rod dynamics via models involving fractional derivatives or operators of two different orders”, *Shock Vib. Digest* **36**:1 (2004), 3–26.
- [Rossikhin and Shitikova 2006] Y. A. Rossikhin and M. V. Shitikova, “Analysis of free non-linear vibrations of a viscoelastic plate under the conditions of different internal resonances”, *International Journal of Non-Linear Mechanics* **41**:2 (2006), 313–325.
- [Rossikhin and Shitikova 2008] Y. A. Rossikhin and M. V. Shitikova, “Nonlinear free damped vibrations of suspension bridges with uncertain fractional damping”, *J. Eur. Syst. Autom.* **42**:6–8 (2008), 879–894.
- [Rossikhin and Shitikova 2009] Y. A. Rossikhin and M. V. Shitikova, “New approach for the analysis of damped vibrations of fractional oscillators”, *Shock Vib.* **16**:4 (2009), 365–387.
- [Samko et al. 1993] S. G. Samko, A. A. Kilbas, and O. I. Marichev, *Fractional integrals and derivatives: theory and applications*, edited by S. M. Nikol’skiĭ, Gordon and Breach, Yverdon, 1993.
- [Schäfer 2000] I. Schäfer, “Beschreibung der Dämpfung in Stäben mittels fraktionaler Zeitableitungen”, *Z. Angew. Math. Mech.* **80**:5 (2000), 356–360.
- [Schäfer and Kempfle 2004] I. Schäfer and S. Kempfle, “Impulse responses of fractional damped systems”, *Nonlinear Dynam.* **38**:1–2 (2004), 61–68.
- [Schäfer and Seifert 2002] I. Schäfer and H. J. Seifert, “Description of the impulse response in rods by fractional derivatives”, *Z. Angew. Math. Mech.* **82**:6 (2002), 423–427.
- [Schmidt and Gaul 2006] A. Schmidt and L. Gaul, “On the numerical evaluation of fractional derivatives in multi-degree-of-freedom systems”, *Signal Process.* **86**:10 (2006), 2592–2601.
- [Seredyńska and Hanyga 2000] M. Seredyńska and A. Hanyga, “Nonlinear Hamiltonian equations with fractional damping”, *J. Math. Phys.* **41**:4 (2000), 2135–2156.
- [Seredyńska and Hanyga 2005] M. Seredyńska and A. Hanyga, “Nonlinear differential equations with fractional damping with applications to the 1dof and 2dof pendulum”, *Acta Mech.* **176**:3–4 (2005), 169–183.

- [Sheu et al. 2007] L.-J. Sheu, H.-K. Chen, J.-H. Chen, and L.-M. Tam, “Chaotic dynamics of the fractionally damped Duffing equation”, *Chaos Solitons Fract.* **32**:4 (2007), 1459–1468.
- [Singh and Chatterjee 2006] S. J. Singh and A. Chatterjee, “Galerkin projections and finite elements for fractional order derivatives”, *Nonlinear Dynam.* **45**:1-2 (2006), 183–206.
- [Sjöberg and Kari 2003] M. Sjöberg and L. Kari, “Nonlinear isolator dynamics at finite deformations: an effective hyperelastic, fractional derivative, generalized friction model”, *Nonlinear Dynam.* **33**:3 (2003), 323–336.
- [Wahi and Chatterjee 2004] P. Wahi and A. Chatterjee, “Averaging oscillations with small fractional damping and delayed terms”, *Nonlinear Dynam.* **38**:1-2 (2004), 3–22.

Received 26 Sep 2008. Revised 4 Aug 2009. Accepted 18 Aug 2009.

YURIY A. ROSSIKHIN: yar@vgasu.vrn.ru

*Department of Structural Mechanics, Voronezh State University of Architecture and Civil Engineering,
84, 20-letija Oktjabrja Street, Voronezh 394006, Russia*

MARINA V. SHITIKOVA: shitikova@vmail.ru

*Department of Structural Mechanics, Voronezh State University of Architecture and Civil Engineering,
84, 20-letija Oktjabrja Street, Voronezh 394006, Russia*

TATIANA SHCHEGLOVA: laguna@vmail.ru

*Department of Structural Mechanics, Voronezh State University of Architecture and Civil Engineering,
84, 20-letija Oktjabrja Street, Voronezh 394006, Russia*

A TWO-TEMPERATURE GENERALIZED THERMOELASTIC MEDIUM SUBJECTED TO A MOVING HEAT SOURCE AND RAMP-TYPE HEATING: A STATE-SPACE APPROACH

HAMDY M. YOUSSEF

We construct a model of two-temperature generalized thermoelasticity for an elastic half-space with constant elastic parameters. The Laplace transform and state-space techniques are used to obtain the general solution for any set of boundary conditions. The general solution obtained is applied to the specific problem of a half-space subjected to a moving heat source with constant velocity and ramp-type heating. The inverse Laplace transforms are computed numerically. The effects of different values of the heat source velocity, the two-temperature parameter, and the ramping time parameter are compared.

A list of symbols can be found on page 1648.

1. Introduction

P. J. Chen and collaborators [Chen and Gurtin 1968; Chen and Williams 1968; Chen et al. 1969] formulated a theory of heat conduction in deformable bodies, which depends upon two temperatures: the conductive temperature φ and the dynamical temperature T . For time-independent situations, the difference between these two temperatures is proportional to the heat supply. In the absence of any heat supply, the two temperatures are identical [Chen and Gurtin 1968]. For time-dependent problems, however, and for wave propagation problems in particular, the two temperatures can be different regardless of the presence of a heat supply. The two temperatures, T and φ , and the strain are found to have representations in the form of a traveling wave plus a response, which occurs instantaneously throughout the body [Boley and Tolins 1962].

Warren and Chen [1973] investigated the wave propagation in the two-temperature theory of thermoelasticity. In [Youssef 2006b] we investigated this theory in the context of the generalized theory of thermoelasticity.

In most earlier studies, mechanical or thermal loading on the bounding surface is considered to be in the form of a shock. However, the sudden jump in the load is merely an idealized situation, because it is impossible to realize a pulse described mathematically by a step function; even a very rapid rise time (on the order of 10^{-9} s) may be slow in terms of the continuum. This is particularly true in the case of second sound effects when the thermal relaxation times for typical metals are less than 10^{-9} s. It is thus felt that a finite rise time of the external load (mechanical or thermal) applied on the surface should be considered while studying a practical problem of this nature. Considering this aspect of rise time, Misra et al. [1991a; 1991b; 1992] solved some problems involving ramp-type heating. In [Youssef 2005] we used the state-space approach to solve the generalized thermoelasticity problem of an infinite material with a spherical

Keywords: generalized thermoelasticity, two-temperature, heat source, ramp type.

cavity and variable thermal conductivity subjected to ramp-type heating. Later we found the solutions of the problem of a generalized thermoelastic infinite medium with a cylindrical cavity subjected to a ramp-type heating and loading [2006a] and the two-dimensional generalized thermoelasticity problem for a half-space subjected to ramp-type heating [2006c]. In [Youssef and Al-Lehaibi 2007] we used the state-space approach in the problem of two-temperature generalized thermoelasticity while in [Bassiouny and Youssef 2008] we solved the two-temperature generalized thermopiezoelectricity problem of a finite rod subjected to different types of thermal loading. In [Youssef 2008] solved the two-dimensional problem of a two-temperature generalized thermoelastic half-space subjected to ramp-type heating. Al-Huniti et al. [2001] discussed the dynamic response of a rod due to a moving heat source under the hyperbolic heat conduction model.

Here we consider a half-space filled with an elastic material with constant elastic parameters. The governing equations are written in the context of two-temperature generalized thermoelasticity theory. A moving heat source with constant velocity is applied to the medium. Laplace transforms and state-space techniques are used to obtain the general solution for any set of boundary conditions. The general solution obtained is applied to a half-space subjected to ramp-type heating with a traction-free bounding plane. The inverse Laplace transforms are computed numerically using the Riemann sum approximation method. The effects of the heat source velocity, the two-temperature parameter, and the ramping time parameter are estimated.

1.1. Formulation of the problem. According to our model, the heat conduction equation takes the form [Youssef 2006b]

$$K\varphi_{,ii} = \left(\frac{\partial}{\partial t} + \tau_0 \frac{\partial^2}{\partial t^2}\right)(\rho C_E \theta + \gamma T_0 e) - \left(1 + \tau_0 \frac{\partial}{\partial t}\right) Q, \quad i = 1, 2, 3. \quad (1)$$

The constitutive equations take the form

$$\sigma_{ij} = 2\mu e_{ij} + \lambda e_{kk} \delta_{ij} - \gamma \theta \delta_{ij}, \quad i = 1, 2, 3, \quad (2)$$

where δ_{ij} is the Kronecker delta function

The equations of motion without body forces take the form

$$\sigma_{ij,j} = \rho \ddot{u}_i, \quad i = 1, 2, 3. \quad (3)$$

The relation between the heat conduction and the thermodynamic heat takes the form

$$\varphi - T = a\varphi_{,ii}, \quad i = 1, 2, 3, \quad (4)$$

where a is a nonnegative parameter called the two-temperature parameter [Youssef 2006b].

Now, we will suppose an elastic and homogeneous half-space $x \geq 0$ which obeys Equations (1)–(4) and is initially quiescent, where all the state functions depend only on the dimension x and the time t .

The displacement components for a one-dimensional medium have the form

$$u_x = u(x, t), \quad u_y = u_z = 0. \quad (5)$$

The strain component takes the form

$$e = e_{xx} = \frac{\partial u}{\partial x}. \quad (6)$$

The heat conduction equation takes the form

$$K \frac{\partial^2 \varphi}{\partial x^2} = \left(\frac{\partial}{\partial t} + \tau_0 \frac{\partial^2}{\partial t^2} \right) (\rho C_E T + \gamma T_0 e) - \left(1 + \tau_0 \frac{\partial}{\partial t} \right) Q. \tag{7}$$

The constitutive equation takes the form

$$\sigma_{xx} = \sigma = (2\mu + \lambda)e - \gamma(T - T_0). \tag{8}$$

The equation of motion takes the form

$$\frac{\partial^2 \sigma}{\partial x^2} = \rho \frac{\partial^2 e}{\partial t^2}. \tag{9}$$

The relation between the heat conduction and the thermodynamic heat takes the form

$$\varphi - T = a \frac{\partial^2 \varphi}{\partial x^2}. \tag{10}$$

For simplicity, we will use the nondimensional variables

$$x \leftarrow c_0 \eta x, \quad t \leftarrow c_0^2 \eta t, \quad \tau_0 \leftarrow c_0^2 \eta \tau_0, \quad \theta \leftarrow \frac{\theta}{T_0}, \quad \varphi \leftarrow \frac{\varphi}{T_0}, \quad \sigma \leftarrow \frac{\sigma}{2\mu + \lambda}, \quad Q \leftarrow \frac{Q}{K_0 c_0^2 \eta^2 T_0},$$

where

$$c_0^2 = \frac{2\mu + \lambda}{\rho}, \quad \eta = \frac{\rho C_E}{K}.$$

Hence, we have the system of equations

$$\frac{\partial^2 \varphi}{\partial x^2} = \left(\frac{\partial}{\partial t} + \tau_0 \frac{\partial^2}{\partial t^2} \right) (\theta + \varepsilon e) - \left(1 + \tau_0 \frac{\partial}{\partial t} \right) Q, \quad \sigma = e - b\theta, \quad \frac{\partial^2 \sigma}{\partial x^2} = \frac{\partial^2 e}{\partial t^2}, \quad \varphi - \theta = \beta \frac{\partial^2 \varphi}{\partial x^2}, \tag{11}$$

where

$$\varepsilon = \frac{\gamma}{\rho C_E}, \quad b = \frac{\gamma T_0}{\lambda + 2\mu}, \quad \beta = a c_0^2 \eta^2.$$

Applying the Laplace transform

$$\bar{f}(s) = \int_0^\infty f(t) e^{-st} dt$$

to the equations in (11), we obtain

$$\frac{d^2 \bar{\varphi}}{dx^2} = (s + \tau_0 s^2) \bar{\theta} + (s + \tau_0 s^2) \varepsilon \bar{e} - (1 + \tau_0 s) \bar{Q}. \tag{12}$$

We consider that the medium is subjected to a moving heat source of constant strength releasing its energy continuously while moving along the x -axis in the positive direction with a constant velocity v . This moving heat source is assumed to be of the nondimensional form [Al-Huniti et al. 2001]

$$Q = Q_0 \delta(x - vt), \tag{13}$$

where Q_0 is the constant heat source strength and δ is the delta function.

After using a Laplace transformation, we get

$$\bar{Q} = \ell \exp\left(\frac{s}{v} x\right), \quad \ell = \frac{Q_0}{v}. \tag{14}$$

To simplify the notation we set $h = \frac{s}{v}$. Then we have

$$\frac{d^2\bar{\varphi}}{dx^2} = (s + \tau_0s^2)\bar{\theta} + (s + \tau_0s^2)\varepsilon\bar{e} - (1 + \tau_0s)\ell e^{-hx}, \tag{15}$$

$$\bar{\sigma} = \bar{e} - b\bar{\theta}, \quad \frac{d^2\bar{\sigma}}{dx^2} = s^2\bar{e}, \quad \bar{\theta} = \bar{\varphi} - \beta\frac{d^2\bar{\varphi}}{dx^2}, \tag{16}$$

where all the initial state functions are equal to zero.

Eliminating \bar{e} and $\bar{\theta}$ from these equations, we obtain

$$\frac{d^2\bar{\varphi}}{dx^2} = (1 + \varepsilon b)s\alpha_1\bar{\varphi} + s\varepsilon\alpha_1\bar{\sigma} - \ell\alpha_1e^{-hx}, \quad \text{where } \alpha_1 = \frac{1 + \tau_0s}{1 + \beta(s + \tau_0s^2)(1 + b\varepsilon)}, \tag{17}$$

and

$$\frac{d^2\bar{\sigma}}{dx^2} = \alpha_2\bar{\sigma} + \alpha_3\bar{\varphi} + \alpha_4\ell e^{-hx}, \tag{18}$$

where

$$\alpha_2 = s^2(1 - \beta\varepsilon s b\alpha_1), \quad \alpha_3 = s^2b(1 - \beta s\alpha_1(1 + b\varepsilon)), \quad \alpha_4 = s^2b\beta\alpha_1.$$

Then, we have

$$\bar{\theta} = (1 - \beta s\alpha_1(1 + b\varepsilon))\bar{\varphi} - \beta\varepsilon s\alpha_1\bar{\sigma} + \beta\alpha_1\ell e^{-hx}. \tag{19}$$

2. State-space approach

Choosing as state variables the temperature of heat conduction $\bar{\varphi}$ and the stress component $\bar{\sigma}$ in the x -direction, equations (18) and (19) can be written in matrix form as

$$\frac{d^2\bar{V}(x, s)}{dx^2} = A(s)\bar{V}(x, s) + F(s)e^{-hx}, \tag{20}$$

where

$$\bar{V}(x, s) = \begin{bmatrix} \bar{\varphi}(x, s) \\ \bar{\sigma}(x, s) \end{bmatrix}, \quad A(s) = \begin{bmatrix} s(1 + b\varepsilon)\alpha_1 & s\varepsilon\alpha_1 \\ \alpha_3 & \alpha_2 \end{bmatrix}, \quad F(s) = \begin{bmatrix} -\ell\alpha_1 \\ \ell\alpha_4 \end{bmatrix}.$$

Solutions of (20) that remain bounded for large x (that is, not involving diverging exponentials) can be written as

$$\bar{V}(x, s) = \exp(-\sqrt{A(s)}x)C(s) + D(s)e^{-hx}, \tag{21}$$

where $C(s) = \begin{bmatrix} C_1(s) \\ C_2(s) \end{bmatrix}$ is to be determined, and $D(s) = \begin{bmatrix} D_1 \\ D_2 \end{bmatrix} = (h^2I - A(s))^{-1}F(s)$, with $I = \begin{bmatrix} 1 & 0 \\ 0 & 1 \end{bmatrix}$.

We will use the Cayley–Hamilton theorem to find the matrix $\exp(-\sqrt{A(s)}x)$. The characteristic equation of $A(s)$ is

$$k^2 - k(s(1 + b\varepsilon)\alpha_1 + \alpha_2) + \alpha_1s((1 + b\varepsilon)\alpha_2 - \varepsilon\alpha_3) = 0; \tag{22}$$

that is, the characteristic roots k_1 and k_2 satisfy

$$k_1 + k_2 = s(1 + b\varepsilon)\alpha_1 + \alpha_2, \quad k_1k_2 = s(1 + b\varepsilon)\alpha_1\alpha_2 - s\varepsilon\alpha_1\alpha_3. \tag{23}$$

Next we write the spectral decomposition of $A(s)$ in terms of the projectors E_1 and E_2 of $A(s)$ (see [Cullen 1972] for details):

$$A(s) = k_1 E_1 + k_2 E_2 \tag{24}$$

By definition, the projectors satisfy $E_1 + E_2 = I$, $E_1 E_2 = E_2 E_1 = 0$, and $E_i^2 = E_i$ for $i = 1, 2$. Thus

$$A E_1 = k_1 E_1^2 + k_2 E_2 E_1 = k_1 E_1. \tag{25}$$

Similarly, $A E_2 = k_2 E_2$, so $A(I - E_1) = k_2 I - k_2 E_1$. Adding this latter equation to (25) we obtain $A = k_2 I + (k_1 - k_2) E_1$, which is to say, $E_1 = (A - k_2 I)/(k_1 - k_2)$. Taking into account (23) to achieve simplifications, and following a similar reasoning for E_2 , we reach the explicit form of the projectors:

$$E_1 = \frac{1}{k_1 - k_2} \begin{bmatrix} k_1 - \alpha_2 & s \varepsilon \alpha_1 \\ \frac{(\alpha_2 - k_2)(k_1 - \alpha_2)}{s \varepsilon \alpha_1} & \alpha_2 - k_2 \end{bmatrix}, \quad E_2 = \frac{1}{k_1 - k_2} \begin{bmatrix} \alpha_2 - k_2 & -s \varepsilon \alpha_1 \\ \frac{(\alpha_2 - k_2)(\alpha_2 - k_1)}{s \varepsilon \alpha_1} & k_1 - \alpha_2 \end{bmatrix}. \tag{26}$$

The matrix $\sqrt{A(s)}$ has the same projectors as $A(s)$ and its characteristic roots p_1, p_2 are given by $p_1 = \sqrt{k_1}$ and $p_2 = \sqrt{k_2}$. That is,

$$B(s) := \sqrt{A(s)} = \sqrt{k_1} E_1 + \sqrt{k_2} E_2 = \frac{A + \sqrt{k_1 k_2} I}{\sqrt{k_1} + \sqrt{k_2}} = \frac{1}{\sqrt{k_1} + \sqrt{k_2}} \begin{bmatrix} \sqrt{k_1 k_2} + s(1 + b \varepsilon) \alpha_1 & s \varepsilon \alpha_1 \\ \alpha_3 & \sqrt{k_1 k_2} + \alpha_2 \end{bmatrix}.$$

Thus the matrix exponential in (21) is given by

$$\exp(-\sqrt{A(s)} x) = \exp(-B(s) x) = \sum_{n=0}^{\infty} \frac{(-B(s) x)^n}{n!}. \tag{27}$$

By the Cayley–Hamilton theorem, the positive powers of B are linear combinations of I and B . Thus, the infinite series in (27) is of the form

$$\exp(-B(s)) = b_0(x, s) I + b_1(x, s) B(s), \tag{28}$$

where b_0 and b_1 are coefficients depending on s and x . To find these coefficients, note that the characteristic roots p_1 and p_2 of B satisfy

$$e^{-p_1 x} = b_0 + b_1 p_1, \quad e^{-p_2 x} = b_0 + b_1 p_2. \tag{29}$$

Solving this linear system, we get $b_0 = \frac{1}{p_1 - p_2} (p_1 e^{-p_2 x} - p_2 e^{-p_1 x})$ and $b_1 = \frac{1}{p_1 - p_2} (e^{-p_1 x} - e^{-p_2 x})$. Hence the entries of the matrix

$$\exp(-B(s) x) = L_{ij}(x, s) \quad i, j = 1, 2,$$

are given by

$$L_{11} = \frac{(k_1 - \alpha_2) e^{-\sqrt{k_1} x} - (k_2 - \alpha_2) e^{-\sqrt{k_2} x}}{k_1 - k_2}, \quad L_{12} = \frac{s \varepsilon \alpha_1 (e^{-\sqrt{k_1} x} - e^{-\sqrt{k_2} x})}{k_1 - k_2},$$

$$L_{22} = \frac{e^{-\sqrt{k_1} x} (\alpha_2 - k_2) - e^{-\sqrt{k_2} x} (\alpha_2 - k_1)}{k_1 - k_2}, \quad L_{21} = \frac{\alpha_3 (e^{-\sqrt{k_1} x} - e^{-\sqrt{k_2} x})}{k_1 - k_2}.$$

Similarly,

$$D_1 = \frac{\ell \alpha_1 (\alpha_2 + s \varepsilon \alpha_4 - h^2)}{(h^2 - k_1)(h^2 - k_2)}, \quad D_2 = \frac{\ell (h^2 \alpha_4 - \alpha_1 \alpha_3 - \alpha_1 \alpha_4 s (1 + b \varepsilon))}{(h^2 - k_1)(h^2 - k_2)}.$$

We can write the solution (21) in the form

$$\begin{bmatrix} \bar{\varphi}(x, s) \\ \bar{\sigma}(x, s) \end{bmatrix} = \begin{bmatrix} L_{11}(x, s) & L_{12}(x, s) \\ L_{21}(x, s) & L_{22}(x, s) \end{bmatrix} \begin{bmatrix} C_1(s) \\ C_2(s) \end{bmatrix} + \begin{bmatrix} D_1(s) \\ D_2(s) \end{bmatrix} e^{-hx}. \tag{30}$$

To get C_1 and C_2 we set $x = 0$ on the last equation, and we get

$$\begin{bmatrix} \bar{\varphi}(0, s) \\ \bar{\sigma}(0, s) \end{bmatrix} = \begin{bmatrix} L_{11}(0, s) & L_{12}(0, s) \\ L_{21}(0, s) & L_{22}(0, s) \end{bmatrix} \begin{bmatrix} C_1(s) \\ C_2(s) \end{bmatrix} + \begin{bmatrix} D_1(s) \\ D_2(s) \end{bmatrix},$$

which gives

$$\begin{bmatrix} C_1(s) \\ C_2(s) \end{bmatrix} = \begin{bmatrix} \bar{\varphi}(0, s) \\ \bar{\sigma}(0, s) \end{bmatrix} - \begin{bmatrix} D_1(s) \\ D_2(s) \end{bmatrix}. \tag{31}$$

Hence, for any set of boundary conditions, we have

$$\begin{aligned} \bar{\varphi}(x, s) &= (\bar{\varphi}(0, s) - D_1) L_{11}(x, s) + (\bar{\sigma}(0, s) - D_2) L_{12}(x, s) + D_1 e^{-hx}, \\ \bar{\sigma}(x, s) &= (\bar{\varphi}(0, s) - D_1) L_{21}(x, s) + (\bar{\sigma}(0, s) - D_2) L_{22}(x, s) + D_2 e^{-hx}. \end{aligned} \tag{32}$$

3. Application

We now consider the boundary conditions on the boundary plane $x = 0$, which are of two forms:

- (1) *Thermal boundary condition.* We suppose that the boundary plane $x = 0$ is subjected to ramp-type heating as follows [Youssef 2005]:

$$\varphi(0, t) = \begin{cases} 0 & \text{if } t \leq 0, \\ \varphi_0 \frac{t}{t_0} & \text{if } 0 < t < t_0, \\ \varphi_0 & \text{if } t \geq t_0, \end{cases} \tag{33}$$

where t_0 is called the ramping parameter and φ_0 is constant. After Laplace transformation, we get

$$\bar{\varphi}(0, s) = \frac{\varphi_0 (1 - e^{-st_0})}{s^2 t_0}. \tag{34}$$

- (2) *Mechanical boundary condition.* We consider the boundary plane $x = 0$ traction-free, so $\sigma(0, t) = 0$, which gives, after Laplace transformation,

$$\bar{\sigma}(0, s) = 0. \tag{35}$$

Applying (34) and (35) to (32) we get the solution for the heat conduction and stress x -component in the Laplace transform domain:

$$\begin{aligned} \bar{\varphi}(x, s) &= \varphi_1(s) e^{-\sqrt{k_1} x} - \varphi_2(s) e^{-\sqrt{k_2} x} + D_1(s) e^{-hx}, \\ \bar{\sigma}(x, s) &= \sigma_1(s) e^{-\sqrt{k_1} x} - \sigma_2(s) e^{-\sqrt{k_2} x} + D_2(s) e^{-hx}, \end{aligned} \tag{36}$$

where

$$\begin{aligned} \varphi_1(s) &= \frac{1}{k_1 - k_2} \left[\left(\frac{\varphi_0(1 - e^{-st_0})}{s^2 t_0} - D_1 \right) (k_1 - \alpha_2) - s \varepsilon \alpha_1 D_2 \right], \\ \varphi_2(s) &= \frac{1}{k_1 - k_2} \left[\left(\frac{\varphi_0(1 - e^{-st_0})}{s^2 t_0} - D_1 \right) (k_2 - \alpha_2) - s \varepsilon \alpha_1 D_2 \right], \\ \sigma_1(s) &= \frac{1}{k_1 - k_2} \left[\left(\frac{\varphi_0(1 - e^{-st_0})}{s^2 t_0} - D_1 \right) \alpha_3 - D_2 (\alpha_2 - k_2) \right], \\ \sigma_2(s) &= \frac{1}{k_1 - k_2} \left[\left(\frac{\varphi_0(1 - e^{-st_0})}{s^2 t_0} - D_1 \right) \alpha_3 - D_2 (\alpha_2 - k_1) \right]. \end{aligned}$$

By substituting the expressions (36) into (19), we obtain

$$\bar{\theta}(x, s) = (1 - \beta k_1) \varphi_1(s) e^{-\sqrt{k_1} x} - (1 - \beta k_2) \varphi_2(s) e^{-\sqrt{k_2} x} + (1 - \beta h^2) D_1(s) e^{-hx}. \tag{37}$$

From (16)₂ and by using (36)₂, we obtain the displacement:

$$\bar{u}(x, s) = -\frac{1}{s^2} (\sigma_1(s) \sqrt{k_1} e^{-\sqrt{k_1} x} - \sigma_2(s) \sqrt{k_2} e^{-\sqrt{k_2} x} + D_2(s) h e^{-hx}). \tag{38}$$

This completes the solution in the Laplace transform domain.

4. Numerical inversion of the Laplace transform

To determine numerically the conductive and thermal temperature, displacement, and stress distributions in the time domain, we used the Riemann sum approximation method. In this method, a function in the Laplace domain is inverted to the time domain through the sum

$$f(t) = \frac{e^{\kappa t}}{t} \left[\frac{1}{2} \bar{f}(\kappa) + \text{Re} \sum_{n=1}^N (-1)^n \bar{f} \left(\kappa + \frac{in\pi}{t} \right) \right], \tag{39}$$

where Re is the real part and *i* is the imaginary number unit. For faster convergence, numerical experiments have shown that the value of κ should satisfy the relation $\kappa t \approx 4.7$ [Tzou 1997].

5. Numerical results and discussion

Copper was chosen as the material for the numerical evaluations. The constants of the problem (see [Bassiouny and Youssef 2008]) were as follows:

$$\begin{aligned} K &= 386 \text{ N/K sec}, & \alpha_T &= 1.78 \times 10^{-5} \text{ K}^{-1}, & C_E &= 383.1 \text{ m}^2/\text{K}, & \eta &= 8886.73 \text{ m/sec}^2, \\ \mu &= 3.86 \times 10^{10} \text{ N/m}^2, & \lambda &= 7.76 \times 10^{10} \text{ N/m}^2, & \rho &= 8954 \text{ kg/m}^3, & \tau_0 &= 0.02 \text{ sec}, \\ T_0 &= 293 \text{ K}, & \varepsilon &= 1.618, & \beta &= 0.01, & b &= 0.01041. \end{aligned}$$

The computations were carried out for $t = 0.2$ and $\varphi_0 = 1.0$. The conductive temperature, the dynamical temperature, the stress and the displacement distributions are represented graphically with respect to *x*.

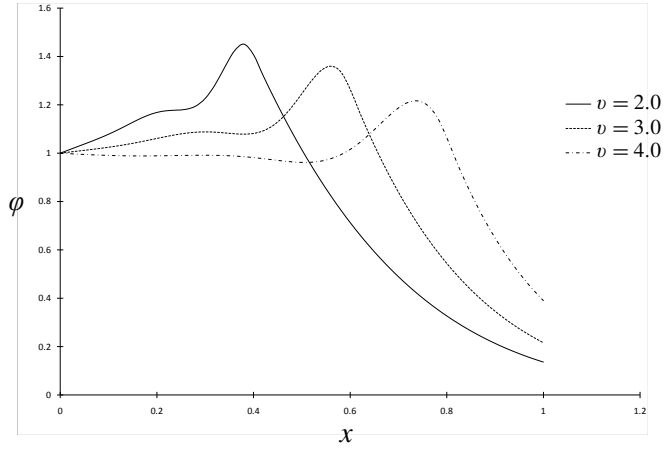


Figure 1. The conductive heat distribution at different values of the heat source velocity.

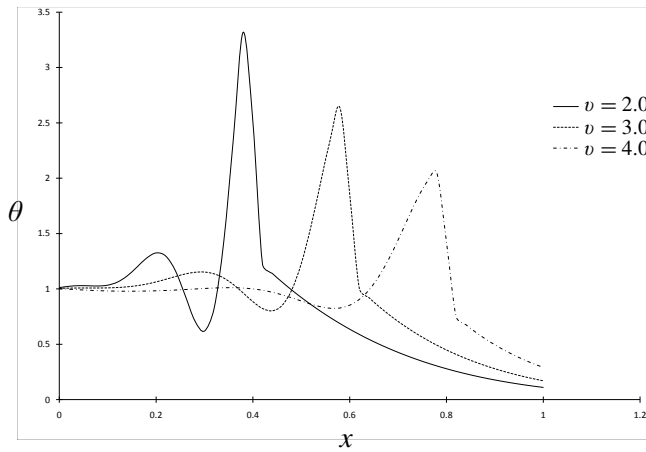


Figure 2. The thermodynamic heat distribution at different values of the heat source velocity.

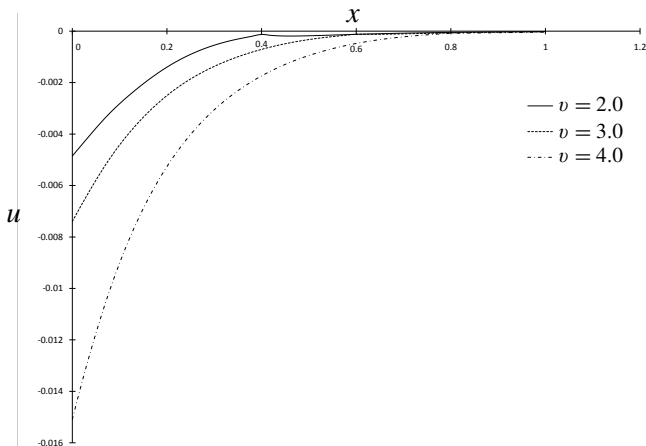


Figure 3. The displacement distribution at different values of the heat source velocity.

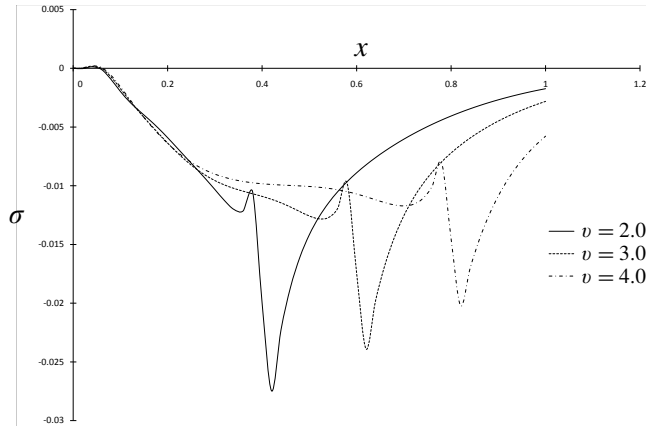


Figure 4. The stress distribution at different values of the heat source velocity.

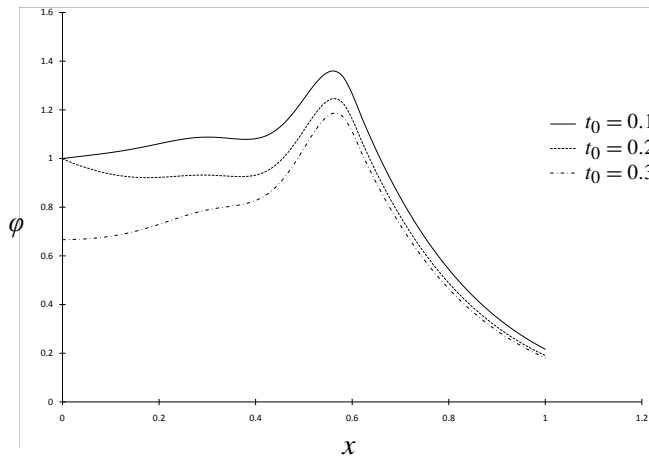


Figure 5. The conductive heat distribution at different values of the ramp time parameter.

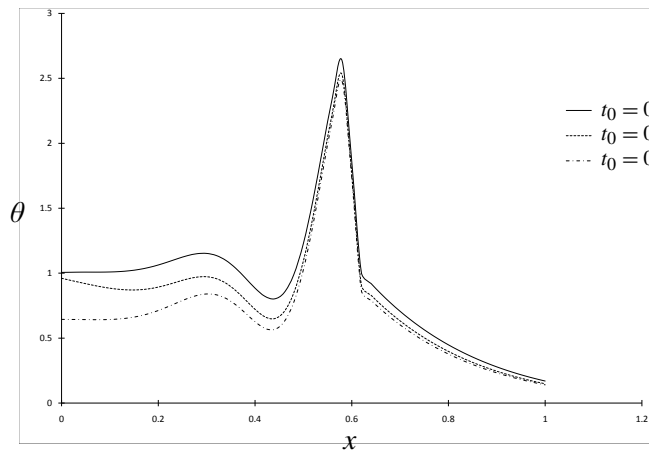


Figure 6. The thermodynamic heat distribution at different values of the ramp time parameter.

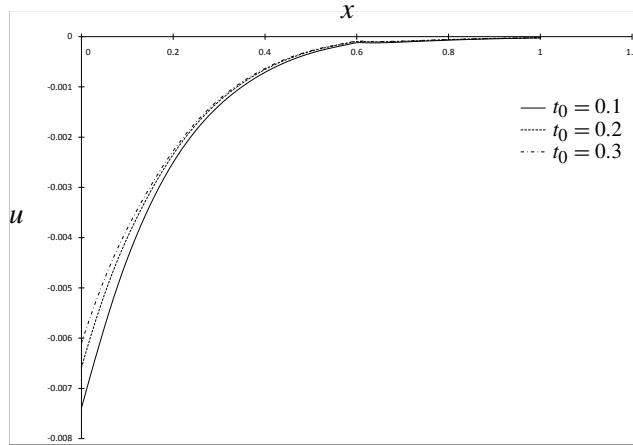


Figure 7. The displacement distribution at different values of the ramp time parameter.

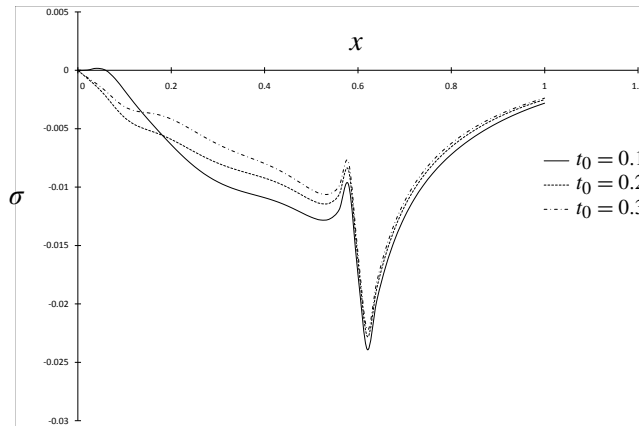


Figure 8. The stress distribution at different values of the ramp time parameter.

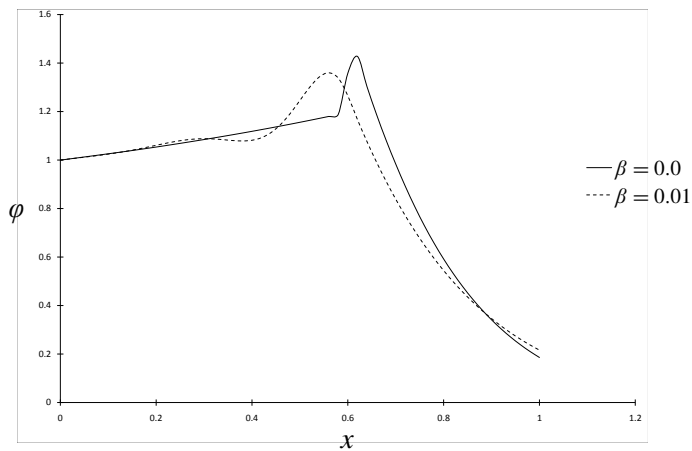


Figure 9. The conductive heat distribution for the L-S and Youssef models.

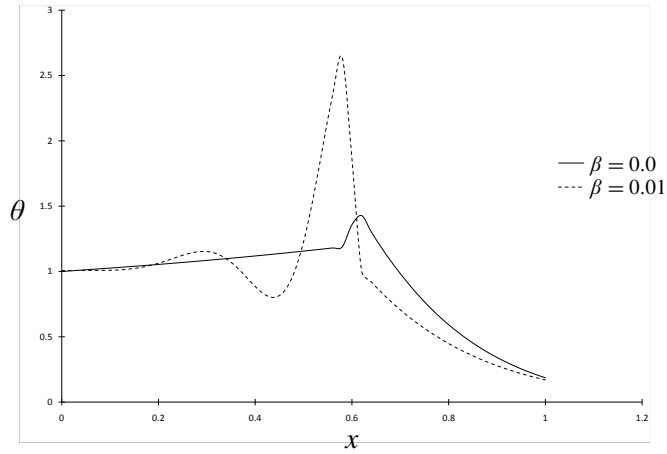


Figure 10. The thermodynamic heat distribution for the L–S and Youssef models.

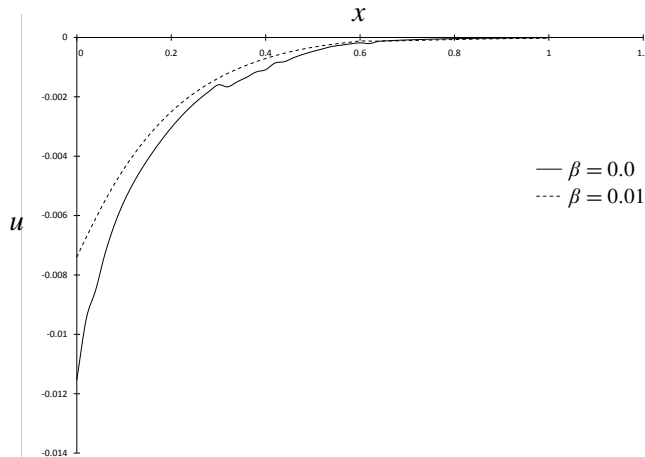


Figure 11. The displacement distribution for the L–S and Youssef models.

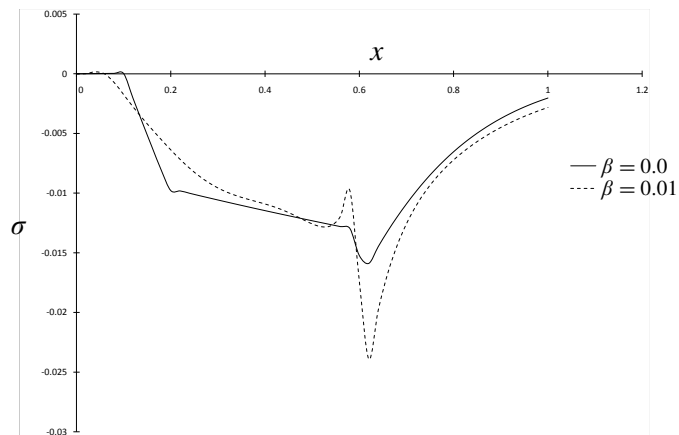


Figure 12. The stress distribution for the L–S and Youssef models.

Figures 1–4 display the conductive heat, the thermodynamic heat, the displacement, and the stress distributions at different values of heat source velocity v ($v = 2.0$, $v = 3.0$ and $v = 4.0$) to show its effect, where we have noticed that the heat source velocity parameter v has a significant effect on all the fields. The peak values of the conductive heat, the thermodynamic heat, and the stress are found at the points when $x = vt$ ($x = 4.0$, $x = 6.0$ and $x = 8.0$) which mean that the heat source releases its maximum energy at the point $x = vt$ and just after this point the values of that fields decrease with high speed.

Figures 5–8 display the conductive heat, the thermodynamic heat, the displacement, and the stress distributions at constant velocity of heat source $v = 3.0$ and different values of the ramping time parameter t_0 ($t_0 = 0.1$, $t_0 = 0.2$, and $t_0 = 0.3$). The figures show that this parameter has significant effect on all the fields. The conductive heat and the thermodynamic heat decrease when the value of t_0 increases and the absolute values of the displacement and the stress also decrease when the value of t_0 increases. This gives this type of heating real character, more than the thermal shocks in previous works.

Figures 9–12 display the conductive heat, the thermodynamic heat, the displacement, and the stress distributions at constant velocity of heat source $v = 3.0$ and constant value of the ramping time parameter $t_0 = 0.1$ but with different values of the nondimensional two-temperature parameter β ($\beta = 0.0$ and $\beta = 0.01$). This shows the difference between the one temperature generalized thermoelasticity of Lord and Shulman (L–S) and the two-temperature generalized thermoelasticity of Youssef. We can see the significant effect of that parameter on all the fields.

The phenomenon of finite speeds of propagation is manifest in all these figures. This is expected, since the thermal wave travels with a finite velocity. It should be mentioned that in Figures 1, 2, 5, 6, 9 and 10 the effects of the ramp-type heating on $x = 0$ of the half-space remain in a bounded region of space in the two generalized theories (Youssef and L–S) and do not reach infinity instantaneously.

Nomenclature

λ, μ Lamé constants	K thermal conductivity
ρ density	τ_0 relaxation times
C_E specific heat at constant strain	c_0 longitudinal wave speed ($= \sqrt{(\lambda + 2\mu)/\rho}$)
t time	η thermal viscosity, $= \rho C_E / K$
T dynamical temperature	ε dimensionless thermoelastic coupling constant ($= \gamma / (\rho C_E)$)
T_0 reference temperature	a two-temperature parameter, $a > 0$
θ dynamical temperature increment ($= T - T_0$)	β dimensionless two-temperature parameter ($= ac_0^2 \eta^2$)
φ conductive temperature	b dimensionless mechanical coupling constant ($= \gamma T_0 / (\lambda + 2\mu)$)
α_T coefficient of linear thermal expansion	t_0 ramping parameter
γ equal to $\alpha_T(3\lambda + 2\mu)$	v heat source velocity
σ_{ij} components of stress tensor	
e_{ij} components of strain tensor	
u_i components of displacement vector	

References

- [Al-Huniti et al. 2001] N. S. Al-Huniti, M. A. Al-Nimr, and M. Naji, “Dynamic response of rod due to a moving heat source under the hyperbolic heat conduction model”, *J. Sound Vib.* **242**:4 (2001), 629–640.

- [Bassiouny and Youssef 2008] E. Bassiouny and H. M. Youssef, “Two-temperature generalized thermopiezoelectricity of finite rod subjected to different types of thermal loading”, *J. Therm. Stresses* **31**:3 (2008), 233–245.
- [Boley and Tolins 1962] B. A. Boley and I. S. Tolins, “Transient coupled thermoelastic boundary value problems in the half-space”, *J. Appl. Mech. (ASME)* **29** (1962), 637–646.
- [Chen and Gurtin 1968] P. J. Chen and M. E. Gurtin, “On a theory of heat conduction involving two temperatures”, *Z. Angew. Math. Phys.* **19**:4 (1968), 614–627.
- [Chen and Williams 1968] P. J. Chen and W. O. Williams, “A note on non-simple heat conduction”, *Z. Angew. Math. Phys.* **19**:6 (1968), 969–970.
- [Chen et al. 1969] P. J. Chen, M. E. Gurtin, and W. O. Williams, “On the thermodynamics of non-simple elastic materials with two temperatures”, *Z. Angew. Math. Phys.* **20**:1 (1969), 107–112.
- [Cullen 1972] C. G. Cullen, *Matrices and linear transformations*, 2nd ed., Addison-Wesley, Reading, MA, 1972.
- [Misra et al. 1991a] J. C. Misra, S. C. Samanta, and A. K. Chakrabarti, “Magneto-thermoelastic interaction in an aeolotropic solid cylinder subjected to a ramp-type heating”, *Int. J. Eng. Sci.* **29**:9 (1991), 1065–1075.
- [Misra et al. 1991b] J. C. Misra, S. C. Samanta, A. K. Chakrabarti, and S. C. Misra, “Magneto-thermoelastic interaction in an infinite elastic continuum with a cylindrical hole subjected to ramp-type heating”, *Int. J. Eng. Sci.* **29**:12 (1991), 1505–1514.
- [Misra et al. 1992] S. C. Misra, S. C. Samanta, and A. K. Chakrabarti, “Transient magneto-thermoelastic waves in a viscoelastic half-space produced by ramp-type heating of its surface”, *Comput. Struct.* **43**:5 (1992), 951–957.
- [Tzou 1997] D. Y. Tzou, *Macro- to microscale heat transfer: the lagging behavior*, Series in chemical and mechanical engineering, Taylor & Francis, Washington, DC, 1997.
- [Warren and Chen 1973] W. E. Warren and P. J. Chen, “Wave propagation in the two temperature theory of thermoelasticity”, *Acta Mech.* **16**:1-2 (1973), 21–33.
- [Youssef 2005] H. M. Youssef, “State-space approach on generalized thermoelasticity for an infinite material with a spherical cavity and variable thermal conductivity subjected to ramp-type heating”, *Canadian Appl. Math. Quarterly* **13**:4 (2005).
- [Youssef 2006a] H. M. Youssef, “Problem of generalized thermoelastic infinite medium with cylindrical cavity subjected to a ramp-type heating and loading”, *Arch. Appl. Mech.* **75**:8-9 (2006), 553–565.
- [Youssef 2006b] H. M. Youssef, “Theory of two-temperature-generalized thermoelasticity”, *IMA J. Appl. Math.* **71**:3 (2006), 383–390.
- [Youssef 2006c] H. M. Youssef, “Two-dimensional generalized thermoelasticity problem for a half-space subjected to ramp-type heating”, *Eur. J. Mech. A Solids* **25**:5 (2006), 745–763.
- [Youssef 2008] H. M. Youssef, “Two-dimensional problem of a two-temperature generalized thermoelastic half-space subjected to ramp-type heating”, *Comput. Math. Model.* **19**:2 (2008), 201–216.
- [Youssef and Al-Lehaibi 2007] H. M. Youssef and E. A. Al-Lehaibi, “State-space approach of two-temperature generalized thermoelasticity of one-dimensional problem”, *Int. J. Solids Struct.* **44**:5 (2007), 1550–1562.

Received 9 Nov 2008. Revised 21 Mar 2009. Accepted 25 Mar 2009.

HAMDY M. YOUSSEF: yousefanne@yahoo.com

Mathematics Department, Alexandria University, Alexandria, Egypt

and

Faculty of Engineering, Umm Al-Qura University, PO Box 5555, Makkah, Saudi Arabia

A PLANE STRESS PERFECTLY PLASTIC MODE I CRACK PROBLEM FOR A YIELD CRITERION BASED ON THE SECOND AND THIRD INVARIANTS OF THE DEVIATORIC STRESS TENSOR, II

DAVID J. UNGER

In the first paper with this title (*J. Mech. Mater. Struct.* 3:4 (2008), 795–807), the solution of a stress function of a mode I perfectly plastic crack problem was found analytically for two of the three sectors that comprise the solution of the problem for a yield condition based on the second and third invariants of the deviatoric stress tensor. Here an exact solution is derived for the remaining sector of this crack problem, which comprises the singular solution of the governing differential equation.

1. Introduction

In [Unger 2008] we obtained a statically admissible solution for the opening mode of fracture under plane stress loading conditions for a yield condition containing both the second and third invariants of the deviatoric stress tensor. The second-order nonlinear differential equation of the singular solution of this particular crack problem was reduced to a first-order differential equation of the thirtieth degree in the previous analysis. At that time an analytical solution was believed to be intractable and an approximation was used to solve the problem. Here the singular solution is reduced to quadrature by introducing a parametric formulation of the yield condition. This process allows the exact solution to be evaluated in implicit form with the aid of incomplete elliptic integrals of the first and third kinds.

In terms of the deviatoric stress invariants the yield condition employed in [Unger 2008] assumes the algebraic form

$$J_2^3 - \left(\frac{3}{2}J_3\right)^2 = \frac{2}{81}\sigma_0^6, \quad (1)$$

where

$$J_2 \equiv \frac{1}{3}(\sigma_1 + \sigma_2)^2 - \sigma_1\sigma_2 \quad \text{and} \quad J_3 \equiv \frac{1}{3}(\sigma_1 + \sigma_2)\left(\frac{2}{9}(\sigma_1 + \sigma_2)^2 - \sigma_1\sigma_2\right) \quad (2)$$

are the second and third invariants [Chakrabarty 1987] of the deviatoric stress tensor, σ_1 and σ_2 being the principal stresses and σ_0 the yield stress in tension. A representation of this yield condition is shown in Figure 1 in the principal stress plane (σ_1, σ_2) along with a comparison with the Mises and Tresca yield conditions. A rotation of the coordinate axes to (ξ, η) in the principal stress plane, given by

$$\sigma_1 = \frac{\xi + \eta}{\sqrt{2}}, \quad \sigma_2 = \frac{\xi - \eta}{\sqrt{2}}, \quad (3)$$

Keywords: plane stress, mode I crack, perfectly plastic, yield condition, second and third invariants of deviatoric stress tensor, differential algebraic equation, DAE.

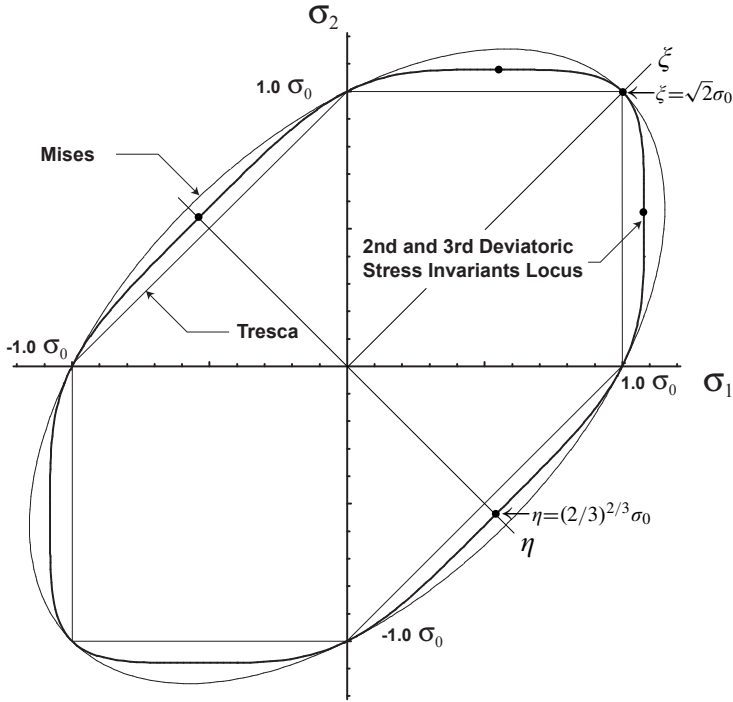


Figure 1. Three yield loci in the principal stress plane. The black dots on the darker curve correspond, clockwise from second quadrant, to $\mu = -\infty, -\frac{1}{3}, 0, \frac{1}{3}, \infty$,

further allows the yield condition to be expressed as a comparatively simple algebraic equation in the form of the sextic

$$2\zeta^6 + 45\zeta^4\eta^2 + 81\eta^6 = 16\sigma_0^6. \tag{4}$$

The homogeneous structure of the left-hand side of (4) suggests the introduction of the ratio μ :

$$\eta = \mu\zeta. \tag{5}$$

By substituting η from (5) into (4) and solving for ζ in terms of μ , one obtains the following parametric representation of the yield locus:

$$\zeta = \frac{2^{2/3}\sigma_0}{(2 + 45\mu^2 + 81\mu^6)^{1/6}}, \quad \eta = \frac{2^{2/3}\sigma_0\mu}{(2 + 45\mu^2 + 81\mu^6)^{1/6}}. \tag{6}$$

Equations (3) and (5) allow the identification of the parameter μ in terms of the principal stresses as

$$\mu = \frac{\sigma_1 - \sigma_2}{\sigma_1 + \sigma_2}. \tag{7}$$

The locations of several specific values of μ are indicated on the yield locus in Figure 1.

2. Singular solution

In order to satisfy the equations of equilibrium in the plane, a stress function in polar coordinates (r, θ) was introduced in [Unger 2008]. The stresses, which are independent of the coordinate r , assume the following relationships with the stress function $f(\theta)$ and its first two derivatives with respect to θ , $f'(\theta)$ and $f''(\theta)$:

$$\sigma_\theta = 2f(\theta), \quad \tau_{r\theta} = -f'(\theta) = -p, \quad \sigma_r = f''(\theta) + 2f(\theta) = p \frac{dp}{df} + 2f, \quad (8)$$

where σ_r and σ_θ are the normal stresses in the radial and transverse directions, respectively, and $\tau_{r\theta}$ is the in-plane shear stress. In terms of the previously defined stress coordinates (ζ, η) , the following relationships exist among the in-plane stresses:

$$\zeta = \frac{\sigma_1 + \sigma_2}{\sqrt{2}} = \frac{\sigma_r + \sigma_\theta}{\sqrt{2}}, \quad \eta = \frac{\sigma_1 - \sigma_2}{\sqrt{2}} = \frac{\sqrt{(\sigma_r - \sigma_\theta)^2 + 4\tau_{r\theta}^2}}{\sqrt{2}}. \quad (9)$$

We next define a function Q and its first derivative q with respect to f :

$$Q \equiv \frac{p^2}{2} + 2f^2 = \frac{\tau_{r\theta}^2 + \sigma_\theta^2}{2}, \quad (10)$$

$$q \equiv \frac{dQ}{df} = p \frac{dp}{df} + 4f = \sigma_r + \sigma_\theta = \sqrt{2}\zeta = \frac{2^{7/6}\sigma_0}{(2 + 45\mu^2 + 81\mu^6)^{1/6}}. \quad (11)$$

The chain rule of differentiation and (11) imply that

$$\frac{dq}{df} = \frac{dq}{d\mu} \frac{d\mu}{df} = -\frac{2^{1/6}6\mu(27\mu^4 + 5)\sigma_0}{(81\mu^6 + 45\mu^2 + 2)^{7/6}} \frac{d\mu}{df}. \quad (12)$$

The Clairaut operator U [Zwillinger 1989, pp. 158–160], associated with a certain class of differential equations to which the governing equation of this problem belongs, is defined by

$$U \equiv f \frac{dQ}{df} - Q = fq - Q. \quad (13)$$

The operational procedure to find the singular solution of a Clairaut equation is to first solve the differential equation for the operator U . Next, differentiate this expression with respect to the independent variable to generate a second equation. The elimination of the first derivative of the dependent variable with respect to the independent variable between the original equation and the second equation constitutes the singular solution to the problem [Zwillinger 1989, pp. 158–160]. In our case the dependent variable is Q and the independent variable is f . The first derivative of Q with respect to f is defined as q .

It is readily determined that the following relationships hold true from (6), (8), (9)–(11), and (13):

$$\sqrt{(\sigma_r - \sigma_\theta)^2 + 4\tau_{r\theta}^2} = \sqrt{q^2 - 8U} = \sqrt{2}\eta = \frac{2^{7/6}\sigma_0\mu}{(2 + 45\mu^2 + 81\mu^6)^{1/6}}. \quad (14)$$

By substituting q from (11) into (14) and solving for U one finds

$$U = \frac{\sigma_0^2(1 - \mu^2)}{2^{2/3}(2 + 45\mu^2 + 81\mu^6)^{1/3}}. \quad (15)$$

Differentiating U from (13) with respect to f and using the definition of q from (11), one establishes that

$$\frac{dU}{df} = q + f \frac{dq}{df} - \frac{dQ}{df} = f \frac{dq}{df}. \tag{16}$$

Introducing the parametric relationship between U and μ from Equation (15) and differentiating it with respect to the function f produces

$$f \frac{dq}{df} = \frac{dU}{df} = \frac{dU}{d\mu} \frac{d\mu}{df} = -\frac{2^{1/3} \mu (81\mu^4 + 30\mu^2 + 17) \sigma_0^2}{(81\mu^6 + 45\mu^2 + 2)^{4/3}} \frac{d\mu}{df}. \tag{17}$$

Dividing (17) by (12), a parametric representation of the singular solution f is found in terms of the parameter μ as

$$f = \left(f \frac{dq}{df} \right) / \frac{dq}{df} = \frac{(81\mu^4 + 30\mu^2 + 17) \sigma_0}{2^{5/6} 3 (27\mu^4 + 5) (81\mu^6 + 45\mu^2 + 2)^{1/6}}. \tag{18}$$

Solving for Q from (13) and substituting the parametric relationships for variables defined in (11), (15), and (18), one finds that

$$Q = fq - U = \frac{\sigma_0^2 (81\mu^6 + 81\mu^4 + 75\mu^2 + 19)}{2^{2/3} 3 (27\mu^4 + 5) (81\mu^6 + 45\mu^2 + 2)^{1/3}}. \tag{19}$$

Solving (10) for p and then substituting the parametric relationships for f and Q , established in (18) and (19), produces the parametric relationship

$$p = \sqrt{2Q - 4f^2} = \frac{2^{1/6} \sigma_0 (9\mu^2 - 1)^{3/2} (9\mu^4 + 3\mu^2 + 4)^{1/2}}{3 (27\mu^4 + 5) (81\mu^6 + 45\mu^2 + 2)^{1/6}}. \tag{20}$$

Differentiating f from (18) with respect to μ produces

$$\frac{df}{d\mu} = -\frac{3\sigma_0 \mu (9\mu^2 - 1)^2 (243\mu^8 + 324\mu^6 + 234\mu^4 + 148\mu^2 + 75)}{2^{5/6} (27\mu^4 + 5)^2 (81\mu^6 + 45\mu^2 + 2)^{7/6}}. \tag{21}$$

Dividing (21) by (20), defines the function $h(\mu)$ as

$$h(\mu) \equiv \frac{1}{p} \frac{df}{d\mu} = \frac{d\theta}{d\mu} = -\frac{9\mu (9\mu^2 - 1)^{1/2} (243\mu^8 + 324\mu^6 + 234\mu^4 + 148\mu^2 + 75)}{2 (9\mu^4 + 3\mu^2 + 4)^{1/2} (27\mu^4 + 5) (81\mu^6 + 45\mu^2 + 2)}, \tag{22}$$

which is the first derivative of the polar coordinate θ with respect to the parameter μ .

By integrating $h(\mu)$ over $d\mu$, one finds the parametric relationship between the polar angle θ and the parameter μ

$$\theta = \int h(\mu) d\mu + \beta, \tag{23}$$

where β is a constant of integration equal to π . The symbolic mathematics computer program Mathematica® 7 was used to evaluate this indefinite integral analytically. For conciseness, the result is reproduced

here in decimal form as

$$\theta = \sum_{j=1}^6 C_j(\mu) + \pi, \tag{24}$$

$$C_1(\mu) \equiv (-0.327975 + 0.498185i)F(\psi | m), \tag{25}$$

$$C_2(\mu) \equiv (-0.971129 + 0.0747711i)\Pi(-1.25 + 0.968241i; \psi | m), \tag{26}$$

$$C_3(\mu) \equiv -(0.0622228 + 0.148923i)\Pi(-0.8090192 + 0.468624i; \psi | m), \tag{27}$$

$$C_4(\mu) \equiv (0.16139 - 0.00170961i)\Pi(0.896508 - 0.265318i; \psi | m), \tag{28}$$

$$C_5(\mu) \equiv (0.315179 + 0.921599i)\Pi(1.5625 - 0.242062i; \psi | m), \tag{29}$$

$$C_6(\mu) \equiv (0.884757 - 1.34392i)\Pi(1.787511 + 4.153800i; \psi | m), \tag{30}$$

where

$$\psi \equiv \sin^{-1}\left(i\sqrt{\frac{2(9\mu^2-1)}{5+3i\sqrt{15}}}\right), \quad m \equiv \frac{5+3i\sqrt{15}}{5-3i\sqrt{15}}, \tag{31}$$

and the first $F(\psi | m)$ and third $\Pi(n; \psi | m)$ incomplete elliptical integrals are defined by

$$F(\psi | m) \equiv \int_0^\psi \frac{dz}{\sqrt{1-m\sin^2 z}}, \quad \Pi(n; \psi | m) \equiv \int_0^\psi \frac{dz}{(1-n\sin^2 z)\sqrt{1-m\sin^2 z}}. \tag{32}$$

Functions $C_1(\mu)$ and $C_6(\mu)$ in (24) are real valued functions despite the use of complex variable notation in their representation. On the other hand, functions $\{C_2(\mu), C_5(\mu)\}$ and $\{C_3(\mu), C_4(\mu)\}$ constitute complex conjugates and must be added together in pairs to obtain real valued functions. The original exact symbolic output, which involves numerous radicals, has been truncated in decimal form here to save space. Consequently, if one wishes to manipulate the truncated form of the solution, for instance, for plotting, one may need to take the real part of Equation (24) computationally to avoid receiving an error message related to a tiny but nonzero imaginary part.

3. Crack problem

The branch of the general solution to the governing differential equation appropriate for this crack problem was obtained in [Unger 2008] and will not be repeated here. The general solution applies to sectors AOB and BOC of the crack geometry shown in the insert of Figure 2. The singular solution, defined parametrically by (18) and (24), governs the leading sector of the crack problem COD as illustrated in Figure 2. An iterative computer program was developed to determine the parameters of the general solution and to find the corresponding angles which divide the three distinct regions of the half plane subject to equilibrium. The solution parameters defined in [Unger 2008] were found by this iterative procedure as

$$c = 0.15501\sigma_0, \quad \alpha = -0.39503, \tag{33}$$

while the corresponding angles were determined as

$$\theta_{AOB} = 0.52000 = 29.79^\circ, \quad \theta_{AOC} = 1.76886 = 101.35^\circ. \tag{34}$$

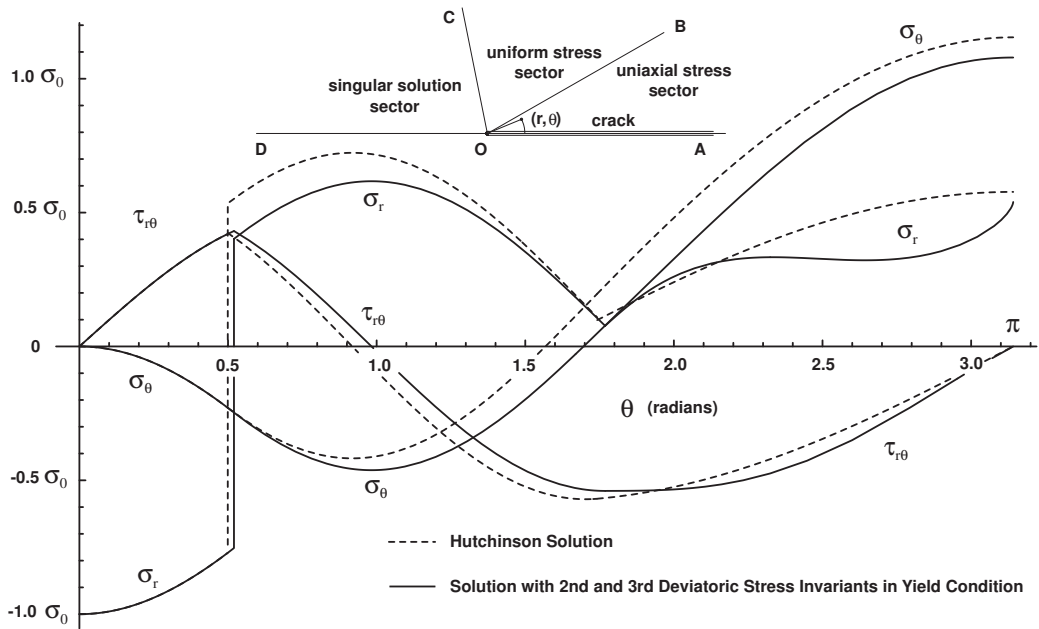


Figure 2. Comparison of perfectly plastic stress fields of the mode I fracture problem.

The stresses obtained from the stress functions are also plotted in Figure 2. For comparison the analogous solution obtained in [Hutchinson 1968] using the Mises yield condition is also shown. The results obtained here are qualitatively similar to those obtained in [Unger 2008] using an approximate singular solution. Quantitatively, the angle θ_{AOB} , determined using the approximate singular solution, differs from the value obtained using the exact singular solution by about 2.6% error. Correspondingly, the approximate value of θ_{AOC} differs from the exact value by about 1.3% error.

References

- [Chakrabarty 1987] J. Chakrabarty, *Theory of plasticity*, pp. 21–23, McGraw-Hill, New York, 1987.
- [Hutchinson 1968] J. W. Hutchinson, “Plastic stress and strain fields at a crack tip”, *J. Mech. Phys. Solids* **16**:5 (1968), 337–347.
- [Unger 2008] D. J. Unger, “A plane stress perfectly plastic mode I crack problem for a yield condition based on the second and third invariants of the deviatoric stress tensor”, *J. Mech. Mater. Struct.* **3**:4 (2008), 795–807.
- [Zwillinger 1989] D. Zwillinger, *Handbook of differential equations*, Academic Press, Boston, 1989.

Received 25 May 2009. Accepted 13 Jun 2009.

DAVID J. UNGER: du2@evansville.edu

Department of Mechanical and Civil Engineering, University of Evansville, 1800 Lincoln Avenue, Evansville, IN 47722, United States

<http://mece.evansville.edu/faculty/unger.asp>

SUBMISSION GUIDELINES

ORIGINALITY

Authors may submit manuscripts in PDF format on-line. Submission of a manuscript acknowledges that the manuscript is *original and has neither previously, nor simultaneously, in whole or in part, been submitted elsewhere*. Information regarding the preparation of manuscripts is provided below. Correspondence by email is requested for convenience and speed. For further information, consult the web site at <http://www.jomms.org> or write to

jomms.steele@stanford.edu

LANGUAGE

Manuscripts must be in English. A brief abstract of about 150 words or less must be included. The abstract should be self-contained and not make any reference to the bibliography. Also required are keywords and subject classification for the article, and, for each author, postal address, affiliation (if appropriate), and email address if available. A home-page URL is optional.

FORMAT

Authors are encouraged to use L^AT_EX and the standard article class, but submissions in other varieties of T_EX, and, exceptionally in other formats, are acceptable. Electronic submissions are strongly encouraged in PDF format only; after the refereeing process we will ask you to submit all source material.

REFERENCES

Bibliographical references should be listed alphabetically at the end of the paper and include the title of the article. All references in the bibliography should be cited in the text. The use of B^IB_T_EX is preferred but not required. Tags will be converted to the house format (see a current issue for examples), however, in the manuscript, the citation should be by first author's last name and year of publication, e.g. "as shown by Kramer, et al. (1994)". Links will be provided to all literature with known web locations and authors are encouraged to provide their own links on top of the ones provided by the editorial process.

FIGURES

Figures prepared electronically should be submitted in Encapsulated PostScript (EPS) or in a form that can be converted to EPS, such as GnuPlot, Maple, or Mathematica. Many drawing tools such as Adobe Illustrator and Aldus FreeHand can produce EPS output. Figures containing bitmaps should be generated at the highest possible resolution. If there is doubt whether a particular figure is in an acceptable format, the authors should check with production by sending an email to

production@mathscipub.org

Each figure should be captioned and numbered so that it can float. Small figures occupying no more than three lines of vertical space can be kept in the text ("the curve looks like this:"). It is acceptable to submit a manuscript with all figures at the end, if their placement is specified in the text by comments such as "Place Figure 1 here". The same considerations apply to tables.

WHITE SPACE

Forced line breaks or page breaks should not be inserted in the document. There is no point in your trying to optimize line and page breaks in the original manuscript. The manuscript will be reformatted to use the journal's preferred fonts and layout.

PROOFS

Page proofs will be made available to authors (or to the designated corresponding author) at a web site in PDF format. Failure to acknowledge the receipt of proofs or to return corrections within the requested deadline may cause publication to be postponed.

Journal of Mechanics of Materials and Structures

Volume 4, N^o 9 November 2009

- Buckling of stiffened composite panels with stringer terminations**
ENZO COSENTINO and PAUL WEAVER 1505
- An asymptotic analysis of anisotropic heterogeneous plates with consideration of end effects**
JUN-SIK KIM 1535
- Remarks on the accuracy of algorithms for motion by mean curvature in bounded domains**
SIMON COX and GENNADY MISHURIS 1555
- Laminated and sandwich panels subject to blast pulse loading**
UGO ICARDI and LAURA FERRERO 1573
- Uniformity of stresses inside an anisotropic elliptical inhomogeneity with an imperfect interface**
XU WANG 1595
- Modeling dislocation sources and size effects at initial yield in continuum plasticity**
SAURABH PURI, ANISH ROY, AMIT ACHARYA and DENNIS DIMIDUK 1603
- Forced vibrations of a nonlinear oscillator with weak fractional damping**
YURIY A. ROSSIKHIN, MARINA V. SHITIKOVA and TATIANA SHCHEGLOVA 1619
- A two-temperature generalized thermoelastic medium subjected to a moving heat source and ramp-type heating: A state-space approach**
HAMDY M. YOUSSEF 1637
- A plane stress perfectly plastic mode I crack problem for a yield criterion based on the second and third invariants of the deviatoric stress tensor, II**
DAVID J. UNGER 1651